TECHNISCHE UNIVERSITÄT MÜNCHEN
TUM School of Engineering and Design

Compaction Characteristics of Thermoset Automated Fiber Placement

Ralf Knott

Vollständiger Abdruck der von der TUM School of Engineering and Design der Technischen Universität München zur Erlangung des akademischen Grades eines

Doktors der Ingenieurwissenschaften

genehmigten Dissertation.

Vorsitz:	Prof. Dr.-Ing. Markus Ryll
Prüfer der Dissertation:	Prof. Dr.-Ing. Klaus Drechsler
	Prof. Paul Compston, Ph.D.

Die Dissertation wurde am 15.03.2022 bei der Technischen Universität München eingereicht und durch die TUM School of Engineering and Design am 12.05.2022 angenommen.

Technische Universität München
TUM School of Engineering and Design
Lehrstuhl für Carbon Composites
Boltzmannstraße 15
D-85748 Garching bei München

Tel.:+ 49 (0) 89 / 289 - 15092
Fax: + 49 (0) 89 / 289 - 15097
Email: info.lcc@ed.tum.de
Web: www.asg.ed.tum.de/lcc

Declaration

Ich erkläre hiermit ehrenwörtlich, dass ich die vorliegende Arbeit selbstständig und ohne Benutzung anderer als der angegebenen Hilfsmittel angefertigt habe; die aus fremden Quellen (einschließlich elektronischer Quellen) direkt oder indirekt übernommenen Gedanken sind ausnahmslos als solche kenntlich gemacht. Die Arbeit wurde in gleicher oder änlicher Form noch keiner anderen Prüfungsbehörde vorgelegt.

Ort, Datum	Ralf Knott

Acknowledgement

I would like to thank many people at this point, without whom I wouldn't have been able to do this work.
First, I want to thank my academic supervisor Prof. Klaus Drechsler for giving me the opportunity to work on this topic, for providing an environment full of opportunities and individual freedom and for your feedback on my work.
Second, I express my gratitude to Prof. Paul Compston for taking over the co-examination of the thesis. Thank you for your feedback on my work, and also for providing me the opportunity for CT measurements at ANU.
The deputy heads of the Chair of Carbon Composites (LCC) Elisabeth Ladstätter and Swen Zaremba as well as my research group leader Christoph Ebel always supported me, had an open door and provided flexibility in my work. Thank you for this! During my years at the LCC, I had the pleasure to work with many nice and smart colleagues that inspired and taught me a lot, and also contributed significantly to me having a good time. Thank you especially to my AFP colleagues Klaus, Benno, Stefan, Andreas, Roland and Daniel as well as my REXUS teammates Jonathan and Stefan. Thank you to Luciano and Daniel for advising and supporting my laboratory trials, and Reiner and Clemens for keeping the workshop up and running. Thanks also to the many students that supported me with my thesis, but also with my other topics at the LCC. Your motivation and perseverance has inspired and driven me, and I am happy to see some of you as my successors at the LCC. Thanks a lot also to my proofreaders Andreas, Stefan and Swen for your effort and the valuable feedback.
I want to thank my parents Ute and Helmut and my brother Thomas for always supporting me and providing me an environment in which I was able to thrive and follow my own path. Finally, I want to thank my wife Carola and my daughter Cleo for your motivation, forbearance and loving support.

Munich, December 2021

Ralf Knott né Engelhardt

Abstract

Automated Fiber Placement (AFP) is a well-established process in aerospace manufacturing with advantages regarding deposition accuracy and flexibility, reproducibility and potential lay-up rate compared to manual lay-up. Process parameters are typically optimized regarding deposition quality and deposition rate – not taking into account ancillary processes like vacuum debulking, despite its influence on the overall process efficiency. Compaction is a key parameter of prepreg lay-up realizing laminate consolidation during deposition, additional vacuum debulking steps and during curing. The application of vacuum debulking is often based on trial and error, unquantified experience or manufacturing specifications for manual lay-up. Automated lay-up offers the potential to improve compaction during deposition, allowing a reduction of additional debulking efforts.

In this thesis, the compaction characteristics of Thermoset Automated Fiber Placement (TS-AFP) and vacuum debulking are analyzed on laboratory and industrial full-scale. The influence of parameter variations on compaction behavior, mechanical performance and process efficiency is assessed.

Experimental methods were developed to characterize laminate compaction on laboratory and full-scale. The effect of vacuum debulking was quantified for different temperatures and laminate configurations. On laboratory scale, the dominance of the process parameters temperature and pressure was identified. On full-scale, the influence of the AFP process on the deposition quality was proven. An optimized AFP process parameter set was developed and evaluated. Compaction during AFP processing was increased, while the need for separate vacuum debulking steps was eliminated. It was shown, that the optimized AFP process parameter set leads to equal or better mechanical performance compared to the benchmark including dedicated vacuum debulking steps. Process efficiency analyses showed that the proposed approach is economically competitive or even superior to the benchmark for typical AFP use cases. The proposed optimization allows exploiting more of the potential of automated lay-up and opens new possibilities towards reduced curing efforts.

Kurzfassung

Automated Fiber Placement (AFP) ist ein etablierter Prozess in der Luft- und Raumfahrtindustrie, mit Vorteilen hinsichtlich Ablagegenauigkeit und -flexibilität, Reproduzierbarkeit und der potenziellen Legeleistung im Vergleich zu manueller Fertigung. Die Prozessparameter werden in der Regel auf Ablagequalität und -rate optimiert – ohne Nebenprozesse wie das Vakuum-Zwischenkompaktieren zu berücksichtigen, obwohl es die Effizienz des Gesamtprozesses beeinflusst. Kompaktierung ist ein wesentlicher Parameter in der Herstellung eines Prepreg-Laminats, der bei der Ablage selbst, in separaten Vakuum-Zwischenkompaktierungsschritten und während der Aushärtung aufgebracht wird. Die Anwendung der Zwischenkompaktierung basiert oft auf unquantifizierten Erfahrungswerten oder Fertigungsspezifikationen für die manuelle Fertigung. Automatisierte Legeprozesse bieten das Potenzial, die Kompaktierung während der Ablage zu verbessern, was eine Reduzierung separater Zwischenkompaktierungsschritte ermöglicht.

In dieser Arbeit werden die Kompaktierungseigenschaften von Thermoset Automated Fiber Placement (TS-AFP) und Vakuum-Zwischenkompaktierung im Labor- und industriellen Maßstab analysiert. Der Einfluss von Parametervariationen auf das Kompaktierungsverhalten, die mechanischen Eigenschaften und die Prozesseffizienz wird bewertet.

Ein optimierter AFP-Prozessparametersatz wurde entwickelt und bewertet. AFP-Kompaktierung wurde erhöht, während separate Ziwschenkompaktierungsschritte eliminiert wurden. Der Einfluss der Zwischenkompaktierung wurde für verschiedene Temperaturen und Laminatkonfigurationen quantifiziert. Im Labormaßstab wurde die Dominanz der Prozessparameter Temperatur und Druck festgestellt. In unskalierten Versuchen wurde der Einfluss des AFP-Prozesses auf die Legequalität nachgewiesen. Es konnte gezeigt werden, dass die optimierten AFP-Prozessparameter im Vergleich zum Benchmark zu gleichwertigen oder besseren mechanischen Eigenschaften führt. Analysen der Prozesseffizienz haben gezeigt, dass der vorgeschlagene Ansatz für typische AFP-Anwendungsfälle wirtschaftlich konkurrenzfähig oder dem Benchmark sogar überlegen ist. Die vorgeschlagene Optimierung ermöglicht es, mehr des Potenzials automatisierter Legeverfahren auszuschöpfen und eröffnet neue Möglichkeiten zur Reduzierung des Aushärtungsaufwands.

Table of contents

List of Figures

List of Tables

Nomenclature

List of symbols

Latin letters

a	Ply alignment or fiber orientation	–
A	Area	m^2
$A_{av.p.p.}$	Average area per ply of a laminate	m^2
A_r	Contact area of a compaction roller	m^2
A_{re}	Area of a reinforcement ply	m^2
A_S	Bending beam theory constant	m^2
A_{SH}	Strain hardening coefficient	–
A_{skin}	Area of a skin ply	m^2
A_{total}	Area of all plies	m^2
c	Compaction type	–
C_{high}	UTM samples with sequential compaction (SQ) with high compaction parameter settings	–
C_{low}	UTM samples with sequential compaction (SQ) with low compaction parameter settings	–
D_{high}	UTM samples with lay-up compaction and debulking with high compaction parameter settings	–
D_{low}	UTM samples with lay-up compaction and debulking with low compaction parameter settings	–
d_r	Roller diameter	mm
$E_3(t)$	Time dependent through-thickness modulus	N/mm^2
E_e	Equilibrium modulus	N/mm^2
E_f	Flexural modulus or modulus of the fiber	N/mm^2
E_i	Relaxation modulus	N/mm^2
E_m	Modulus of the matrix	N/mm^2
E_{meas}	Measured modulus (opposed to normalized modulus)	N/mm^2
$E_{norm,11}$	Normalized modulus parallel to the fibers	N/mm^2
$E_{norm,22}$	Normalized modulus perpendicular to the fibers	N/mm^2

E_r	Elastic modulus of a compaction roller	N/mm^2
E_T	Tensile modulus	N/mm^2
E_{T11}	Tensile modulus parallel to the fibers determined as secant modulus between $F_R/10$ and $F_R/2$	N/mm^2
E_{T22}	Tensile modulus perpendicular to the fibers determined as secant modulus between $F_R/10$ and $F_R/2$	N/mm^2
F	Force	N
$F(t)$	Time dependent force	N
F_R	Load at failure	N
F_{max}	Maximum force	N
F_z	Load in z-direction	N
L	4-point bending test support span	mm
L_{high}	UTM samples with lay-up compaction only (no debulking) with high compaction parameter settings	–
L_{low}	UTM samples with lay-up compaction only (no debulking) with low compaction parameter settings	–
m_{SH}	Strain hardening coefficient	–
n	Number of plies	–
n_P	Number of Prony series coefficients	–
n_{re}	Number of reinforcement plies	–
n_{skin}	Number of skin plies	–
$P_{IR,max}$	Maximum power of the infrared heat source	W
p	Pressure	MPa
p_0	Initial pressure $p_0 = 0\ Pa$	Pa
p_c	Compaction pressure	Pa
p_d	Debulking pressure	Pa
p_r	Resin pressure	Pa
p_{tm}	Pressure applied for thickness measurement $p_t m = 25 Pa$	Pa
r_r	Radius of a compaction roller	m
R_z	Roughness depth	–
R^2	Coefficient of determination	–
s'	Deflection of the sample center during a 4-point bending test for $\varepsilon = 0.0005$	mm
s''	Deflection of the sample center during a 4-point bending test for $\varepsilon = 0.0025$	mm
T	Temperature	°C
t	Thickness	mm
t_f	Final thickness	mm

t_{il}	Initial laminate thickness	mm
t_{ip}	Initial ply thickness	mm
t_{meas}	Measured thickness	mm
t_{ref}	Reference thickness as defined in the test standard	mm
u_z	Laminate displacement in z-direction	mm
$\overline{u}_z$	Theoretical roller deformation in z-direction	mm
V_0	Initial fiber volume fraction	–
V_a	Available (maximum possible) fiber volume fraction	–
V_f	Fiber volume fraction	–
w	width	mm

Greek letters

ΔF	Difference of force between s' and s'' during a 4-point bending test	N
Δs	Difference of deflection between s' and s'' during a 4-point bending test	mm
ε	Strain	–
ε_1	Tensile strain 0.0005	–
ε_2	Tensile strain 0.0025	–
ε'_f	Flexural strain 0.0005	–
ε''_f	Flexural strain 0.0025	–
ν_r	Poisson's ratio of a compaction roller	–
ρ_0	Yield stress	N/mm^2
ρ_f	Fiber density	kg/cm^3
ρ_{is}	Instantaneous stress	N/mm^2
$\rho_{nominal}$	Nominal density according to the data sheet	kg/cm^3
ρ_{norm}	Normalized density	kg/cm^3
σ	Stress	N/mm^2
$\overline{\sigma}$	Effective stress on the fiber bed	N/mm^2
σ_1	Tensile strength at $\varepsilon_1 = 0.0005$ (0.05%)	N/mm^2
σ_2	Tensile strength at $\varepsilon_1 = 0.0025$ (0.25%)	N/mm^2
σ_f	Flexural (bending) strength	N/mm^2
σ_{fn}	Average effective stress in the fiber network	N/mm^2
σ_l	Total stress on a laminate	N/mm^2
σ_T	Ultimate tensile strength	N/mm^2
σ_{T11}	Ultimate tensile strength parallel to the fibers	N/mm^2
σ_{T22}	Ultimate tensile strength perpendicular to the fibers	N/mm^2

τ_{12}	Apparent interlaminar shear strength (ILSS)	N/mm^2
φ	Fiber volume content (FVC)	–
φ_{norm}	Normalized fiber volume content (FVC)	–
φ_{calc}	Calculated fiber volume content (FVC)	–

List of abbreviations

AC	autoclave curing
AFP	Automated Fiber Placement
ANU	Australian National University
AR	aspect ratio
ATL	Automated Tape Laying
BD	bi-directional
bm	benchmark compaction
BP	blocked ply
CAD	computer aided design
CF	carbon fiber
CFRP	carbon fiber reinforced polymer
CP	cross ply 0/90
CPT	cured ply thickness
CSF	compressive stress failure
CT	computer tomography
DFP	Dry Fiber Placement
DIC	digital image correlation
DLR	German Aerospace Center
DMA	dynamic mechanical analysis
DOC	degree of cure
DSC	differential scanning calorimetry
EoD	effect of defects
ESA	European Space Agency
EU	European Union
FAW	fiber areal weight
FE	finite element
FEA	finite element analysis
FPP	fiber patch placement
FRP	fiber reinforced polymer
FVC	fiber volume content
GF	glass fiber
ILSS	interlaminar shear strength
IM	intermediate modulus
IPCC	Intergovernmental Panel on Climate Change
IR	infrared
LCC	Chair of Carbon Composites

LCM	Liquid Composite Molding
LED	light emitting diode
LRZ	Leibniz supercomputing center
mc	minimized compaction
MCL	minimum cut length
MFFD	multi functional fuselage demonstrator
MP	mega pixel
NASA	National Aeronautics and Space Administration
NC	numerical control
NDT	non destructive testing
oc	optimized compaction
OC1	"optimized compaction 1" parameter set
OC2	"optimized compaction 2" parameter set
prepreg	pre-impregnated
QI	quality inspection
REXUS	rocket experiments for university sutdents
RT	room temperature
RTM	Resin Transfer Molding
SB	semi blocked ply
SBS	short beam shear test
SC	soft curing
SIM	simultaneous stack compaction
SLS	Space Launch System
SQ	sequential compaction
SRIM	Structural Reaction Injection Molding
TP	thermoplastic
TP-AFP	Thermoplastic Automated Fiber Placement
TS	thermoset
TS-AFP	Thermoset Automated Fiber Placement
TSF	tensile stress failure
TUM	Technical University of Munich
UD	unidirectional
UMAT	user defined material model
UT	ultrasonic testing
UTM	universal testing machine
VBO	vacuum bag only
VC	vacuum curing
VVC	void volume content

1 Introduction

With the increasing demand for mobility in a globalized world, the associated environmental impact is also growing. It is now *"unequivocal that human influence has warmed the atmosphere, ocean and land"*, as stated by the IPCC in 2021 [1]. To achieve climate neutrality, the European Green Deal by the European Commission defined the need to reduce transport emissions by 90 % by 2050 compared to 1990 [2]. Mass reduction through lightweight design is one of the necessary approaches to increase the efficiency of mobility and reduce its emission footprint.

The high specific strength and stiffness of fiber reinforced polymer (FRP), especially carbon fiber reinforced polymer (CFRP), makes it a predestined material for lightweight applications [3]. State of the art aircraft, as the *Airbus A350XWB* or the *Boeing 787*, apply CFRP composite materials for more than 50 % by weight of the primary structure. The high demands in aerospace manufacturing regarding rate and efficiency, but also quality and its reproducibility, make automated manufacturing indispensable. [4]

Automated Fiber Placement (AFP) is one of the key technologies for the automated composite manufacturing for aerospace applications. A placement head deposits carbon fiber (CF) reinforced unidirectional (UD) tapes along a programmed path on a tool surface. The separate, additive deposition of tapes enables the creation of a complex laminate of high performance. Thermoset Automated Fiber Placement (TS-AFP) is using prepreg tapes with uncured thermoset resin. Advantages of the AFP process are the high precision and repeatability of the deposition, with the option to implement a tape-individual fiber orientation along the load path. The individual cut and feed of narrow tapes leads to a high material efficiency potential with a near-net-shape lay-up and allowing low scrap rates.

The TS-AFP lay-up process is regularly interrupted by vacuum debulking after a certain amount of plies to ensure a defined compaction state of the laminate. This requires a bagging of the laminate followed by compaction through vacuum application for typically 10 to 30 minutes. This iteration of ply deposition and vacuum debulking is repeated until the laminate is fully deposited, followed by a resin curing process step. For aerospace applications, this is commonly done in an

autoclave under the application of temperature and additional pressure. Here, the final laminate compaction is realized, including void reduction and resin curing. [5]

The time-consuming application of vacuum debulking is in many cases based on trial and error, unquantified experience or manufacturing specifications based on manual lay-up. Automated lay-up processes like AFP offer a more defined and repeatable compaction during deposition, potentially allowing a minimization of additional debulking steps. This potential benefit of the AFP process has not yet been publicly analyzed and taken into account for the optimization of the overall process efficiency.

1.1 Objectives

The overall objective of this thesis is to analyze the compaction characteristics of the TS-AFP process chain in order to optimize its efficiency. A major advantage of automated material deposition is its accuracy and repeatability compared to manual processes. However, this advantage is not yet exploited when it comes to material compaction. Additional vacuum debulking steps are still applied, as in times of manual lay-up. The goal of this thesis is therefore to analyze if and to what extent the defined compaction within the TS-AFP process can be used to reduce the effort for vacuum debulking. The objectives necessary to answer this question are:

- **Characterization of vacuum debulking**
  The application of vacuum debulking is still the benchmark in industrial applications of the TS-AFP process chain. It is in many cases applied based on manufacturing procedures created for manual material deposition and relying on unquantified experience. The compaction effect of vacuum debulking shall be characterized for different temperatures and lay-up architectures. For this, an experimental method is to be developed. This can be found in Chapter 3.

- **Characterization of TS-AFP compaction**
  The compaction characteristics of TS-AFP have to be characterized with respect to variations of the process parameters and the application of additional vacuum debulking steps during the TS-AFP lay-up process. Experimental methods for the quantification of the thickness progression during the process shall be developed for full-scale and laboratory scale experiments. The influence of the compaction related process parameter variations on the mechanical properties of the laminate shall be characterized. This is addressed in Chapter 4 and Chapter 5.

- **Derivation and evaluation of an optimized TS-AFP parameter set**
  An optimized parameter set is to be developed based on the compaction characterization. The optimized parameter set shall be applied and evaluated. The goal is, to increase the deposition quality, i.e. the homogenity of the laminate by a reduction of inter-ply voids through deposition. The matrix dominated material properties reached by the AFP process shall be improved to enable a reduction of separate vacuum debulking. This is part of Chapter 5 and Chapter 6.

- **Assessment of the economic efficiency and industrial applicability**
  The optimized process parameter set shall be evaluated for its process efficiency impact and its industrial applicability in use case scenarios representative for aerospace manufacturing. An overall reduction of the combined process time of AFP lay-up and vacuum debulking shall be enabled by the optimized process parameters. This is addressed in Chapter 6.

1.2 Outline

The thesis is structured in five main chapters, apart from the introduction in Chapter 1 and the conclusions and outlook in Chapter 7.

Chapter 2 reports the state of the art of the AFP process and prepreg CFRP material. The TS-AFP equipment used for this thesis is described and a literature review on compaction of prepreg materials and compaction in the AFP process is presented.

In **Chapter 3**, the compaction during vacuum debulking is characterized with continuous thickness measurements at varying process parameters.

Chapter 4 describes the replication and analysis of AFP compaction in laboratory scale. Cyclic compaction experiments are implemented on small scale using a rheometer and on medium scale using a universal testing machine (UTM). A numerical simulation model is applied to replicate the cyclic experiments.

Compaction experiments on full-scale level using a TS-AFP machine are presented in **Chapter 5**. The compaction behavior during lay-up is analyzed with thickness measurements during processing. The influence of varying compaction parameters and curing methods on the mechanical performance is characterized.

Chapter 6 includes a process efficiency analysis, evaluating the potential of optimized AFP process parameters. An AFP process time model is developed, validated and applied to a process parameter sensitivity analysis and a use case study.

2 Theory and state of the art

This chapter provides a literature overview on the relevant theory and state of the art. The introduction to AFP in Sec. 2.1 gives insights to the process principle and technology, the AFP process chain, AFP applications and state of research as well as the TS-AFP equipment used in this thesis. Sec. 2.2 includes a short overview on material basics of composites and prepreg material and lists the details of the material used in this thesis. In Sec. 2.3, the theory and state of research of compaction is presented for composite and prepreg materials as well as for AFP.

2.1 Automated Fiber Placement (AFP)

Automation of the manufacturing of CFRP aerospace structures is an ongoing trend in the light of increasing production volumes and cost pressure at high requirements regarding quality. Automated Fiber Placement (AFP) and Automated Tape Laying (ATL) are placement technologies typically used for the automated manufacturing of aerospace structures. In both processes, prepreg UD tape is deposited by an automated placement system. The advantages compared to manual lay-up are especially the repetitive positioning accuracy and a potentially high deposition rate. [6, 7]

ATL processes wide tapes and is limited to geometries of low complexity. Typical applications are fuselage panels or wing skins. AFP deposits several narrow tapes and has a higher flexibility regarding drapability and geometric accessibility, allowing for more complex structures. The process is used for small to medium sized panels and skins, but also complex double curved frames, cones and ramped sandwich panels. [5, 8–10]

In this section, the AFP process principle, technology and process chain are explained with a focus on TS-AFP. AFP applications and the state of research are shown, followed by the TS-AFP equipment used in this thesis.

2.1.1 AFP process principle and technology

In the Automated Fiber Placement (AFP) process, CF tapes are deposited by a placement system. The tape material can be either pre-impregnated with thermoset (TS) or thermoplastic (TP) matrix, or dry bindered CF. A placement head sequentially deposits the tapes on a tooling surface in an additive manner. The trajectory of the placement head is determined by numerical control (NC) code generated in an offline programming software. The tapes are fed to the compaction head and pressed on the tooling surface by a compaction roller. The movement of the placement system relative to the tooling pulls off the tapes from the material storage. A heat source heats up the substrate and incoming tape and to ensure tack or consolidation of the tape on the substrate.

Fig. 2.1 shows the elements of a typical AFP system at the example of a *Coriolis Composites* AFP machine.

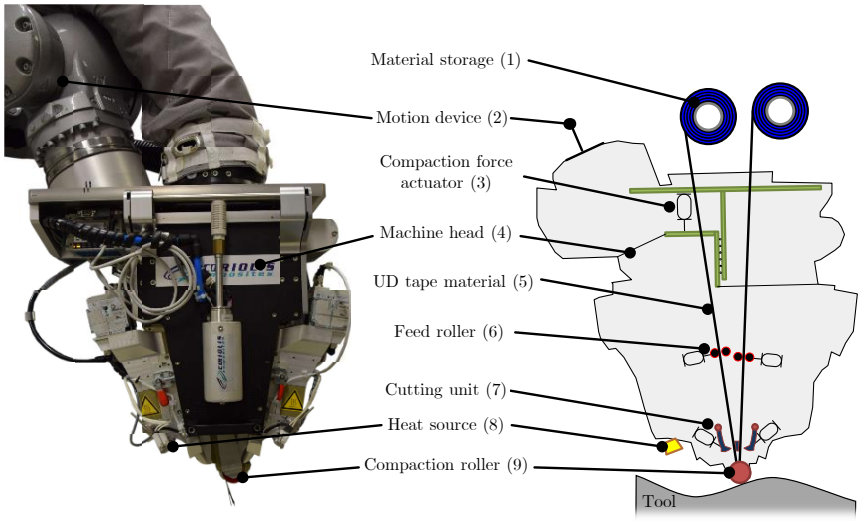

Figure 2.1: *Coriolis Composites* AFP machine (left) and its design principle (right). [11]

The tape material is stored on individual spools in a **material storage (1)** either directly on the placement head or in a separate creel. For thermoset matrix systems, the material storage can be required to be actively cooled to avoid contamination and ensure stable material conditions. In case of the *Coriolis Composites* system, the tapes are guided in separate air cooled tubes towards the placement head. A drum drive called *Multiwinch ®* feeds the tapes towards the head, maintaining a constantly low tape tension [12, 13]. The **motion device (2)** moves the placement head relative to the tool. Six degrees of freedom are required to maintain the desired orientation of the head towards a 3D tooling surface. The motion device is typically either a gantry or column portal or a six axis robot. A portal system

can cover very big part sizes at high accuracy and velocity, but requires a lot of space and initial investment cost. Robot guided AFP systems are flexible and have a good accessibility at low investment costs, but have a limited reach even when equipped with an additional linear axis. A defined compaction force is applied by a **compaction force actuator (3)**, which is typically a pneumatic actuator in the placement head. In case of geometric irregularities of the tool surface, the actuator can adjust the clearance of the placement head. The **machine head (4)** covers all components required for the tape deposition. Typical industrial AFP heads process 4 to 32 tapes at a width of $^1/_8''$ to $^1/_2''$. Each tape is guided, fed and cut individually. The AFP head shown in Fig. 2.1 is air cooled. The **UD tape material (5)** is either prepreg with TS or TP matrix, or dry bindered CF tape. Slit-tape is the most common tape type for aerospace applications, tow-preg offers potential for further cost reduction. Details on the material system are described in Sec. 2.2. The tapes are moved to the nip point below the compaction roller by **feed rollers (6)**. Once the tape is fixed below the compaction roller, the feed rollers are retracted and the tape is passively pulled off by the movement of the placement head. At the end of each track, the tapes are cut by a **cutting unit (7)**. As each tape can be cut individually, making a near-net-shape lay-up with low scrap rates in a range of 2 % to 6 % possible [4, 14–16]. The distance from the cutting unit to the nip point defines the minimum cut length (MCL). This MCL is a process restriction that has to be considered in the design and programming of the lay-up. For industrial AFP machines, the MCL typically ranges from 90 mm to 140 mm [5]. The maximum velocity at cut is another process restriction and influenced by the design of the cutting unit. Rotating cutters can reach higher velocities of up to 1 m/s than e.g. guillotine knives. [17, 18] A **heat source (8)** irradiates the substrate to increases the temperature at the nip point, ensuring sufficient adhesion of the deposited tape [19]. State of the art in industrial TS-AFP applications are infrared (IR) lamps. Thermoplastic Automated Fiber Placement (TP-AFP) requires higher energy input to both substrate and incoming tape, typically by laser systems, to heat the thermoplastic polymer above its melting point [20]. The **compaction roller (9)** applies the pressure of the placement head to the deposited tape and substrate. The roller is flexible to adapt to geometric complexities and irregularities of the deposition surface to maintain a full compaction of the tape without bridging effects. The roller typically consists of a silicone or polyurethane foam layer around a metal bearing core covered with an outer release coating film [4, 11]. TP-AFP processes require a cooled roller to withstand the high process temperatures [21]. Additional compaction plates trailing the compaction roller can

be required for full track compaction during angled deposition around small radii, like the deposition of spars.

2.1.2 AFP manufacturing process chain

The overall process chain of AFP manufacturing is summed up in the steps below [22]. Required inputs are the component geometry defined in CAD and the definition of a global lay-up based on the mechanical analysis and design.

1. Planning and programming
2. Production preparation
3. AFP processing
4. Curing
5. Finishing
6. Quality inspection

The **planning and programming** includes the definition of the ply book with all relevant boundary conditions and its implementation in the offline programming. In the ply book, all details of the lay-up are defined. This includes e.g. ply number, identification and contour, fiber orientation and material. The boundary conditions are typically defined in manufacturing specifications with general and process specific guidelines. The ply book is transferred to machine code via offline programming, usually in an equipment manufacturer specific CAD software. With the offline programming, a variety of AFP process specific details are defined. These are e.g. the staggering strategy, track distance, order and direction of track deposition, the process parameters or the separation of a ply into different sections. The program has a direct influence on the process efficiency, the lay-up quality and the scrap rate. A simulation of the machine movements based on the generated tool paths offers the opportunity to check for collisions and singularities of the robot. [5]

In the **production preparation**, the tool is mounted and aligned in the production cell. A calibration of dedicated reference points on the tool allows and adjustment of the program to the actual tool position to avoid lay-up distortions. A dry run of the program at reduced velocity is done to avoid collisions of the robot or ancillary parts like tubes or cables that are not considered in the simulation. The programming is iterated if required based on the results of the dry run. The tool surface is cleaned and impregnated with release agent. The prepreg tapes are

unfrozen according to the data sheet, material or process specification, installed in the creel and fed to the placement head past the feed unit.

The **AFP processing** consists of the additive deposition of plies divided into single tracks, as described in Sec. 2.1.1. The deposition is interrupted for intermediate vacuum debulking steps based on the manufacturing specifications or the experience of the manufacturer. For each ply, the lay-up is interrupted for a visual inspection looking for lay-up defects. This step can be avoided if an online process monitoring system is used as described in Sec. 2.1.3. Additional process interruptions can be caused by material reloading, cleaning or maintenance steps. The downtime can be minimized by adding two separate work cells to one AFP machine, as e.g. implemented in the production facilities at *Premium Aerotec* in Augsburg (cf. Fig. 2.2).

Figure 2.2: TS-AFP manufacturing of *Airbus A350* door surround frames at *Premium Aerotec frame center* in Augsburg. [23]

For aerospace prepreg applications, **curing** is typically done in an autoclave. If required, the laminate is transferred from the lay-up tool to a curing tool. The laminate is covered in a vacuum bag including peel ply and bleeder fabric. The autoclave curing cycle of an aerospace grade prepreg material system typically includes two heating ramps, two isothermal dwell times and a cool down ramp (cf. Fig. 2.3). The resin viscosity decreases significantly during the first heating ramp. The first dwell time is dedicated to void reduction, defined resin bleeding and homogenous heating of the entire laminate. The viscosity drops during the second heating ramp before the cross-linking starts and the viscosity rapidly increases. The second dwell time has to be long enough for all reactive partners to finalize the cross-linking. For aerospace grade material, this curing temperature is typically 180 °C. [24]

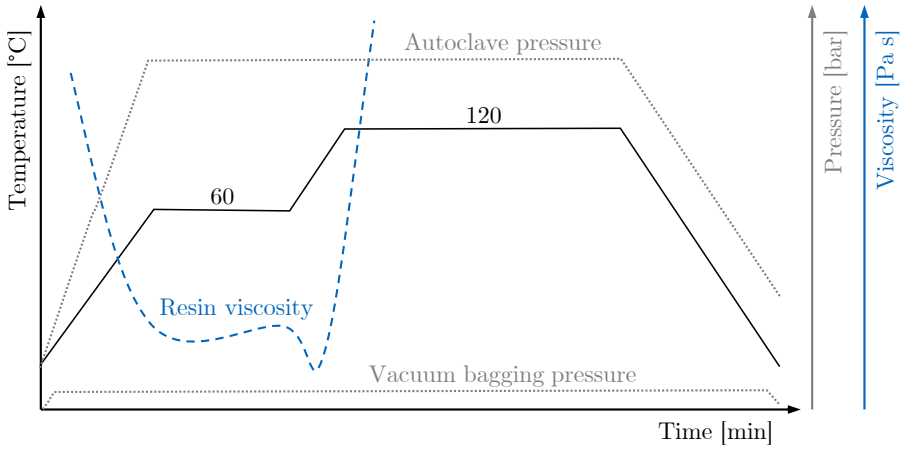

Figure 2.3: Typical curing cycle of prepreg laminates in an autoclave. Adapted from [5]

Finishing is done after the curing and involves cleaning and machining. The cured component is unpacked and demolded. Neat resin on the laminate surface is removed if required and the part is trimmed to its final contour. Cut-outs, inserts and other design features can be added if required. [25]

Quality inspection in aerospace composite manufacturing is typically done by inspecting 100 % of the produced parts via non destructive testing (NDT). Ultrasonic testing (UT) is a typical NDT method for CFRP components in serial production, as it can be automated and integrated in a production line with reliable results on a qualitative basis. After the quality inspection, the components are ready to be assembled or packed for shipping to assembly. [26]

2.1.3 Applications and state of research for AFP

TS-AFP is state of the art with many applications in the aerospace industry, e.g. fuselage panels, keel beam, the spars, skins and stringers of the wing or door surround structures of the *Airbus A350* [9, 27], fuselage sections of the *Boeing 787* [28], a payload adapter for the *Ariane 5* rocket [9] or large sandwich panels for the *NASA Space Launch System (SLS)* rocket [29].

Current research on TS-AFP is focusing on the one hand on experimental and numerical process optimization with the goal to increase the overall process efficiency with optimized process parameters and a reduction of ancillary and subsequent process steps [4, 34–37]. A deeper understanding of the heating characteristics and alternative heat sources to IR lamps, such as light emitting diode (LED) or flash lamps, allow higher lay-up velocities or improved quality [19, 38–40]. Numerical modelling leads to new potentials at the prediction of defects and the analysis of effect of defects (EoD) [41–46]. AFP allows the load path oriented deposition of

a) Airbus A350 door surround structure

b) Airbus A350 fuselage section

c) Boeing 787 fuselage section

d) Airbus A350 rear spar

Figure 2.4: TS-AFP lay-up of a) *Airbus A350* door surround structure at *Premium Aerotec* with a *Coriolis Composites C1* [30], b) *Airbus A350* wing skin with a *MTorres TORRESFIBERLAYUP* gantry machine [27, 31], c) *Boeing 787* fuselage section at *Spirit AeroSystems* with a *Electroimpact* machine [32], d) *Airbus A350* rear spar at *GKN* with a *MTorres TORRESFIBERLAYUP* column machine [33].

fibers leading to laminates with variable stiffness. This potential is not yet exploited in practice, but investigated in many studies and demonstrator projects [47–51]. Therefore the limits of in plane steering and the influence of material and process have to be characterized and optimized [52–57]. Material tack is of particular importance for AFP to ensure first ply adhesion and to minimize tack induced lay-up defects. Reproducible measurement of tack - offline and online - and the corresponding adaption of process parameters is hence of particular interest [58–63]. The detection of lay-up defects is currently done by visual inspection, which is time and labor intensive and prone to errors. A variety of mostly laser profilometer based automated inspection systems are in development and about to be implemented by the industry [64–68].

Thermoplastic polymers have potential advantages over thermoset polymers due to their chemical properties. They can be softened repeatably and do not require storage at low temperatures. New processes and efficient process chains are thus possible enabling higher volume production. TP-AFP can be especially efficient when in situ consolidation makes a subsequent consolidation in an autoclave ob-

solete. Current research is analyzing and optimizing the heating characteristics to enable 3D geometries with increasing complexity [21, 69–72]. In situ consolidation on of AFP tape on different substrates enables integral lightweight designs without additional adhesion or fastening efforts [70, 73–78]. TP-AFP with in situ consolidation is not yet established but focus of intense research efforts by the aerospace industry. Smaller demonstrators like a helicopter tail boom [79] or a rocket booster casing [80] have already proven its potential. The upper half demonstrator of the EU CleanSky multi functional fuselage demonstrator (MFFD) is supposed to take in situ consolidation to a next level regarding size and complexity [81]. Airworthiness of the technology has been proven by *Technical University of Munich* with the launch of an in situ consolidated structural module as part of a research rocket mission by DLR and ESA [34, 78, 82, 83].

Dry Fiber Placement (DFP) potentially has economic benefits, as it is not reliant on expensive prepreg as semi-finished product and provides the opportunity for out-of-autoclave curing. The key challenges yet to be solved are the permeability in z-direction and geometric stability of the preform [84–88].

Adapted versions of automated tape placement for specific applications have been developed and industrialized. In the fiber patch placement (FPP) process, separate fiber patches are placed on a mold, allowing the creation of complex preform geometries. In current research activities, the process is expanded to the automated placement of other structural components, like honeycomb core material. [89, 90]

Apart from applications in the aerospace industry, there are ongoing efforts to apply automated tape placement in the automotive or wind industry. However, the high cost pressure in these industries requires further process optimization. [4]

2.1.4 AFP equipment used in this thesis

The full-scale experiments of this thesis were conducted on a modified *Coriolis Composites C1* AFP machine in the *TUM Processing Lab* of the Chair of Carbon Composites at TUM (cf. Fig. 2.5). The placement head processes $8 \times 1/8''$ tapes summing up to a track width of $1''$ or 25.4 mm. A tiltable compaction roller mechanism allows bidirectional lay-up. The heat input is generated by an IR lamp with a max. power of 430 W. With a linear axis and a rotating tool carrier, the robot guided machine can work on tools of a maximum size of approximately $3\,m \times 2\,m$. The tapes are stored in a separate creel and guided through air cooled tubes to the placement head. A drum drive *Multiwinch ®* reduces the tape tension to a minimum. More details of the single components are described in Sec. 2.1.1.

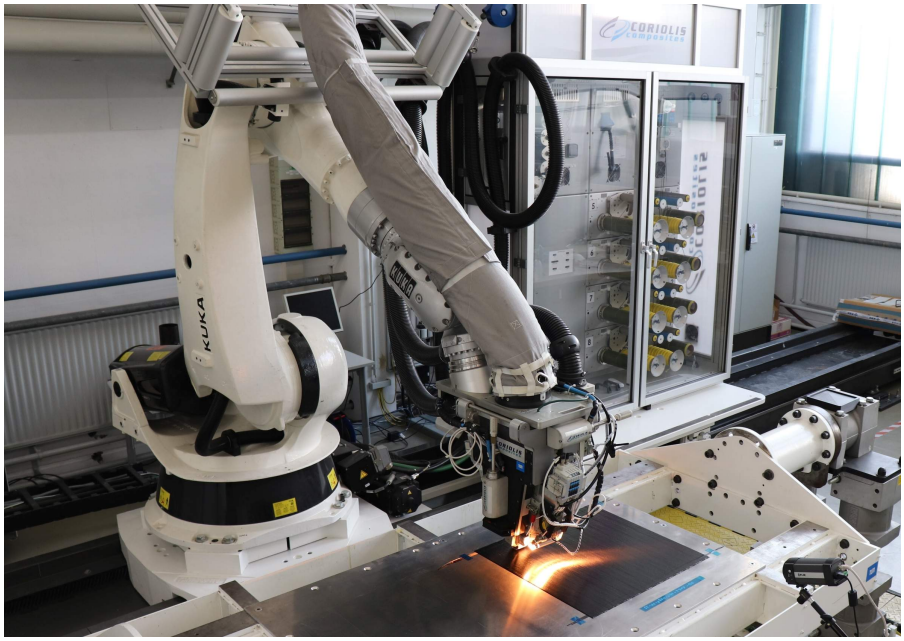

Figure 2.5: TS-AFP equipment by *Coriolis Composites* at *TUM Chair of Carbon Composites*.

2.2 Pre-impregnated (prepreg) carbon fiber reinforced polymers

This section provides a short overview on the basics of composites and prepreg material followed by details of the material used in this thesis.

2.2.1 Material basics of composites and prepreg

Fiber reinforced polymer (FRP) is a composite material system consisting of a polymer matrix and reinforcement fibers. For structural applications, the fibers are typically glass fiber (GF) or carbon fiber (CF). The most common matrix systems are either thermoset (TS) or thermoplastic (TP) polymers. The mechanical strength and stiffness of the composite are predominantly defined by the fibers, while the matrix fixes the fibers in their position, stabilizes them at compressive and shear loading and allows load transfer between the fibers. [3]

FRP composite materials have particularly good specific strength and stiffness ratios, and are therefore well suited for high performance lightweight applications (cf. Fig. 2.6 a). The composition of fiber and matrix leads to anisotropic material properties dependent on the fiber orientation, fiber length, fiber volume content and the laminate architecture (cf. Fig. 2.6 b). Natural structural materials in many cases are composites of hard and soft phases arranged in hierarchical structures ranging from nano- to macroscale, e.g. wood or bones [91]. Fig. 2.6 c shows the

complex fiber reinforced composite structure of bamboo with cellulose fibers being embedded in a lignin-hemicellulose matrix.

a) Specific stiffness and strength

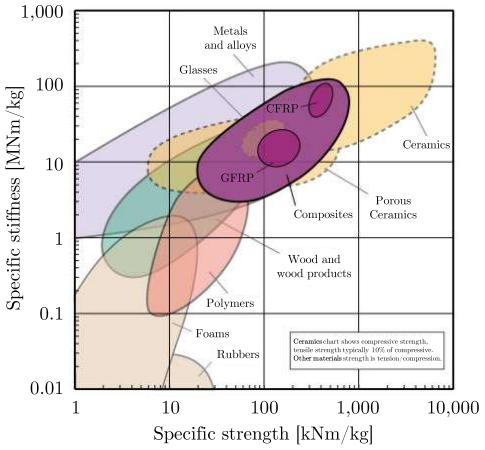

b) Elastic modulus over fiber volume

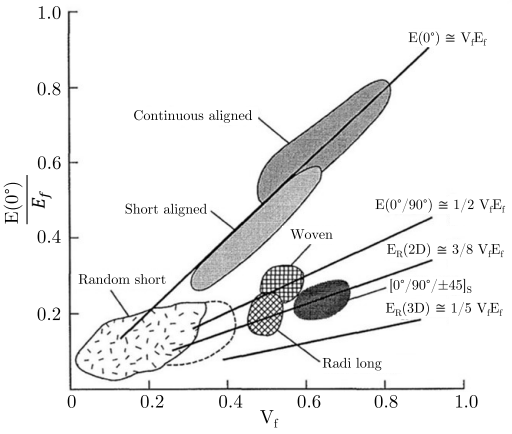

c) Composite structure of bamboo

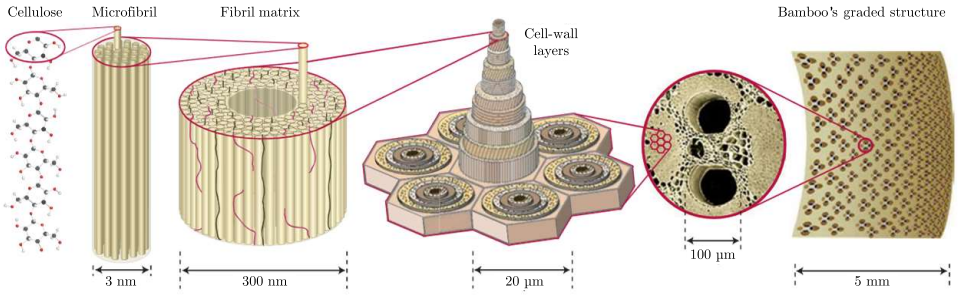

Figure 2.6: a) Specific stiffness and specific strength comparison of different materials. [92]
b) Obtainable elastic modulus (normalized by the fiber modulus E_f) for different composite arrangements with respect to fiber volume and fiber orientation. [6]
c) Composite structure of bamboo from nano- to macroscale. [91]

There are various ways of combining fiber and matrix to a composite component, ranging from manual lay-up and impregnation of dry fibers to fully automated deposition of pre-impregnated (prepreg) material in AFP or ATL processes. The choice of material or semi-finished product and manufacturing process depends on performance and quality requirements as well as boundary conditions such as production volume, cycle time or budget. Aerospace applications typically require the application of prepreg material due to its high performance and quality potential. Prepreg is a semi-finished material manufactured by impregnating UD fibers or woven fabric with thermoset resin. This separate process step allows tight tolerances of the resin content, its distribution and the fiber areal weight (FAW). [5]

Aerospace grade toughened prepreg materials have dissolved thermoplastic additives dispersed in the thermoset matrix to improve the fracture toughness and impact performance. The toughening also affects the processing characteristics with elevated viscosity and changes in the inter-ply friction. [37, 93, 94]

For processing in AFP systems, prepreg is converted to so called slit-tape. A UD prepreg parent tape of 600 mm width or more is cut into several narrow slit-tapes of a dedicated width with roller cutters. Typical widths for AFP applications are 3.2 mm ($^1/_8''$), 6.4 mm ($^1/_4''$) and 12.7 mm ($^1/_2''$). Slit-tape can be manufactured with high accuracy allowing cut width tolerances in the range of 0.1 mm, making it a semi-finished product with high performance and high versatility, but also high cost caused by the additional process steps. As an alternative, a fiber roving can be directly spread and impregnated to a so called tow-preg. Eliminating the intermediate step of a parent tape, tow-pregs can be significantly cheaper than slit-tapes, but it is challenging to meet the accuracy requirements for aerospace applications. This is why tow-preg is so far mostly limited to processes with lower performance requirements such as filament winding. [5]

2.2.2 Material used in this thesis

The materials used in this thesis were the toughened aerospace grade UD carbon prepreg systems *HexPly ® 8552/IM7* and *HexPly ® 8552/AS4* by *Hexcel*. It was used in either unslit UD condition or as slit-tape with a width of $^1/_8''$ or 3.175 mm. *HexPly 8552/IM7* has a nominal cured ply thickness of 0.130 mm with a nominal fiber volume content of 57.70 % and a nominal resin content of 35 % weight at a fiber areal weight of 134 g/m^2. *HexPly 8552/AS4* has a nominal cured ply thickness of 0.131 mm with a nominal fiber volume content of 57.42 % and a nominal resin content of 35 % weight at a fiber areal weight of 134 g/m^2. [94, 95] The mechanical properties of both material systems are summed up in Tab. 2.1.

Table 2.1: Material properties of 8552/IM7 and 8552/AS4 based on the data sheet. [95]

Property	Fiber orientation	Test temp.	Unit	IM7	AS4
Tensile strength	0°	25°C	MPa	2.724	2.207
		91°C		2.538	-
	90°	25°C		64	81
		93°C		92	75
Tensile modulus	0°	25°C	GPa	164	141
		91°C		163	-
	90°	25°C		12	10
		93°C		10	8
Compression strength	0°	25°C	MPa	1.690	1.531
		91°C		1.483	1.296
Compression modulus	0°	25°C	GPa	150	128
		91°C		162	122
ILSS	0°	25°C	MPa	137	128
		91°C		94	122

2.3 Compaction characteristics of prepreg materials

Compaction – here defined as the consolidation of an uncured laminate – is an important factor in the processing of composite materials as it influences the fiber volume and void content as well as the fiber angle deviation on micro and macro level. Sufficient compaction during ply deposition can avoid the inter-ply entrapment of air and avoid an excessive bulk factor during autoclave curing potentially leading to fiber angle deviations or local fiber waviness. Automated deposition methods as AFP allow a defined and reproducible application of compaction pressure during processing. [4, 5, 35]

A variety of experimental studies and modelling approaches have been made over the decades. This section includes a literature study of the composite and prepreg compaction characteristics in Sec. 2.3.1 and of AFP compaction in Sec. 2.3.2.

2.3.1 Composite and prepreg compaction characteristics

Hill [96] studied the inhomogeneity of stress and strain in two phase composites on a macroscpoic level as part of his theory on self-consistent mechanics of composite materials. This is still a ground base for many theoretical models on composite compaction.

In an experimental approach, Gutowski et al. [97] investigated the deformation of impregnated fiber beds with a compression mold set-up allowing a defined combination of fiber beds and oil. They stated that the behavior of the impregnated fiber network under compression at zero oil pressure can be approximated as nonlinear elastic. The applied load was assumed to be carried by the viscous flow of the resin in the fiber bed and by its elastic deformation. A model was set up replicating the stiffness of the composite based on the beam theory with the fibers being bending beams with multiple contact points. The experimental results showed good agreement with the model. The average effective stress in the fiber network is a function of the fiber volume V_f [98, 99]:

$$\sigma_{fn} = A_S \frac{\sqrt{\frac{V_f}{V_0}} - 1}{\left(\sqrt{\frac{V_a}{V_f}} - 1\right)^4} \tag{2.1}$$

with A_S being a bending beam theory constant including the fiber bending stiffness and the span length of the fiber network, V_a the available or maximum possible fiber volume fraction. The initial fiber volume fraction V_0 is defined as the fiber volume fraction V_f at $\sigma_{fn} = 0$. Gutowski et al. [97] described the composite deformation via a deformable fiber bed saturated with resin.

Robitaille and Gauvin [100–102] experimentally analyzed the compaction characteristics of textile reinforcements for the Liquid Composite Molding (LCM) processes Resin Transfer Molding (RTM) and Structural Reaction Injection Molding (SRIM). They focused on the compaction and relaxation of textile reinforcements, the behavior of fluid-saturated woven textiles and textile reorientation during compaction. The studies visualized the compaction and relaxation profiles of several successive compaction cycles and showed the effect of compaction on fiber reorientation by tow spreading and on the fiber volume content of the final laminate.

Smith and Poursartip [103] as well as Hubert and Poursartip [104] developed the first models of compaction and resin flow for thermoset matrix systems. They emphasized the main matrix flow mechanisms during processing – percolation flow and shear flow. Percolation or bleeding flow is characterized by resin flow relative to the fiber bed under pressure, comparable to the squeezing of a sponge. Shear flow is defined as the viscous flow of resin and fibers combined. Percolation flow is dominant for low viscosity resins under bleeding conditions. Shear flow occurs for high viscosity matrix systems, especially thermoplastic polymers. [105]

Hubert and Poursartip [107] further developed a method to directly measure the compaction profile of composite prepreg. The total stress on the laminate σ_l is

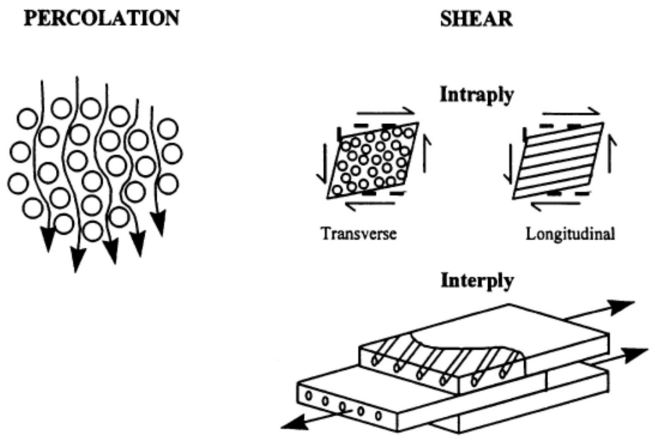

Figure 2.7: Percolation flow (left) and shear flow (right) as main flow mechanisms during processing according to Hubert and Poursartip [104], based on ÓBrádaigh [106].

described as the combination of the effective stress on the fiber bed $\overline{\sigma}$ and the resin pressure p_r.

$$\sigma_l = \overline{\sigma} + p_r \tag{2.2}$$

Based on Darcy's law, resin flow can be described as flow through a porous medium with anisotropic permeability [108]. It can further be coupled with the elastic compaction of the fiber bed, resulting on a visco-elastic flow-compaction material model. Earlier experimental approaches for the quantification of compaction and transverse permeability were done by measurements on a dry fiber bed after dissolving the resin from the prepreg [109, 110]. This process led to problems due to rearrangements of the fiber bed causing deviations in its compaction behavior. Hubert and Poursartip avoided this with an experimental set-up allowing the defined compaction of prepreg samples [107], based on earlier developments by Gutowski et al. [99]. This allowed the reproducible measurement of the displacement in z-direction u_z over the applied load F_z (cf. Fig. 2.8). The prepreg samples are compacted gradually to different levels of displacement with a dwell time allowing a stress reduction. Thus the elastic response of the material, the fiber bed effective stress, can be deduced and was implemented to a finite element (FE) process model.

Somashekar et al. [111] analyzed the viscoelastic behavior and non-elastic deformation of fiber beds in an experimental approach for applications in LCM processes. They measured an increasing permanent deformation of the fiber bed with the number of compaction cycles. Stress relaxation and hysteresis were observed indicating non-elastic behavior. Comas-Cardona et al. [112] measured the plastic

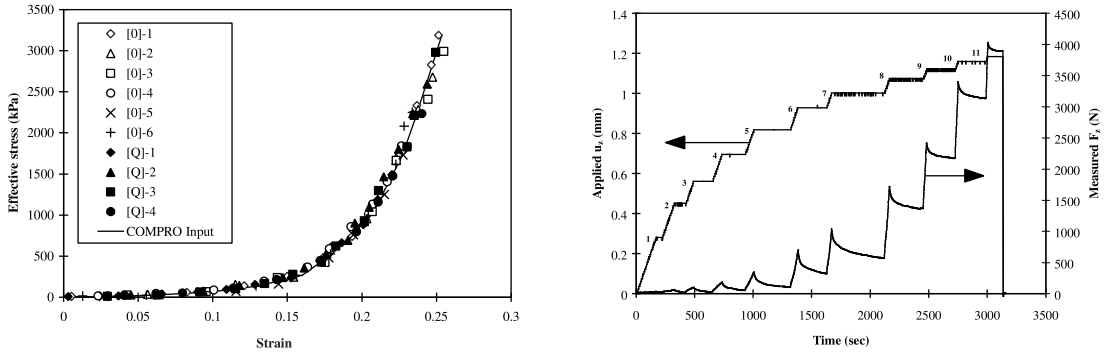

Figure 2.8: Compaction (left) and relaxation (right) curves of CF/epoxy prepreg sample compaction experiments by Hubert and Poursartip. [107]

deformation of fiber beds in dry and impregnated state in a similar approach. They found a non-linear elastic-plastic behavior under compression and pointed out the linear correlation between plasticity development and deformation.

Michaud et al. [113] characterized the compaction of prepreg in vacuum bag only (VBO) processing conditions with the goal to minimize the void content. In an experimental approach similar to Hubert and Poursartip [107] they analyzed the maximum fiber volume content at a given pressure. The initial resin content and the extent of resin bleeding during processing showed a strong influence on the final fiber volume content. The study showed a potential fiber volume content of up to 60 % at VBO conditions.

Li et al. [110] published an experimental analysis of the compaction and the corresponding transverse permeability of prepreg laminates as a function of fiber volume fraction. They proposed a simple experimental set-up to measure the compaction curve and the saturated transverse permeability of an uncured prepreg sample stack. Their experimental results were compared to the compaction model by Gutowski et al. [114] and showed good agreement.

2.3.2 AFP compaction characteristics

The compaction roller of the AFP process applies pressure on the incoming tape and on the already deposited substrate. In TS-AFP, the heat input enhances the prepreg tack, ensuring adhesion of the tape on the tool surface or the substrate. Toughened prepreg material, as typical in aerospace applications, is partially impregnated allowing air to escape through internal channels during evacuation [93]. The application of pressure and heat leads to through-thickness resin flow to fully impregnate the tapes. A combination of shear and squeeze flow in TS-AFP leads to a compaction of the prepreg material. The general knowledge on prepreg com-

paction presented in Sec. 2.3 is combined with AFP specific properties of high rate local pressure application via a flexible compaction roller in a variety of studies.

Sarrazin and Springer [115] developed a 2D FE thermo-mechanical stress model for both TS-AFP and TP-AFP. One focus was the effect of the pressure applied by the compaction roller on the laminate during deposition. The pressure applied by a radial roller geometry was found to introduce interlaminar shear stresses and normal stresses opposite to the direction of pressure application at the edges of contact (cf. Fig. 2.9). The extent decreases with the number of plies and thickness of the laminate, but is still assumed to be a potential cause for delaminations.

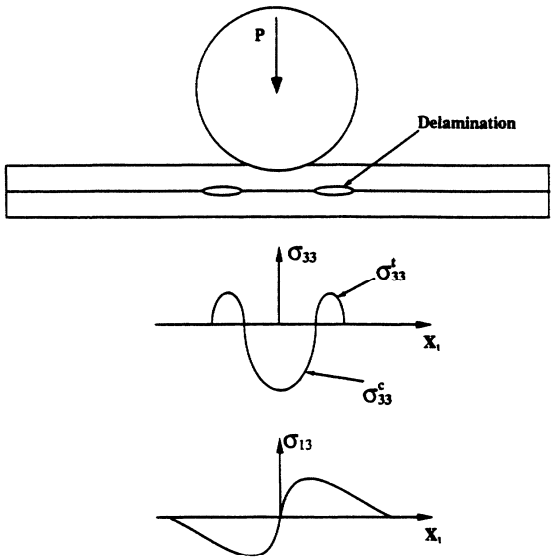

Figure 2.9: Components of the stresses by a radial compaction roller. [115]

Lukaszewicz and Potter [7] analyzed the through-thickness compression response of prepreg material in the TS-AFP with the goal to generate input for an AFP process model. In a laboratory scale test set-up they compacted CF prepreg samples of 8 plies with a size of $100\,mm \times 60\,mm$ in between two heated compaction plates in a UTM. The compaction was applied by applying a defined displacement. The through-thickness strain was measured via digital image correlation (DIC), allowing the calculation of the through-thickness modulus E_3 with

$$E_3(t) = \frac{F(t) \cdot A}{\varepsilon} \tag{2.3}$$

with the applied force $F(t)$, the sample area A and the measured strain ε. A visco-elastic as well as an elastic-plastic material description were formulated, and experimental results were compared to these formulations. The visco-elastic effects, i.e. time- dependent mechanical properties, were modeled by means of a Prony series [116] according to

$$E(t) = E_e + n\sum_{i=1}^{n} E_i e^{t/\rho_i} \tag{2.4}$$

with E_e being the equilibrium modulus, E_i the relaxation modulus, ρ_i the relaxation time and n_P the number of Prony series coefficients. The simplified elastic-plastic material model is stated as strain hardening of the material by applying a power law [117] as

$$\rho_{is} = A_{SH}\varepsilon^{m_{SH}} + \rho_0 \tag{2.5}$$

with ρ_{is} being the instantaneous stress, ε the plastic strain, A_{SH} and m_{SH} strain hardening coefficients and ρ_0 the yield stress. With this study, Lukaszewicz and Potter showed that the time dependency of the compression modulus can be neglected for AFP compaction processing conditions, as the contact time of the compaction roller is very short. For compaction durations smaller than 0.1 s, the material behavior can be considered time-independent with an error of less than 1.5 %. [7]

[19] investigated the through-thickness compaction characteristics of toughened epoxy prepreg material as part of his development of a thermo-mechanical coupled simulation model of the TS-AFP process. Small prepreg stacks of $20\,mm \times 20\,mm$ were exposed to several short compaction cycles in a rheometer replicating AFP processing conditions. The varied parameters were compaction pressure, temperature compaction time, release time and fiber orientation. The material was exposed to eight compaction cycles and maximum compaction and maximum release was recorded for each cycle. During compaction the material exhibited a non-linear stiffness increase, during release the laminate increased in thickness showing elastic behavior.

Nixon-Pearson et al. [37] and Belnoue et al. [118] focus on the thickness evolution of prepreg stacks corresponding to consolidation for the purpose of understanding the fundamental mechanics during automated processing. They come to the conclusion that toughened prepreg systems exhibit both percolation and shear flow simultaneously during consolidation. This coupling however has scarcely been discussed in the literature. Therefore a new formulation of the prepreg compaction model is developed and proposed.

The experimental work by Nixon-Pearson et al. for the coupled process model [37] characterizes the main compaction mechanisms of toughened prepreg. The investigation focuses on the material behavior at the edges of the material. This is contrary to previous studies, where edges are fully constrained which represents the boundary conditions in the middle of a laminate [107]. The CF prepreg

sample stacks with 16 plies and a size of 30 $mm \times 30\,mm$ were compacted in a dynamic mechanical analysis (DMA) equipment. Variation parameters were the compaction pressure, pressure rate, temperature and fiber orientation. Apart from UD and cross ply 0/90 (CP), the fiber orientation included a blocked ply (BP) ply configuration with groups of 4 plies of similar orientation ($[90_4, 0_4]_2$) and semi blocked ply (SB) ply cconfiguration with groups of 2 plies of similar orientation ($[90_2, 0_2]_4$). The temperature ranged from 30 °C to 90 °C with a maximum nominal pressure of 0.26 MPa and a maximum pressure rate of 0.1 MPa s^{-1}. The processing conditions were supposed to replicate the AFP process, hot temperature debulking and pre-cure consolidation during autoclave processing. Loading of the specimen was performed by means of a monotonic loading and a dwell-ramp characteristic. Monotonic loading was carried out by a continuous increase to 60 N in 1200 s. The dwell-ramp run consisted of five 240 s steps with fast incremental load increase of 10 N starting from 20 N.

The results from Nixon-Pearson et al. show different compaction characteristics for different fiber orientations and temperatures. A higher compaction, coupled with higher increase in width, was achieved by BP compared to CP. This indicates a greater spreading of BP samples which corresponds to the assumption of occurrence of shear flow. On the other hand, different loading characteristics, monotonic and dwell-ramp loading, caused no difference in final thickness of the laminate for other parameters kept constant. Temperatures between 30 °C and 60 °C show an impact on the degree of compaction whereas for temperatures above 70 °C the compaction curves converge to a threshold. An analysis of the microstructure before and after compaction showed clear evidence for the presence of percolation and shear flow.

Belnoue et al. [118] developed the hyper-visco-elastic material model based on the experimental results by Nixon-Pearson et al. [37]. The model combines percolation and bleeding flow and provides a smooth transition between them. A main advantage of the model is the requirement of only three material parameters along with the tape dimensions. The parameters can be attained from compaction experiments as done by Nixon-Pearson [37]. The results of the studies by Nixon-Pearson et al. [37] and Belnoue et al. [118] were used to better understand and predict the defect formation in AFP laminates [43]. The ability of the resulting model to capture wrinkles formed during manufacturing was proven for lab-scale specimens [46, 119]. In a next step, kinematically enhanced constitutive modeling can help to overcome the limitations of scalability of the laboratory scale modeling and allow the simulation of full scale industrial components [120].

The pressure in AFP is typically applied with a flexible compaction roller. For specific applications with small radii, like a spar geometry, an additional trailing compaction plate can be required for a full track compaction [121]. The theoretical pressure distribution underneath the compaction roller is defined by the theory of contact mechanics of solid elastic bodies by Hertz [122]. The theoretical deformation of the compaction roller in z direction $\overline{u}_z$ is

$$\overline{u}_z = -\frac{2}{\pi E^\star} \int_{x_{min}}^{x_{max}} \int_{-a}^{a} \frac{p(s)}{x-s} ds\, dx \tag{2.6}$$

with $E^\star = \frac{E_r}{1-\nu_r^2}$, E_r as the elastic modulus of the roller, ν_r its Poisson's ratio and the assumption of a flat rigid tool surface [123]. The theoretical maximum pressure is underneath the roller axis in the center of the contact area. From this peak, the pressure reduces quadratic to zero at the edges of the contact area. The pressure distribution $p(x)$ relative to the distance to the contact center x can be determined as

$$p(x) = \frac{2F}{\pi A_c^2} \left(A_c^2 - x^2\right)^{1/2} \tag{2.7}$$

with $F = \frac{\pi A_c^2 E^\star}{4 r_r}$, A_c as contact area and r_r as roller radius. This allows the calculation of the theoretical pressure distribution underneath a deformed cylindrical compaction roller of homogeneous material on a flat rigid surface. Fig. 2.10 shows the theoretical roller deformation and the resulting pressure distribution [11]. Typical industrial compaction rollers consist of several materials, like a metal bearing core, a flexible silicone or foam layer and a thin release coating layer. This leads to compaction characteristics deviating from the Hertzian theory, as shown by Lichtinger et al. [124]. They characterized an industrial scale compaction roller with varying pressures and tool geometries and developed a FE based orthotropic material model (cf. Fig. 2.10).

Fig. 2.10 c) shows a comparison by Lichtinger et al. [124] of the pressure distribution based on Hertzian contact mechanics, the experimental roller characterization and the results of the FE modeling. The Hertzian pressure distribution is a quadratic function of the contact length with a peak in the center of the contact area and no pressure on the edges of the contact area. The experimental and numerical results show a significant deviation with a more uniform pressure distribution along the contact length and peak pressures near the edges of the contact area. This is explained by the non-homogeneous roller material with a stiff coating layer on the outer surface. This deviation from the theoretical pressure distribution might be beneficial for the reduction of bridging effects on concave tooling surfaces and

a) Experimental procedure to measure the pressure distribution

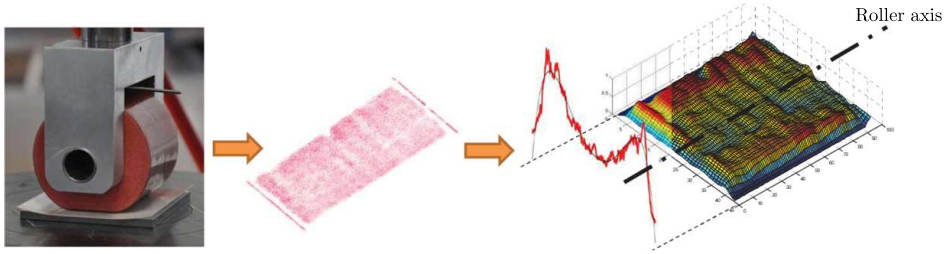

b) Theoretical roller deformation

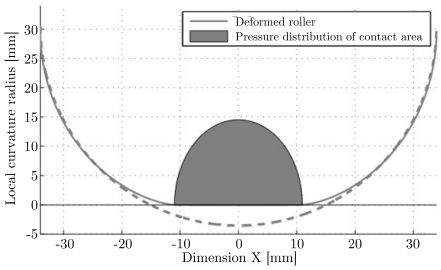

c) Results for theory, experiment & simulation

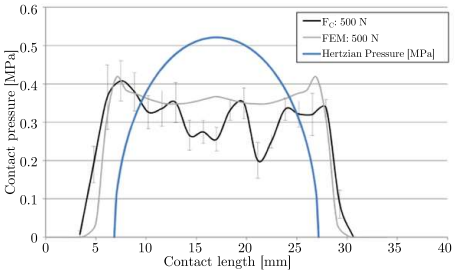

Figure 2.10: Procedure and results of the AFP roller compaction study by Lichtinger. [11]

potentially reduce the risk of shear and delaminations predicted by Sarrazin and Springer [115]. [11]

3 Vacuum debulking compaction

The quality of a cured laminate is predetermined by the accuracy of the deposition process. Plies have to be positioned with respect to the desired fiber orientation and compacted to avoid excessive entrapment of voids in between the plies. An established measure to guarantee a defined compaction state is to cover the laminate in a vacuum bag and compact it with vacuum pressure – so-called vacuum debulking. This is typically done after a specific number of plies for 10 to 30 minutes. The process step is interrupting the ply deposition process and therefore has a direct influence on the overall process time. The bag application is a labor-intensive manual process with a high use of consumables such as bagging film or tacky tape. For serial production, reusable bags and sealants can be used, but are considerably more expensive. The laminate can be heated during vacuum debulking by internal tooling heating or external IR heaters, but most common is vacuum debulking at room temperature. [5, 109]

The compaction effect of vacuum debulking is not yet quantified with a systematic parameter variation in published literature. In this chapter, an experimental method for the continuous measurement of the thickness progress of a laminate during vacuum debulking is developed and applied. The experiments include a variation of laminate temperature, fiber orientation, number of plies and geometric complexity. After a description of the applied materials and methods, the results are presented and discussed. The chapter ends with a list of limitations and a conclusion. Parts of the results of this chapter were obtained in the theses of Irmanputra [125] and Bissinger [126] under the supervision of the author.

3.1 Materials and methods

This section includes a description of the applied equipment and material. The experimental procedure that was developed to allow the continuous thickness measurement is explained, followed by the procedure of data aquisition and evaluation.

3.1.1 Equipment

For the debulking experiments, prepreg laminate samples were compacted on a heated table and scanned using a triangulation scanner. The heated table electrically heats its steel surface up to temperatures of 200 °C. An aluminum plate was mounted on top, serving as tool surface. The level and distribution of the temperature were monitored using thermocouples and a IR camera *FLIR A325sc*.

For the contactless measurement of the thickness progression over time, a laser triangulation scanner *GOM ATOS Capsule* was used. By detecting the projections of structured light with two stereo cameras, the system can detect 3D surface profiles in a measurement volume of $320\,mm \times 240\,mm \times 290\,mm$ with an accuracy of 18 µm [127]. The vacuum debulking was realized with a diaphragm pump *MV 10 NT* by *Vacuubrand* at a min. vacuum of 5 mbar [128].

3.1.2 Material

The material used for this set of experiments was the toughened aerospace grade UD prepreg *HexPly 8552/AS4* by *Hexcel*. The material system has a nominal cured ply thickness of 0.130 mm, a nominal fiber volume fraction of 57.42 % and a nominal resin content of 35 % weight [95]. All samples were manually laminated and tested in uncured state. The out-time of all samples was tracked and kept within a range of ± 3 h at testing. More details on the applied material systems can be found in Sec. 2.2.2.

3.1.3 Experimental procedure

The goal of this set of experiments was to continuously track the thickness compaction or debulking behavior of uncured prepreg laminates during vacuum debulking. The varied parameters were tool temperature, number of plies, fiber orientation and geometry (cf. Tab. 3.1).

Temperature and fiber orientation were varied in a full-factorial set of experiments, number of plies and geometry in additional fractional factorial experiments. The samples were manually laid-up with a size of $200\,mm \times 200\,mm$ at either 16, 32 or 64 plies and either unidirectional (UD) or cross ply 0/90 (CP) fiber orientation. The plies were compacted only by the self-weight of a handheld compaction roller in order to avoid excessive and undefined pre-compaction. The applied test temperatures were 30 °C, 50 °C, 70 °C, 90 °C and 110 °C. After the tool surface reached the desired temperature $\pm 5°C$, the sample was placed on the surface and heated for 15 minutes. The sample temperature was monitored with thermocouples on the

lower and upper sample surface. Vacuum debulking was applied for 25 minutes at 5 mbar.

Table 3.1: Overview of all vacuum debulking experiment variations.

Test type	Geometry	Fiber orientation	No. of plies	Temperature [°C]
full-factorial	flat	UD/CP	16	30/50/70/90/110
fract.-factorial	flat	UD	16/32/64	70
fract.-factorial	corner	UD	16	30/70

3.1.4 Data acquisition and evaluation

The thickness progression was continuously tracked with a *GOM ATOS Capsule* laser triangulation scanner. The scanning area included one third of the sample surface and a part of tool surface including reference points around the vacuum bag (cf. Fig. 3.1 a). A heat insulation foil was added to the tool surface to avoid excessive heating of the measurement system. The vacuum bags were prepared with a stochastic speckle pattern to allow continuous tracking. The measuring frequency was set in several intervals as a compromise of accuracy and data processing effort based on pretrials (cf. Tab. 3.2). The biggest effects were expected within the first seconds, followed by a convergence towards a certain thickness.

Table 3.2: Measuring frequency of the thickness scans during the vacuum debulking experiments.

Interval	Time [s]	Measuring frequency [Hz]
1	0-20	2
2	21-60	0.5
3	61-300	0.25
4	301-700	0.125
5	701-1300	0.1
6	1301-1500	0.07

The proprietary software *GOM Correlate* was used for the data evaluation. An inspection area with a distance of 40 mm to the edge of the laminate was defined

to exclude edge effects. The thickness was determined as perpendicular distance of the reference tool plane and the facets of the surface component on the inspection area. A fitting plane was added with Gaussian best fit based on all measurement points, allowing the determination of a mean thickness and standard deviation (cf. Fig. 3.1). A relative compaction was calculated for better comparison of the different samples by relating the thickness reduction to the initial thickness.

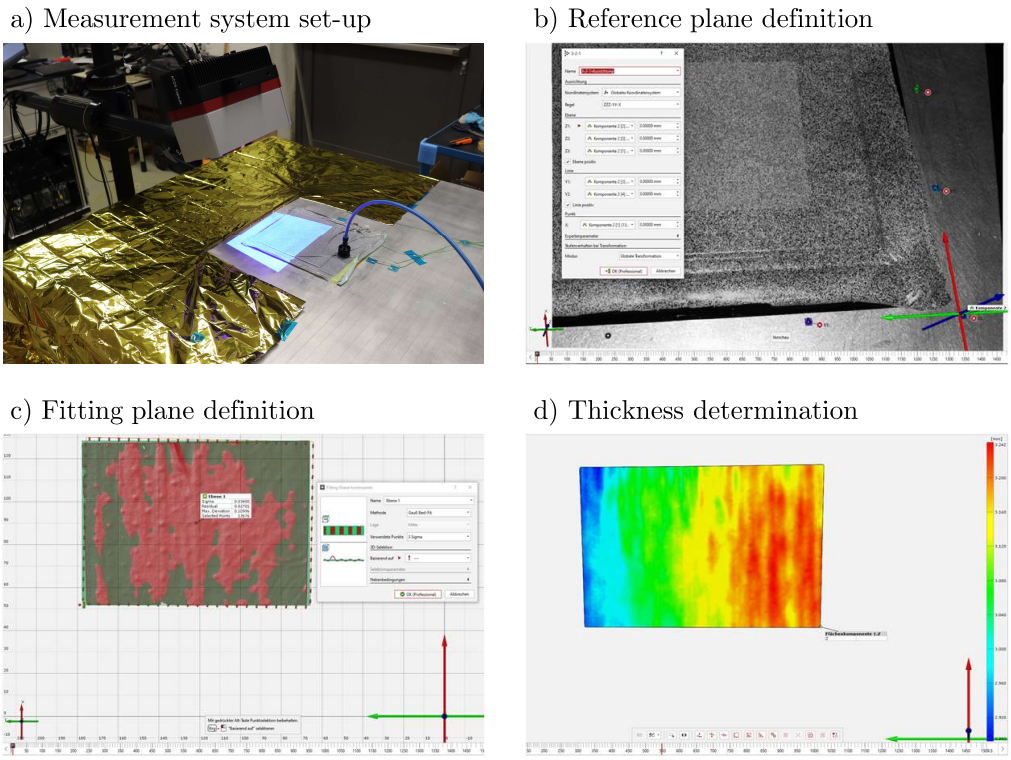

Figure 3.1: Data acquisition and evaluation procedure of the vacuum debulking experiments.

3.2 Results and discussion

The presentation of results in this section is sorted by the varied parameter, showing its isolated influence on the compaction. This includes the effect of temperature, fiber orientation and number of plies. The results are shown as compaction progress over time, either relative to the initial thickness or in absolute terms.

Effect of the temperature

Fig. 3.2 and Fig. 3.3 show the relative compaction over time of CP and UD samples at different temperatures. The general trend is an increased compaction with rising temperature, ranging from overall compactions of min. 2.2 % for UD 30 °C to max.

9.7 % for CP 110 °C. The majority of the compaction happens within the first 300 s. With rising temperature, the variance of the results increases.

Fig. 3.2 shows the compaction results of CP laminates at 30 °C, 50 °C, 70 °C and 110 °C. The final compaction rises with temperature from 2.6 %, over 3.3 % and 6.7 % to 9.3 %. The progress shows a steep drop within the first 100 s to 300 s with a flattening until 1500 s. 90 % of the compaction was reached after 215 s for 30 °C, 235 s for 50 °C, 395 s for 70 °C and 207 s for 110 °C.

Fig. 3.3 shows the compaction results of UD laminates at 30 °C, 50 °C, 70 °C and 90 °C. The final compaction rises from 2.0 % at 30 °C, over 3.2 % at 30 °C and 6.2 % at 70 °C to 6.4 % at 90 °C. The progress is similar to the CP samples, with a steep drop within the first 100 s to 300 s and a flattening until 1500 s. 90 % of the compaction was reached after 157 s for 30 °C, 165 s for 50 °C, 333 s for 70 °C and 253 s for 90 °C.

These results show the laminate temperature is a dominant influence on the compaction potential and correspond to the findings of other studies on the compaction behavior of thermoset prepreg laminates [97, 118, 129–131].

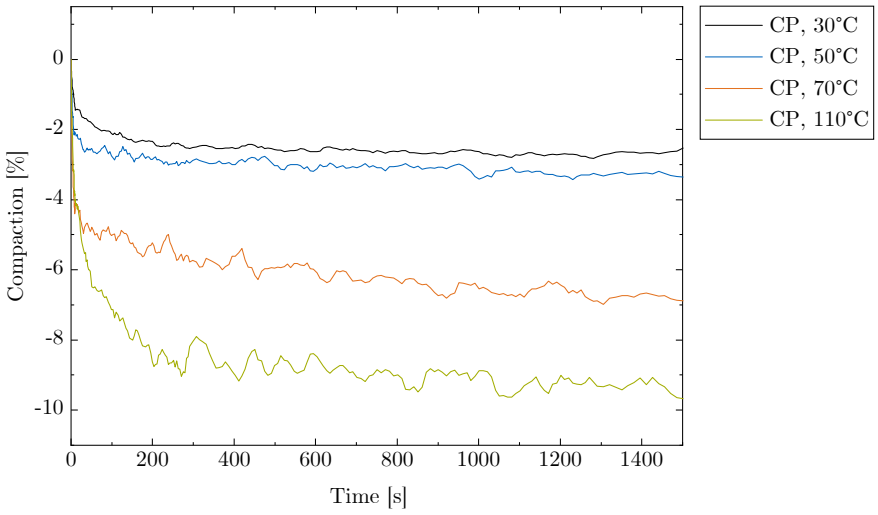

Figure 3.2: Relative compaction over time of 16 ply CP samples at different temperatures.

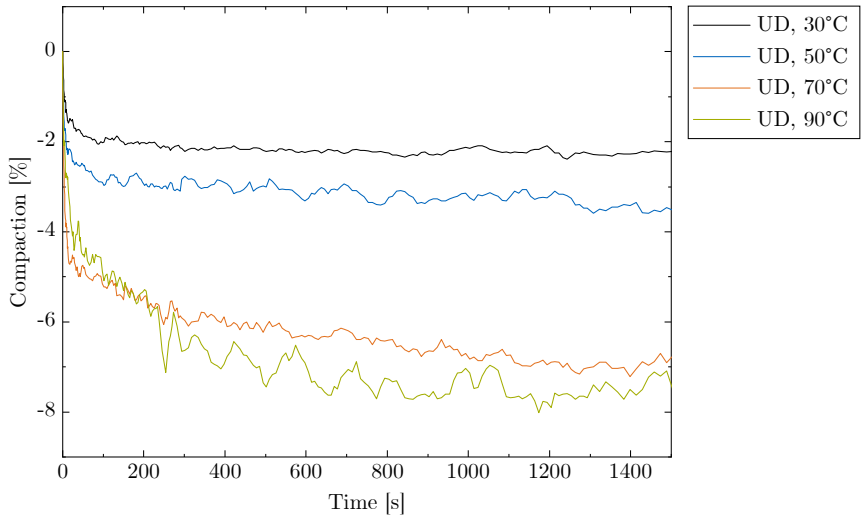

Figure 3.3: Relative compaction over time of 16 ply UD samples at different temperatures.

Effect of the fiber orientation

A comparison of the available data at similar temperature levels for UD and CP fiber orientation is shown in Fig. 3.4. The thickness progression shows a similar behavior for the respective temperature levels, with no distinct difference regarding the fiber orientation. The final thickness reduction of the UD and CP samples was 2.2 % and 2.3 % at 30 °C, 3.5 % and 3.4 % at 50 °C and 6.9 % for both at 70 °C. These results are contrary to published compaction studies including fiber orientation variations, which show a tendency of more compaction for UD laminates compared to CP fiber orientation [37, 118, 130].

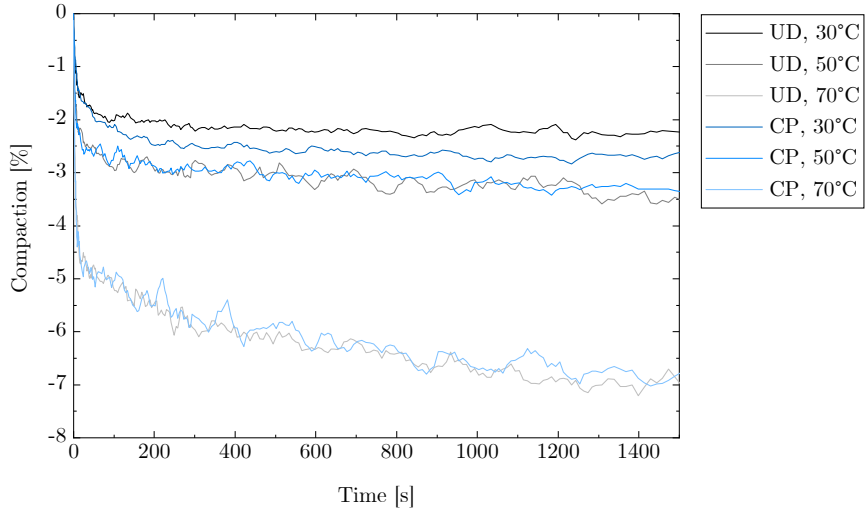

Figure 3.4: Relative compaction over time of 16 ply UD and CP samples at different temperatures.

Effect of the number of plies

The number of plies was varied in a fractional factorial set of experiments, comparing the standard 16 plies to 32 and 64 plies. The results are shown with absolute compaction in Fig. 3.5 and with relative compaction in Fig. 3.6. The graph of the 64 ply sample misses data points in the range of $t = 35 - 110s$, as described in the limitations below.

The initial thickness of the samples was 13.2 mm with 64 plies, 6.4 mm with 32 plies and 3.2 mm with 16 plies. The absolute compaction increased with the number of plies from 0.23 mm over 0.35 mm to 0.58 mm (cf. Fig. 3.5). The relative compaction however decreased from 6.7 % over 5.3 % to 4.4 % with the number of plies.

The majority of the compaction is again achieved in the first 300 s. The 16 ply sample converges to a plateau, reaching 90 % of the measured compaction after 242 s. This 90 % compaction threshold shifts with increasing number of layers to 662 s for 32 plies and 1104 s for 64 plies, indicating further potential for compaction for these samples. The reduced relative compaction with the number of plies can be caused by the increased resistance for movement of entrapped air in z-direction.

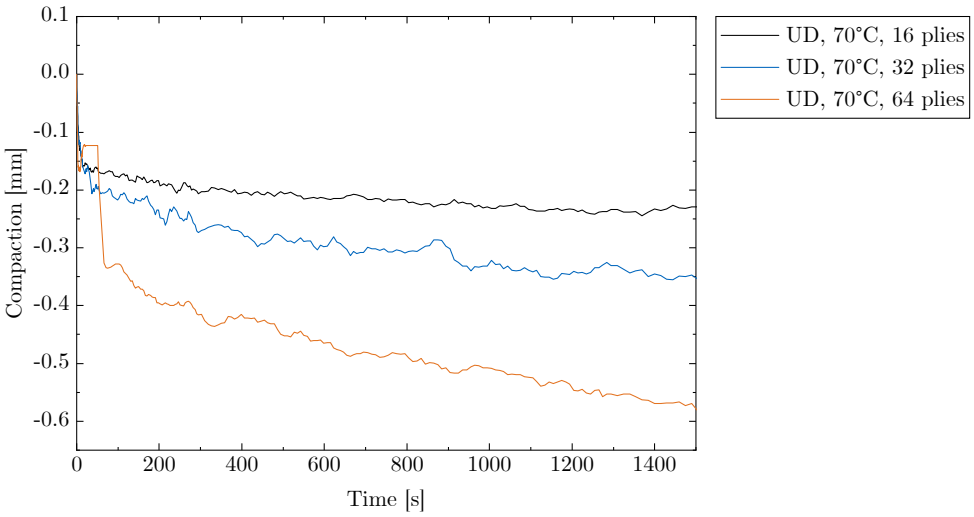

Figure 3.5: Absolute compaction over time of UD samples with different numbers of layers.

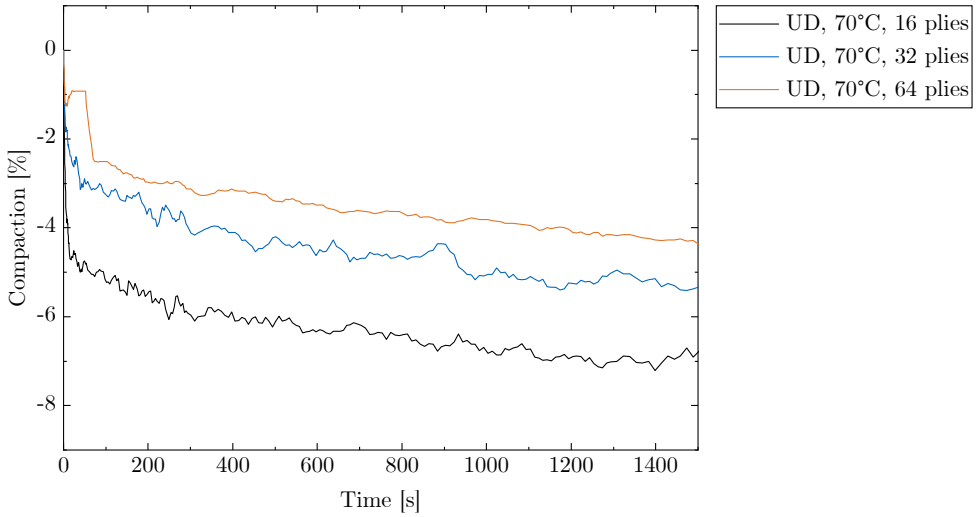

Figure 3.6: Relative compaction over time of UD samples with different numbers of layers.

3.3 Limitations

- A software error during the measurement of the CP 90 °C and UD 110 °C samples led to a corruption of the measurement data. This data is missing in the evaluation.

- The vacuum sealing tacky tape has failed at the beginning of the UD 70 °C CP sample measurement. This is the reason for missing measurement points in the range $t = 35 - 110s$, leading to straight lines in Fig. 3.6 and Fig. 3.5.

- The corner geometry samples could not be evaluated for several reasons. The manual preparation of the complex geometries led to high variations, especially in the corner regions of interest. It was difficult for the vacuum bag to be arranged without wrinkles and without bridging at the same time, leading again to high variations, especially in the concave radii. The resulting data quality did not allow an evaluation.

- The measurement at high temperatures led to higher variations compared to the low temperature samples. The sensor is equipped with an internal cooling system. A heat insulating film was added to the tool surface to avoid excessive heating. Still, the head temperature rose by approximately 5 °C.

- The limited size of the samples can lead to an increased compaction due to additional evacuation at the edges compared to larger laminates in actual production scenarios. However, the compaction happened uniformly within

the scope of the measurement accuracy over the entire surface of the samples, so it is assumed that this effect is negligible.

3.4 Conclusion

A set of experiments was conducted studying the laminate compaction during vacuum debulking. The varied parameters were process temperature, number of layers, fiber orientation and sample geometry. The thickness progression was tracked using a laser triangulation scanner.

The experimental procedure allows the continuous tracking of the thickness progression of an uncured laminate during vacuum debulking. The results show a strong influence of the process temperature with an increase of the overall compaction from around 2 % at 30 °C to more than 6 % at 90 °C and more than 9 % at 110 °C respectively. This could justify the effort for vacuum debulking at elevated temperatures if increased compaction or reduced debulking time is required. The variation of the fiber orientation from UD to CP did not result in distinct differences in the thickness progression. A variation of the number of layers per sample from 16 to 32 and 64 showed a higher absolute compaction with increasing number of layers, but a decrease in the relative compaction from 6.7 % for 16 layers and 5.3 % for 32 layers to 4.4 % for 64 layers. The geometry variations could not be evaluated for technical reasons, as the measurement set-up was not suitable for measurements, especially in concave radii as described in the limitations. The thickness progress showed that the majority of the compaction for the standard 16 ply samples took place within the first 300 s. Longer debulking times seem only appropriate, when a higher number of plies is to be debulked at once.

4 AFP compaction on laboratory scale

AFP is a complex process with many internal and external influencing and noise parameters. Main internal factors are the process parameters lay-up velocity, compaction pressure and heat input. Looking at the complexity of the overall process system, there are additional potential sources for variation – depending on the individual design of the system – e.g. creel temperature, tape tension, tool temperature, cooling tube pressure and many more. The material with its varying properties due to aging can be considered as an external factor of variation. Changing environmental conditions like temperature or humidity add external noise. Although the goal of an industrialized serial production is to keep all these factors as constant as possible, considerable variations can never be fully excluded. These factors together with the high effort for set-up and running of the industrial equipment make scientific experiments on full-scale level challenging and extensive. Experiments on laboratory scale have the goal to replicate the full-scale environment on a smaller level. Their potential advantage is to have defined boundary conditions and a high degree of repeatability, excluding unintended factors of variation. The same applies to process simulations. Both require simplifications and assumptions that have to be evaluated in order to clearly identify the transferability of the results and its limits.

This chapter includes two sets of laboratory scale compaction experiments and an approach to simulate cyclic compaction. In Sec. 4.1, an experimental method for cyclic compaction of uncured laminate stacks on a rheometer is presented. Sec. 4.2 shows a similar set of cyclic compaction experiments but conducted on a UTM, allowing for bigger sample sizes. In Sec. 4.3, a finite element (FE) based approach to simulate the cyclic compaction behavior is described. Parts of the results of this chapter were obtained in the theses of Etchegaray Bello [132], Lörch [133], Díaz de la Hoz [134] and Vogl [135] under the supervision of the author. The results of Sec. 4.1 were published by Etchegaray Bello, Engelhardt et al. [136]. The raw data of Sec. 4.1 was published by Etchegaray Bello, Engelhardt et al. [137].

4.1 Cyclic compaction of laminate stacks using a rheometer

In the following set of experiments, small stacks of uncured prepreg layers were compacted by a rheometer stamp with different levels of pressure and temperature. The goal was to replicate the AFP lay-up sequence on a laboratory scale level, allowing to analyze the influence of pressure and temperature on the resulting laminate compaction based on prior studies by Lichtinger [11] and Nixon-Pearson et al. [37]. This section is subdivided in the description of the applied materials and methods, the results and their discussion, limitations and a conclusion. The study was published by Etchegaray Bello, Engelhardt et al. [136].

4.1.1 Materials and methods

Equipment

A modular rheometer *Anton Paar MCR302* was used to apply compaction cycles at different temperatures (cf. Fig. 4.1). The rheometer was equipped with an external cooling system *Anton Paar Viscotherm VT2*. An adapted sample tray with increased wall thickness was used to avoid tray deformation resulting in thickness measurement distortions. The rheometer punch was adapted to a circular cross-section of 8 mm diameter. The rheometer can apply controlled compressive forces up to 50 N. With Eq. 4.1, the resulting pressure was calculated:

$$F = p \cdot A \tag{4.1}$$

The equivalent AFP compaction forces (cf. Tab. 4.1) were derived for a roller width $w_r = 30\,\text{mm}$ and average contact length of $l_r = 20\,\text{mm}$ with a roller diameter of $d_r = 39\,\text{mm}$. The setting allowed compaction pressures in the force setting range from 100 to 500 N for the respective AFP system. A pre-heating time of 300 s to reach constant temperature levels was determined via thermocouple temperature measurements in the sample tray.

Material

The samples consisted of toughened aerospace grade UD prepreg. For the full-factorial main set of experiments, *HexPly 8552/AS4* by *Hexcel* [95] was used. The material system has a nominal cured ply thickness of 0.130 mm, a nominal fiber volume fraction of 57.42 % and a nominal resin content of 35 % weight. The slit tape samples included in the fractional factorial set of experiments consisted of *Hexcel HexPly 8552/IM7* [95] $^1/_8''$ slit-tape by *Hexcel* as used for AFP processing.

Figure 4.1: Experiment set-up of the rheometer compaction experiments with adapted punch cylinder, adapted tray and uncured prepreg standard samples before (top right) and after (bottom right) compaction.

Table 4.1: Compaction pressure, rheometer force setting and equivalent AFP equipment force.

Compaction pressure [MPa]	Rheometer force [N]	AFP force equivalent [N]
0.1	5.03	60
0.2	10.05	120
0.3	15.08	180
0.4	20.11	240
0.5	25.13	300
0.6	30.16	360
0.7	35.19	420
0.8	40.21	480

This system has a nominal cured ply thickness of 0.131 mm, a nominal fiber volume fraction of 57.70 % and a nominal resin content of 35 % weight. All samples were laminated and tested in uncured state with a max. test duration of 20 minutes at a maximum of 85 °C, in a range without significant influence on the degree of cure [94, 138]. The out-time of all samples was tracked and kept within a range of ± 3 h at testing. More details on the applied material systems can be found in Sec. 2.2.2.

Experimental preparation and procedure

The samples were prepared by manual lay-up of oversized plies with the respective number of plies for each set of experiments. For the slit-tape samples, a 50 %

staggering from ply to ply was included. The plies were compacted only by the self-weight of a handheld compaction roller in order to avoid excessive and undefined pre-compaction. The single samples with a size of $20\,mm \times 20\,mm$ were cut out by an automated cutter system *Zünd M-1200 CV*.

A full-factorial set of experiments was implemented with the main parameters pressure and temperature. The influence of the number of plies, fiber orientation and material type were investigated on a fractional-factorial sample basis (cf. Tab. 4.2). For all sets, the previously stacked laminate samples were exposed to several compaction cycles, replicating the compaction profile during deposition in the AFP process as developed by Lichtinger [11]. The number of compaction cycles applied, corresponded to the number of plies of the samples. Three repetitions were done for each parameter variation. The tests were randomized except for the temperature levels, which were grouped for reasons of practicability.

A compaction cycle includes a compaction time of 3 s, followed by a release time of 30 s (cf. Fig. 4.2). The closed rheometer tray with the sample was first heated up to the desired test temperature for 300 s to ensure a homogeneous temperature. The initial thickness of the sample was then measured by contacting it with the rheometer punch with a force of 0.1 N. After this initial measurement, a loop with the respective amount of compaction cycles was started. The desired force was applied at a rate of 90 µm/s. Points of interest were the initial thickness, the thickness after compaction and the thickness after release. The data were processed for analysis with MATLAB. Random overloads led to some missing points in the thickness profile that were filled with linear interpolation. The data of the single loop segments were combined, mean values for each parameter variation were calculated, and the relative thickness changes were normalized for better comparison.

Table 4.2: Overview of all rheometer experiment variations.

Test type	Material	No. of plies	Fiber orient.	Temperature [°C]	Pressure [MPa]
full-factorial	unslit	16	UD	25/35/45/55/ 65/75/85	0.1/0.2/0.3/0.4/ 0.5/0.6/0.7/0.8
fract.-factorial	unslit	16/24/32	UD	55	0.5
fract.-factorial	unslit	16	CP	55	0.5
fract.-factorial	slit-tape	16	UD	25/55/85	0.5

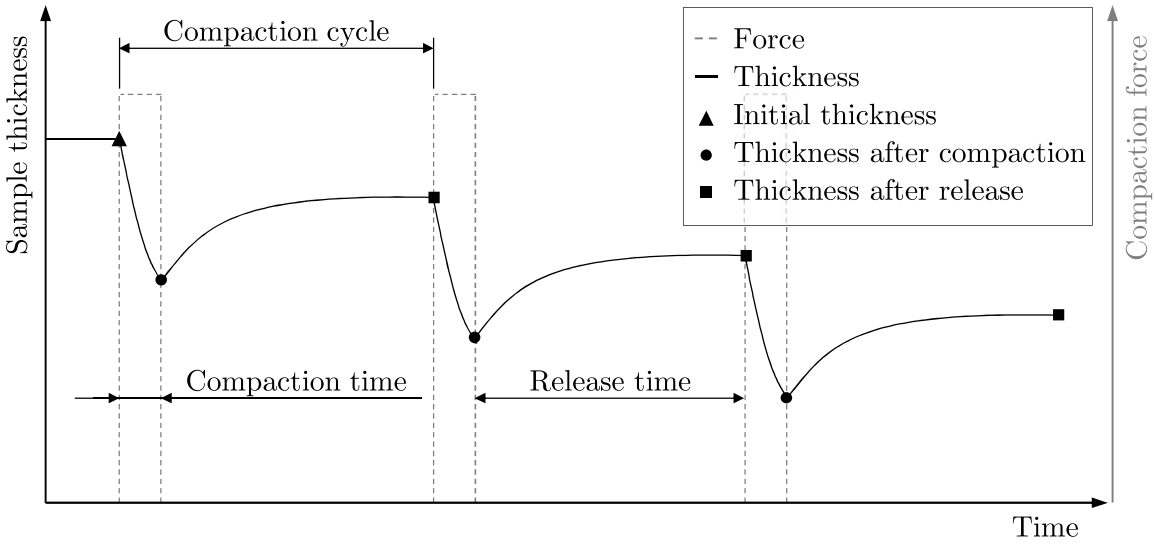

Figure 4.2: Thickness force profile of the rheometer compaction experiments, showing three exemplary cycles replicating the compaction profile of AFP.

4.1.2 Results and discussion

In Fig. 4.3, the actual thickness and force profile of an exemplary standard experiment with 16 compaction cycles can be seen. The uncured prepreg laminate shows viscoelastic material behavior, and a non-linear increase of the stiffness of the material with compaction. The thickness increases with release of the compaction pressure, showing elastic relaxation.

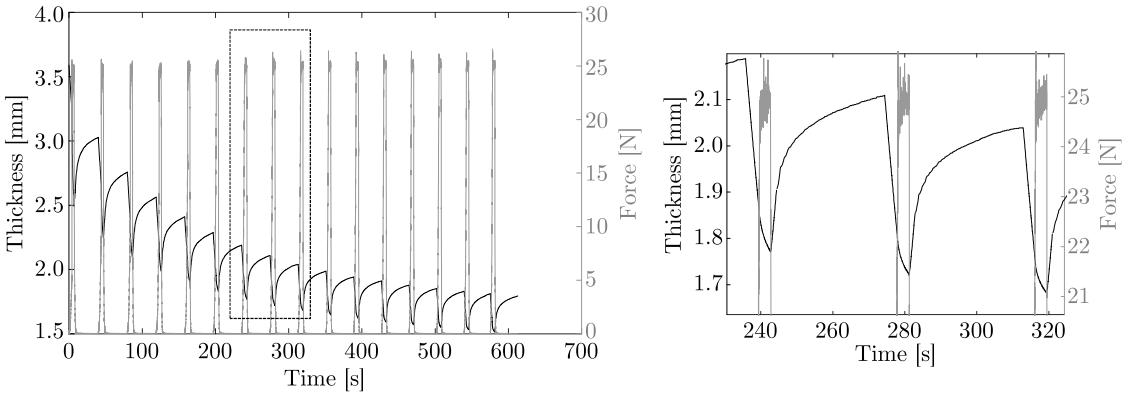

Figure 4.3: Exemplary thickness and force profile of a 16-cycle compaction program with T=55°C, p=0.5 MPa.

Effect of pressure and temperature

In the main set of experiments, pressure and temperature were varied in a full-factorial design. Fig. 4.4 shows the normalized thickness profile during the 16

compaction cycles for the different levels of compaction pressure and temperature. The thickness change is normalized via

$$t_n = \frac{t}{t_i} \tag{4.2}$$

leading to a common starting point at $t_n = 1$ for all graphs and showing the relative thickness change over time.

For all experiments, the thickness change increases with temperature and the number of compaction cycles. A compaction limit can be seen for specific conditions that will be discussed below (cf. Fig. 4.4). For 0.1 MPa compaction pressure, the thickness reduction increases over the entire range of temperature levels. The greatest thickness reduction to 69 % results after the 16$^{\text{th}}$ compaction cycle at 85 °C. For temperatures below 55 °C, the thickness plateaus with the last cycles. The combination of low pressure and low temperature does not allow a further compaction for the given scenario. For temperatures of 55 °C and above, no such limit can be seen at this pressure level. The biggest relative effect of a temperature increase can be seen from 55 °C to 65 °C, where the relative difference is up to 11.8 %. The thickness profiles at 0.2 MPa show a similar low compaction at low temperatures, but only for temperatures below 45 °C. The highest thickness reduction occurs again at 85 °C after 16 cycles, with a final thickness after release of 52.8 % compared to the initial thickness. It is difficult to make a clear distinction at high temperatures due to the standard deviations of the final thickness (cf. Fig. 4.5). However, it is assumed that for this pressure level, the compaction limit at 85 °C initially occurs. The temperature differs from the reported temperature by Ivanov et al. [139], where the compaction limit was reached at approximately 60 °C to 70 °C at a pressure of 0.26 MPa with 18-ply samples of M21/T700. The final thickness reduction at the compaction limit is similar. The thickness reduction for 0.3 MPa increases already at lower temperatures compared to the lower pressure levels. The greatest reduction is again reached at 85 °C after 16 cycles at a level of 53.1 %. This reduction is similar to the one at 0.2 MPa. The thickness profile at 75 °C starts to converge to similar values as 85 °C, with only 1.2 % difference in the final thickness. This is in good agreement with the result of Nixon et al. [37], that above a specific temperature the compaction limit is independent of a further temperature increase. The temperature threshold for their test conditions was found at 70 °C. For 0.4 MPa the compaction limit is reached at 65 °C after the 11$^{\text{th}}$ cycle. The thickness reduction for 65 °C and all temperatures above converge to a level of approximately 49 % of the initial thickness. For 0.5 MPa and above,

the maximum thickness reduction stabilizes around 50 %. The compaction limit is reached already at a temperature of 55 °C.

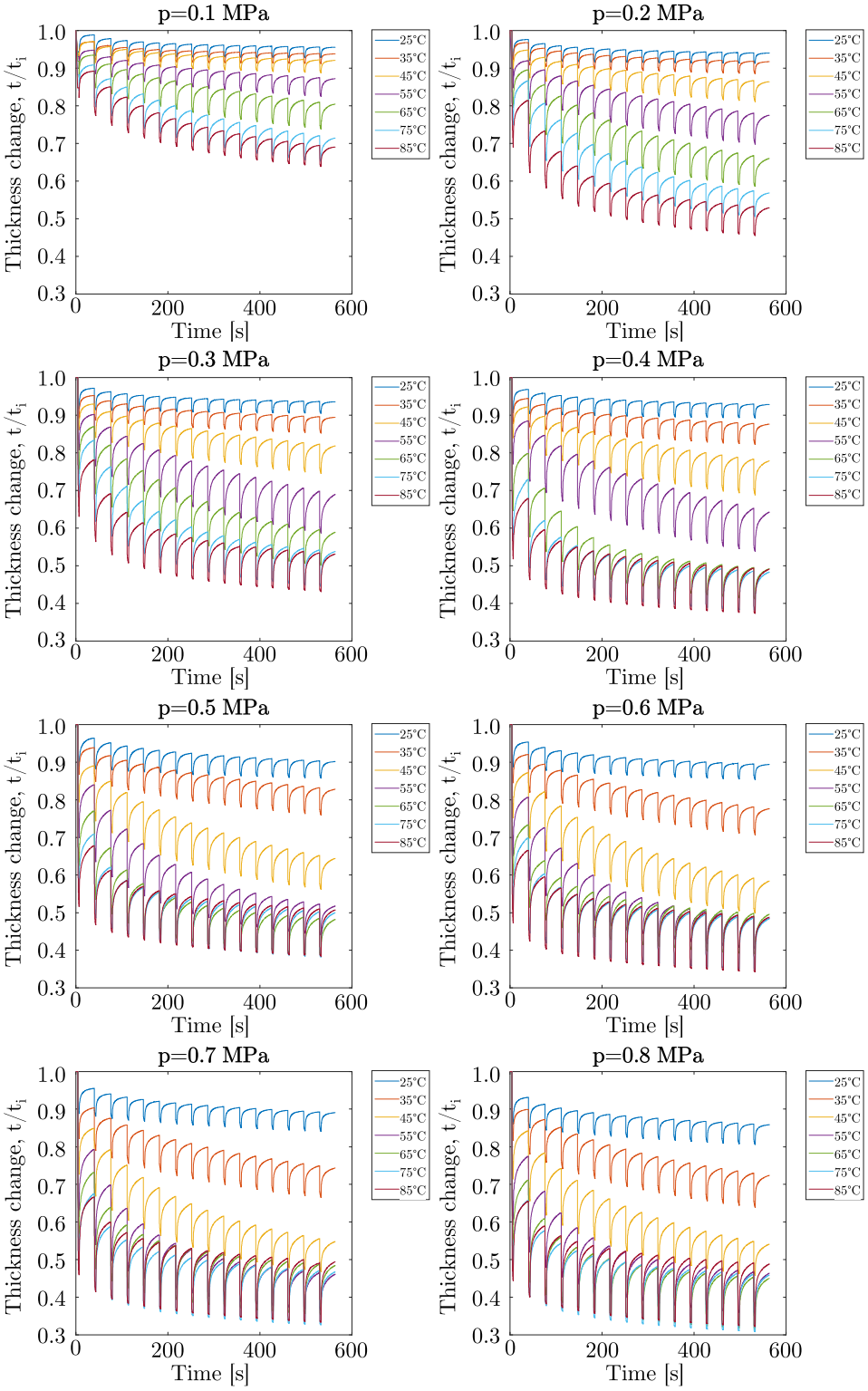

Figure 4.4: Normalized thickness change over 16 cycles with different compaction pressures and temperatures.

Fig. 4.5 shows the normalized overall thickness change for all temperature and pressure variations, including their standard deviation. It can be seen that the effect of increased pressure on the compaction is low for low temperatures of 25 °C and 35 °C. The temperature threshold by which the compaction limit is reached varies with the pressure applied. A higher compaction pressure decreases the required temperature to reach the compaction limit. Once the compaction limit is reached, higher temperatures or pressures do not lead to a further compaction for the given set-up.

Comparable lab-scale compaction studies by Ivanov et al. [139] and Nixon et al. [37] show a compaction and transverse widening limit that corresponded to the onset of bleeding. This effect was attributed to the transition from squeezing to bleeding flow in the range of 60 °C to 70 °C at a pressure of 0.26 MPa.

The presented results show that a compaction limit is reached for experiment conditions of 55 °C and 0.5 MPa, with about 50 % thickness reduction compared to the initial thickness value. Since an overall compaction limit is reached, higher temperature levels do not promote further stack thickness reduction. It is assumed, that there is no flow transition from squeezing to bleeding flow taking place, which would lead to a shift of the compaction limit with increasing pressure and temperature [37, 139]. Another possible reason for this could be related to the geometry of the samples and its smaller area in relation to the rheometer punch, as the force is only applied in the middle of the prepreg material and the non-compacted border of the specimen might restrict bleeding flow.

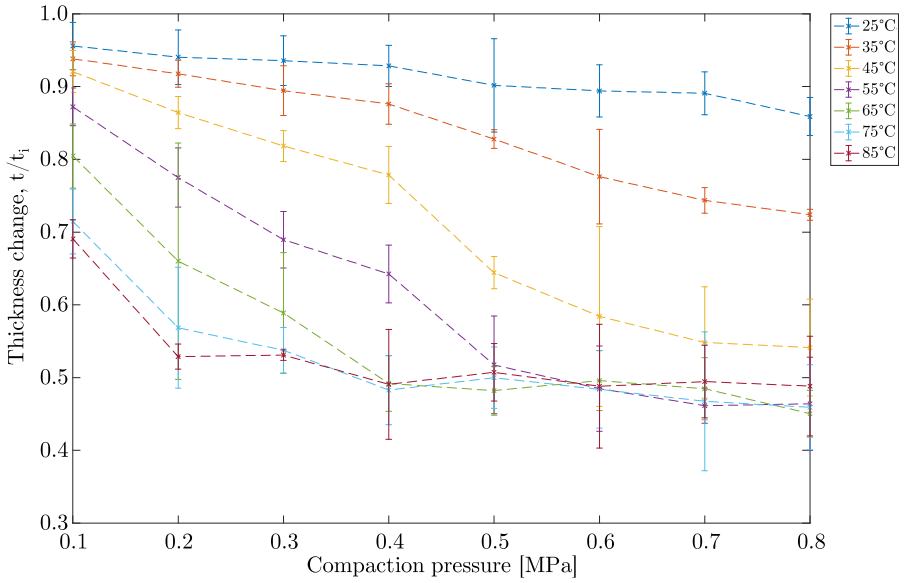

Figure 4.5: Normalized thickness change, comparing the final thickness after 16 compaction cycles to the initial thickness for different temperature and pressure levels.

The relaxation response shown in Fig. 4.6 corresponds to the compaction behavior. With rising temperature and pressure, the thickness increase during release time rises, with limitations above 55 °C in parallel to the limit observed in the compaction behavior. The thickness profile during release shows a steep, almost linear increase for the majority of the relaxation, followed by a smaller non-linear flattening to a level below the thickness before compaction (cf. Fig. 4.3).

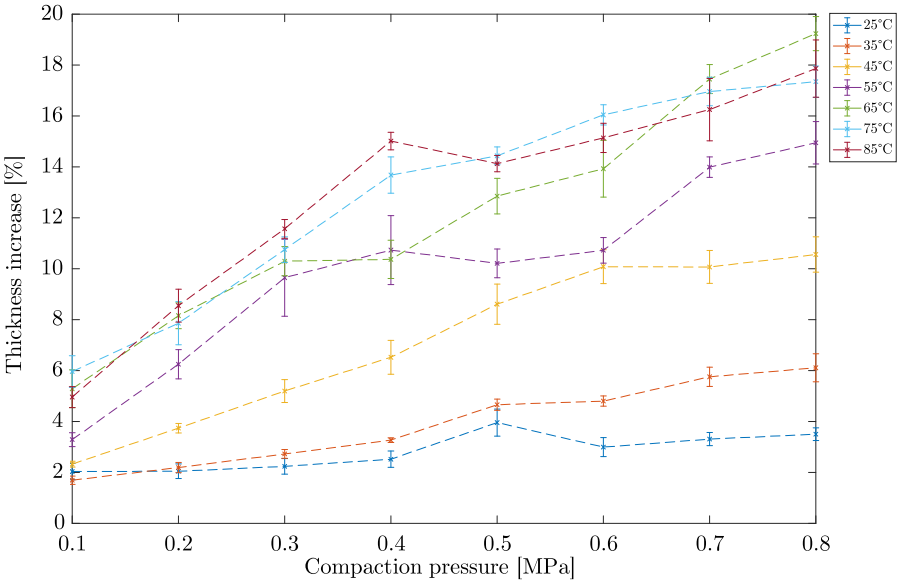

Figure 4.6: Mean thickness increase during release time of all cycles for different temperature and pressure levels.

Effect of the number of plies

In addition to the full-factorial variation of pressure and temperature, single factors such as the ply number were varied in a separate set of experiments. The tests were performed at 55 °C with a pressure of 0.5 MPa and UD lay-up (cf. Tab. 4.2). In Fig. 4.7, the thickness profile for the compaction of samples with 16, 24 and 32 plies is shown with normalized (left) and absolute (right) thickness. The general progress of the compaction is similar. The time per cycle increases with ply number due to force-controlled programming of the rheometer. Higher absolute sample thicknesses lead to longer travel distances to reach a certain reaction force. After high compaction ratios during the first cycles, it converges towards a limit. With increased number of cycles, the compaction per cycle decreases. For the 16-ply samples, the mean thickness reduction compared to the previous cycle was around 1 % for the last two cycles. They experienced only 0.5 % to 0.7 % compaction after the 12th cycle. For the 32-ply samples, this compaction value was reduced to 0.4 % after the 12th cycle. The thickness change compared to the initial

thickness was 51.7 % for 16 plies, 46.1 % for 24 plies and 45.7 % for 32 plies (cf. Fig. 4.8). The average thickness reduction per cycle was 3.0 % for 16 plies, 2.2 % for 24 plies and 1.7 % for 32 plies.

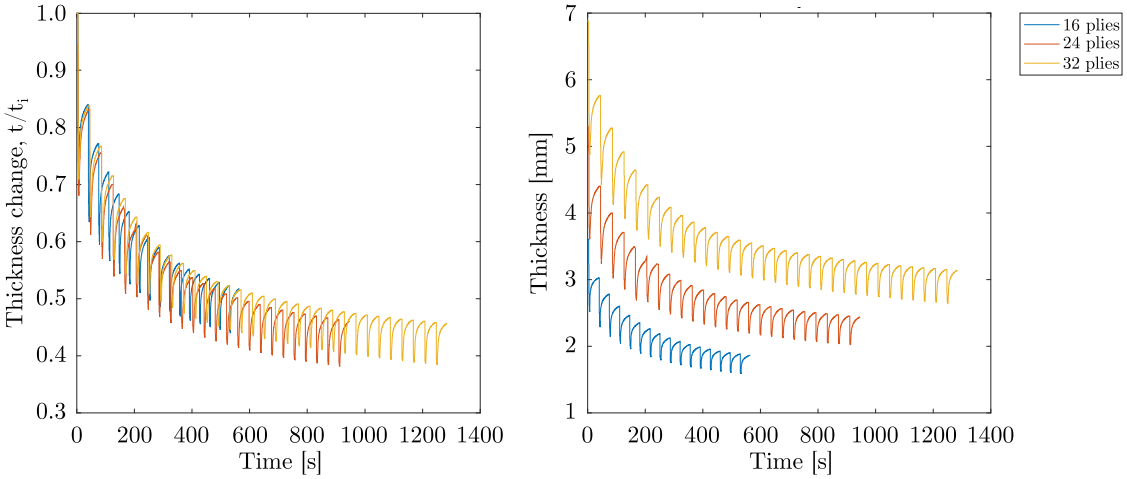

Figure 4.7: Compaction profile of samples with different ply numbers with normalized (left) and absolute (right) thickness profile.

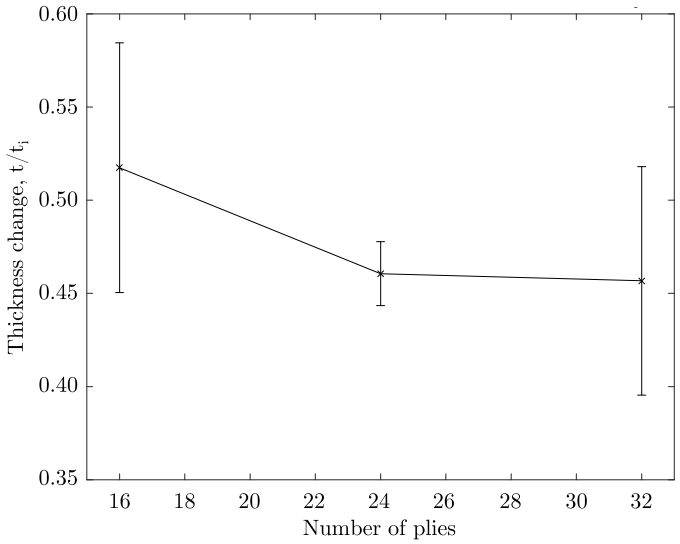

Figure 4.8: Normalized thickness reduction for different ply numbers.

Effect of the fiber orientation

The influence of the fiber orientation was analyzed by samples with CP fiber orientation to the standard UD samples. All tests were performed at 55 °C with a pressure of 0.5 MPa (cf. Tab. 4.2). Fig. 4.9 shows a much higher compaction of the UD laminate compared to the CP samples. The UD samples were compacted to 48.2 % of their initial thickness, whereas the CP samples maintained 84.0 % of their

initial thickness. These results correspond to other studies showing a much higher compaction of UD laminates compared to non-UD lay-up [11, 37, 139]. Non-UD plies are isolated, especially regarding transverse widening, and reach a locking configuration earlier compared to UD plies [37].

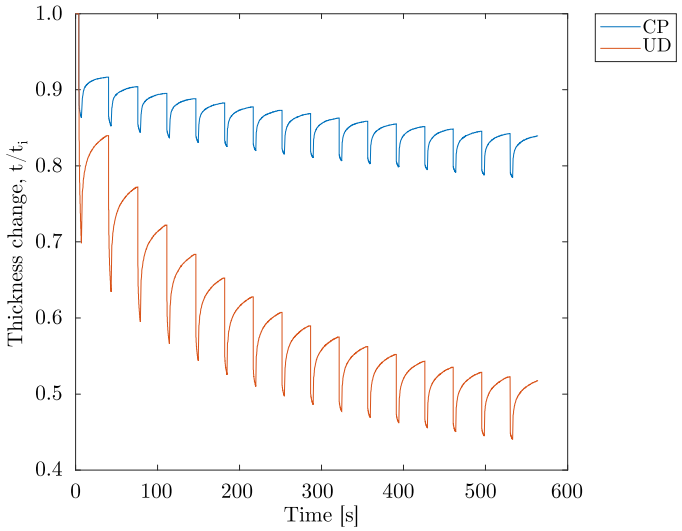

Figure 4.9: Normalized compaction profile of samples with cross-ply (CP) and unidirectional (UD) fiber orientation.

Effect of the material

The standard samples of this set of experiments consist of unslit prepreg sheet material. Here, slit-tape samples were compared to the standard samples to analyze the influence of the tape geometry with regard to the AFP process. The slit-tapes had a width of $^1/_8''$ and were placed manually as described in Sec. 4.1.1. Fig. 4.10 shows the compaction profiles of standard and slit-tape samples at three different temperatures. At 25 °C, the profiles are well aligned, showing only minor differences in the release response. The initial thickness is reduced to about 90 % for both tape types. At 55 °C, the slit-tape samples experienced less compaction compared to the standard samples. They were reduced to 54.4 % of their initial thickness, compared to 51.8 % for the standard set-up. For the highest temperature level, there is a big divergence of the profiles. The slit-tape samples were compacted to 39.2 % of their initial thickness, the standard samples to 50.8 %. There is no clear trend visible with rising temperature. A possible explanation is a difference in the compaction limits of the different sample set-ups. As described in the full-factorial variation of temperature and pressure above, the standard samples reach a compaction limit at 55 °C and 0.5 MPa pressure. There is only a minor thickness reduction beyond the compaction limit. The slit-tape samples experience signific-

ant additional compaction at 85 °C, so it seems they have a compaction limit at a higher temperature-pressure-combination.

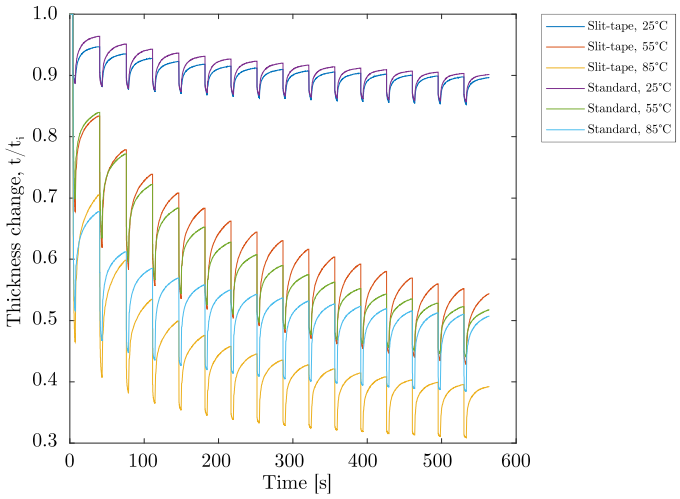

Figure 4.10: Normalized compaction profile of standard and slit-tape material samples at different temperatures.

4.1.3 Limitations

The experimental procedure on laboratory scale is a compromise of the replication of the AFP processing conditions on the one hand, and the feasibility of a reproducible experiment with a limited number of variables on the other hand. This compromise leads to inevitable simplifications that have to be considered when analyzing the results.

- The samples were laid-up to a complete laminate stack prior to the compaction experiment and compacted with even pressure over the entire stamp surface (cf. Sec. 4.1.1). This differs to the sequential lay-up and compaction of the actual AFP process. For reasons of feasibility, the stack compaction is established for laboratory scale AFP compaction experiments [7, 11, 37, 118]. A relative comparison of the compaction behavior of the samples within one set of experiments is legitimate and allows qualitative conclusions for the full-scale AFP process. Sec. 4.2 includes a comparison of full-stack or simultaneous compaction to sequential compaction.

- The samples were prepared by manual lay-up, leading to variations in their initial compaction state and potentially leading to unsystematic variations in the results of the experiments.

- The standard unslit samples and the slit-tape consisted of material systems with identical matrix system but differing fibers for availability reasons (cf. Sec. 4.1.1). As the compaction behavior is dominated by the properties of the matrix system and both material systems have a similar FVC, the difference is assumed to be negligible for this set of experiments.

4.1.4 Conclusion

A set of experiments with cyclic compaction of laminate samples in a rheometer was performed, replicating AFP compaction conditions in laboratory scale. Stacks of uncured prepreg were exposed to cyclic, short-term compaction and release steps at varying pressure, temperature, fiber orientation and number of plies. The results show a significant increase of the compaction with rising temperature and pressure. The relative overall compaction after 16 cycles varies from 4 % at 0.1 MPa and 25 °C to 55 % at 0.8 MPa and temperatures of 55 °C and above. Samples with UD fiber orientation show a significantly higher compaction than CP samples. A compaction limit was identified starting at 0.5 MPa and 55 °C, with about 50 % thickness reduction compared to the initial thickness value. Above these parameters, no significant additional compaction is observed. Comparable lab-scale compaction studies by Ivanov et al. [139] and Nixon et al. [37] show a compaction and transverse widening limit that corresponded to the onset of bleeding. This effect was attributed to the transition from squeezing to bleeding flow in the range of 60 °C to 70 °C at a pressure of 0.26 MPa. It is assumed, that no flow transition from squeezing to bleeding flow taking place in the presented set of experiments, as this transition would lead to a shift of the compaction limit with increasing pressure and temperature [37, 139]. Further studies have to be performed to verify whether and, if so, under what conditions the transition from squeezing to bleeding flow appears during AFP processing. This could be used to acheive more homogenous laminate quality, potentially even without an autoclave.

4.2 Cyclic compaction of laminate stacks using a universal testing machine

In this set of experiments, pre-stacked laminates of uncured prepreg were compacted via compaction plates in a universal testing machine (UTM) with different levels of pressure and temperature. The goal was to replicate the AFP lay-up sequence on a laboratory scale level similar to the experiments in Sec. 4.1, but with an extended sample size to exclude scaling or edge effects.

This section includes a description of the applied materials and methods as well as the results with their discussion. The limitations are listed followed by a conclusion.

4.2.1 Materials and methods

Equipment

The compaction was realized with a 250 kN UTM by *Hegenwald & Perschke* equipped with a 100 kN load cell and a heat chamber for test temperatures in a range from −40 °C to 350 °C (cf. Fig. 4.11 left). Customized steel compaction plates with a size of 220 $mm \times 220\,mm$ and flatness tolerances of max. 0.05 mm on both sides were mounted for the sample compaction (cf. Fig. 4.11 top right). The strain measurement was done contactless with a 2.8 mega pixel (MP) video extensometer by *LIMESS* with a 75 mm f/1.8 C-mount lens (cf. Fig. 4.11 bottom right). A 2× teleconverter was installed between camera body and lens, leading to an effective focal length of 150 mm. The theoretical resolution of this set-up is 1 µm.

Material

The samples were laminated with the toughened aerospace grade UD prepreg *HexPly 8552/AS4* by *Hexcel* [95]. This material system has a nominal cured ply thickness of 0.130 mm and a nominal fiber volume fraction of 57.42 %. All samples were laminated and tested in uncured state with a maximum test duration of 25 minutes at max. 55 °C, in a range without significant influence on the degree of cure [94, 138]. The out-time of all samples was tracked and kept within a range of ± 3 h at testing. More details on the applied material system can be found in Sec. 2.2.2.

Experimental preparation and procedure

The samples had a size of 200 $mm \times 200\,mm$ with 16 plies. They were built by manual lay-up of plies, pre-cut by an automated cutter system *Zünd M-1200 CV*.

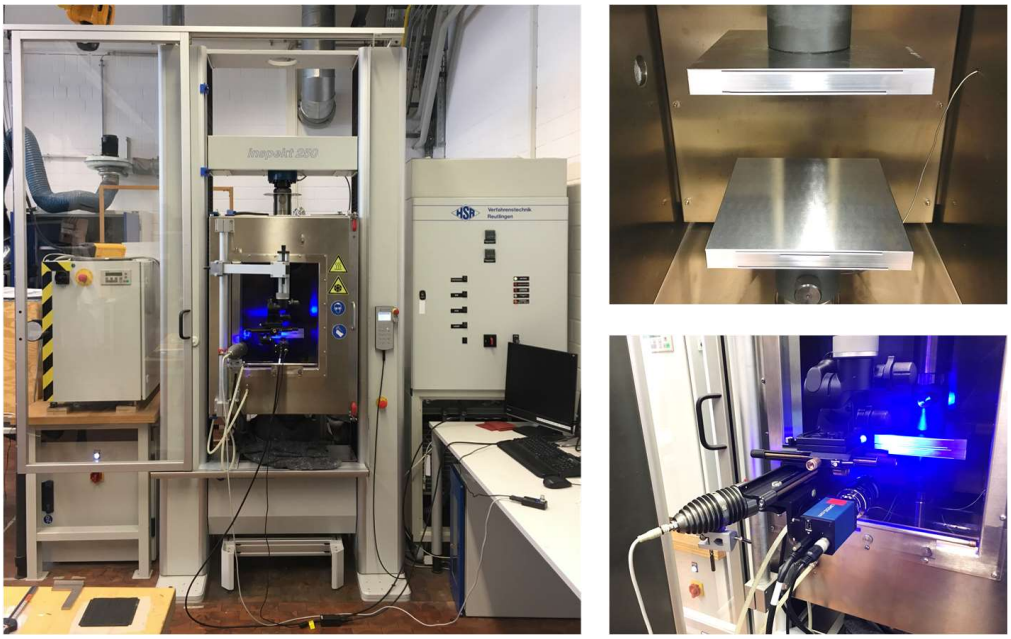

Figure 4.11: Experiment setup of the compaction experiments on the 250 kN universal testing machine (UTM) (left) with compaction plates (top right) and video extensometer (bottom right).

The compaction during deposition was realized with the self-weight of a handheld compaction roller in order to avoid excessive and undefined pre-compaction.

In the main set of experiments, a full-factorial two level variation of the parameters temperature, pressure, fiber orientation and application of dedicated debulking steps was implemented (cf. Tab. 4.3). The samples were compacted as a full laminate stack, with all plies being compacted simultaneously. Fiber orientation was varied from unidirectional (UD) to cross ply 0/90 (CP). Test temperatures were varied from 25 °C to 55 °C representing room temperature and high temperature AFP process conditions. Pressure was varied between 0.1 MPa and 0.5 MPa as these are considered as minimum and maximum AFP process pressures. Debulking steps were replicated by applying 0.1 MPa pressure with the compaction plates for 15 min after every 8^{th} compaction cycle. This represents a typical debulking interval after every 8^{th} ply.

In an additional fractional-factorial set of experiments, the laminate was built and compacted sequentially. The samples were laminated in the UTM and compacted by it after each ply. This set was implemented to check for the influence of the simultaneous full stack compaction as simplification compared to the sequential compaction closer to actual AFP processing conditions. As the laminate had to be accessed after each compaction, all samples had to be compacted at room temperature (cf. Tab. 4.3).

Table 4.3: Overview of all UTM experiment variations.

Test type	Compaction c	Fiber orient. a	Temperature T [°C]	Pressure p [MPa]	Debulking p_d [MPa]
full-factorial	simultan. full stack	UD/CP	25/55	0.1/0.5	-/0.1 (15 min every 8$^{\text{th}}$ cycle)
fractional-factorial	sequential	UD/CP	25	0.5	-

For all sets, the previously stacked laminate samples were exposed to several compaction cycles replicating the compaction profile during deposition in the AFP process – similar to the rheometer compaction study presented in Sec. 4.1. The number of compaction cycles applied, corresponded to the number of plies of the samples. This simplified replication of the AFP process compaction by a simultaneous compaction of a full laminate stack is applied in several AFP compaction studies [7, 11, 37, 118]. For all experiments, the parameter variations were repeated three times. The order was randomized except for the temperature levels, which were grouped for reasons of practicability.

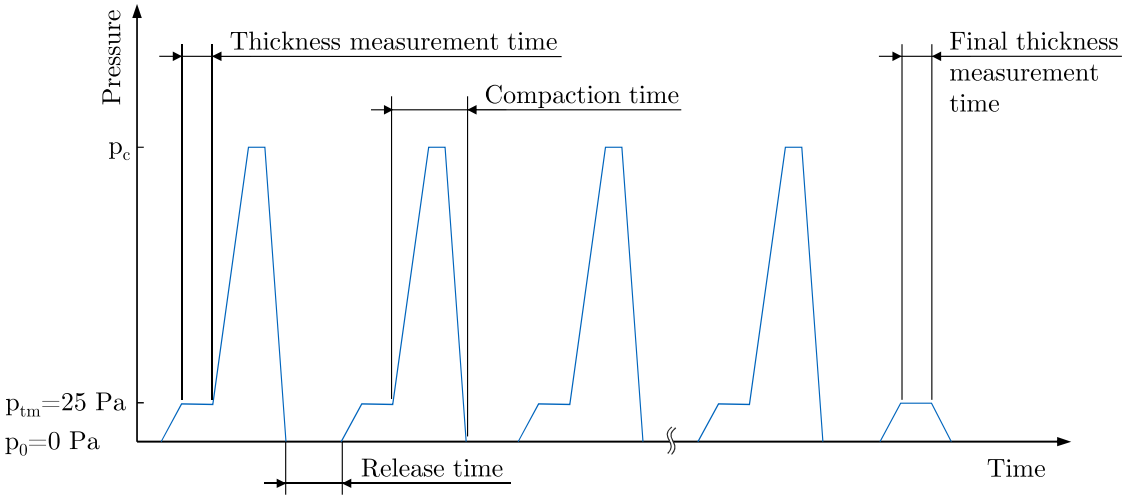

Figure 4.12: Compaction procedure without debulking steps as implemented on the UTM.

Fig. 4.12 shows the compaction procedure implemented in the UTM for the experiments without debulking, Fig. 4.13 with debulking. The thickness of the samples was measured prior to each compaction cycle by applying a minimum compaction of $p_{tm} = 25\ N$ for 5 s. The desired compaction pressure p_c was applied in the

next step at a rate of 10 kN/s. After reaching the desired compaction pressure, the compaction plate was removed at a rate of 50 mm/min. This resulted in an overall compaction application time of 2.6 s with a holding time of the compaction pressure of 0.25 s (cf. UTM raw data in Sec. A.1). The release time after each compaction cycle was 30 s. This routine was repeated 16 times. After the last compaction cycle, the final sample thickness was measured again by applying $p_{tm} = 25\ N$. The experiments with applied debulking varied from this procedure only by an additional applied debulking pressure $p_d = 0.1\ MPa$ for 15 min after the 8^{th} and 16^{th} compaction cycle (cf. Fig. 4.13).

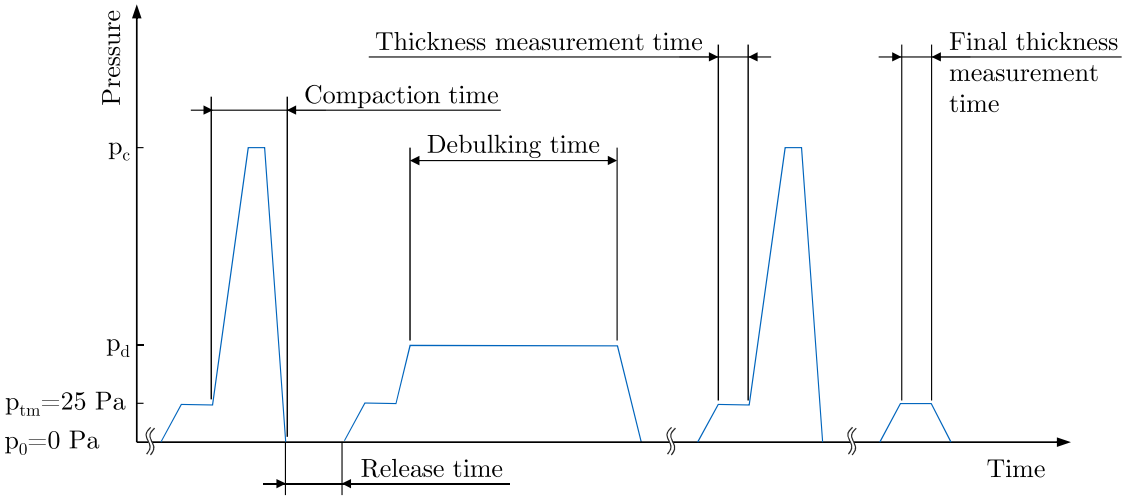

Figure 4.13: Compaction procedure with debulking steps as implemented on the UTM.

Evaluation methods

The sample thickness was measured initially and after each compaction cycle, as indicated in Fig. 4.12 and Fig. 4.13. The data was visualized as thickness over compaction cycle in Fig. 4.14, Fig. 4.15 and Fig. 4.16 to get an overview over the compaction profile. All main effects and interactions of the varied parameters were evaluated using linear regression analysis and visualized in Fig. 4.17 and Fig. 4.18. The laminates were cured to a degree of cure (DOC) above 60 % applying a soft curing method to secure a defined state for handling of the samples without manipulating the laminate properties (cf. Sec. 5.2.1). For an excerpt of the samples with minimum and maximum compaction parameter settings, the void volume content (VVC) was determined (cf. Tab. 4.4) via measurement of sample volume and density based on ASTM D3171-5 [140].

Table 4.4: Overview of the VVC sample parameters.

Sample	Fiber orient. a [-]	Compaction c [-]	Temperature T [°C]	Pressure p [MPa]	Debulking p_d [MPa]
L_{low}	CP	SIM	25	0.1	-
L_{high}	UD		55	0.5	
D_{low}	CP		25	0.1	0.1
D_{high}	UD		55	0.5	
C_{low}	CP	SQ	25	0.1	-
C_{high}	UD		25	0.5	

4.2.2 Results and discussion

The results are first analyzed based on the thickness progress of the stack compaction without debulking and with additional debulking steps as well as the sequential compaction samples. In a second step, the results of the full-factorial experiments with and without debulking are analyzed for their interactions and interdependencies. The varied parameters and their setting (low ↓, high ↑) are given in the legend of the respective figure (cf. Tab. 4.3).

Compaction without debulking

Fig. 4.14 shows the thickness progress over 16 compaction cycles without debulking. There is a clear trend of thickness reduction for all samples. The maximum final thickness is reached with the CP samples at low pressure and low temperature. The smallest final thickness occurred for UD samples with high pressure and high temperature. These configurations have a relative thickness difference of 5.7 %. Apart from the minimum and maximum final thickness, there is no clear trend visible in the order of results. The initial thickness varies considerably, making a normalization diffucult. This is presumably due to the manual lay-up of the samples and the very low force used for thickness measurement. A considerable number of the thickness progress graphs in Fig. 4.14 intersect between the initial thickness and after the first compaction step. The order of the samples changes after the initial compaction, but remains constant for most samples up to the final compaction.

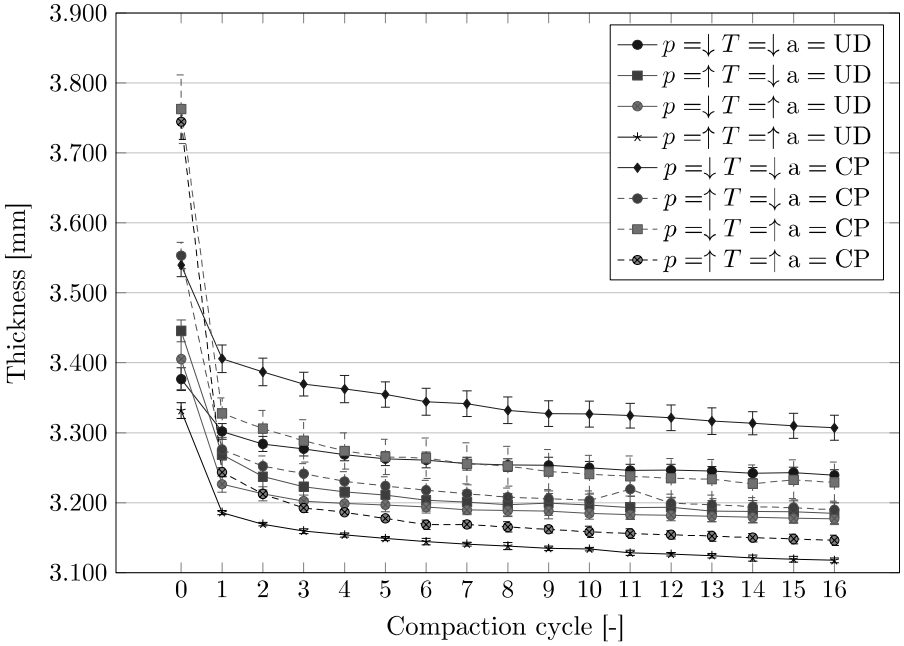

Figure 4.14: Compaction profile of samples without debulking.

Compaction with debulking

Fig. 4.15 shows the thickness progress over 16 compaction cycles for all samples with additional debulking steps. The thickness before and after the final debulking step is indicated as compaction cycle number 17 and 18 on the x-axis. There is again a clear overall trend of thickness reduction for all samples with distinct thickness reduction during the two debulking steps. The initial thickness varies randomly and the order in the overall thickness changes similar to the experiments without debulking mostly after the first compaction cycle. After the 8^{th} compaction cycle prior to the first debulking, the CP samples with low pressure and low temperature shows the biggest thickness. The UD samples with high pressure and high temperature have the lowest overall thickness at this point. This trend is similar to the experiments without debulking. The deviation between the minimum and maximum thickness after the 8^{th} compaction is 5.2 %. The first debulking step brought a significant compaction for all samples of 3.0 % on average, together with a rearrangement of the thickness order. The relative difference of the sample thickness was decreased to 1.6 %. For the compaction cycles after the first debulking step, there is no additional thickness decrease visible. The second debulking step leads to a final thickness reduction by 1.0 % on average. The relative thickness difference is with 2.3 % considerably smaller than without debulking. The UD samples with low pressure and low temperature setting had the biggest final thickness value. The smallest overall thickness was reached with the UD samples with high pressure and high temperature. The short-term compaction contributed 66.7 % to the

overall compaction, the debulking 33.3 %. Excluding the initial compaction step, the debulking causes 78.2 % of the total thickness decrease.

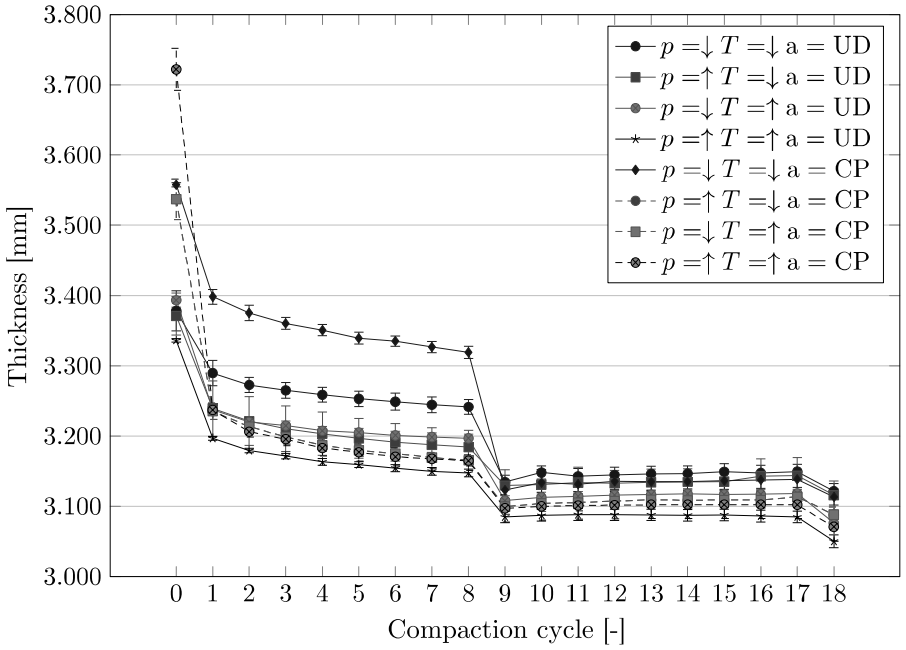

Figure 4.15: Compaction profile of samples with debulking.

Sequential compaction

Fig. 4.16 shows the normalized thickness progress of the samples with sequential compaction (SQ) compared to samples with simultaneous stack compaction (SIM). The thickness is normalized by the nominal ply thickness of the material divided by the number of plies present during the respective compaction step. The results show a clear trend of thickness reduction for all compaction cycles and all parameter combinations. The initial thickness has a noticeable difference, with the SQ samples being 16.1 % thicker than the SIM samples. After 16 compaction cycles, this difference is reduced to 1.6 %. For the UD samples, the final thickness difference is 0.9 %, for the CP samples it is 2.4 %. A potential explanation for the difference is the differing total number of compaction cycles per ply. For the SIM samples, all 16 plies are compacted 16 times simultaneous in a full stack compaction, leading to an accumulated sum of 256 ply compactions. In the SQ set-up, the number of compactions per ply decreases towards the top from 16 compactions for the first layer to one compaction for the final layer. This leads to an accumulated sum of $\sum_{n=1}^{16} n = 136$ ply compactions.

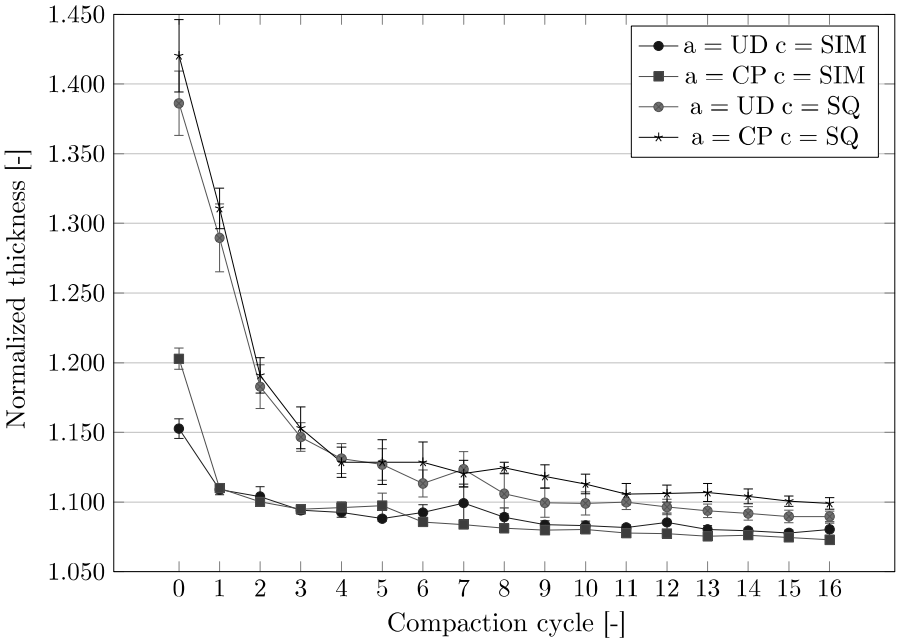

Figure 4.16: Compaction profile of samples with sequential compaction.

Parameter effects and interactions

Fig. 4.17 shows the single factor main effects of the full-factorial parameter variation. Compaction pressure p and temperature T showed a similar effect on the final thickness. A pressure increase from 0.1 MPa to 0.5 MPa decreased the final thickness of the laminate by 0.048 mm or 1.5 % of the total laminate thickness. Increasing the process temperature from 25 °C to 55 °C led to a final thickness reduction of 0.052 mm or 1.6 %.

The effect of fiber orientation or ply alignment a showed a tendency to lower thickness reduction for CP compared to UD by 0.018 mm or 0.6 %. Taking into account the two-sided confidence interval of 0.02 mm, this effect was of low significance.

The single effect of the application of debulking steps, indicated as debulking pressure p_d in Fig. 4.17, is dominant among the single parameter main effects. The application of 0.1 MPa debulking pressure for 15 minutes leads to an average compaction potential of 0.106 mm or 3.3 % of the total laminate thickness. The compaction potential for debulking is here 55.2 % higher compared to the compaction pressure and 51.3 % higher compared to the process temperature. The experimental procedure led to the fact, that all high temperature samples were debulked at the elevated temperature of 55 °C. This leads to an overestimation of the debulking effect when comparing it to debulking at room temperature.

All significant interactions of the main parameters are shown in Fig. 4.18. The two graphs per line a, b, c and d show the same interaction effect depicted with a swapped base for better comprehension of the effect. The interaction between

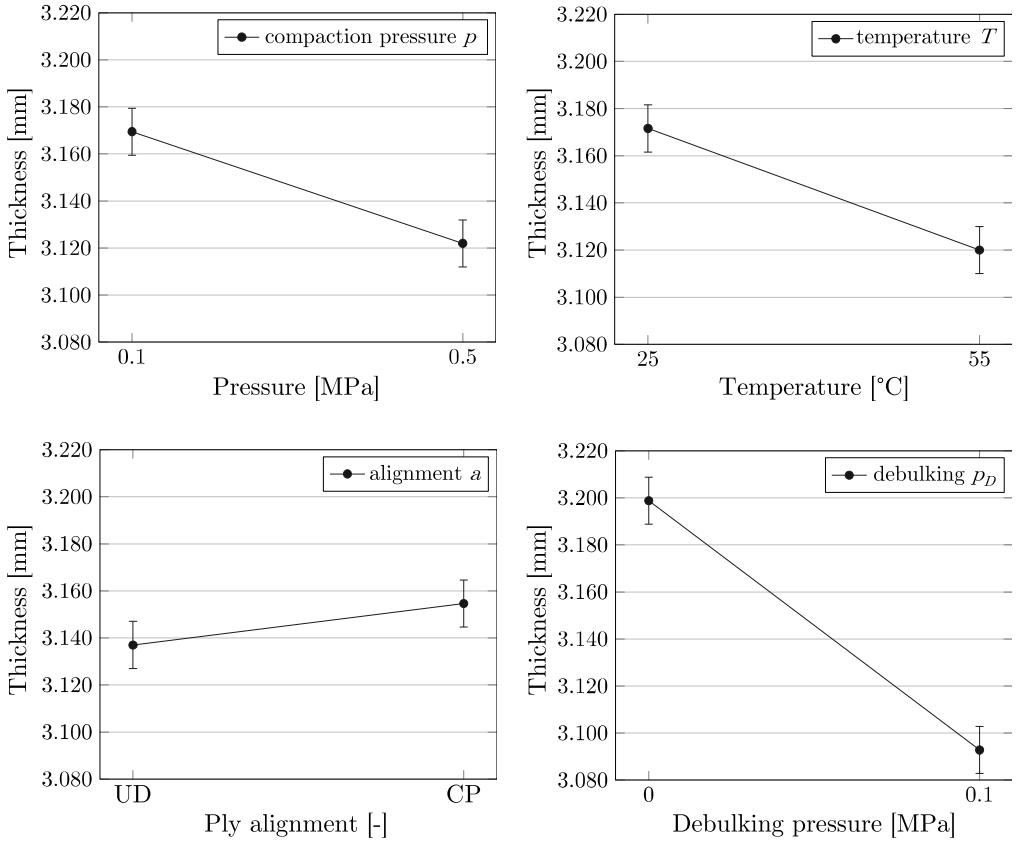

Figure 4.17: Main effects for the full-factorial parameter variation.

compaction pressure and debulking pressure (cf. Fig. 4.18 a) shows, that the compaction potential of debulking is reduced with increasing compaction pressure by 45.2 %. When debulking is applied, the effect of the compaction pressure setting becomes insignificant, illustrated by the overlapping two-sided confidence intervals in Fig. 4.18 a for $p_d = 0.1\,MPa$. The compaction potential of the compaction pressure is reduced by 78.8 % when debulking is applied. This indicates that the potential for compaction by increasing compaction pressure diminishes as the debulking takes a predominant share of the overall compaction. On the other hand, this shows the potential for compaction when the vacuum debulking effort is reduced.

Another strong interaction of two main parameters was identified for the ply alignment and the debulking pressure (cf. Fig. 4.18 b). The ply alignment has an influence on the final thickness as long as no debulking is applied. With applied debulking, the effect of the alignment is reduced to an insignificant difference.

a) Interaction compaction pressure p – debulking pressure p_d

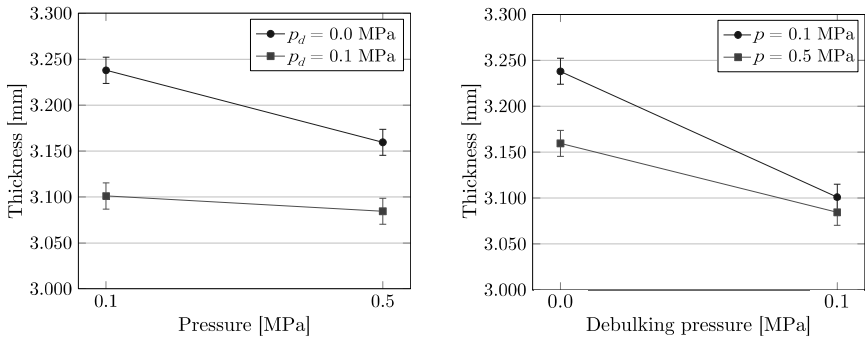

b) Interaction ply alignment a – debulking pressure p_d

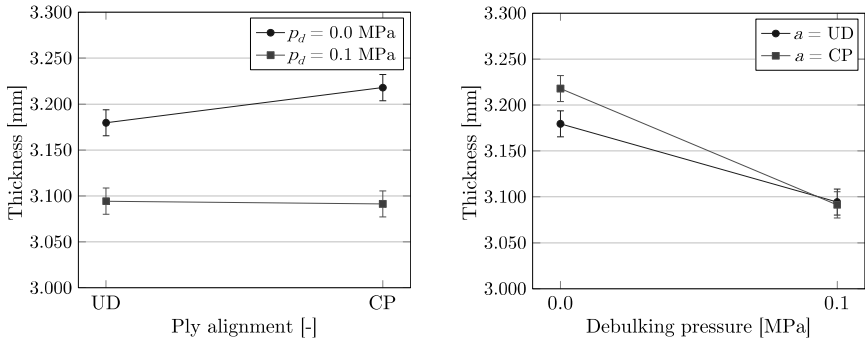

c) Interaction compaction pressure p – ply alignment a

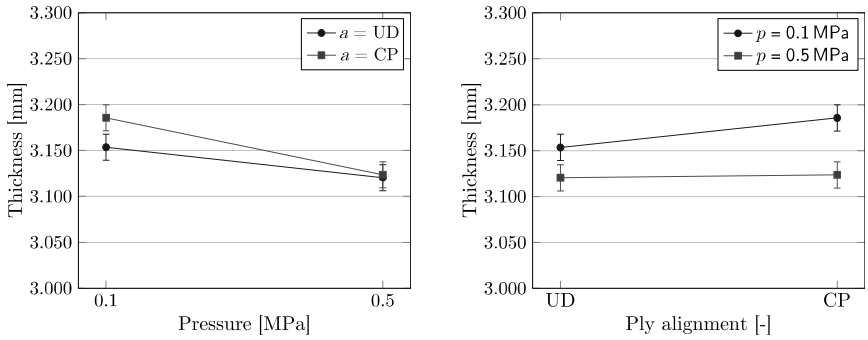

d) Interaction temperature T – debulking pressure p_d

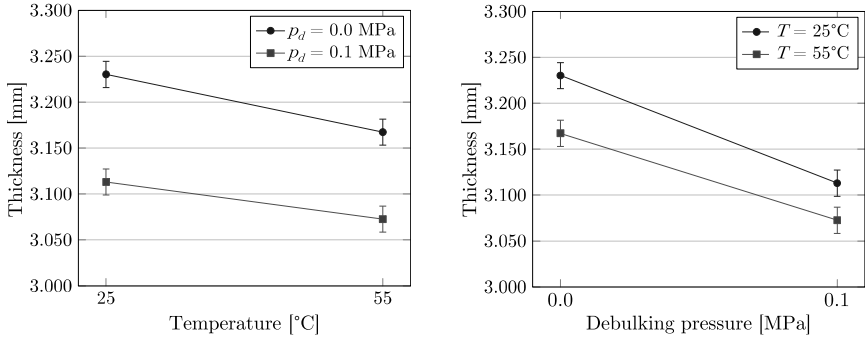

Figure 4.18: Parameter interactions for the full-factorial parameter variation.

The interaction between compaction pressure and ply alignment is similar, but of smaller overall effect size (cf. Fig. 4.18 c). Ply alignment has an influence on the final thickness only for low compaction pressure. An elevated compaction pressure eliminates this influence. With increasing pressure, the compaction potential is bigger for CP lay-up compared to UD fiber orientation.

The interaction of the parameters process temperature and debulking pressure is small, indicated by the almost parallel lines in Fig. 4.18 d. An elevated process temperature slightly reduces the compaction potential of applied debulking. The application of debulking on the other hand slightly reduced the compaction potential of elevated temperature settings.

Void content analysis

Fig. 4.19 shows the results of the void volume content (VVC) determination in soft cured state (cf. Sec. 5.2.1), with the goal to compare the laminate properties as deposited. The samples include minimum ("low") and maximum ("high") compaction regarging tempeature and pressure settings, with debulking ("D") and without debulking ("L") as well as samples with sequential compaction ("C"). The parameters of all samples are summed up in Tab. 4.4. The VVC ranges from 3.5 % for C_{high} to 13.7 % for L_{low}. All samples with high compaction parameters show a low VVC and vice versa. The highly compacted stack compaction samples L_{high} and D_{high} both have a VVC of 4.2 %. This suggests that for high pressure and temperature, additional vacuum debulking does not result in a lower VVC. A lower final thickness of the debulked samples may result from additional shear flow, leading to a further spreading of fiber and matrix compared to the undebulked samples. The VVC of the sequentially compacted samples with high compaction settings C_{high} is slightly lower than for L_{high} and D_{high}. A possible cause may be the reduced resistance in z-direction as the laminate thickness is built up sequentially. This comparison has to be considered with care, as C_{high} was unlike the other highly compacted samples tested at room temperature for feasibility reasons (cf. Tab. 4.4). Comparing the samples with low compaction settings L_{low}, D_{low} and C_{low}, they show a higher variation in their VVC but also a higher scatter within one parameter setting. From L_{low} to D_{low} the VVC is decreased by 4.6 %. This shows a high influence of the debulking application when the rest of the compaction parameters has a low setting. L_{low} and C_{low} have identical settings, except for the simultaneous stack compaction for L_{low} and the sequential compaction for C_{low}. For the sequential compaction, the VVC decreases by 2.6 % . Together with the difference of L_{high} and C_{high} this suggests, that the VVC of the simultaneously

compacted samples is overestimated compared to the sequential lay-up of AFP processing.

Fig. 4.19 also includes the normalized density ρ_{norm} of the samples as considered for the void content analysis. The density is normalized by dividing the measured sample density by the nominal density $\rho_{nominal} = 1.58\, g/cm^3$ of the prepreg material according to the data sheet [95]. The highly compacted samples all reach a normalized density above 95 %, while the low compaction samples reach 91 % or lower. Comparing the results of VVC and normalized density, an inversely proportional correlation becomes present. All highly compacted samples have a low variance and scatter in the normalized density results. The normalized density for the low compaction samples shows a bigger deviation with L_{low} having the highest VVC and lowest ρ_{norm} and D_{low} having the lowest VVC and highest ρ_{norm}. This suggests that the determination of the normalized density can be an option for a comparison of different laminates.

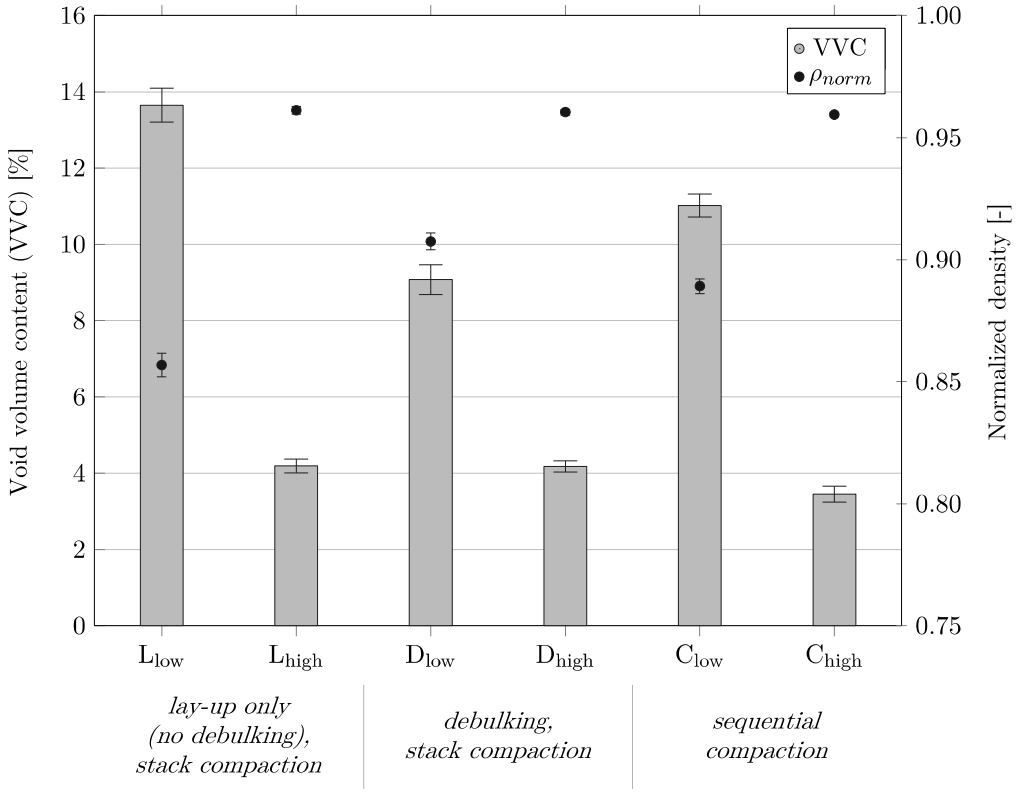

Figure 4.19: Void volume content and normalized density of samples with low and high compaction parameter settings.

4.2.3 Limitations

The experimental procedure on laboratory scale is a compromise of the replication of the AFP processing conditions on the one hand, and the feasibility of a reproducible experiment with a limited number of variables on the other hand. This compromise leads to inevitable simplifications that have to be considered when analyzing the results.

- All samples with simultaneous stack compaction (SIM) were laid-up to a complete laminate stack prior to the compaction experiment and compacted with even pressure over the entire sample surface (cf. Sec. 4.2.1). This differs to the sequential lay-up and compaction of the actual AFP process. For reasons of feasibility, the stack compaction is established for laboratory scale AFP compaction experiments [7, 11, 37, 118]. A relative comparison of the compaction behavior of the samples within one set of experiments is legitimate and allows qualitative conclusions for the full-scale AFP process. A fractional factorial set of experiments with sequential compaction (SQ) was conducted to check for systematic differences between SIM and SQ compaction. The results showed similar qualitative behavior and compaction profiles, with a tendency to higher final thickness but lower VVC for the SQ samples.
- The experimental procedure led to the fact that all samples combining debulking and high temperature were debulked not at room temperature, but at the elevated temperature of 55 °C. This leads to an overestimation of the debulking effect when comparing it to debulking at room temperature.
- The debulking procedure was replicated by an even pressure of 0.1 bar for 15 min after 8^{th} and 16^{th} compaction cycle. Unlike for the actual vacuum debulking as applied in industrial applications, no vacuum was present. This leads to an underestimation of the void removal, especially in z-direction.
- The samples were prepared by manual lay-up, leading to variations in their initial compaction state. This is visible at the initial thickness in the compaction profiles.

4.2.4 Conclusion

A set of experiments with cyclic compaction of laminate samples in a UTM was performed, replicating AFP compaction conditions in laboratory scale. Stacks of uncured prepreg were exposed to cyclic, short-term compaction and release steps at varying pressure, temperature, fiber orientation and number of plies. The results

show a significant thickness reduction for all samples with the highest compaction with high pressure, high temperature and UD fiber orientation. The lowest compaction was shown for low pressure, low temperature and CP fiber orientation. A comparison of full-stack simultaneous stack compaction (SIM) and sequential compaction (SQ) identified a higher overall compaction for the full-stack procedure, presumably due to the higher average number of compaction steps per ply.

An increase of pressure and temperature showed positive effects on thickness reduction on a similar scale. Dedicated debulking had the biggest impact on the compaction, equalizing the thickness differences of the different sample combinations. The effect was amplified by the experimental procedure though, leading to an overestimation of debulking. CP fiber orientation allowed less compaction compared to UD orientation.

Significant interactions were identified for the parameter combinations pressure and debulking, fiber orientation and debulking, pressure and fiber orientation as well as temperature and debulking. The compaction potential of debulking was reduced with increasing compaction pressure. When debulking was applied, the effect of the compaction pressure setting became insignificant. VVC was analyzed in soft cured state, showing the laminate properties as deposited. A clear trend of reduced VVC with higher compaction was shown. For high compaction parameter settings, additional debulking did not lead to further VVC reduction. It was identified, that the full-stack simultaneous compaction leads to an overestimation of the VVC compared to sequential compaction as appearing in full-scale AFP processing.

4.3 Cyclic compaction simulation

This section describes an finite element (FE) based approach to simulate the cyclic compaction behavior similar to the set of laboratory scale compaction experiments covered in Sec. 4.2. This is based on applying the hyper-viscoelastic model developed by Belnoue et al. [118] of the University of Bristol.

The section includes an overview on the set-up of the FE model, the results and their discussion with a conclusion.

4.3.1 Set-up of the finite element model

An FE based model was set up to replicate the compaction behavior of the UTM experiments described in Sec. 4.2. The model was built using Abaqus FEA Standard and implementing the user defined material model (UMAT) subroutine of the hyper-viscoelastic material model by Belnoue et al. [118] of the University of Bristol.

The experimental set-up of Sec. 4.2 was replicated with rigid compaction plates and a 16 ply UD laminate in between. Since the laminate is symmetrical, only a quarter of the in-plane dimension was created with the respective symmetry conditions to improve the computation time of the model. The thickness progression is measured via the displacement of the center node defined at the center of the laminate at the upper ply (cf. Fig. 4.20). The model was run on the Linux super-computing cluster segment CoolMUC-2 of the Leibniz supercomputing center (LRZ).

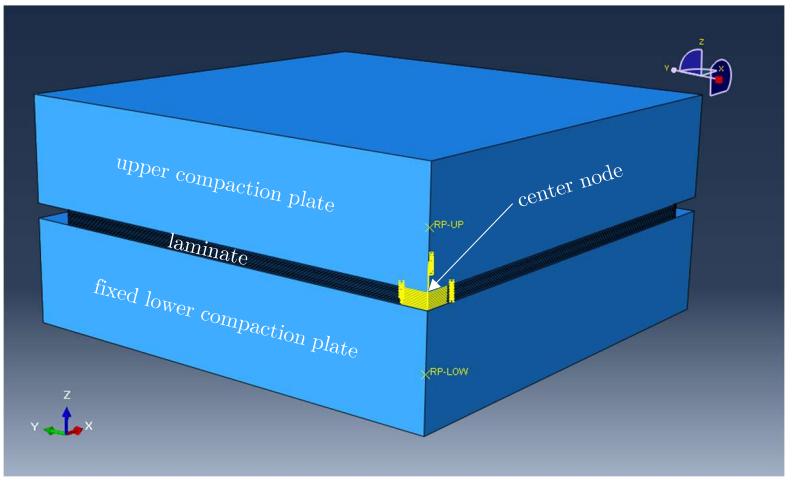

Figure 4.20: Overview of the symmetric quarter model built in Abaqus with upper compaction plate, laminate and fixed lower compaction plate.

Upper and lower compaction plate were defined as rigid bodies with a dimension of $110\,mm \times 110\,mm \times 25\,mm$. All plies were designed as deformable bodies with a dimension of each $100\,mm \times 100\,mm \times 0.219\,mm$. The initial thickness of the laminate stack was supposed to be equal to the mean of the initial thicknesses $t_{il} = 3.504\,mm$ for 16 plies of the experiments in Sec. 4.2. This results in an initial ply thickness of $t_{ip} = 0.219\,mm$. Both plates and all 16 plies were meshed within ABAQUS and defined as standard 8-node solid elements with reduced integration "C3D8R". The plates were assigned with the material properties of aluminum with a density of $2.7\,\mathrm{g/cm^3}$, a modulus of elasticity of 70 GPa and a Poisson ratio of 0.3. The material properties of the plies were assigned by the UMAT with the according material type carbon/epoxy IM/8552 prepreg, which was used for the model validation by Belnoue et al. [37, 118]. The lower compaction plate was defined as fixed against translation and rotation in all directions. For the upper plate, only translation in z-direction was allowed. Along the symmetry axes of the laminate, a lateral spreading was restricted. The contacts between the separate instances were defined as surface-to-surface contacts. Each ply was separately defined as master surface to the neighboring instances, that were defined as slave surfaces. In the contact of the upper and lowermost ply, the compaction plate was defined as master surface, the ply as slave. The cyclic loads were defined as single steps, applying a uniform load on a reference point on the upper compaction plate. The experimental compaction pressure of 0.1 MPa corresponds to a force of 1000 N for the quarter model contact area of $100\,mm \times 100\,mm$. Temperature was applied to the model via a predefined field. Output was generated as field output requests at an interval of 0.1 s.

4.3.2 Results and discussion

Fig. 4.21 shows representative results of the simulation runs. Displacement was measured at the central node of the upper compaction plate (cf. Fig. 4.21 a, c). The thickness at the end of the release time was defined as the thickness after a compaction cycle. It is displayed over all compaction cycles and in comparison to the experimental results of Sec. 4.2 in Fig. 4.21 b and d.

For the simulation without debulking, the initial maximum displacement ranges from -0.2343 mm to -0.2450 mm from cycle 1 to 16 with a steep relaxation close to the initial thickness. In detail, the progress of the final displacement is nonlinear with decreasing compaction over the compaction cycles (cf. Fig. 4.22). This is comparable to the experimental results on a qualitative level, but the quantity of the effect is too small in the range of two orders of magnitude (cf. Fig. 4.21 b). The

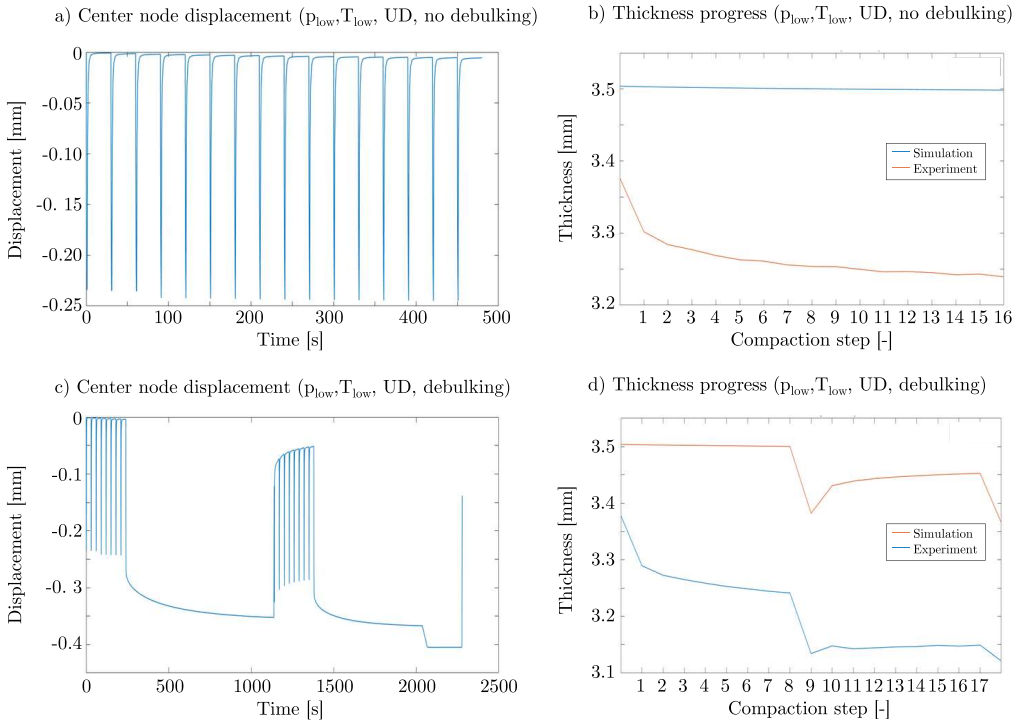

Figure 4.21: Simulation results showing the center node displacement (a, c) and thickness progress (b, d) for cyclic compaction with (d) and without (b) debulking.

initial offset of the experiment and simulation thickness progress is explained by the high variation of initial thickness in the experimental samples due to manual lay-up. The modelled thickness is set to the mean value of all experimental samples and therefore varies from single samples. The compaction simulation including debulking shows a similar displacement and thickness progress for the first 8 cycles. A distinct thickness reduction is reached during the 15 min debulking, much higher than for the compaction cycles. The absolute thickness reduction of the first debulking cycle is in a similar range for experiment and simulation with 0.107 mm and 0.118 mm, respectively. For the second debulking step, 0.028 mm were realized in the experiments compared to 0.086 mm for the simulation. The overall final thickness reduction was 0.257 mm for the experiment and 0.138 mm for the simulation.

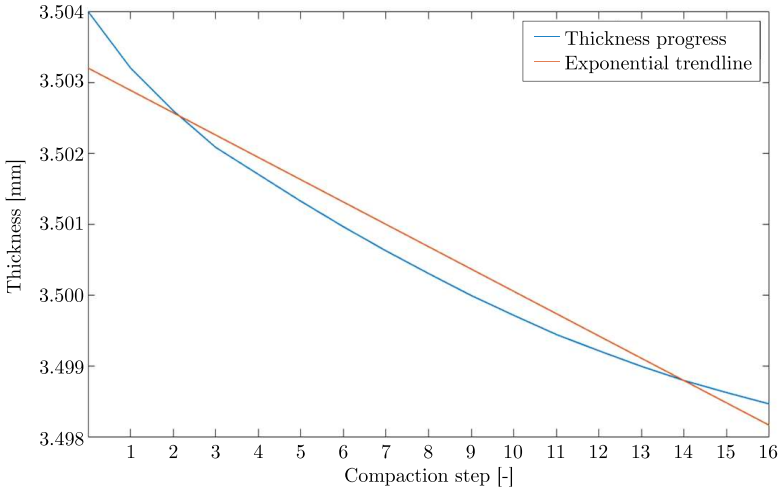

Figure 4.22: Thickness progress detail of the simulation results for p_{low}, T_{low}, UD, no debulking.

4.3.3 Conclusion

An FE model was set up with the goal of replicating laboratory the scale UTM compaction experiments described in Sec. 4.2 and creating a tool for efficient parameter variations for a given set-up. The model was built using Abaqus FEA Standard and implementing the UMAT subroutine of the hyper-viscoelastic material model by Belnoue et al. [118]. The results show a qualitative agreement with the experimental data. Quantitatively, however, there is an offset in the range of two orders of magnitude. The source of the discrepancy could not be identified within the scope of this thesis, but is most likely to be connected to the switch from shear to bleed flow in the UMAT. The simulation could not be applied as planned, and a comparison with more experimental runs is dispensable with this quantitative mismatch. An improvement of the approach must be part of follow-up work, in order to allow efficient simulation based parameter variations for a given set-up.

5 AFP compaction on full-scale

In the previous chapters, the AFP process chain was analyzed by scaled or partial experiments or simulations with the goal to find a realistic representation of the process at a feasible extent with a set of experiments including parameter variations. For a complex process like AFP, this is always a compromise, neglecting factors of variation and noise that are not to be excluded for a full-scale industrialized process. In this chapter, different sets of full-scale experiments are presented to exclude systematic bias of the results and to ensure practical relevance of the effects shown.

In Sec. 5.1 of this chapter, a set of experiments on the full-scale AFP compaction behavior during processing is described. It focuses on process parameter variations and their influence on the thickness progression during processing. Sec. 5.2 includes the evaluation of the influence of compaction variations on the mechanical performance of full-scale AFP laminates.

Parts of the results of this chapter were published by Engelhardt et al. [82, 141]. The studies were implemented with support of the student theses by Brath [142], Aufenanger [143] and Vogl [144] under the supervision of the author.

5.1 Compaction behavior during AFP processing

This section describes the investigation of the compaction behavior of prepreg tapes for full-scale AFP processing conditions in combination with vacuum debulking and subsequent autoclave curing. A series of experiments was performed to analyze the influence of AFP process parameters and debulking frequency on laminate compaction.

The section is subdivided into the description of the applied materials and methods, the results and their discussion and a conclusion.

5.1.1 Materials and methods

Equipment

Full-scale fiber placement was realized with an industrial AFP machine by *Coriolis Composites* (cf. Sec. 2.1.4), with the main process parameters heat input controlled by the power output P of the IR lamp, compaction pressure p applied by the silicone roller and lay-up velocity v. Thickness measurements of the laminates were performed with an optical 3D triangulation scanner *GOM ATOS III*. The scanner projects structured light on the measurement object and inspects its reflection via two cameras (cf. Fig. 5.1). The geometry of the object distorts the planar 2D pattern of the structured light, allowing a computation of the 3D geometry of the object. The scanner was equipped with lenses for a measuring volume of $320\,mm \times 320\,mm \times 240\,mm$ and a min. accuracy of 0.016 mm according to the measurement system manufacturer *GOM GmbH* [145]. [146]

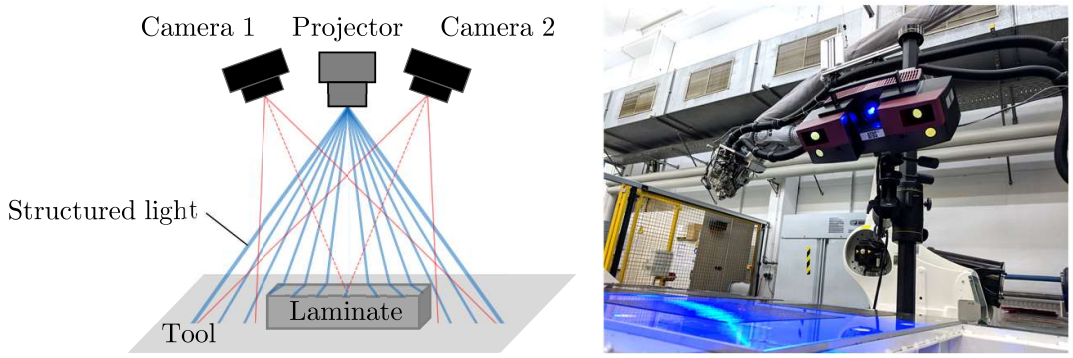

Figure 5.1: Optical thickness measurement principle (left) and set-up on site (right).

Material

The material system used in this study was *HexPly 8552/IM7* with a FAW of 134 gram per square meter, a matrix weight content of 34 % and a nominal cured ply thickness of 0.131 mm [95]. The material was processed as UD slit tape at a width of $^1/_8{}''$. More details on the applied material system can be found in Sec. 2.2.2.

Experimental set-up

Flat samples of 16 plies with a size of $200\,mm \times 200\,mm$ were laid up on a flat aluminum tooling with different parameter settings in a full-factorial experiment design and one repetition per parameter set (cf. Fig. 5.2). The varied parameters were heat input via lamp power of the IR heater P, compaction force of the silicone roller F resulting in a variation of the compaction pressure p, lay-up velocity v and debulking frequency f (cf. Tab. 5.1). The variations included a "low" and "high"

setting, representing the lower and upper limit of the typical process window for each parameter. Thickness measurements were performed after every eighth ply and after debulking if applicable. Laminate surface temperature was logged with an IR camera *FLIR A325sc* mounted on the lay-up head.

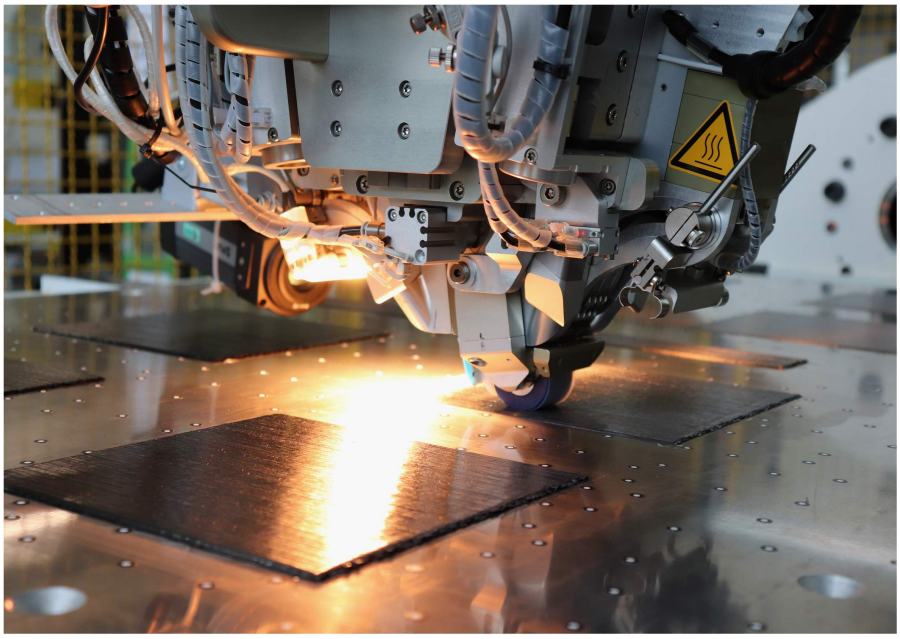

Figure 5.2: Experimental set-up with sample lay-up and reference points.

All samples were subsequently cured in an autoclave according to the data sheet. A first dwell step was held at 7 bar and 110 °C for 60 minutes. The final curing step at 7 bar and 180 °C was held for 120 minutes. Heating and cooling rates were 3 K/ min.

Table 5.1: AFP process parameter settings.

Parameter		Unit	low	high
Infrared lamp power	P	[W]	215 (50 %)	430 (100 %)
Compaction force	F	[N]	100	500
Lay-up velocity	v	[m/s]	0.04	0.12
Debulking frequency	f	[-]	-	15 min at RT after every 8^{th} ply

Data acquisition and evaluation

In a first step, the empty tooling surface was scanned, including the reference points around the lay-up area. After lay-up, the laminate was scanned perpendicular to the fiber direction, again including the reference points. Reference and laminate scan were exported as point clouds and positioned based on the reference points. A rectangular area with 30 mm distance to the laminate edges was defined as measurement area. Perpendicular vectors between the polygonized surfaces defined the thickness of the laminate for each polygon area. This resulted in an average of more than 200,000 measurement points per sample surface and parameter variation, allowing statistically valid data evaluation. The mean of the thickness distribution and its standard deviation were calculated for analysis. Fig. 5.3 shows an exemplary scan of two neighboring samples and their thickness distribution in the form of a histogram.

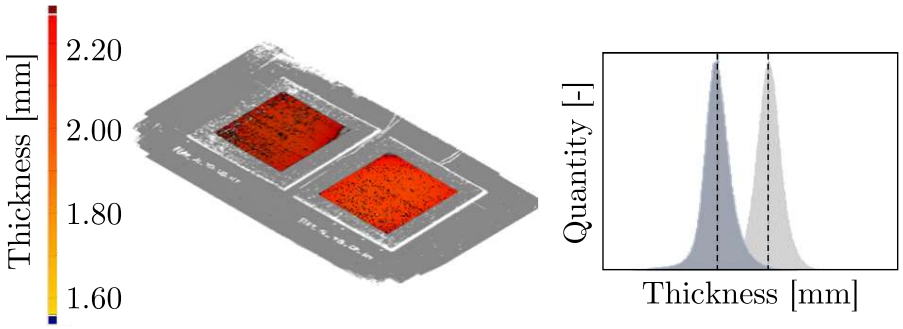

Figure 5.3: Exemplary thickness scan (left) and histogram (right) of two samples.

5.1.2 Results and discussion

Fig. 5.4 shows the laminate surface temperature resulting from the heat input controlled by the IR lamp power P. The graphs include the temperature progression from ply 2 to 16 for the different power settings with and without debulking. Radiation reflections on the aluminum tooling did not allow valid measurements for the first ply. The different power settings "low" and "high" led to a significant difference in the surface temperature with up to 20 °C for the final layers. Debulking caused an interruption of the lay up process for the set up of the prepared vacuum bag of around 5 minutes and the vacuum debulking time of 15 minutes. This led to a significant drop in the temperature build-up by more than 10 °C after the eighth ply for high heat input. The mean temperature was 42.8 °C for P_{high} and 29.1 °C for P_{low}. The average standard deviation of the single measurements for the defined

measurement area within the lay-up track was 2.8 °C, but is not depicted in the graph for reasons of clarity and comprehensibility.

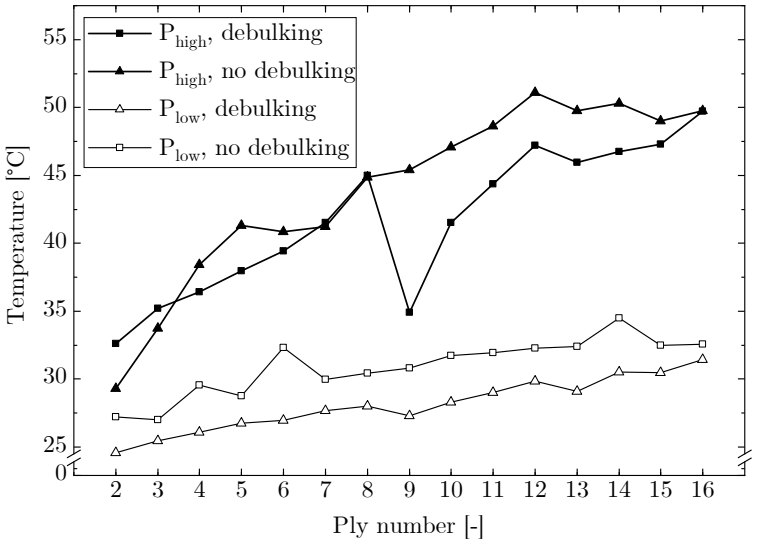

Figure 5.4: Temperature build-up during the lay-up of the 16 plies of all samples.

All thickness results were analyzed for single factor effects of the main process parameters as well as for their interdependent effects. Fig. 5.5 shows the single effects of the main parameters via the uncured thicknesses 't' after 16 layers, grouped for the low and high settings for the respective factors.

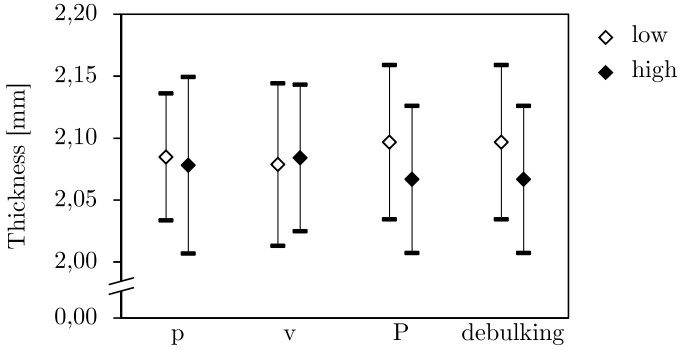

Figure 5.5: Single factor effects on the uncured laminate after 16 plies.

The full-factorial variation of the process parameters leads to a mix of all parameter settings in this form of depiction, causing high standard deviations and a blurring of the mean values. It can be seen that the mean differences between "low" and "high" setting are the biggest for the heat input and debulking. Debulking led to a thickness reduction of 0.9 % after eight plies and 0.8 % after 16 plies. Fig. 5.6 shows the single effects of the main parameters after 16 plies, including the respective thicknesses after curing. The average bulk factor or compaction rate

during curing is 7.7 %. With respect to the standard deviations, no clear trend is visible for the single factor variations.

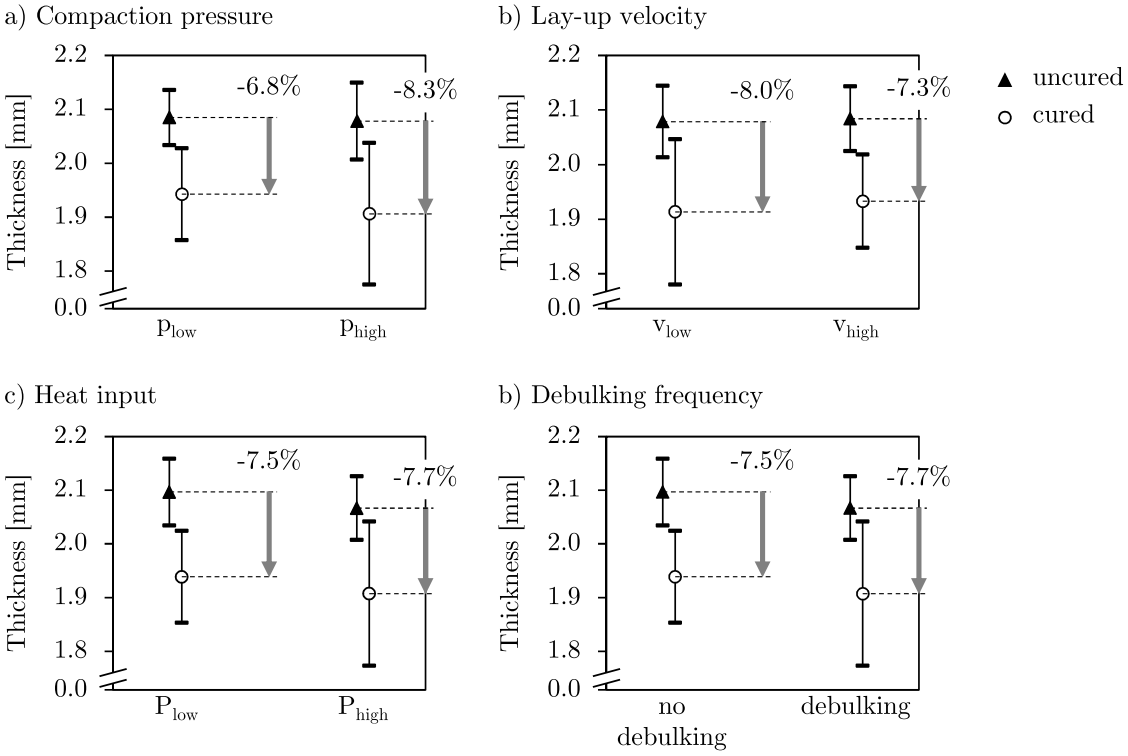

Figure 5.6: Single parameter effects on the uncured and cured laminate.

Fig. 5.7 shows the significant interdependent effects for different factor combinations. The graphs include combined factor variations for two factors each. With increasing difference of the connecting graph slopes, the interaction between the two factors rises. The two graphs contained in lines a), b) and c) of Fig. 5.7 contain the same interaction effect, but depicted with a swapped base for better comprehension of the effect. With the standard deviation and its ratio to the effect size, an interpretation at this stage difficult. Taking into account the statistic factors as described below, a careful interpretation is done. Fig. 5.7 a) shows the interaction between compaction pressure p and lay-up velocity v. For a low compaction pressure, the influence of the lay-up velocity is minimized (Fig. 5.7 a, left). The combination of high compaction pressure and low velocity, resulting in a longer compaction time, leads to the highest compaction within this combination (Fig. 5.7 a, right). Fig. 5.7 b) contains the interdependent effects of compaction pressure and debulking frequency. A high compaction pressure reduces the influence of the vacuum debulking, but its influence remains visible. In Fig. 5.7 c, the interaction between the heat input via the IR lamp power P and the application of debulking is depicted.

These factors show the strongest interaction within this study. With applied debulking, the effect of heat input is reduced to a minimum (Fig. 5.7 c, left). A high process temperature on the other hand reduces the compaction potential of debulking to a minimum (Fig. 5.7 c, right). Based on the respective laminate thickness, the interaction of heat input and debulking frequency (Fig. 5.7 c) with 1.53 % thickness change has the biggest influence on the compaction, followed by compaction pressure and lay-up velocity (Fig. 5.7 a) with 1.08 % and compaction pressure and debulking frequency (Fig. 5.7 b) with 0.71 %.

The ratio of standard deviations to measured effect as shown in the results makes an interpretation of the effects difficult. The very high amount of more than 200,000 measurement points per sample still allows the application of statistical methods for the interpretation of the results. Assuming the absence of systematic errors with a constant desired plate thickness, a theoretical confidence interval of 5 % around the mean can be calculated. The resulting confidence interval of $\pm 0.5 \cdot 10^{-3}$ mm is two orders of magnitude smaller than the shown standard deviations, increasing the shown effects' significance. Additional repetitions per parameter variation would increase the population of data points within the statistical data set and therefore the significance of the evaluation. [147, 148]

Process temperature is a hard to control parameter on a full scale industrial process, as shown in Fig. 5.4. Temperature builds up over time with continuous lay-up and is dependent of part geometry and laminate thickness. This brings additional challenges to the interpretation of the results. The results show the biggest influence on the compaction of the uncured laminate by the heat input and the application of debulking. These two factors show interdependent effects, suggesting a potential to replace the influence of the vacuum debulking by elevated process temperatures.

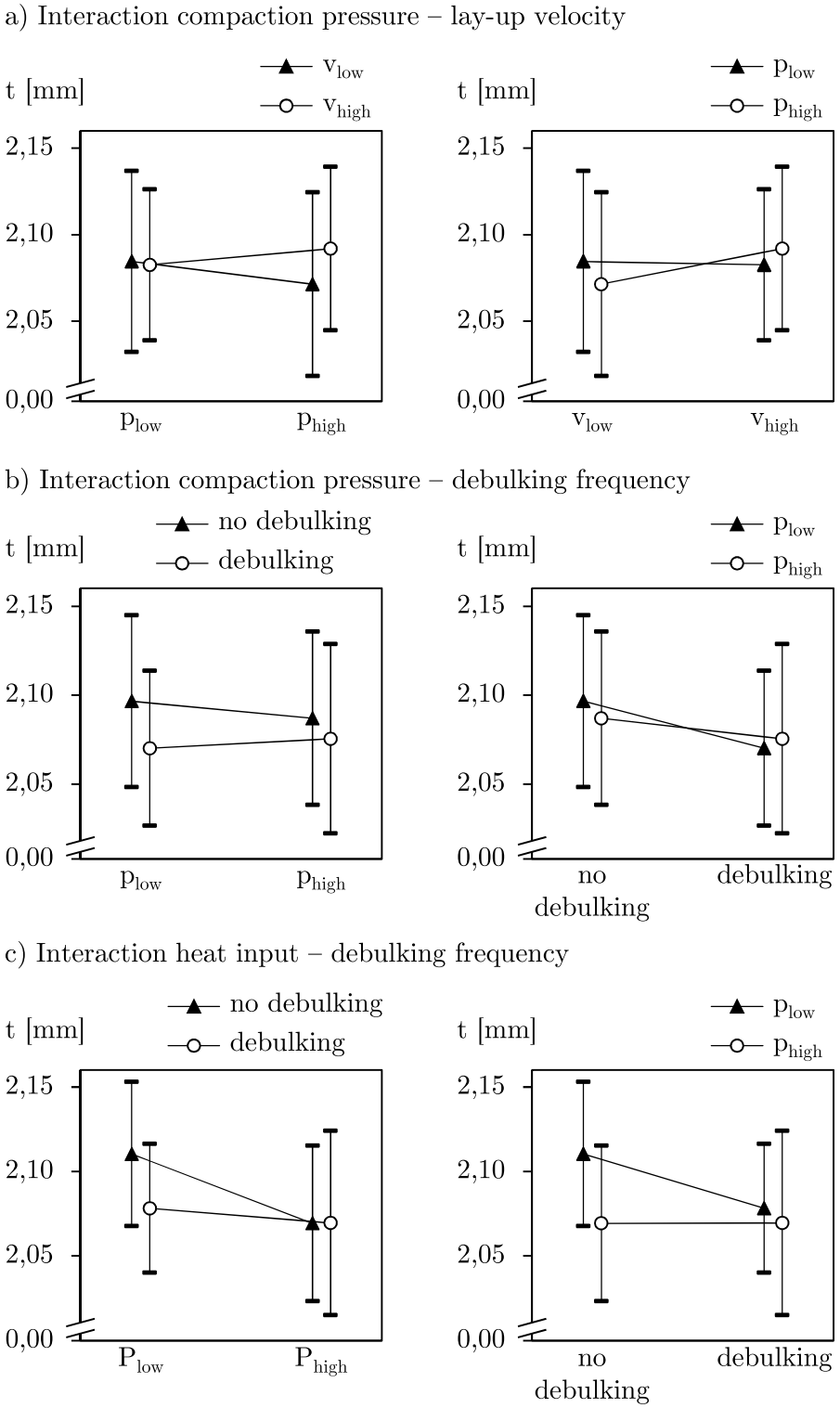

Figure 5.7: Interdependent effects of selected parameter variations on the uncured laminate thickness after 16 plies.

5.1.3 Conclusion

Full-scale AFP lay-up experiments with varying lay-up velocity, heat input via IR lamp power, compaction pressure and debulking frequency were conducted. Their influence on cured and uncured laminate compaction was investigated using a 3D-triangulation scanner to measure the thickness of the laminate at different stages. Heat input and the application of debulking have shown the biggest influence on the compaction of the uncured laminate. Autoclave curing led to an average compaction rate of 7.7 %, showing no clear trend regarding the AFP and debulking parameter variations. Debulking after 8 and 16 plies added a thickness reduction of less than 1 %. Interdependent effects of the factor variations identify the most prominent interaction for the parameters heat input and debulking frequency. It was shown, that for the given set-up, taking into account the theoretical confidence interval due to the high amount of measurement points, adjusted heat input settings can help to replace the compaction influence of vacuum debulking.

5.2 Influence of compaction and curing on the mechanical performance

This section summarizes a set of experiments where AFP laminates with different compaction and curing states were evaluated regarding their mechanical performance, internal and surface structure, as well as their void content. For the mechanical characterization, tensile tests, 4-point-bending tests and interlaminar shear strength (ILSS) tests were applied. The internal structure was evaluated via micro CT. For the surface structure evaluation, an optical profilometer was used. The void content was determined via segmentation of the micro CT images.

The section is subdivided into the description of the applied materials and methods, the results and their discussion and a conclusion.

5.2.1 Materials and methods

This sub-section provides an overview on the used equipment and material as well as the experimental procedure and the applied evaluation methods.

Equipment

An industrial AFP machine by *Coriolis Composites* was used for the prepreg deposition (cf. Sec. 2.1.4). The machine processes $8 \times 1/8''$ tapes and compacts them with a silicone compaction roller with a diameter of $d_r = 39\,\text{mm}$. The heat input is generated with an IR lamp with a max. power of $P_{IR,max} = 430\,\text{W}$. Laminate surface temperature during tape deposition was logged with an IR camera *FLIR A325sc* mounted on the lay-up head. More details on the used TS-AFP equipment can be found in Sec. 2.1.4.

The mechanical characterization was performed on a standard 50 kN UTM by *Hegenwald & Perschke*. Strain measurement was realized contactless via a 2.8 MP video extensometer by *LIMESS* with a 75 mm f/1.8 C-mount lens. For the surface structure analysis, a 3D profilometer *Keyence VR-5000* with a resolution in z-direction of 1 µm was used [149]. Micro CT scans were performed at ANU using a flat panel detector with a resolution of 3.000×3.000 pixels with a micro-focus X-ray source of 80 kV. The scanning resolution or voxel size for the samples was 1.6 µm.[150]

Material

The samples were manufactured with aerospace grade *HexPly 8552/IM7* UD carbon prepreg by *Hexcel* [95]. The material system has a nominal cured ply thickness

of 0.131 mm and a nominal fiber volume fraction of 57.70 %. More details on the used material system can be found in Sec. 2.2.2. Tab. 2.1 shows the mechanical properties according to the data sheet.

Experimental procedure

AFP laminates with three different compaction parameter sets and three different curing states were manufactured, leading to nine variations in total. The process parameter sets included benchmark compaction (bm), minimized compaction (mc) and optimized compaction (oc) parameters (cf. Tab. 5.2). Benchmark settings are based on typical parameters as they are used for low to medium complexity aerospace laminate manufacturing. The optimized parameters include the maximum settings for heat input and pressure as predefined in the parameter settings of the AFP equipment used, in addition with a low velocity setting. Minimized compaction is realized by a minimum compaction force, no heat input and a high velocity setting. Each laminate consisted of 16 plies and had a size of $500\,mm \times 500\,mm$, allowing to extract 7 samples each for tensile tests in 0°- and 90°-orientation, 4-point bending tests in 0°- and 90°-orientation and ILSS tests as well as samples for microscopy, VVC determination and micro CT. The benchmark compaction parameter set represents a typical setting as used in industrial applications. This includes medium to high settings for compaction force, velocity and heat input. Vacuum debulking is applied for 15 minutes at room temperature (RT) after every 8^{th} ply, leading to two debulking cycles for the 16-ply laminates. Based on the results presented in Sec. 5.1, an optimized compaction parameter set was defined. It includes an increased compaction force and heat input at a lower velocity and without separate vacuum debulking. For the minimized compaction parameter set, compaction force and heat input have a "low" setting combined with a "high" velocity and without vacuum debulking. The additive nature of the AFP process results in gradual heating of the substrate due to the repeated heat input with each track. Fig. 5.8 shows the temperature build-up of the substrate measured by the *FLIR A310* IR camera for the benchmark and optimized parameter set as mean of all built laminates. The minimum compaction parameter set is not visualized as it was constant on room temperature level in between 22 °C and 25 °C due to the lack of heat input. The interruption by vacuum debulking after the 8^{th} ply led to a mean temperature drop of 4.3 °C. There was a difference of 15 °C between the benchmark and optimized parameter set at the end of the lay-up.

Autoclave curing (AC) was done according to the data sheet [95] with 120 minutes at 180 °C at a pressure of 7 bar after an initial hold for 60 minutes at 110 °C at 7 bar pressure. Vacuum curing (VC) was performed with the same temperature

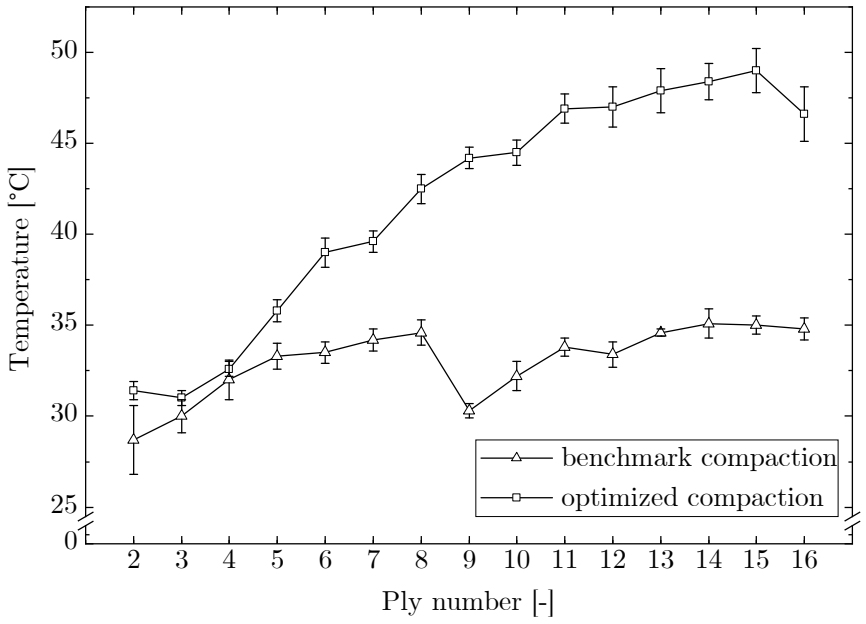

Figure 5.8: Temperature build-up on the AFP-laminate surface during the lay-up of 16 plies.

profile as for autoclave curing, but with vacuum pressure only. Soft curing (SC) has the goal to maintain the laminate properties as deposited without alteration by excessive heat or pressure. Based on the methods by Lukaszewicz et al. [93] and Nixon et al. [37], a stepwise curing cycle was developed. Starting at a low temperature level, the laminate is cured to its highest isothermally reachable DOC before raising the temperature to a higher level. This keeps the viscosity as high as possible and mitigates flow mechanisms. A sufficient duration at the isothermal levels was extrapolated from material characterization results [94] and checked via differential scanning calorimetry (DSC). The resulting cure cycle starts with 18 hours at 60 °C followed by 4 hours each at 70 °C, 80 °C, 90 °C, 100 °C and 120 °C leading to a DOC of >60 % [82]. The respective sample geometries were cut out using waterjet cutting.

Table 5.2: Variation of AFP process parameters, debulking and curing.

Parameter set	Compaction force [N]	Velocity [m/s]	Heat input [W]	Debulking	Curing
Benchmark (bm)	250	0.09	322	15 min every 8^{th} ply	SC/VC/AC
Optimized (oc)	500	0.04	430	-	
Minimized (mc)	100	0.12	0	-	

Evaluation methods

The samples were analyzed by mechanical characterization, optical examination and by determination of the FVC . Tab. 5.3 shows the applied standards and the according sample geometries. For all mechanical tests, a standard 100 kN UTM by *Hegenwald & Peschke* was used. The strain measurement was done contactless with a 2.8 MP video extensometer by *LIMESS* with a 75 mm f/1.8 C-mount lens (cf. Fig. 5.9). A 2× teleconverter was installed between camera body and lens. The effective focal length was 150 mm, leading to a theoretical resolution of 1 µm.

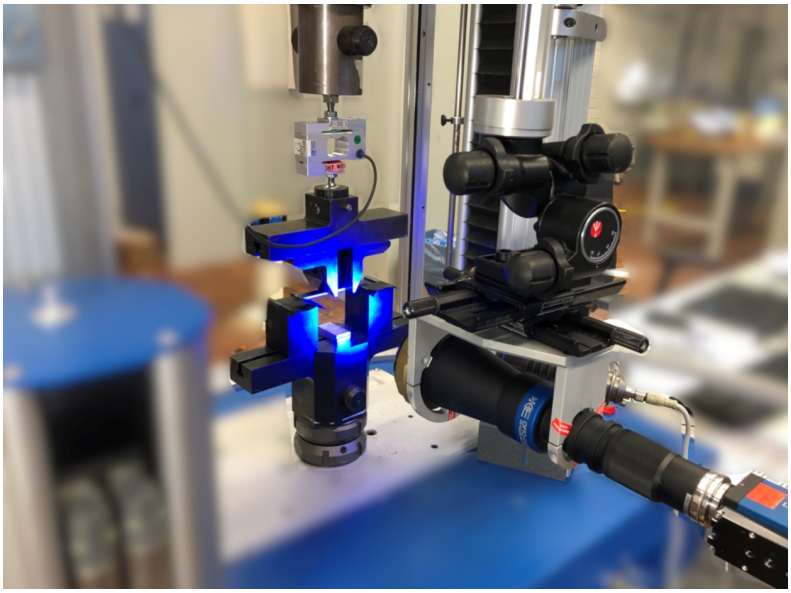

Figure 5.9: Set-up of the 2.8 MP video extensometer by *LIMESS* with a 75 mm f/1.8 C-mount lens and 2x teleconverter.

The tensile tests in 0°- and 90°-direction were done according to DIN EN ISO 527-1 [155] and DIN EN ISO 527-5 [156]. In 0°-direction, the results are dominated by fiber properties. With 90° fiber orientation, the test is dominated by properties of matrix, fiber-matrix interface, internal stresses and voids [157]. Thus, especially

Table 5.3: Applied test standards and sample dimensions.

Test	Standard	Sample dimensions [mm]
ILSS	DIN EN 2563 [151]	20 x 10 x 2
4-point bending (0°, 90°)	DIN EN ISO 14125 [152]	100 x 15 x 2
Tensile (0°)	DIN EN 2561 [153]	250 x 15 x 2
Tensile (90°)	DIN EN 2597 [154]	250 x 25 x 2
Micro CT	-	6 x 2 x 2

the 90°-samples were expected to show the influence of the applied parameter variations. Test speed for all tensile tests was 2 mm/ min. For each parameter variation, 7 samples were tested. Tensile strength σ_{T11} in 0°-direction and σ_{T22} in 90°-direction are calculated by Eq. 5.1 taking into account the load at failure F_R and the sample dimensions. Tensile modulus is determined as secant modulus E_{T11} in 0°-direction and E_{T22} in 90°-direction based on Eq. 5.2:

$$\sigma_T = \frac{F_R}{w\,t} \tag{5.1}$$

$$E_T = \frac{\sigma_2 - \sigma_1}{\varepsilon_2 - \varepsilon_1} \tag{5.2}$$

DIN EN ISO 527-1 defines the points to determine the secant modulus at 0.05 % (1) and 0.25 % (2) strain. For the determination of E_{T22} of the SC samples, (2) had to be adapted to 0.20 % due to the low load and elongation at failure.

The 4-point bending tests in 0°- and 90°-direction were done according to DIN EN 14125 [152]. It is used to determine the strength and deformation properties of composite materials under bending stress. In this set-up, samples are subjected to tensile stresses, compressive stresses and shear stresses, while the influence of the shear stresses can be minimized with a sufficient length to thickness ratio. The bending moment between the two inner pressure fins is constant, leading to theoretically no shear stress in this area. The test speed was set to 5 mm/ min. 7 samples were tested per parameter variation. The flexural or bending strength σ_f is calculated based on Eq. 5.3, taking into account the maximum bending force F_{max}, the distance between the lower support points L and the sample dimensions:

$$\sigma_f = \frac{F_{max} L}{w t^2} \tag{5.3}$$

The flexural or bending module E_f is calculated based on Eq. 5.6, taking into account the deflection s' for $\varepsilon'_f = 0.0005$ (cf. Eq. 5.4) and s'' for $\varepsilon''_f = 0.0025$ (cf. Eq. 5.5):

$$s' = \frac{\varepsilon'_f L^2}{4.7t} \tag{5.4}$$

$$s'' = \frac{\varepsilon''_f L^2}{4.7t} \tag{5.5}$$

$$E_f = \frac{0.21L^3}{wt^3}\left(\frac{\Delta F}{\Delta s}\right) \tag{5.6}$$

The results of the 4-point bending test were normalized to evaluate the influence of the varying FVC. In fiber direction, they were normalized based on Eq. 5.7:

$$E_{norm,11} = E_{mean}\,\frac{t_{meas}}{t_{ref}} \tag{5.7}$$

The mean thickness of the samples t_{meas} is divided by the theoretical reference thickness as defined in the test standard t_{ref}. For the results perpendicular to the fibers, the stiffness of the matrix has to be considered [158]. Taking into account the inverse rule of mixture, the results are normalized using Eq. 5.8:

$$E_{norm,22} = \left(\frac{1}{E_m} - \left(\frac{1}{E_m} - \frac{1}{E_{meas}}\right)\frac{1-\varphi_{norm}}{1-\varphi_{calc}}\right)^{-1} \tag{5.8}$$

with E_m being the modulus of the matrix and φ_{calc} being the calculated FVC of each sample. The FVC is calculated using Eq. 5.9:

$$\varphi = \frac{FAW}{\rho_f\, CPT} \tag{5.9}$$

with ρ_f being the fiber density. The cured ply thickness (CPT) is determined by Eq. 5.10:

$$CPT = \frac{t_{meas}}{n} \tag{5.10}$$

with t_{meas} being the measured ply thickness and n the number of plies.

The ILSS was determined by a short beam shear test (SBS) according to DIN EN 2563 [151]. It is a 3-point bending test with a short distance of the support

points, keeping the bending moment low compared to the shear stress. This way, a shear-induced failure of the specimen can be provoked. Test speed was 1 mm/ min for all ILSS samples. For each parameter variation, 7 samples were tested. The apparent interlaminar shear strength τ_{12} is calculated with the force at failure F_R according to Eq. 5.11:

$$\tau_{12} = \frac{3}{4}\frac{F_R}{wt} \tag{5.11}$$

The micro CT scans were done by ANU using a flat panel detector with a resolution of 3.000 × 3.000 pixels and a micro-focus X-ray source of 80 kV. The samples had a size of $6\,mm \times 2\,mm \times 2\,mm$. 3D images were reconstructed based on gray-scale projections using a helical reconstruction software developed by ANU. The scanning resolution or voxel size for the samples was 1.6 µm. [150]

For the surface scans, a 3D profilometer *Keyence VR-5000* with a resolution in z-direction of 1 µm was used [149]. FVC was determined optically based on a segmentation of the micro CT scans (cf. Fig. 5.10).

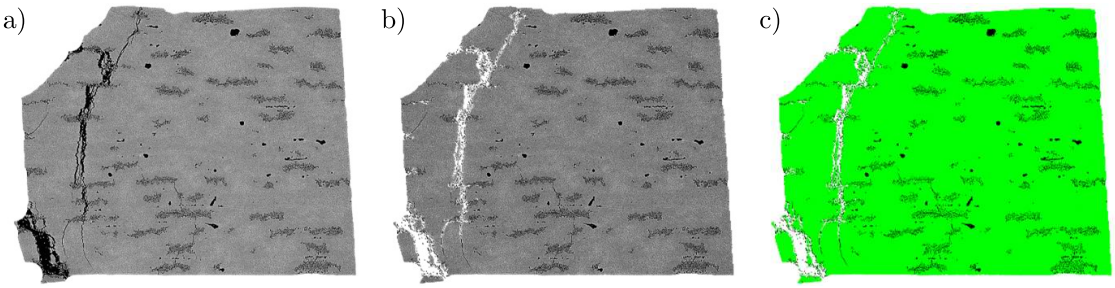

Figure 5.10: Segmentation of the micro CT scans at the example of sample SC-bm: original z-slice (a), z-slice with excluded cracks (b), segmented z-slice with marked composite (green) and void (black) regions (c).

5.2.2 Results and discussion

This section summarizes and discusses the results of the tensile tests in 0°- and 90°-direction, 4-point bending tests in 0°- and 90°-direction, ILSS tests, micro CT scans and void volume content determination.

Tensile test

The tensile properties were tested in 0°- and 90°-direction, with all samples showing linear elastic behavior until failure, as typical for brittle epoxy composite samples [159]. Fig. 5.11 shows the tensile strength, Fig. 5.11 the tensile modulus in fiber direction. The tensile strength in 0°-direction shows a trend with the

best results for AC just followed by VC and a clear difference to SC. The best result was obtained for AC-oc with 2646 MPa. This is a 6.7 % higher result compared to AC-bm and 1.3 % higher compared to AC-mc. The tensile strength of the VC samples is just slightly below the AC samples, with only VC-bm showing a clearer drop with a tensile strength of 2180 MPa. SC samples had a significantly lower tensile strength, especially for SC-mc with 1893 MPa 0° tensile strength. The tensile modulus in fiber direction shows a similar trend, but to a lesser extent. The highest tensile modulus was identified for AC-oc with 154 GPa. SC-mc had again the lowest result with 139 GPa. Within one curing method, the variation is again small. Only SC-mc shows a significant drop compared to the other SC samples. All SC samples failed, showing a strong "brooming effect" with a brush-like separation of the filaments at failure as sign for an especially poor fiber-matrix coupling [157].

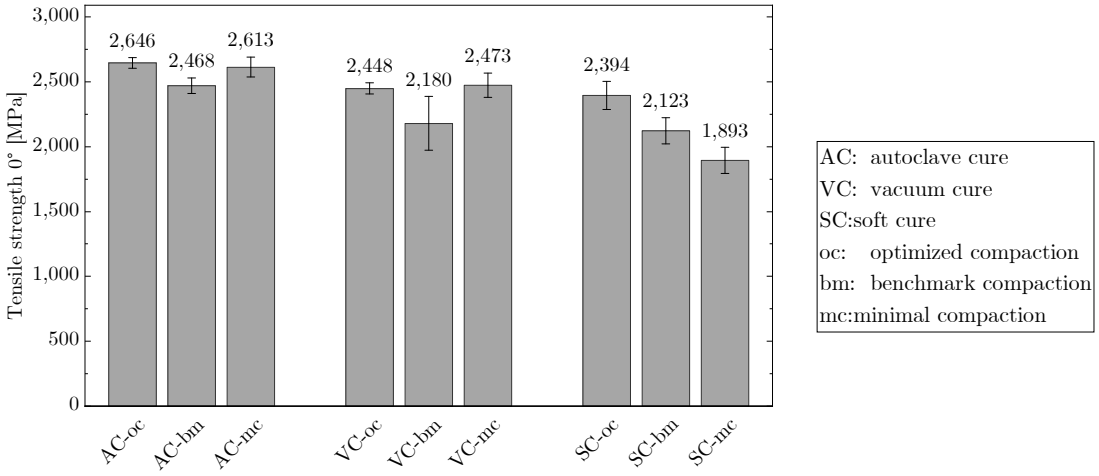

Figure 5.11: Tensile strength in 0°-direction for different compaction and curing parameter variations.

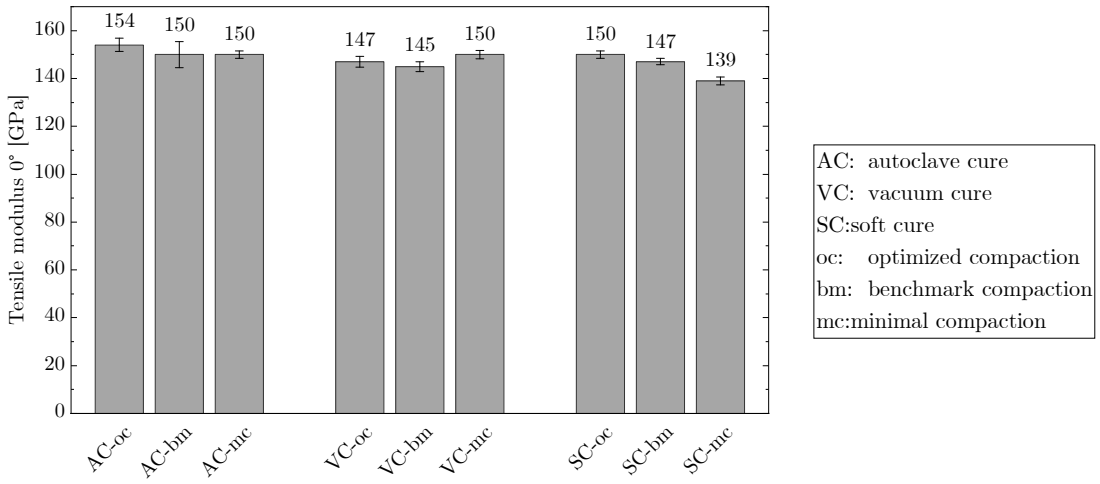

Figure 5.12: Tensile modulus in 0°-direction for different compaction and curing parameter variations.

Fig. 5.13 shows the tensile strength, Fig. 5.14 the tensile modulus perpendicular to the fiber direction. The tensile strength in 90°-direction shows a clear trend for the different curing methods, with the best results for the AC-samples and clear drops of the VC and SC samples. Within the AC samples, there is a slight trend contrary to the expectations visible, as mc showed the best results followed by bm and oc. Considering the high standard deviation, this trend can be neglected. VC-mc shows the highest value within the VC samples, which is again unexpected. For the SC samples, a clear drop from oc over bm to mc with a minimum tensile strength of 7.7 MPa can be seen. The tensile modulus showed again a lower difference between but also within the curing methods compared to the strength values. The highest result was obtained for the AC-oc sample with a tensile modulus of 8.41 GPa. Only the SC samples allow a clear differentiation from oc over bm to mc with the lowest result again for SC-mc with a tensile modulus of 4.94 GPa.

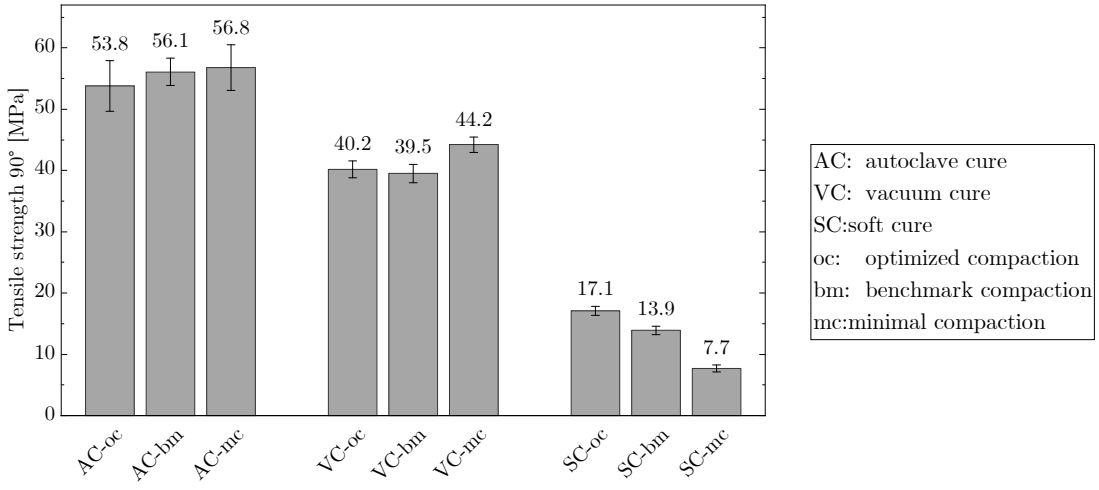

Figure 5.13: Tensile strength in 90°-direction for different compaction and curing parameter variations.

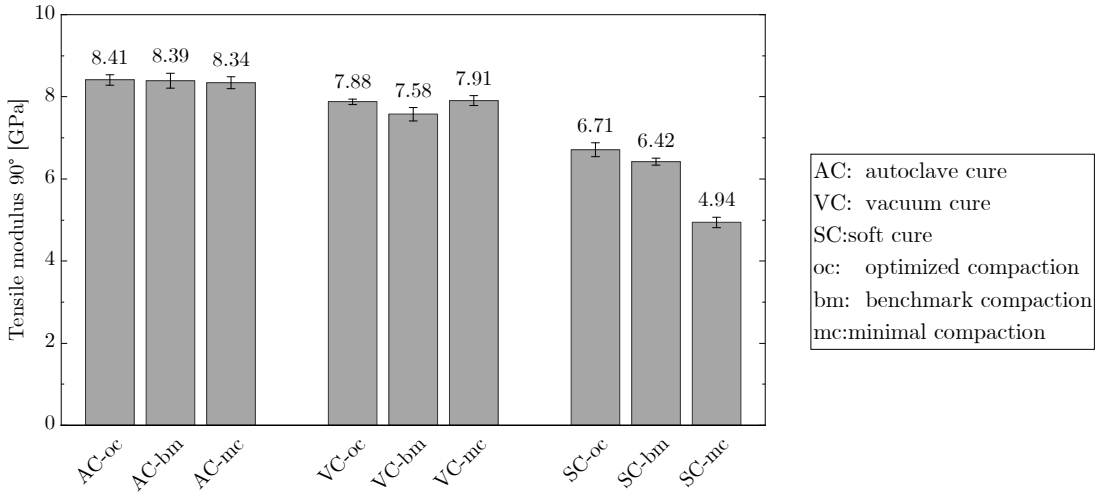

Figure 5.14: Tensile modulus in 90°-direction for different compaction and curing parameter variations.

4-point bending

The flexural properties were tested in 0°- and 90°-direction. All samples had linear elastic behavior (cf. stress-strain curves in Sec. A.2.1). Fig. 5.15 shows the bending strength, Fig. 5.16 the bending modulus in fiber direction. For the bending strength in 0°-direction, a trend with slightly better results for AC compared to VC and a clear drop with SC can be seen. The best result was obtained for AC-oc with 1360 MPa. This is a 3.7 % higher result compared to AC-bm and 2.2 % higher compared to AC-mc. The bending strength of the VC samples was just as good as the AC samples, with only VC-bm having a slightly lower bending strength of 1250 MPa. The SC samples showed a significantly lower bending strength, especially for SC-mc with only 885 MPa bending strength in fiber direction. For the bending modulus in fiber direction, a similar trend was identified, but to a lesser extent. The highest bending modulus was shown for AC-oc with 140 GPa. SC-mc had again the lowest result with 119 GPa. The variation within one curing method is again small. Only SC-mc showed a significant drop compared to the other SC samples. In Tab. 5.4, the failure modes based on the definition in DIN EN ISO 14125 [152] are summarized. The majority of the samples failed under pure compressive stress failure (CSF). SC-samples failed primarily by a mixture of compressive stress failure with buckling of the outer compressed layers. This resembles the defined failure mode of compressive failure and interlaminar shear failure, but indicates a poor fiber-matrix bonding.

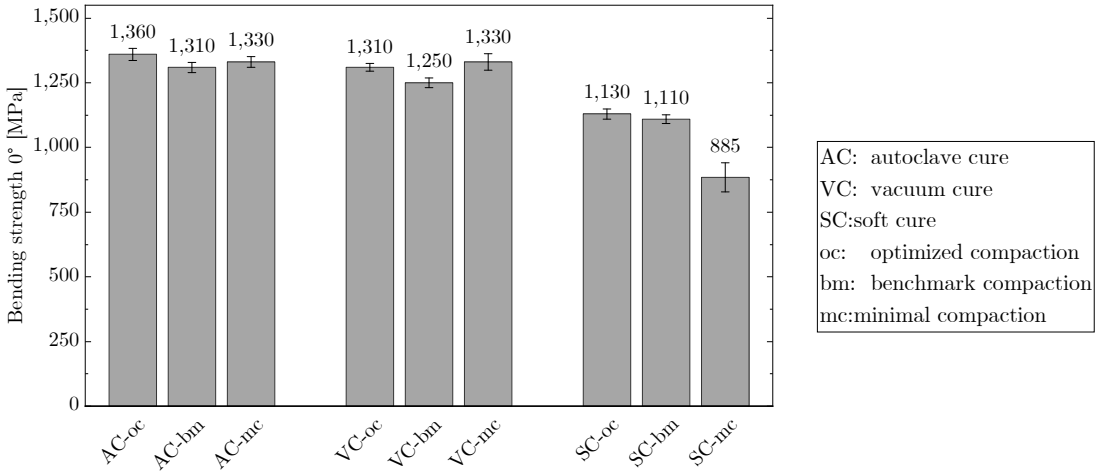

Figure 5.15: Bending strength in 0°-direction for different compaction and curing parameter variations.

Fig. 5.17 shows the bending strength, Fig. 5.18 the bending modulus perpendicular to the fiber direction. For the bending strength in 90°-direction, a clear trend for the different curing methods, with the best results for all AC samples and clear

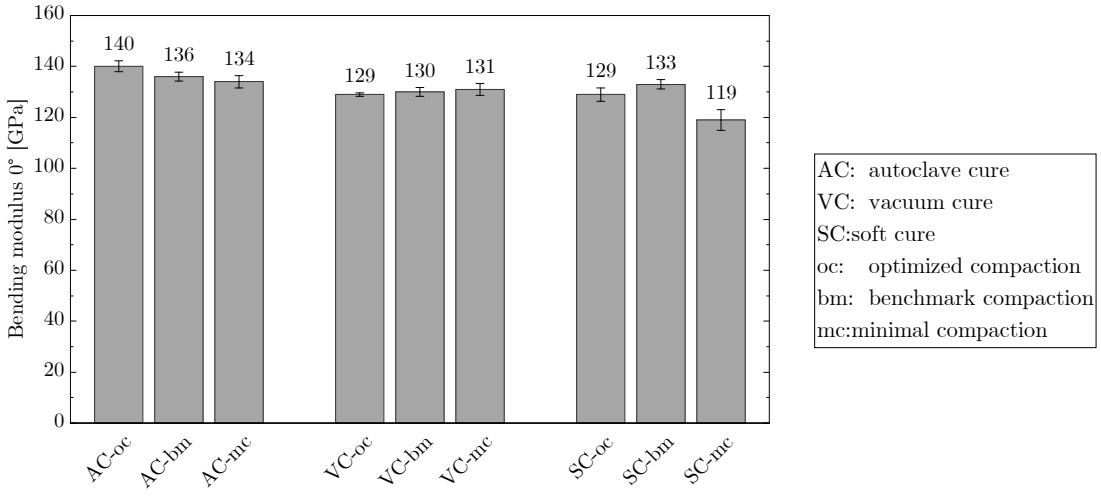

Figure 5.16: Bending modulus in 0°-direction for different compaction and curing parameter variations.

Table 5.4: Failure modes of the 4-point bending samples with 0°-degree fiber orientation.

Failure mode	AC oc	AC bm	AC mc	VC oc	VC bm	VC mc	SC oc	SC bm	SC mc
Compr. stress failure (CSF)	**3**	**4**	**4**	**5**	**5**	**3**	1	-	1
CSF (incl. interlam. shear)	2	2	3	-	2	**3**	**6**	**5**	**5**
Tenslie stress failure (TSF)	1	-	-	-	-	-	-	1	-
TSF (incl. surface break)	-	-	-	2	-	-	-	-	-
Number of tests	6	6	7	7	7	6	7	6	6

drops of the VC and SC samples. Within the AC samples, there is only a minor advantage of the oc configuration, with a maximum bending strength of 82 MPa. VC-mc shows the highest value within the VC-samples, which is unexpected and hard to explain with the information at hand. In the SC-samples, there is a clear drop from oc over bm to mc with a minimum bending strength of 15.8 MPa. The bending modulus shows again a lower difference between but also within the curing methods compared to the strength values. Still, the highest result is obtained for the AC-oc samples with a bending modulus of 8.33 GPa. Only the SC samples allow a clear differentiation from oc over bm to mc with the lowest result again for SC-mc with a bending modulus of 4.37 GPa. The failure modes according to DIN EN ISO 14125 are listed in Tab. 5.5. Most samples were assigned compressive stress failure (CSF). Since the majority of the samples showed an instant failure through the entire thickness at the moment of fracture, the exact failure mode was hard to

determine. UD samples perpendicular to the fibers are expected to predominantly have tensile stress failure (TSF), as their properties are dominated by the matrix.

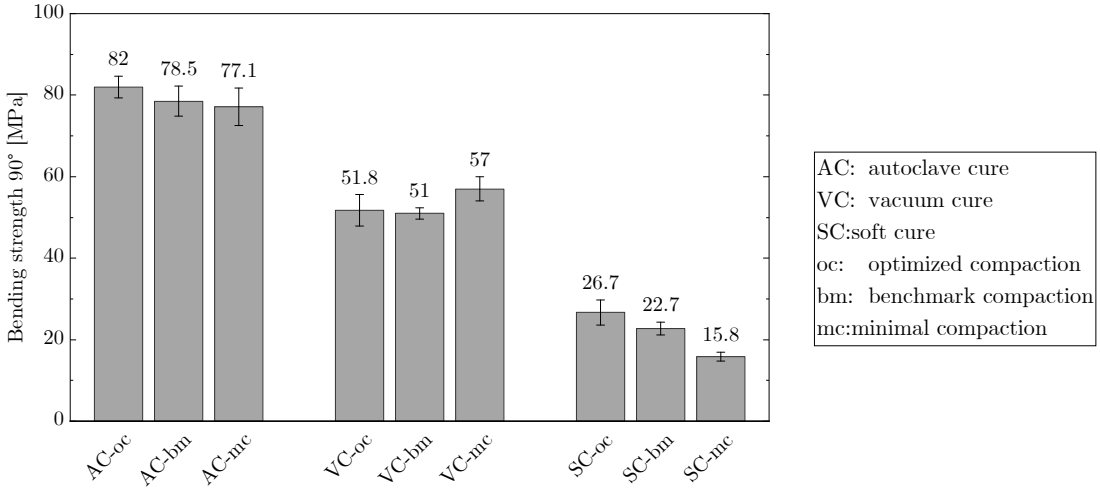

Figure 5.17: Bending strength in 90°-direction for different compaction and curing parameter variations.

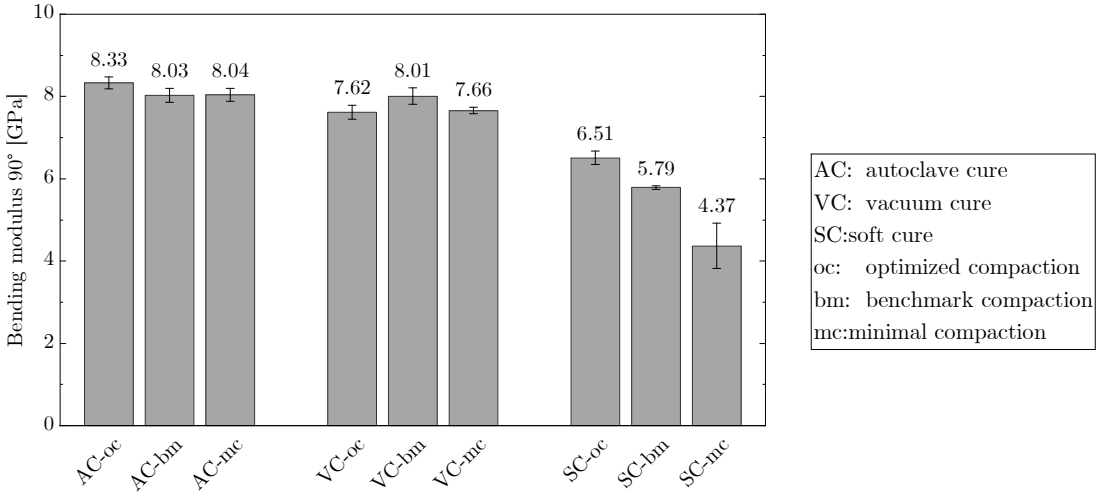

Figure 5.18: Bending modulus in 90°-direction for different compaction and curing parameter variations..

Fig. 5.19 sums up all results of the 4-point bending test by curing method, emphasizing the trend of decreasing properties from AC over VC to SC most dominant for the strength values in 90° direction.

In general, the FAW can be assumed constant for the flat prepreg samples for the given processing conditions. The different curing methods showed different bleeding behaviors. In the autoclave, the high pressure and temperature led to intense bleeding. With vacuum pressure only, the bleeding behavior was reduced.

Table 5.5: Failure modes of the 4-point bending samples with 90°-degree fiber orientation.

Failure mode	AC oc	AC bm	AC mc	VC oc	VC bm	VC mc	SC oc	SC bm	SC mc
Compr. stress failure (CSF)	**6**	**7**	**7**	**7**	**7**	**6**	**7**	-	-
CSF (incl. interlam. shear)	-	-	-	-	-	-	-	-	-
Tenslie stress failure (TSF)	-	-	-	-	-	-	-	-	-
TSF (incl. surface break)	-	-	-	-	-	-	**7**	**6**	**7**
Number of tests	6	7	7	7	7	6	7	6	7

During soft curing, the lack of pressure led to almost no bleeding. Thus, the three different curing methods can lead to a difference in the FVC. The results were normalized to estimate the influence of this effect, but showed no significant difference to the non-normalized values and no clear trend in their difference (cf. appendix Sec. A.3). This indicates, that the effect of the differing FVC is negligible for the interpretation of this set of experiments. [160]

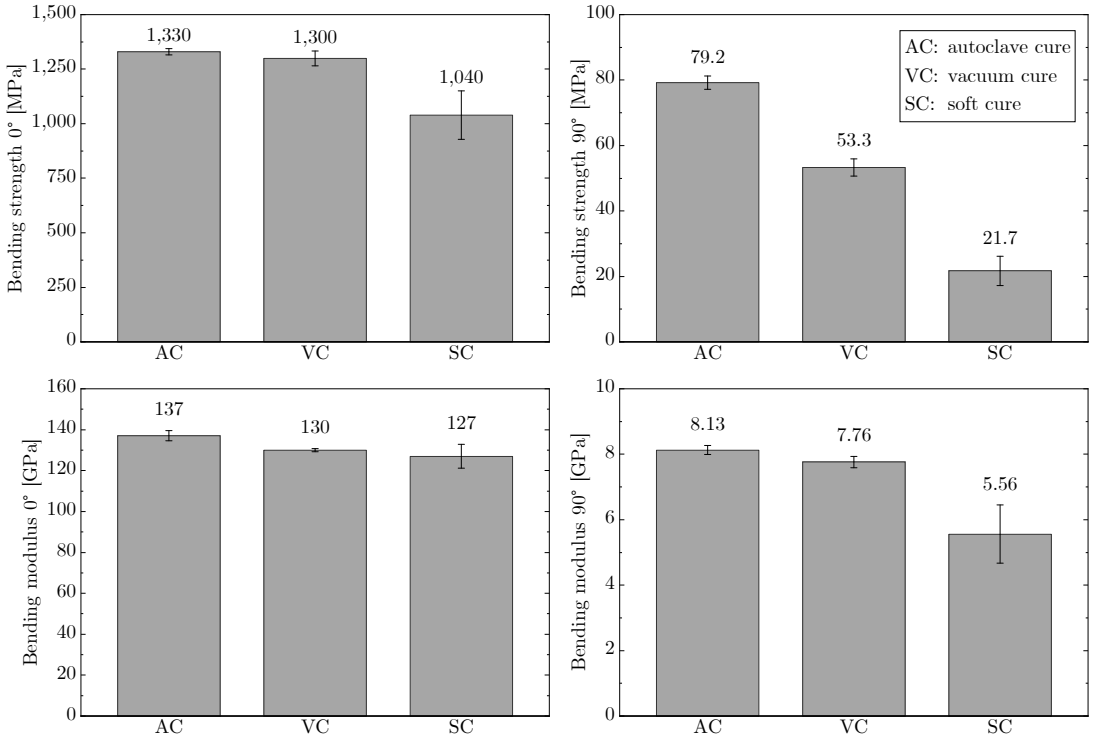

Figure 5.19: Bending strength and modulus in 0°- and 90°-direction summarized by curing method.

Interlaminar shear strength (ILSS)

Fig. 5.20 shows the ILSS test results sorted by curing method (AC, VC, SC) and compaction parameter set (oc, bm, mc). The apparent interlaminar shear strength (ILSS) represents the quality of the fiber-matrix adhesion and is sensitive to the presence of interply voids [161]. It is well suited for relative comparison within a test campaign. However, this value can vary considerably if test conditions or specimen geometry are varied, which is why a comparison with literature values is only possible to a limited extent [162].

The results show a decrease in shear strength from AC over VC to SC, with a particularly strong reduction for SC. Fig. 5.21 summarizes the results by curing method, emphasizing this trend. Within one curing method, the parameter variations show a significant influence only for the SC-samples, with a clear drop from oc over bm to mc. For VC, only the bm configuration shows a reduced shear strength, which is presumably caused by improper vacuum curing (cf. micro CT results and conclusion). From AC to VC, an average increase of the void content by 1.3 % leads to an average drop of the ILSS by 9.8 % (cf. Fig. 5.23). From AC to SC, an average increase of the void content by 5.2 % causes an average drop of the ILSS by 42 %.This is an average drop in the ILSS of 7.8 % per 1 % void

content increase, comparable to literature values with a range of 5 % to 10 % drop [161, 163–169].

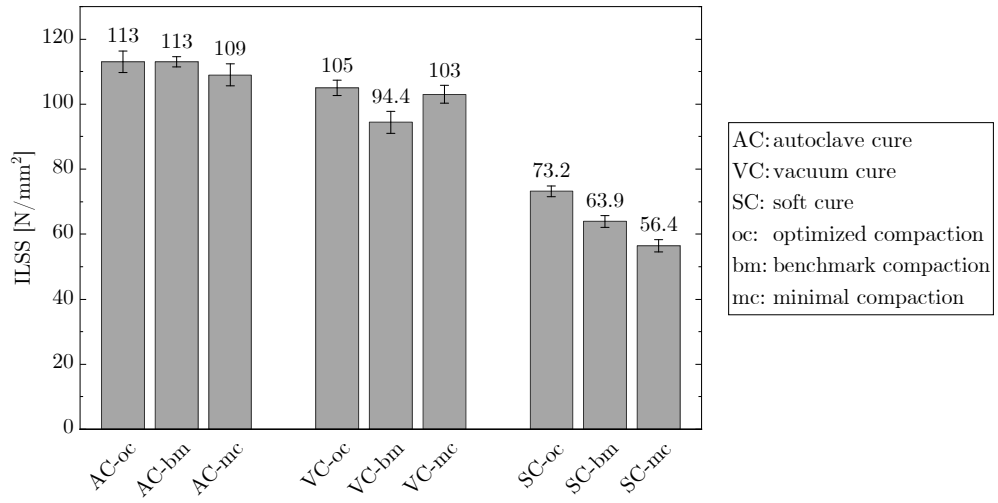

Figure 5.20: Interlaminar shear strength (ILSS) for different compaction and curing parameter variations.

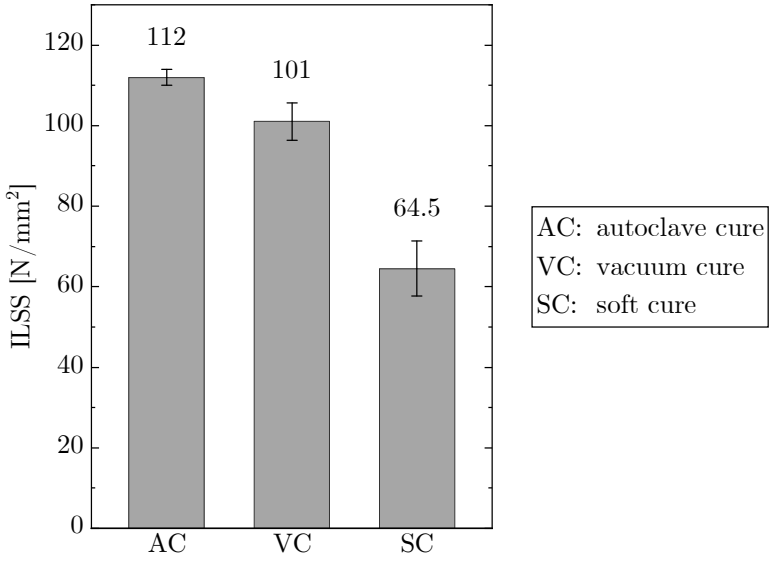

Figure 5.21: Interlaminar shear strength (ILSS) summarized for three different curing parameter variations.

Micro CT

Micro CT scans of the samples were reconstructed to 3D images and cut in slices with x-, y- and z-direction. The z-slices cut the images perpendicular to the UD fibers. Fig. 5.22 shows z-slices of all samples and gives an overview on

their homogeneity and porosity. X- and y-slices can be found in the appendix in Sec. A.4.2.

The different curing methods lead to clear differences in homogeneity as well as quantity and distribution of voids in the laminates. AC samples show a very homogeneous laminate throughout the entire thickness of the sample, with no visible voids. The determined void content is 0.00 % for all AC samples according to the void segmentation based on the scans. All AC samples have a smooth and even surface on the vacuum bagging side (topside in Fig. 5.22). The rectangular cut shape of the samples is unimpaired. Within the AC samples, no optical difference between the different process parameters is visible.

For the VC samples, a clear increase of the void content compared to the AC samples can be seen. A variety of voids in different sizes is visible for all three process parameters, whereas the voids in the VC-oc sample appear to be only small to medium sized compared to the bm and mc sample. The majority of the voids are distributed in the lower two-thirds of the laminate cross-section. Based on the segmentation, the void content is 1.0 % for VC-oc, 2.4 % for VC-bm and 1.4 % for VC-mc. The high porosity of VC-bm is unexpected and not to explain with the given information. An error during processing, e.g. of the vacuum during curing, cannot be ruled out and does not seem unlikely.

The SC samples show considerable inhomogeneity and the greatest void content of the set. There is a smaller number of conglomerated voids compared to the VC samples, but a high amount of dry tape regions that were not fully impregnated. For the SC-mc sample, additional big voids in a regular distribution can be identified. The distance and distribution of these voids indicate that these are the edges of the $^1/_8''$ AFP tapes. The shape of the SC samples is not rectangular, as the poor laminate quality led to spallings during cutting and grinding of the specimen. This is presumably also the reason for the visible cracks.

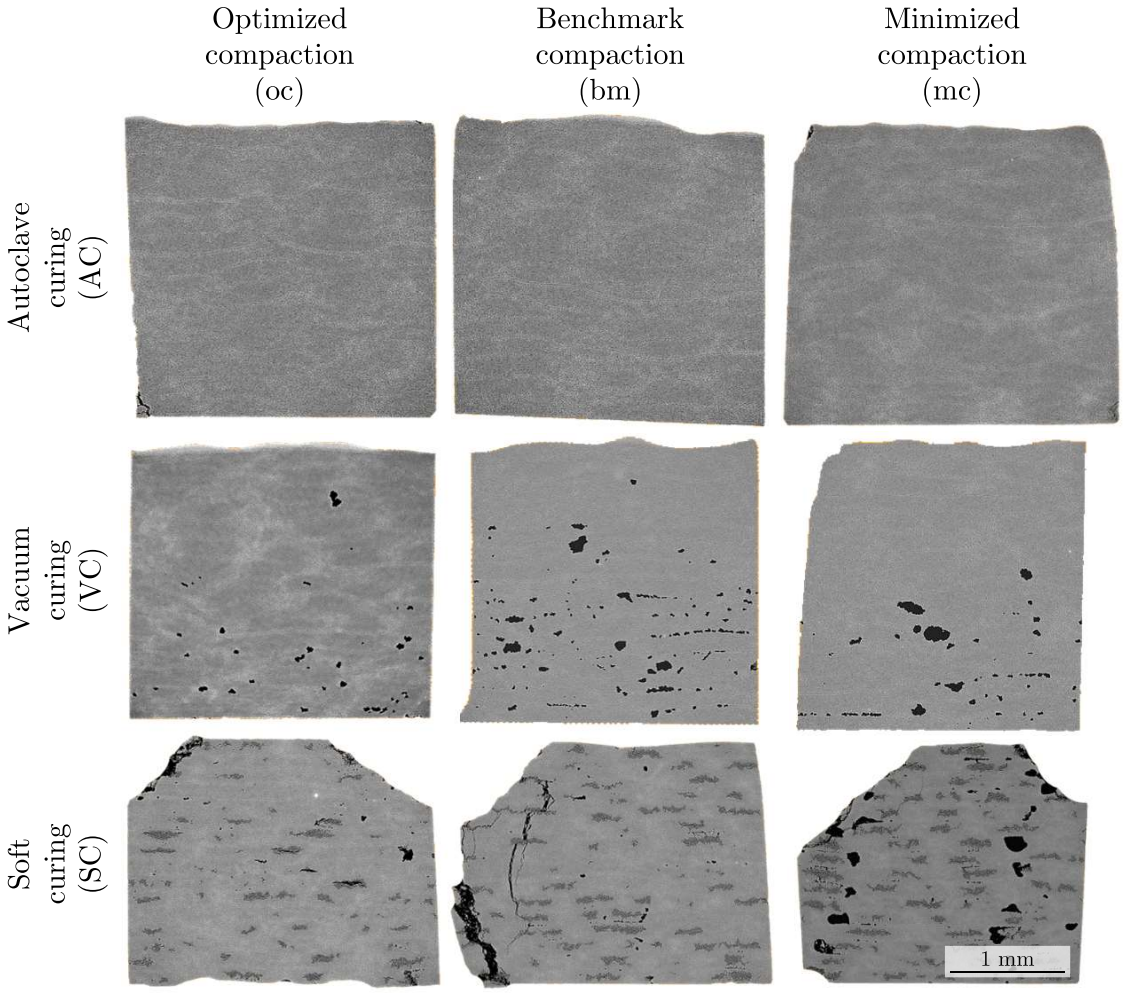

Figure 5.22: Micro CT overview showing the z-slices of the different combinations of process and curing parameters.

Void volume content

Fig. 5.23 shows the VVC results, determined via segmentation of the micro CT scans (cf. Fig. 5.10). A clear difference in the curing methods can be seen, with an average VVC of 0.0 % for AC, 1.6 % for VC and 5.2 % for SC. All AC samples have 0.0 % VVC within the scope of the measurement resolution. For VC, the VVC ranges from 1.0 % to 2.4 %, whereas the result for the VC-bm configuration is considered as unexpectedly high. This irregularity is in line with the mechanical results as described above. By far the highest VVC and the biggest scatter is shown for the VC configuration, ranging from 3.1 % to 8.6 %. Especially SC-mc has a very high VVC with 8.6 %. The VVC results are in line with the mechanical characterization and the visual impression given by the micro CT scans.

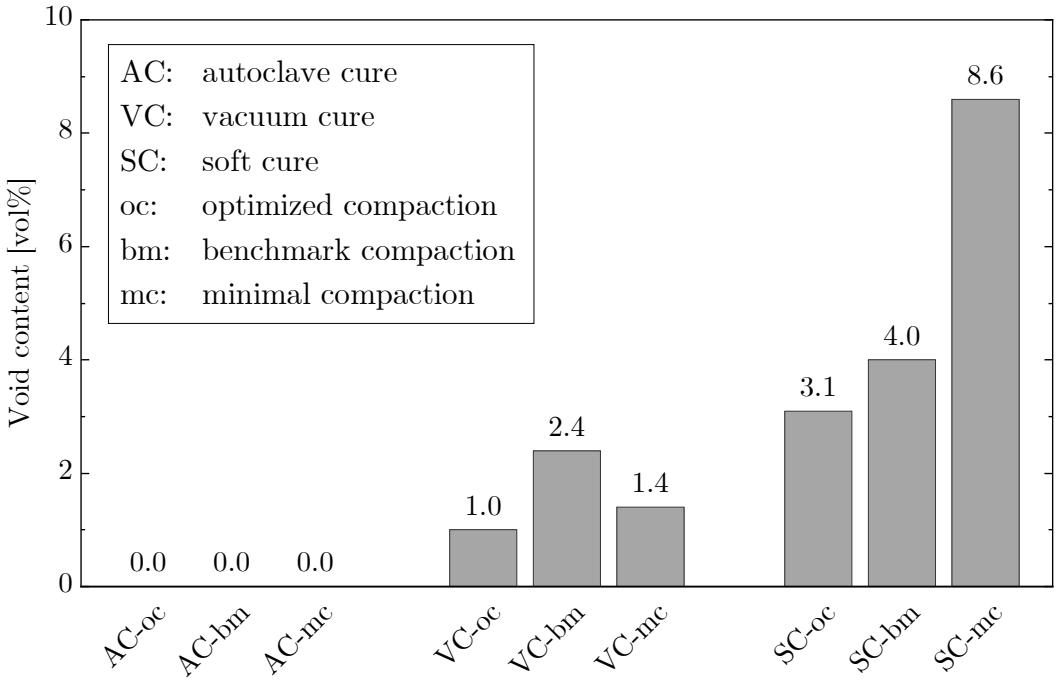

Figure 5.23: Void volume content (VVC) of the different combinations of process and curing parameters determined via segmentation of the micro CT scans.

Surface scans

Fig. 5.24 shows the surface profiles of representative areas of the different process and curing parameter samples. As the scans consist of a relative profiles, they do not allow an absolute comparison. The color scale was aligned individually for each sample with a central reference plane of the scan area.

For all three curing methods, the surface structures show clear differences. The AC samples have a resin rich surface with no visible tape or fiber structure, characterized by the perforated foil and breather fabric. The VC samples are similar to the AC samples with less of the fine-grained structure (cf. also roughness profiles in appendix Sec. A.5). All SC samples have a different texture with clear visibility of the tape structure. Tape edges are clearly visible, and a lack of matrix on the surface can be identified. The mean surface roughness depth was measured as $R_{z,AC} = 107.1$, $R_{z,VC} = 135.2$ and $R_{z,SC} = 1147.9$ based on DIN EN ISO 25178 [170].

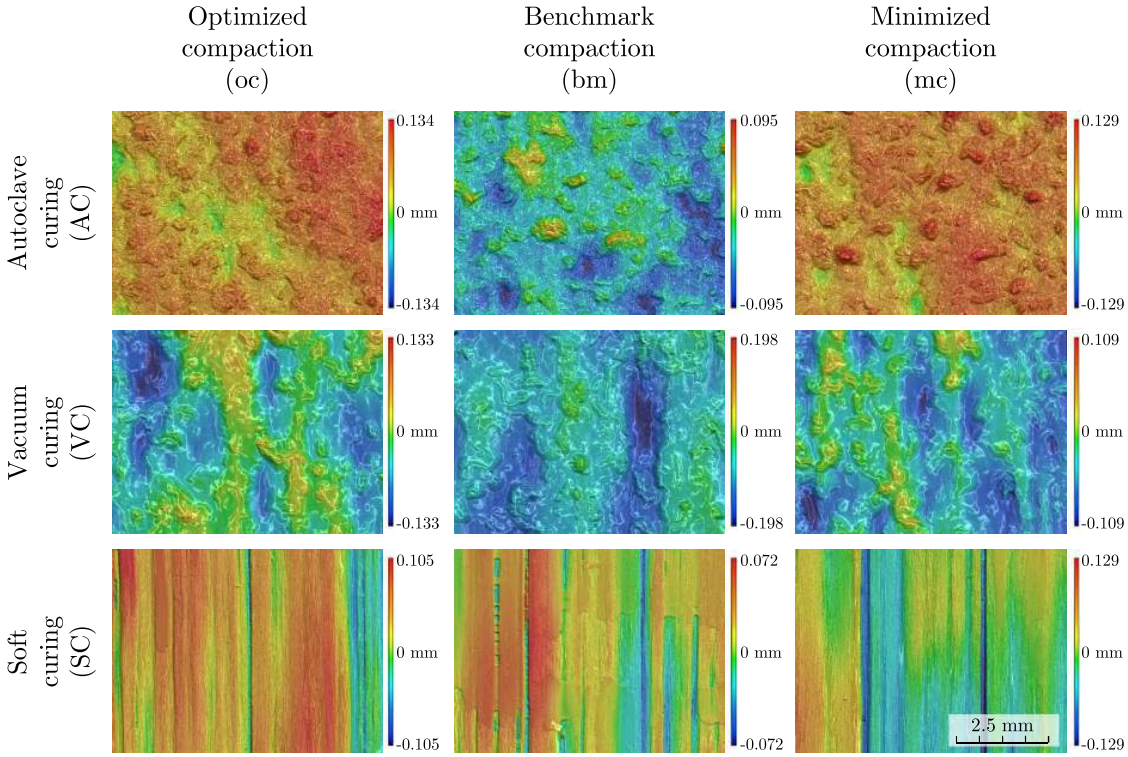

Figure 5.24: 3D profilometer surface scans of the different combinations of process and curing parameters.

5.2.3 Conclusion

A set of full-scale AFP experiments was executed to analyze the influence of process parameter variations on the mechanical laminate properties. The parameter variations included a benchmark configuration (bm), a setting with minimum compaction (mc) and an optimized compaction (oc) parameter set. For all settings, three different curing methods were implemented – autoclave (AC), vacuum (VC) and soft curing (SC). The mechanical characterization was done via tensile, 4-point-bending and ILSS tests. In addition, the samples were analyzed by micro CT, optical profilometer and regarding their void volume content (VVC). Comparing the curing methods, a clear drop in all tests can be seen from autoclave over vacuum to soft curing, especially for the matrix dominated properties. The ILSS results are representative for the observed trends and are given as exemplary reference in this conclusion. Summed up by curing method, VC is lower by 10 % compared to AC, SC even by 42 % (cf. Fig. 5.21). For the process parameter variations, it was identified that the differences in mechanical properties are compensated with rising pressure in the defined cure cycles. The soft cured samples allow a differentiation of the parameter sets, with the best results for the compaction optimized configuration followed by the benchmark. Samples with minimized compaction setting show

the worst results. In the ILSS results, this is reflected by a knock-down of 35 % for SC-oc, 43 % for SC-bm and 50 % for SC-mc in relation to the maximum achieved value of 113 N/mm^2 for AC-oc (cf. Fig. 5.20). For vacuum curing, the differences are considerably smaller and for autoclave curing they are equated entirely. In the ILSS results VC-oc dropped by 7 %, VC-bm by 16 % and VC-mc by 9 %. The variation of all AC samples is below 5 % and within the standard deviation (cf. Fig. 5.20). Results of micro CT and VVC analysis support this conclusion with mean void contents of 0.0 % for AC, 1.6 % for VC and 5.2 % for SC (cf. Fig. 5.23).

The study shows that AFP process parameters have an influence on the laminate quality. This influence can be seen in the soft cured configuration, representing the laminate quality as deposited but before pressurized curing. For the given set-up, autoclave curing compensates for these differences. However, it is questionable whether this is also the case in application scenarios with more complex geometries and a larger number of layers. In addition, it is conceivable to reduce the curing effort and possibly even to dispense with an autoclave in the case of higher deposition quality.

The optimized AFP process parameter set was proven to be superior or at least equal in the mechanical laminate properties, depending on the curing method. This shows that for the given set-up, compaction during AFP tape deposition is able to replace compaction by vacuum debulking.

6 Process efficiency analysis

TS-AFP is a well established process with many applications in aerospace manufacturing. For such a process, potential optimizations are only worthwhile if they increase the overall efficiency. In this chapter, an AFP process model is set up to assess the impact of process optimizations as defined in the previous chapters.

The chapter contains first the description of the AFP process breakdown and the according set-up of the AFP process model. Results of the model application include a process model validation, a process parameter sensitivity analysis, a use case study and a list of limitations, all summed up in a conclusion. The AFP process model and first results have been published by Engelhardt et al. [22]. Parts of the results of this section were obtained in the theses of Lörch [171] and Dsouza [172] under the supervision of the author.

6.1 AFP process breakdown

The set-up of a process model requires the identification of all relevant process steps along the manufacturing chain including their sub-steps and all interactions depending on the process scenario [173]. The overall process chain of AFP manufacturing can be summed up in the main steps planning and programming, production preparation, AFP processing, curing, finishing and quality inspection (cf. Sec. 2.1). For the AFP process, all sub-steps and their interactions were identified and modelled. An excerpt of the flow process chart is shown in Fig. 6.1. Ply lay-up is followed by visual inspection and rework if necessary. Debulking steps and maintenance operations interrupt the lay-up process where applicable. Once the iterative lay-up process is finalized, the tool is demounted and handed over to the curing process as the next step in the overall process chain. Laying up one ply consists of the additive deposition of several tracks, the linking movement in between tracks and the machine movement in between its home position and the tool surface (cf. Fig. 6.1, bottom). Another aspect implemented in the tool is the linking type. Linking is the connection of two consecutive lay-up tracks. When all tracks are started at the same side and laid-up in the same direction, this is designated as unidirectional (UD) lay-up direction. The AFP equipment used as reference for

this study allows a tilting of the placement roller and thus a bi-directional (BD) lay-up direction (cf. Sec. 2.1.4. This leads to an alternating lay-up direction from track to track and considerably shorter linking distances and times (cf. Fig. 6.2).

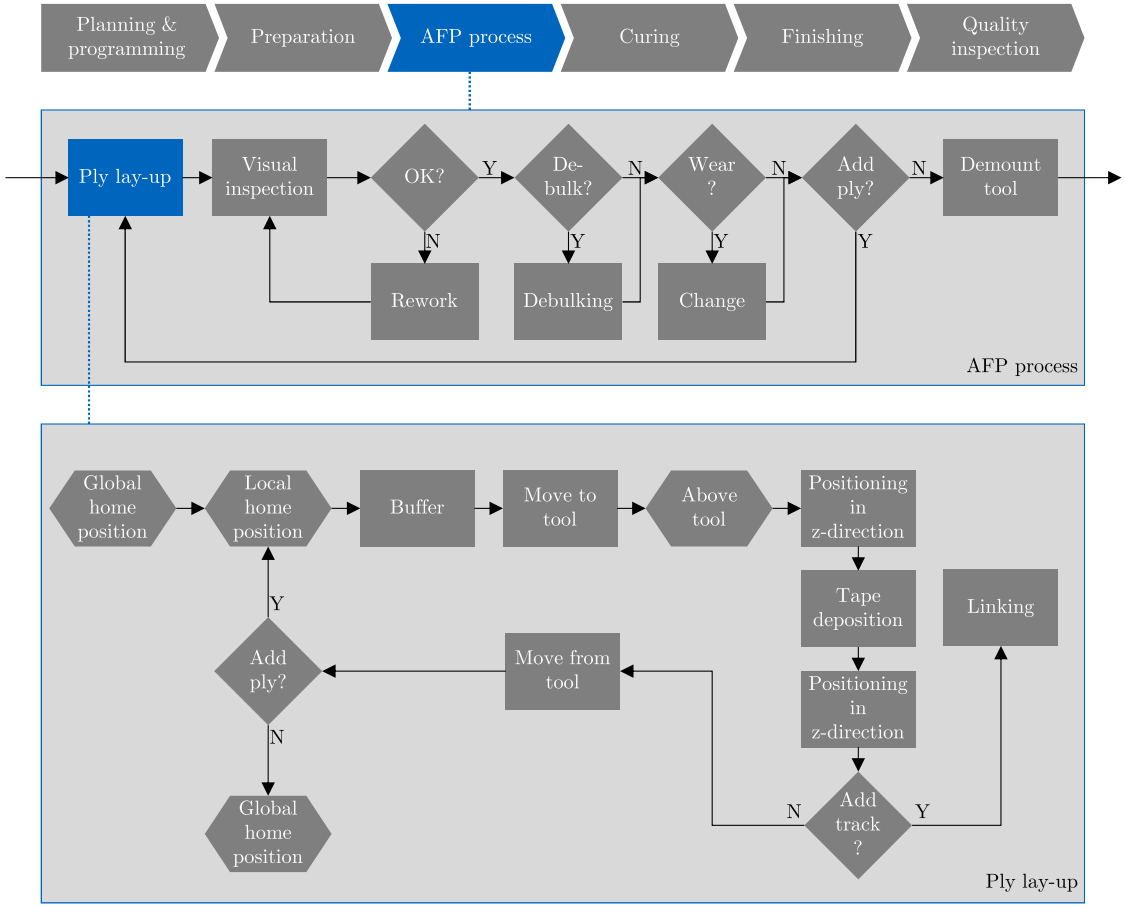

Figure 6.1: Excerpt of the AFP process model with sub-steps of the AFP process and the ply lay-up.

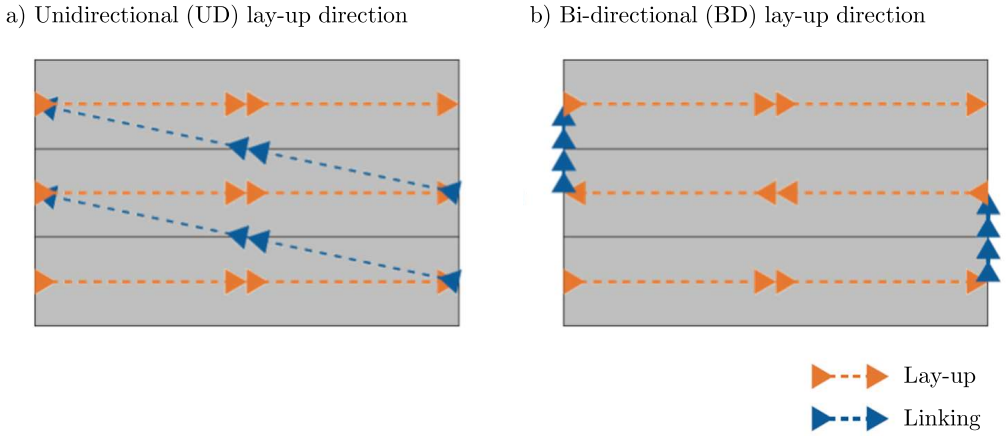

Figure 6.2: unidirectional (UD) and bi-directional (BD) lay-up direction and the corresponding linking movement.

6.2 AFP process model

An AFP process model was set up with the goal to analyze different production scenarios for their AFP process time. The AFP process was modelled using *MATLAB* including all sub-steps and interactions as identified in the process breakdown (cf. Fig. 6.1). Process time is calculated based on the definition of the lay-up and process parameters. Times of the prior and subsequent process steps can be added to the analysis as input values, but are not modeled in detail based on input variables.

The tool allows input and variation of a variety of parameters (cf. Fig. 6.3). Laminates can be defined by adding the desired number of plies, their dimensions and fiber orientation in either 0°, 90° or ± 45° as well as the linking type. The geometry can be either flat or cylindrical ("barrel"). Geometric complexity can not be added by a more detailed definition of the geometry, but has to be considered via a knockdown factor in the lay-up velocity. Varying tape width and number of tapes allows a configuration of the placement head. AFP process specific variables include velocities and acceleration rates and distances for lay-up and linking, with the option to add a first ply reduction. Equipment specific buffer and positioning times are summed up as AFP programming data. Time for visual inspection after each ply can be varied, just as the debulking interval and duration. Replacement intervals and duration of typical wear parts such as cutter blades or IR lamps are considered and can be varied. For analyses of production scenarios including the overall process chain, process times for curing, finishing and quality inspection (QI) can be added together with the number of parts to be produced. Default values for all parameters were determined by either on-site measurements or based on experience (cf. Tab. 6.1 and Tab. A.1). The validity of the process model

was checked by comparing experimental process times with modelling results (cf. Sec. 6.3.1).

a) Laminate data

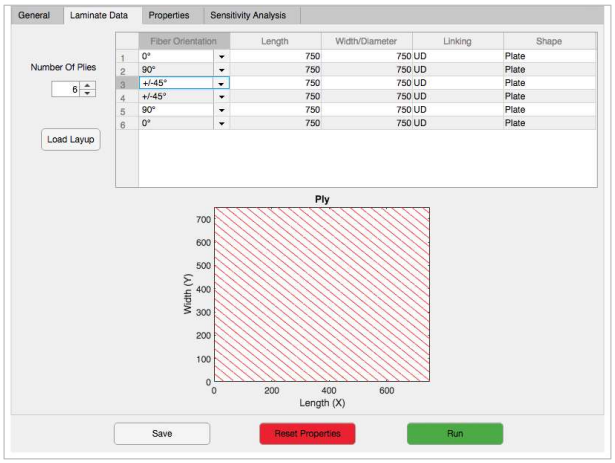

b) Process properties

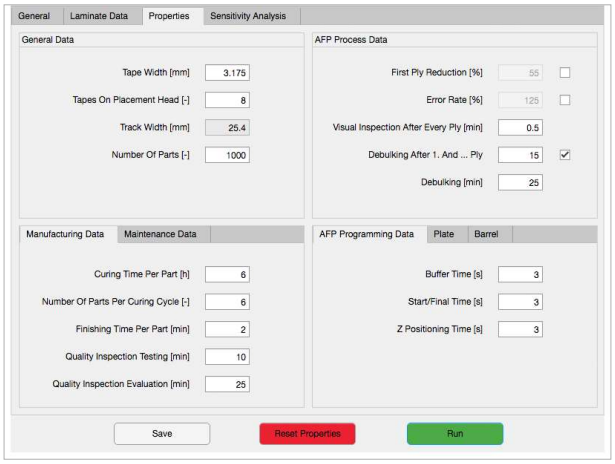

c) AFP programming data

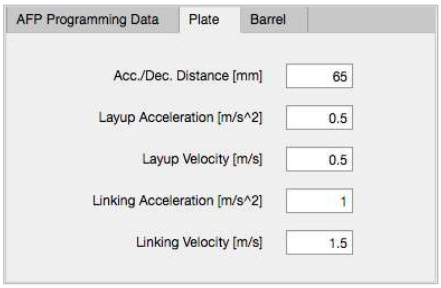

d) Maintenance data – cutter

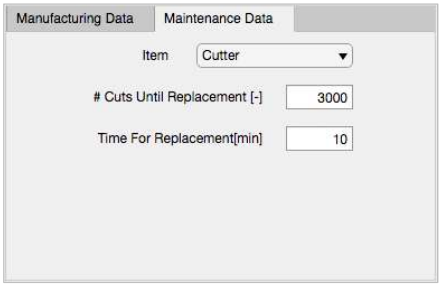

e) Maintenance data – other

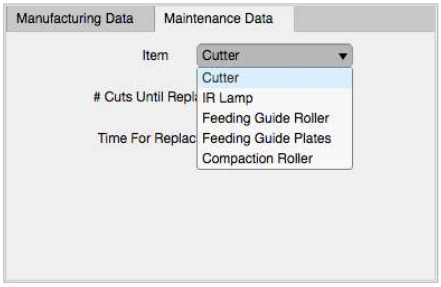

Figure 6.3: GUI of the AFP process model input parameters.

Table 6.1: Default settings of the main parameters of the AFP process model.

Parameter	Unit	Default setting
Tape width	[mm]	3.175
No. of tapes per track	[-]	8
Lay-up velocity	[m/s]	0.5
Lay-up acceleration	$[m/s^2]$	0.5
Linking velocity	[m/s]	1.0
Linking acceleration	$[m/s^2]$	1.5
Buffer time	[s]	3
Time to/from home	[s]	3
Positioning in z-direction	[s]	3
Debulking time	[min]	25
Debulking interval	[n^{th} ply]	15
Time for visual inspection per ply	[s]	30

6.3 Results and discussion

This section contains the data of the model application, starting with a process model validation by a logic check and a comparison of experimental and modelled results. A sensitivity analysis shows the influence of the single process parameters on the AFP process time. In a use case study, the model was applied to different exemplary aerospace production scenarios. The section ends with a list of limitations for the application of the AFP process model.

6.3.1 Process model validation

The AFP process model was validated with a systematic input variation and logic check, followed by a comparison of model results to experimental measurements. Logic integrity of the model was checked by analyzing the AFP process time of a laminate of 18 plies with different fiber orientations, dimensions, aspect ratios and linking types (cf. Tab. 6.2). A systematic variation of the properties allowed a qualitative check for correct set-up relations in the model. Plies 1 to 9 and 10 to 18 are identical except for their linking type.

In Fig. 6.4, the result of the AFP process time for plies 1 to 18 is visualized. The process time is shown as the sum of out-of-ply time, lay-up time and linking time. All movements of the lay-up head in contact with the tool surface are counted as lay-up time. Movement in between tracks is considered as linking time. Out-of-ply

Table 6.2: Input lay-up definition for a qualitative logic check of the AFP process model.

Ply no. [-]	Fiber orient. [°]	Length [mm]	Width [mm]	Linking [-]
1	0	1000	1000	UD
2	90			
3	45			
4	0	1000	200	
5	90			
6	45			
7	0	200	1000	
8	90			
9	45			
10-18	-"-	-"-	-"-	BD

time includes all remaining movements between home position and tool surface, as well as the time for positioning in z-direction. The results show identical times for out-of-ply and lay-up time for plies 1 to 9 and 10 to 18. Identical process times for plies 48 and 5 to 7 show the inverse behavior of the lay-up time when swapping length, width and fiber orientation while keeping aspect ratio and ply area constant. This means the total process time of a ply of $1000\,mm \times 200\,mm$ (length × width) and 0° fiber orientation is equal to the process time of a ply of $200\,mm \times 1000\,mm$ (length × width) and 90° fiber orientation. A similar effect can be seen when comparing ply 13 and 17 as well as ply 14 and 16. The 45° plies 3, 6, 9, 12, 15 and 18 have a longer linking time and out-of-ply time than similar plies with 0° or 90° fiber orientation caused by the additional amount of tracks. Comparing ply 6 and 9 shows a similar inverse behavior as described above, when swapping length and width while keeping the ply area constant. This is due to the fact, that the amount of tracks does not change for 45° plies in this case. These results suggest a consistent logic of the model output for the basic behavior of the AFP system. This verifies the mathematical modeling implemented in the tool on a qualitative level.

A set of experimental measurements was conducted for quantitative validation of the lay-up time modelling and for analysis of the influence of the aspect ratio (AR) of a ply. A total of 32 different plies with 5 different areas and a variety of aspect ratios was deposited and modelled. The results are shown in Fig. 6.5, with the aspect ratio calculated as $AR = width/length$. They show a good agreement of the experimental lay-up times and the modelled results, with an average relative

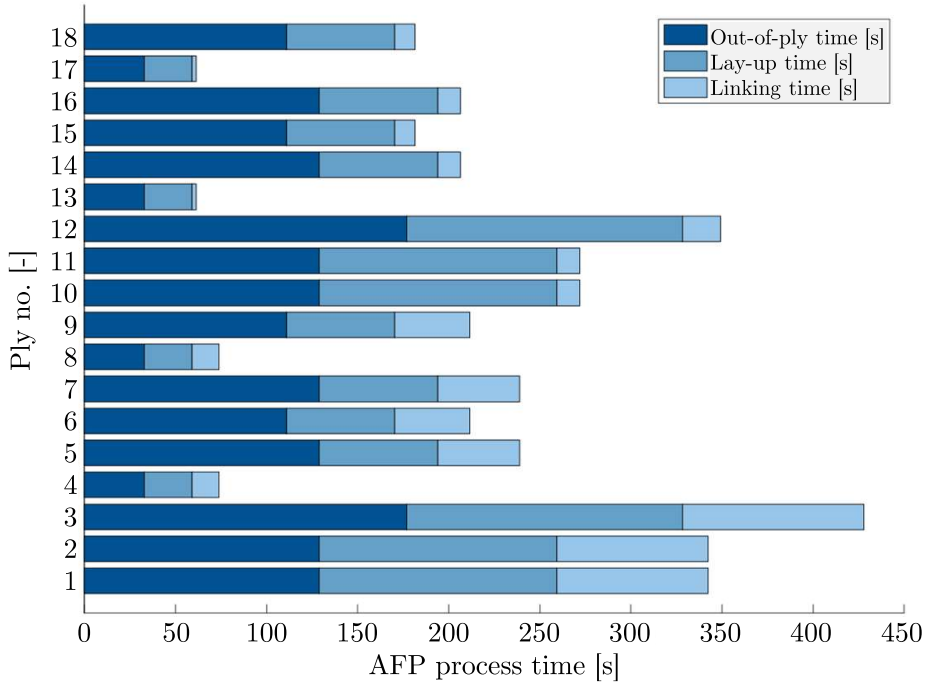

Figure 6.4: AFP process time comparison for qualitative logic check of the AFP process model.

deviation of 5.4 %. This suggests a validity of the modelled lay-up times for flat plate geometries. The analysis of the aspect ratio identifies a clear and systematic trend of rising lay-up time with increasing aspect ratio, similar to the results shown in Fig. 6.4. Narrow plies have a small aspect ratio and fewer tracks than wider plies with bigger aspect ratio. With constant ply area this leads to higher lay-up velocity as there is more room for acceleration and fewer tracks leading to less linking and out-of-ply time.

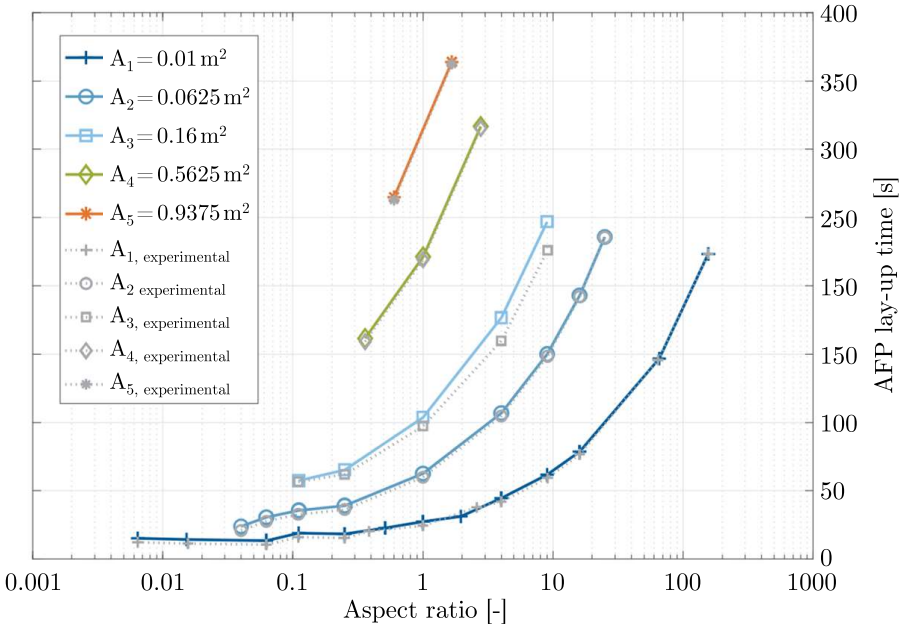

Figure 6.5: Comparison of experimental and model results for the AFP lay-up time for different ply areas and aspect ratios.

6.3.2 Process parameter sensitivity analysis

A sensitivity analysis was conducted to analyze the influence of different process parameters on the AFP process time. The reference laminate defined for this analysis was a flat plate of $1500\,mm \times 1500\,mm$ with 24 plies and an equal distribution of 0°/90°/45° fiber orientation. Parameter settings were varied in a range from -100 % to +100 in 25 % steps starting from a default value as shown in Tab. 6.3. All parameter settings are listed in Tab. 6.3 with the base case parameter setting marked in bold. Debulking interval refers to the number of plies deposited before a vacuum debulking step is applied. Out-of-ply movement time is varied based on the total out-of-ply movement time for the base case, including buffer times, time to and from home position and z-positioning time.

Fig. 6.6 shows the resulting relative deviation of the AFP process time starting from the base parameter settings. The parameters out-of-ply time, visual inspection time and debulking time have a linear positive influence on the AFP process time. Lay-up velocity, debulking interval and number of tapes per track have a negative non-linear influence.

Out-of-ply-time has a strong influence on the AFP process time. Decreasing it by 25 % reduces the AFP process time by 5 %. The influence of the debulking time and time for visual inspection is of similar linear nature, but on a smaller scale.

Varying of the number of tapes per track has a strong non-linear influence, as it influences the number of tracks per ply and the corresponding out-of-ply and

Table 6.3: Process parameter variations for the sensitivity analysis.

Parameter	Unit	Settings
Lay-up velocity	[m/s]	0/0.125/0.25/0.375/**0.5**/0.625/0.75/0.875/1
Time for visual inspection per ply	[s]	0/7.5/15/22.5/**30**/ 37.5/45/52.5/60
Time for debulking	[min]	0/6.25/12.5/18.75/**25**/31.25/37.5/43.75/50
Debulking interval	[n^{th} ply]	0/4/8/11/**15**/19/23/26/30
No. of tapes per track	[-]	0/2/4/6/**8**/10/12/14/16
Out-of-ply movement time (total)	[s]	0/2,214/4,428/6,642/**8,856**/11,070/ 13,284/15,498/17,712

linking time. A decrease from 8 to 6 tapes increases the process time by 40 %. An increase of the number of tapes on the other hand has a big potential to minimize the process time. Tape width has a similar effect, as it increases the track width and decreases the tracks per ply. A bigger track width has a negative influence on the geometric flexibility of the AFP system and can't be increased without careful consideration of the use case.

Lay-up velocity has a strong non-linear influence on the AFP process time, with a sharp increase for lower lay-up velocities but only a small decrease of the process time for higher lay-up velocities converging against 5 % time reduction compared to the base case.

A variation of the debulking interval shows a non-linear increase of the AFP process time for decreasing interval, meaning here a decreasing distance of the single debulking steps and thus more debulking applications. For an increasing interval, there is only a stepwise decrease of the process time visible for an increase of the debulking interval by +75 %. The reason for this is the experimental set-up with a laminate of 24 plies and a base case of debulking application every 15$^{\text{th}}$ ply. An increase of the interval by 25 % to a 19 ply interval or by 50 % to a 23 ply interval does not have an effect on the number of debulking cycles applied. Only a 75 % increase to a 26 ply interval leads to a reduction to 0 debulking intervals and has an effect on the AFP process time.

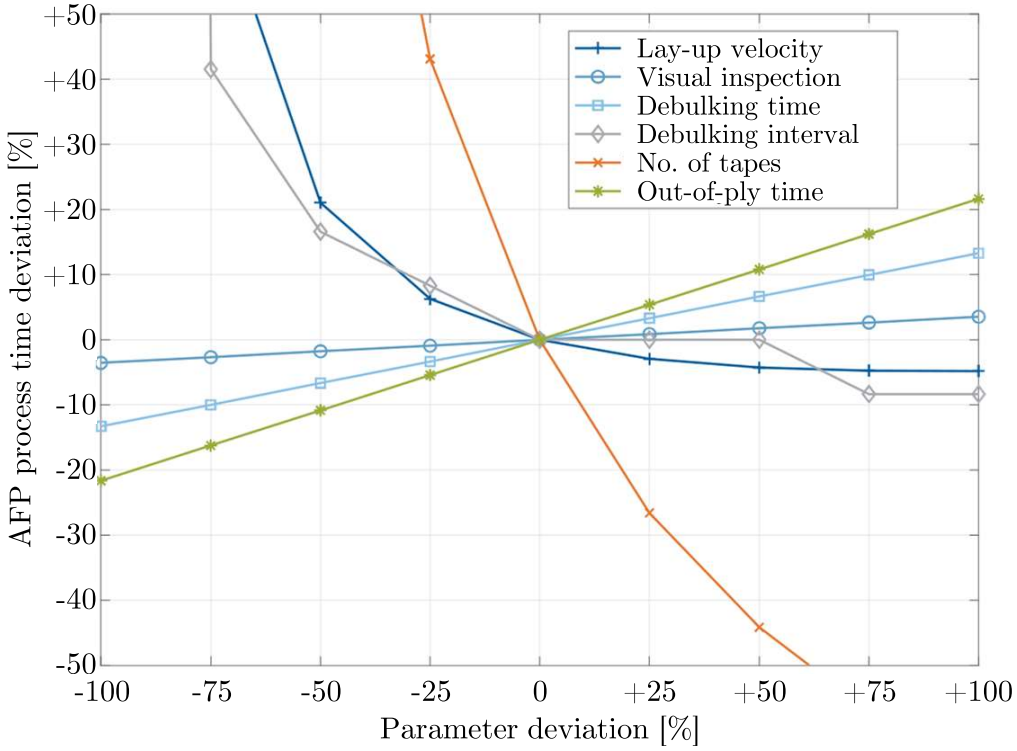

Figure 6.6: Sensitivity analysis of different process parameters, showing their relative influence on the AFP process time.

6.3.3 Use case study

The AFP process model was applied to a use case study comparing the AFP process time for different process parameters and production scenarios. Five different use cases were defined, comprised of laminates of different sizes and ply numbers (cf. Tab. 6.4). The use cases represent low to medium complexity panels with skin plies and smaller reinforcement plies as generic examples for typical aerospace applications. Ply sizes range from below 1 m^2 to more than 10 m^2 and a ply number of up to 225 plies in total.

Parameter variation was limited to lay-up velocity and debulking interval, as these two parameters have a main influence on the AFP process time and are affected by an optimization of the process compaction. Five different parameter sets were defined (cf. Tab. 6.5). The benchmark represents a typical process setting for low to medium complexity aerospace panels with a lay-up velocity of 0.75 m/s and debulking after every 10^{th} ply. Two different “optimized compaction” parameter sets were defined based on the experimental results in the prior sections. Both sets have no debulking steps and compensate this by a lower lay-up velocity. The "optimized compaction 1" parameter set (OC1) is a progressive scenario with a lay-up velocity of 0.5 m/s. For the "optimized compaction 2" parameter set (OC2),

Table 6.4: Use case definition.

Use case	Size	Skin plies	Reinforcement plies
Case 1	very small (<1 m^2)	30 x 1 m^2	15 x 0.1 m^2
Case 2	small (1-2 m^2)	50 x 2 m^2	25 x 0.2 m^2
Case 3	medium (2-5 m^2)	80 x 5 m^2	40 x 0.35 m^2
Case 4	large (5-10 m^2)	100 x 10 m^2	50 x 1.0 m^2
Case 5	very large (>10 m^2)	150 x 15 m^2	75 x 1.5 m^2

a more conservative configuration with 0.25 m/s was chosen. Two additional sets at the theoretical upper and lower limit of the processing window were defined for a general classification of the results. "Minimal compaction" has a very high lay-up velocity and no debulking, leading to very short process times. "Maximum compaction" on the other hand includes a very low velocity and debulking after every 10^{th} ply, leading to very high process times.

Table 6.5: Parameter sets of the use case study.

Parameter set	Lay-up velocity [m/s]	Debulking interval [n^{th} ply]
Benchmark	0.75	10
Optimized compaction 1 (OC1)	0.5	-
Optimized compaction 2 (OC2)	0.25	-
Minimal compaction	1	-
Maximum compaction	0.1	10

Fig. 6.7 shows the AFP process time for the five different cases at different lay-up velocities and debulking intervals. The process time increases from case 1 to 5 with decreasing lay-up velocity and debulking interval. The influence of the lay-up velocity on the AFP process time is big for low velocities, but decreases for velocities above 0.5 m/s. This is in accordance with the results of the sensitivity analysis in Sec. 6.3.2. AFP process time is the sum of lay-up time, out-of-ply time and debulking time. Their shares of the AFP process time are visualized in

Fig. A.63 to Fig. A.67 in the appendix. Debulking time increases with the number of application cycles. Its proportion in the process time decreases with the panel size from case 1 to 5. While it accounts for the majority of the process time for case 1 with a debulking interval of 5 plies, it only has a small share for case 5. This influence of the debulking interval can also be seen in Fig. A.69 in the appendix.

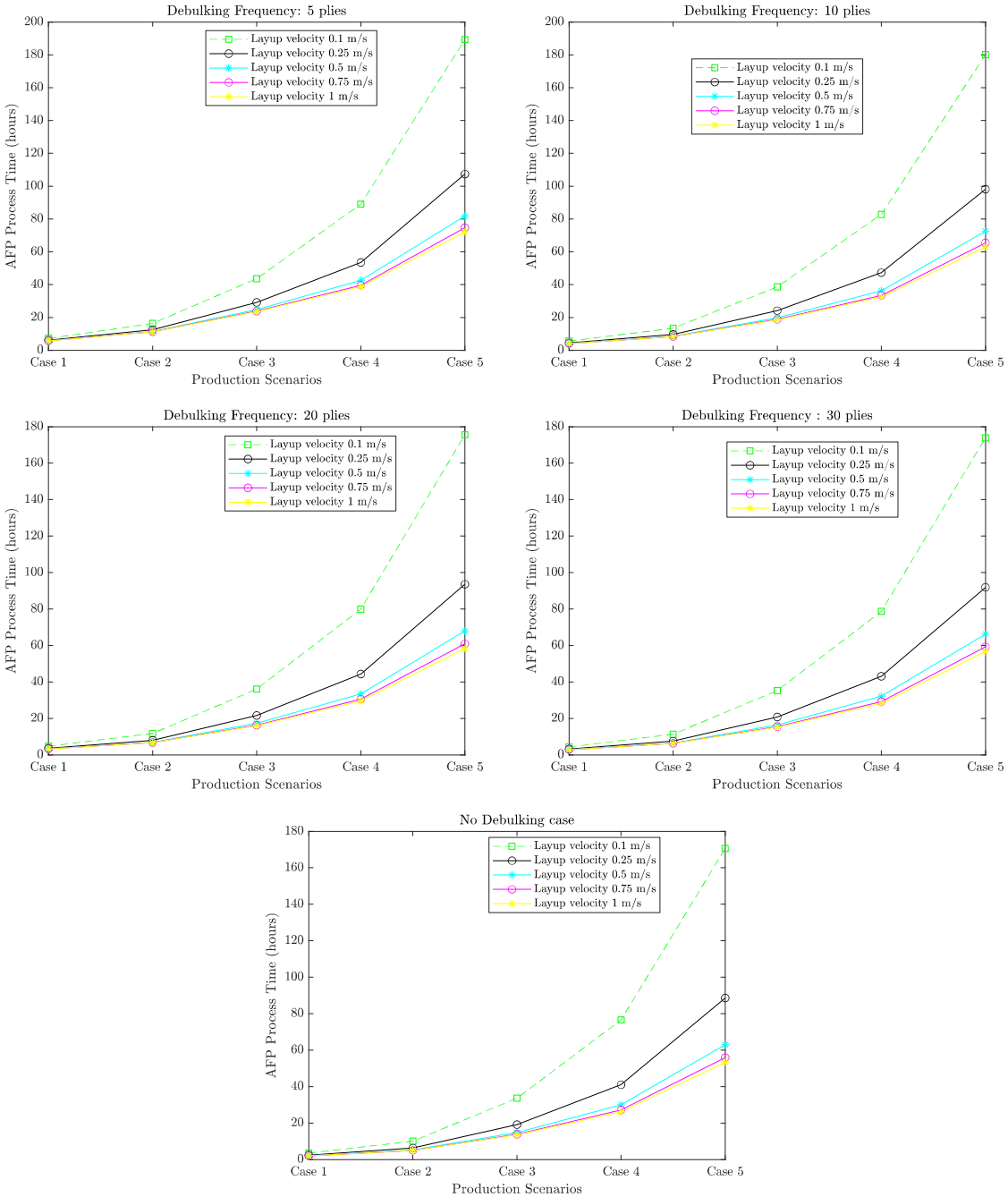

Figure 6.7: Influence of lay-up velocity and debulking interval on the AFP process time.

Fig. 6.8 shows the AFP process time for all different parameter sets. The maximum and minimum compaction parameters represent the boundaries of the process

regarding a theoretical minimum and maximum of the AFP process time. For case 1 and 2 both optimized compaction parameter sets lead to lower AFP production times compared to the benchmark. From case 3 upwards, the conservative "optimized compaction 2" parameter exceeds the benchmark in AFP process time. The more progressive “optimized compaction 1" parameter set stays below the benchmark all along from case 1 to 5.

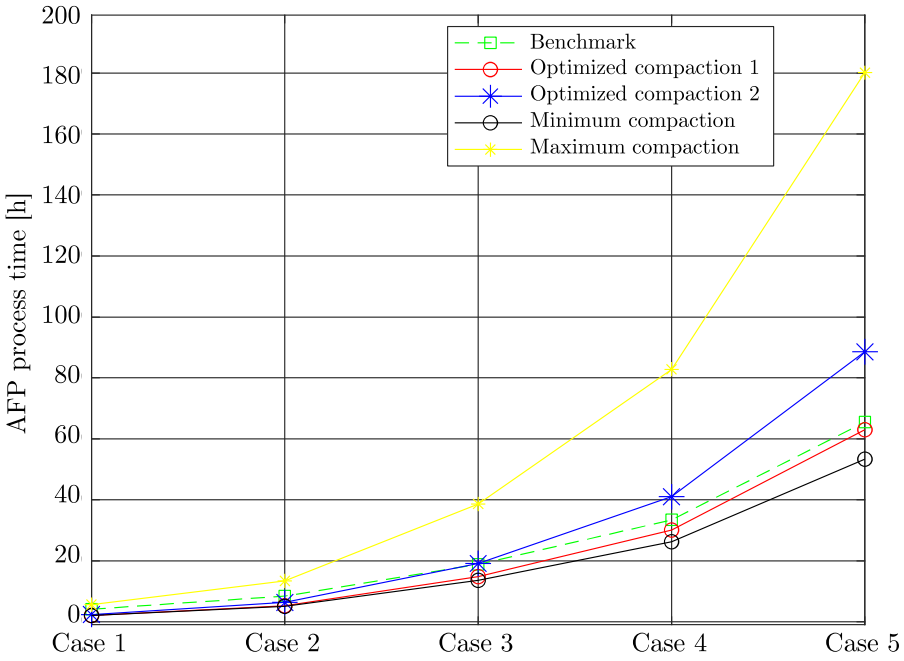

Figure 6.8: AFP process time for different parameter sets and use cases.

OC1 leads to a reduction of the AFP process time of 49 %, 37 %, 21 %, 10 % and 4 % respectively for cases 1 to 5. For OC2, the reduction is 42 % and 25 % for case 1 and 2. For cases 3 to 5 it leads to a surplus of 2 %, 23 % and 35 % in the AFP process time compared to the benchmark.

The sequence from case 1 to 5 does not represent a continuous series of numbers, which makes the interpretation of intersections difficult. The use cases were converted in two different ways, making a more universal interpretation independent of the use case definition possible. For a first approximation, the area of all plies was added to the total area A_{total}. The five use cases have a total ply area of 31.5 m^2, 105 m^2, 414 m^2, 1050 m^2 and 2362.5 m^2 from case 1 to 5. This does not take into account the number of plies and the area per ply. Therefore, the average area per ply $A_{av.p.p.}$ was calculated as

$$A_{av.p.p.} = \frac{n_{skin} \cdot A_{skin} + n_{re} \cdot A_{re}}{n_{skin} + n_{re}} \tag{6.1}$$

summing up the area of skin and reinforcement plies and dividing it by the total number of plies. This value can be used as a rough approximation of the lay-up effort of a use case. The five use cases have an average area per ply of 0.7 m^2, 1.4 m^2, 3.45 m^2, 7.0 m^2 and 10.5 m^2 from case 1 to 5.

For both the total lay-up area A_{total} and the average area per ply $A_{av.p.p.}$, a linear relationship with the AFP process time was found via linear regression. With a coefficient of determination R^2 of >99 % for A_{total} and >95 % for $A_{av.p.p.}$, the fit can be considered as good enough for an approximation of intersection points (cf. Fig. A.71 and Fig. A.72).

Fig. 6.9 shows the linear regression graphs for the total lay-up area, Fig. 6.10 for the average area per ply. The intersection of the benchmark and OC2 parameter sets is shown separately for reasons of visibility. Benchmark and OC2 intersect at a total area of 299.1 m^2 and an AFP process time of 13.39 hours. For the average area per ply, the intersection point is at 2.4 m^2 per ply, with an AFP process time of 13.06 hours.

The results show, that even for the conservatively optimized parameter set OC2, a reduction of the AFP process time compared to the benchmark is possible up to a certain size. The more progressive parameter set OC1 leads to a reduction for all investigated use cases.

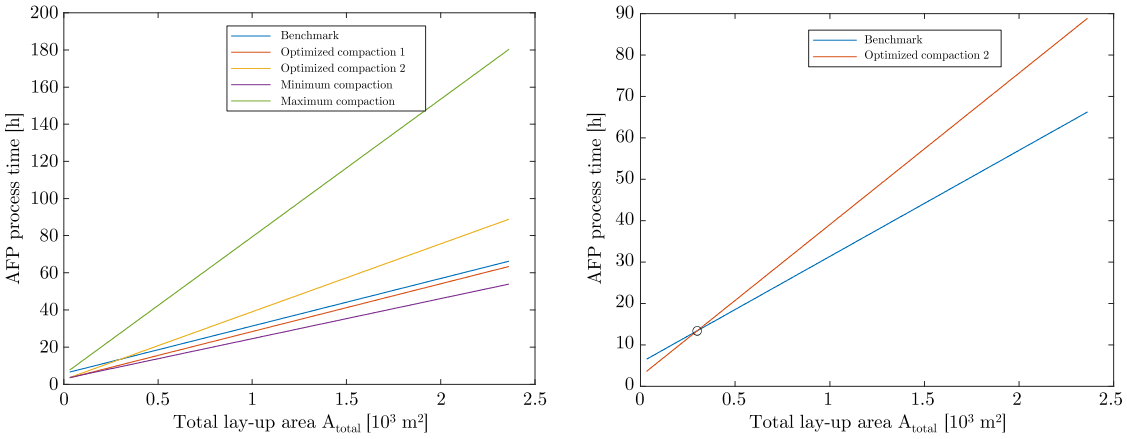

Figure 6.9: Linear regression of the total lay-up area.

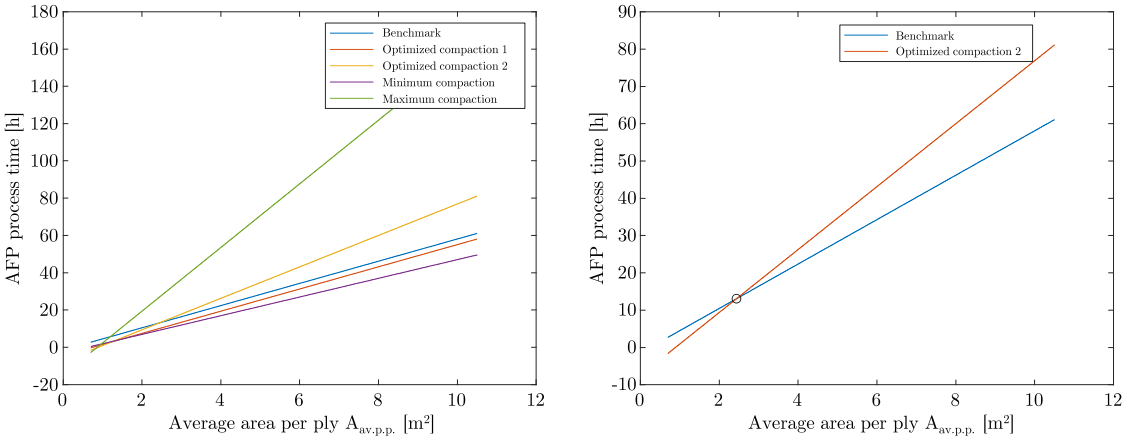

Figure 6.10: Linear regression of the average lay-up area per ply.

6.3.4 Limitations

The set-up of a process model is a compromise of on the one hand the realistic replication of the AFP process and on the other hand the feasibility of a tool and the handling of input and output values with limited complexity. This compromise leads to inevitable simplifications that have to be considered when analyzing the results.

- Geometric complexities cannot be entered into the tool based on their geometry, as only flat panels and rotationally symmetric cylinders can be defined. Geometric complexity has to be taken into account via a knockdown of the lay-up velocity based on the experience of the user of the tool.

- The velocity is the same for all plies within one analysis run of the tool. Only the lay-up velocity of the first ply can be adjusted with a knockdown factor in percent. Local geometric complexities, that would in reality lead to a local variation of the lay-up velocity, can't be replicated and have to be considered in the global lay-up velocity input.

- Both the total lay-up area A_{total} and the average area per ply $A_{av.p.p.}$ are only rough estimates for the total lay-up effort of a laminate. A_{total} does not take into account the number of plies and the single ply areas. Both factors neglect the aspect ratio of the plies. For a set of use cases with fix aspect ratio and a similar ratio of skin and reinforcement plies, the factors can still be used as an indicator for the total lay-up effort. $A_{av.p.p.}$ is a theoretical factor that is valid only within a range of ply numbers similar to the use cases defined in this study. For A_{total} and $A_{av.p.p.}$ and their respective AFP process time,

the exact absolute values are considered less important than their order of magnitude and, above all, the relative comparison of different scenarios.

6.4 Conclusion

An AFP process model was set up based on a process breakdown, including all relevant sub-steps and their interrelations. It allows calculating the AFP process time with a systematic variation of process parameters and boundary conditions. It was applied for a sensitivity analysis and use case studies, assessing the efficiency of the potential process optimizations developed in the previous chapters.

The model was validated, comparing its results to experimental measurements for plies of different size and aspect ratio. Here, the systematic relation of increasing lay-up time with rising aspect ratio was shown. In the sensitivity analysis, it was identified that apart from tape width, time for visual inspection and out-of-ply time, the process parameters debulking interval and debulking duration are promising levers for a process time optimization. Lay-up velocity should not drop below a certain limit, but optimizing it with great effort by more than 25 % is not worthwhile for the given set-up.

A use case study was performed with different AFP process parameter sets and application scenarios, ranging from small to large panels with a maximum of more than $10\,\mathrm{m}^2$ and 200 plies. The parameter sets included a benchmark setting, minimum and maximum compaction as well as two optimized compaction settings, based on the previous chapters. It has been shown that the optimized compaction settings without vacuum debulking are well competitive with the benchmark setting including vacuum debulking. For small to medium sized use cases, both proposed new parameter sets with progressive (OC1) and conservative (OC2) optimization outperform the benchmark regarding the overall AFP process time. Only for very big panels, the conservatively optimized set does not lead to a more efficient AFP process compared to the benchmark. Panels of such this size are not typical AFP applications anymore, but rather for ATL processing. This shows, that the proposed approach in AFP processing without separate vacuum debulking steps but with compaction optimized AFP parameters is economically feasible for typical AFP use cases.

7 Conclusion and outlook

The aim of this thesis is to characterize the compaction behavior for TS-AFP and vacuum debulking for a better process understanding and to enable a higher process efficiency. To achieve this, experiments with systematic parameter variations in laboratory and full-scale were done. A set of compaction-optimized process parameter settings was established and assessed for its efficiency at the example of aerospace specific use cases.

In Chapter 3: "Vacuum debulking compaction", the compaction during vacuum debulking was characterized with variation of the process parameters temperature, fiber orientation and number of plies. An experimental method allowing continuous thickness measurements was developed. The results show a significant influence of temperature during vacuum debulking with an increase of the overall compaction from around 2 % at 30 °C to more than 6 % at 90 °C and more than 9 % at 110 °C respectively. The majority of the compaction for a 16 ply laminate happens within the first 300 seconds of vacuum debulking. Longer debulking times seem only appropriate, when a higher number of plies are to be debulked at once.

Chapter 4: "AFP compaction on laboratory scale" describes the replication and analysis of AFP compaction on laboratory scale. Cyclic compaction experiments were implemented on small scale using a rheometer and on medium scale using a UTM. A numerical simulation model was applied to replicate the cyclic experiments. Temperature and pressure were identified as dominating process parameters. The rheometer experiments identified a wide compaction range from less than 5 % thickness reduction at 25 °C and 0.1 MPa to more than 50 % at 85 °C and 0.5 MPa. UD samples reach significantly higher compaction than samples with varying fiber orientation – with up to three times more compaction for UD samples. Interrelations of the process parameters temperature and pressure with the application of vacuum debulking indicate, that one can potentially be compensated by the other.

Compaction experiments on full-scale level using a TS-AFP machine are presented in Chapter 5: "AFP compaction on full-scale". Compaction behavior during layup was analyzed with thickness measurements during processing. The influence of

varying compaction parameters and curing methods on the mechanical performance was characterized. An optimized AFP process parameter set was proposed and implemented in the characterization. It increases the compaction during AFP processing with increased pressure and temperature at a lower lay-up velocity. Separate vacuum debulking steps are not foreseen. It was shown, that AFP process parameters have an influence on the deposition quality of a laminate. This can be exemplarily observed in the interlaminar shear strength of the soft cured samples, that was improved by 15 % compared to the benchmark and by 30 % compared to the minimal compaction setting. For the given set-up, autoclave curing mostly compensates for these differences in terms of mechanical performance and void content. However, it is questionable whether this is also the case in application scenarios with more complex geometries and a larger number of layers. In addition, it is conceivable to reduce the curing effort and possibly even to dispense with an autoclave if a sufficiently high laminate quality is already reached during deposition. The optimized AFP process parameter set was proven to be superior or – depending on the curing method – at least equal to the benchmark in mechanical laminate properties and void content. This shows that for the given set-up, compaction during AFP tape deposition is able to replace compaction by vacuum debulking.

Chapter 6: "Process efficiency analysis" evaluates the potential of optimized AFP process parameters regarding the overall process efficiency. An AFP process time model was developed, validated and applied to a process parameter sensitivity analysis and a use case study. In the sensitivity analysis, it was identified that the process parameters debulking interval and debulking duration are promising levers for a process time optimization. It was shown that the optimized compaction settings without vacuum debulking are well competitive with the benchmark setting including vacuum debulking. For small to medium sized use cases, both proposed new parameter sets with progressive (OC1) and conservative (OC2) optimization outperform the benchmark regarding the overall AFP process time. With OC1, the AFP process time can be reduced by 49 % for very small panels (use case 1) over 21 % for medium panels (use case 3) to 4 % for very large panels (use case 5). With OC2, a reduction of 42 % and 25 % for use cases 1 and 2 and a similar process time to the benchmark for use case 3 can be achieved. Only for large to very large panels, the conservatively optimized set OC2 does not lead to a more efficient AFP process compared to the benchmark. This shows that the proposed approach in AFP processing without separate vacuum debulking steps but with compaction optimized AFP parameters is economically feasible for typical AFP use cases.

A transfer of the results of this thesis into practice is possible on different levels. The developed method to continuously measure the thickness of an uncured prepreg laminate can be applied to other processes for a contactless compaction quantification (cf. Sec. 3.1). For vacuum debulking of prepreg material, the experimental results of Chapter 3 can be considered. Debulking of more than 300 s was shown not to be required for typical use cases. Hot temperature debulking can be very effective, if additional compaction is required (cf. Sec. 3.2). The developed method for laboratory scale compaction experiments in a rheometer can be used for efficient parameter studies, allowing especially a relative comparison of e.g. different materials (cf. Sec. 4.1.1). For production planning and the assessment of new parameter sets, the AFP process model can be applied (cf. Sec. 6.2). Results of this thesis provide a quantification of the impact of process parameter variations and the curing method on the mechanical characteristics of a laminate. It was shown that the AFP process has a significant influence on the deposition quality. The results show, for standard aerospace processing according to the data sheet, the autoclave is forgiving of deposition shortcomings. With the identified influence of the AFP process on the deposition quality, new possibilities open up with reduced curing intensity. This can be vacuum curing only instead of an autoclave or in a next step even "in situ" consolidation with the according material system allowing a fast curing. Potential examples are radiation curing and thermally fast curing material systems in combination with adapted heat sources and compaction optimized deposition.

In a next step, the studies presented in this thesis can be followed up by extending the geometric complexity and number of plies of the analyzed laminate. Here, improper compaction will have an even higher influence and may lead to in and out of plane fiber distortions that can be avoided by adapted AFP process parameters. A transfer of the applied principles to other material systems can be evaluated by comparative experiments. For toughened epoxy prepreg systems, a qualitatively similar behavior to the presented results is to be expected, but has to be quantified. If vacuum debulking shall be further applied, additional investigations of high temperature debulking e.g. with the help of external IR radiators can help to further improve its effect. The applied compaction process simulation model can be enhanced and further adapted to AFP specific applications. In combination with the experimental data, it can be extended to an efficient tool to evaluate the compaction behavior for individual scenarios. The proposed optimized AFP process parameter set without separate vacuum debulking can be applied to a practical use case, allowing an industrial full-scale comparison. The AFP equipment can be optimized to further increase the compaction potential. Possible approaches

can be an increased roller diameter where the application allows it, or a separate compaction roller or even set of rollers trailing the deposition roller. Heat sources with a bigger impact area and not necessarily higher energy density – for example via large LED panels – could improve the heat penetration and thus allow improved compaction. The optimization results of this thesis and the outlook for additional improvements show the high potential of automated CFRP deposition via the TS-AFP process allowing the efficient manufacturing of high performance aerospace structures.

A Appendix

A.1 Raw data of the UTM compaction experiments

The graphs below show representative UTM raw data of the experiments in Sec. 4.2 accompanying the result interpretation in Sec. 4.2.2. The graphs are referred to in Sec. 4.2.2.

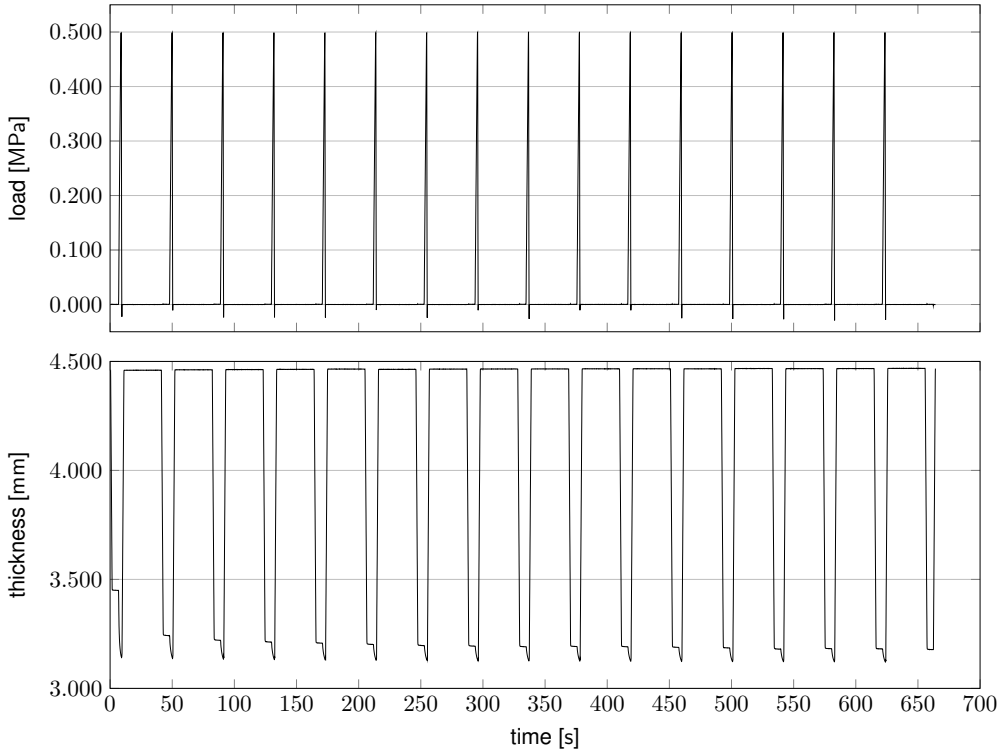

Figure A.1: UTM raw data showing a set of 16 compaction cycles and the corresponding thickness data.

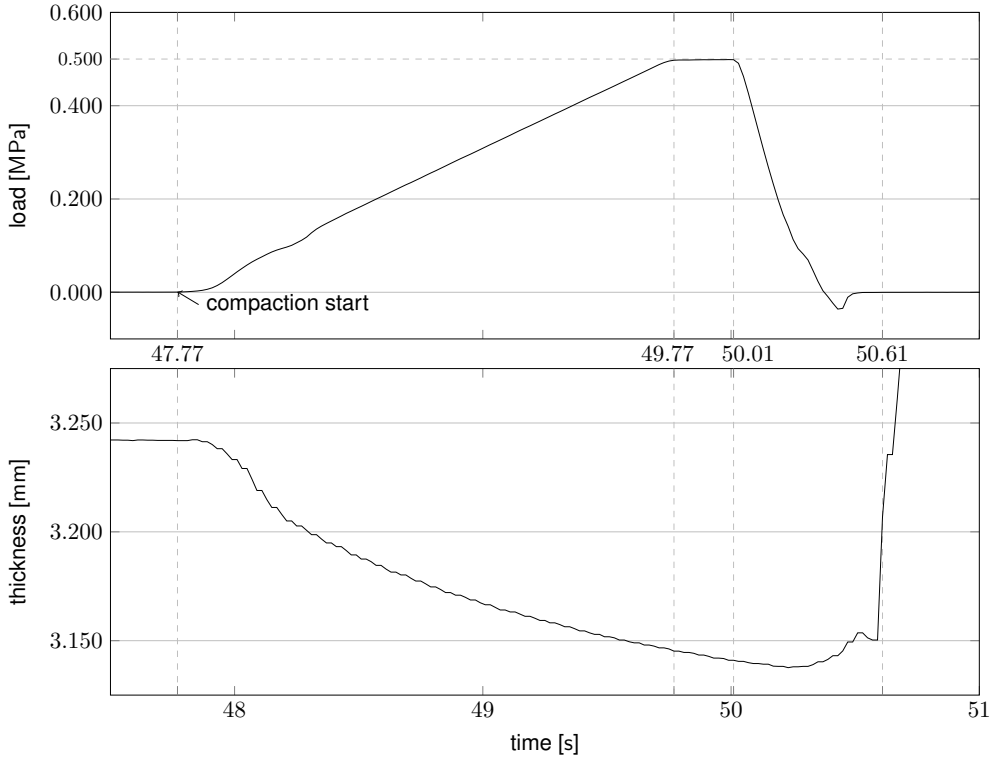

Figure A.2: UTM raw data showing a representative compaction pressure peak and the corresponding thickness data.

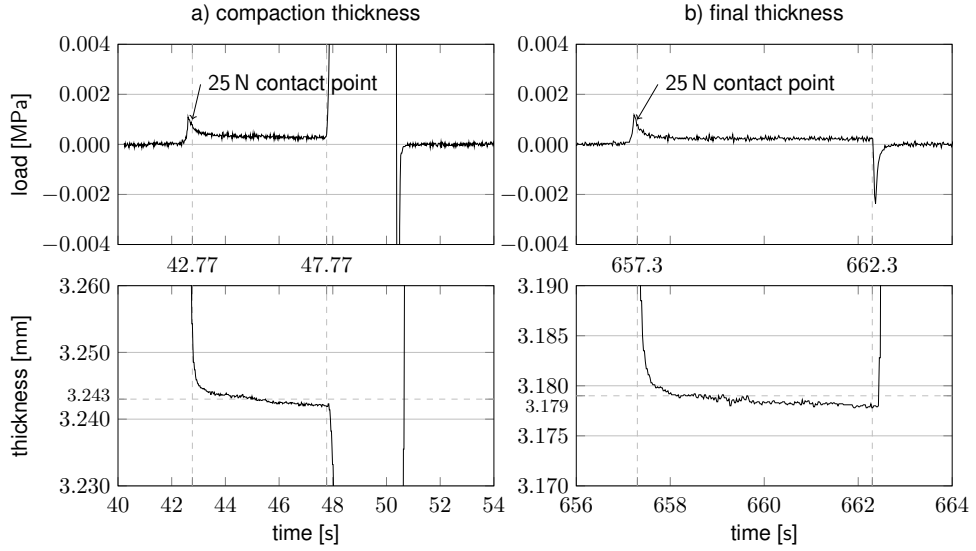

Figure A.3: UTM raw data showing a representative thickness measurement procedure.

A.2 Stress-strain curves of the mechanical characterization

A.2.1 4-point bending tests

Stress-strain graphs of the 4-point bending tests as part of the material characterization in Sec. 5.2. The graphs listed below are accompanying the result discussion in Sec. 5.2.2, emphasizing the linear elastic behavior. The graphs are referred to in Sec. 5.2.2.

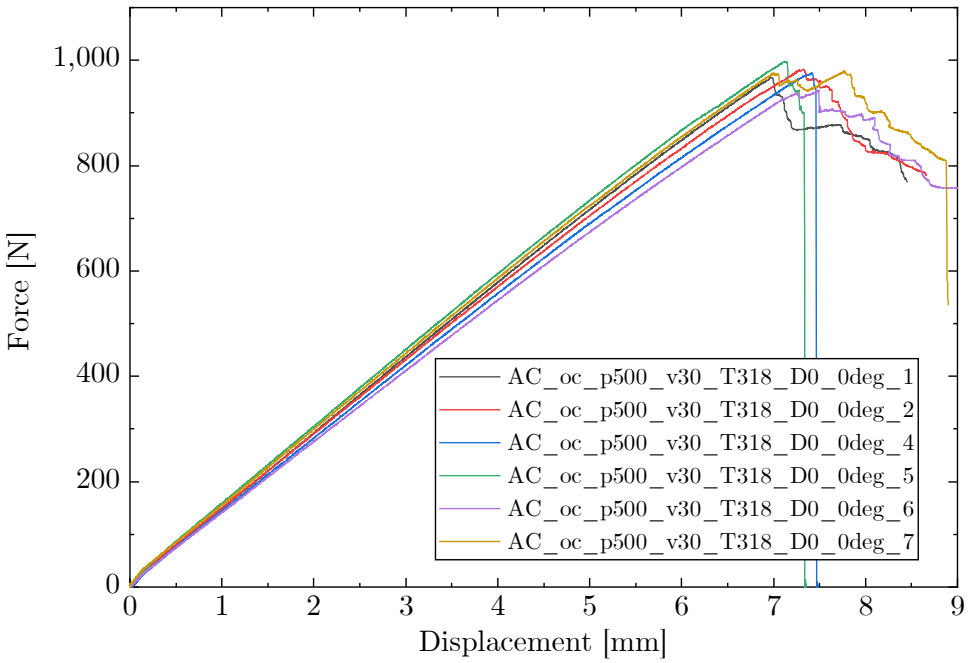

Figure A.4: Stress-strain curves of the AC-oc 4-point-bending samples in 0°-direction.

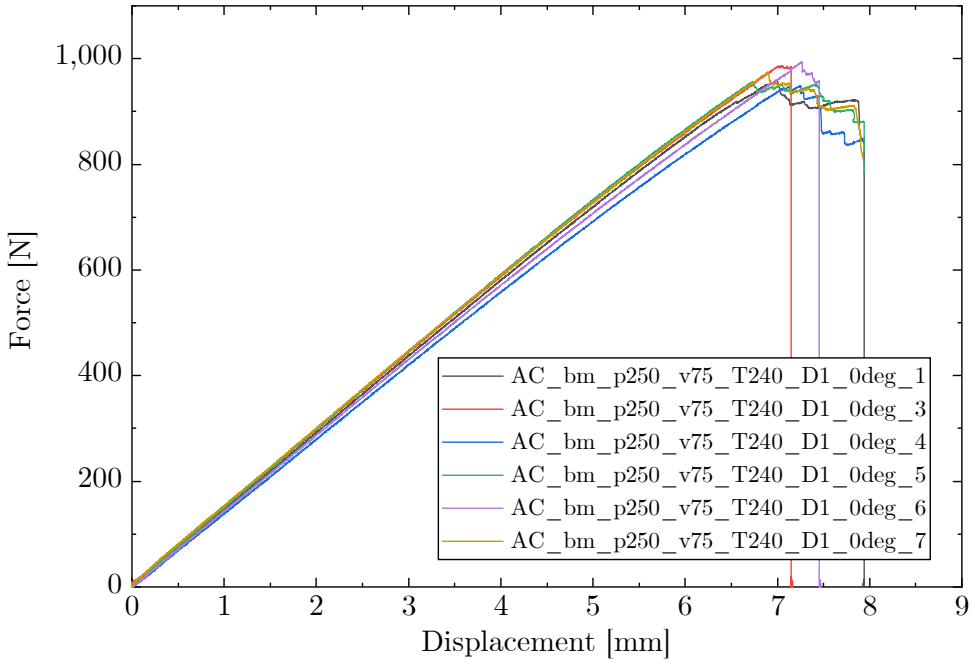

Figure A.5: Stress-strain curves of the AC-bm 4-point-bending samples in 0°-direction.

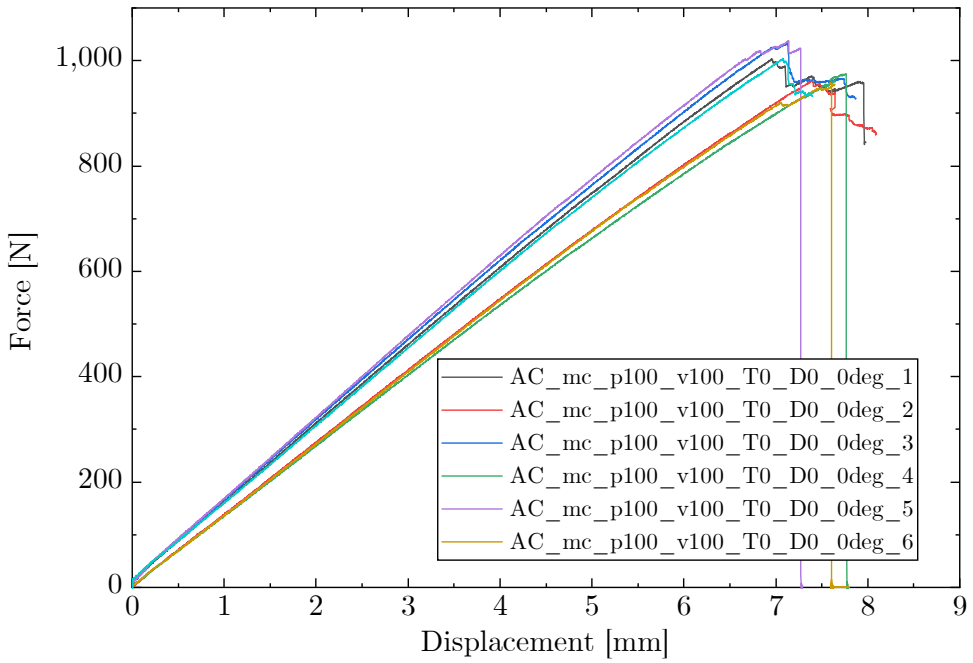

Figure A.6: Stress-strain curves of the AC-mc 4-point-bending samples in 0°-direction.

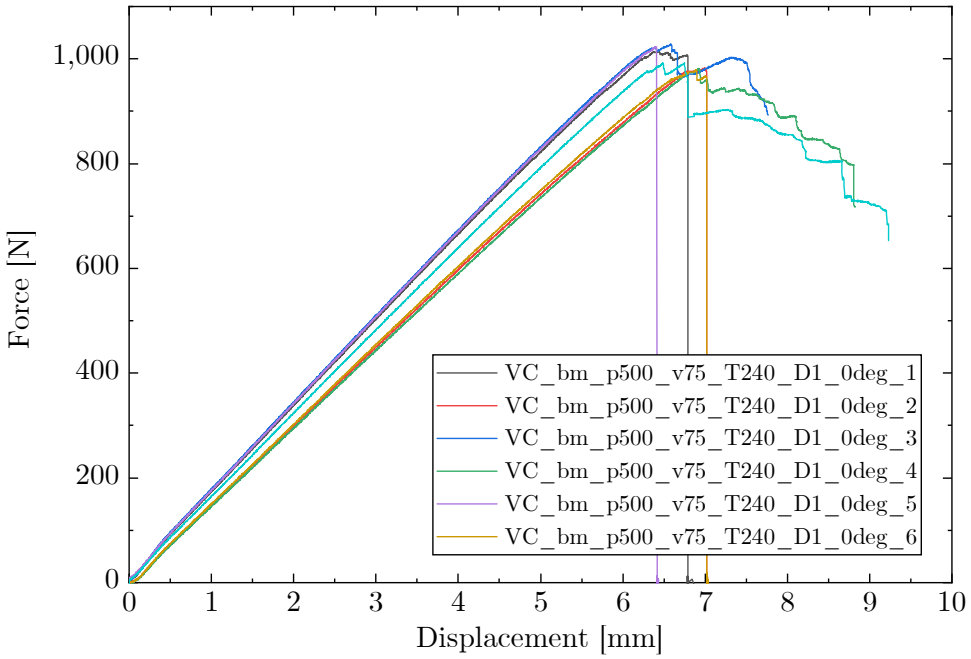

Figure A.7: Stress-strain curves of the VC-oc 4-point-bending samples in 0°-direction.

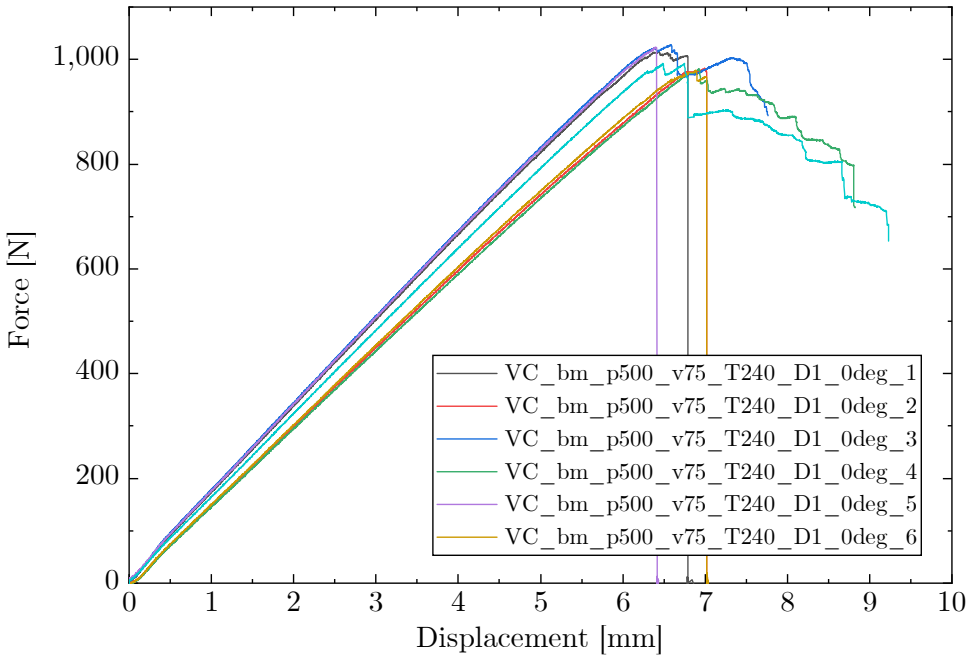

Figure A.8: Stress-strain curves of the VC-bm 4-point-bending samples in 0°-direction.

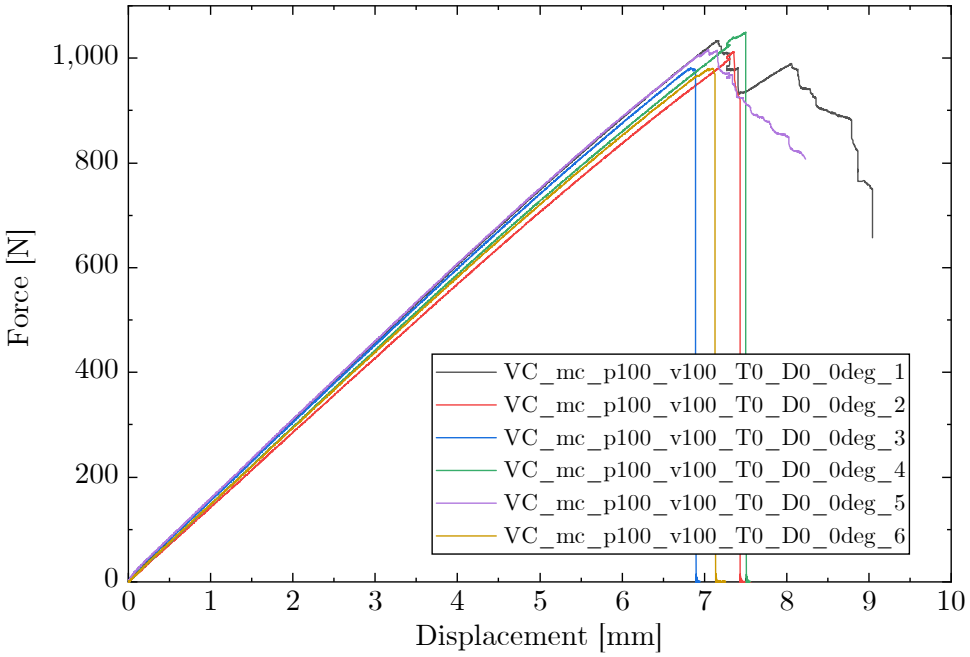

Figure A.9: Stress-strain curves of the VC-mc 4-point-bending samples in 0°-direction.

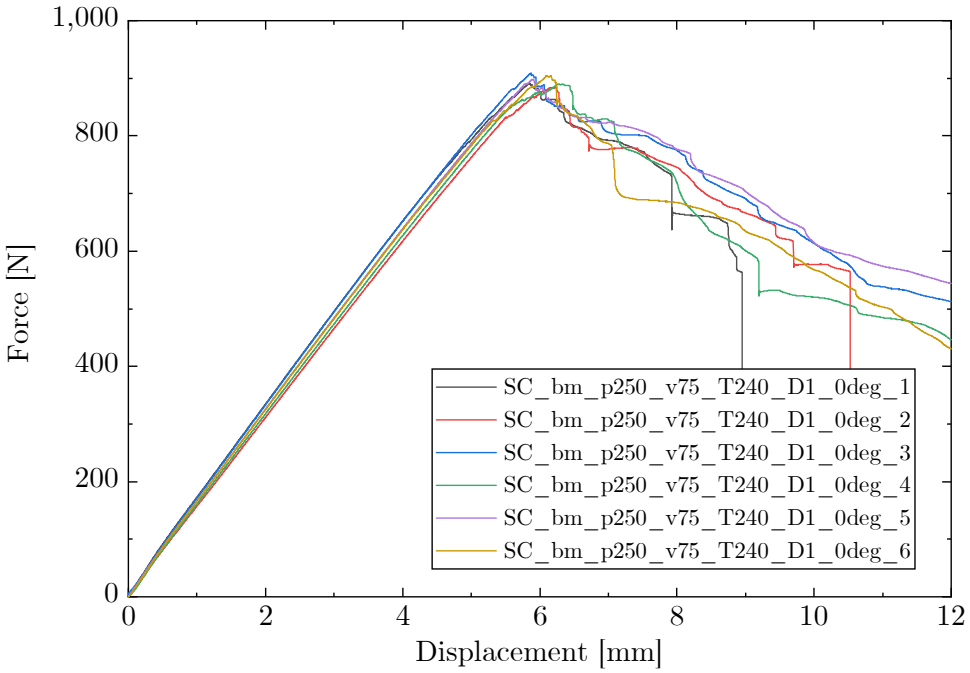

Figure A.10: Stress-strain curves of the SC-oc 4-point-bending samples in 0°-direction.

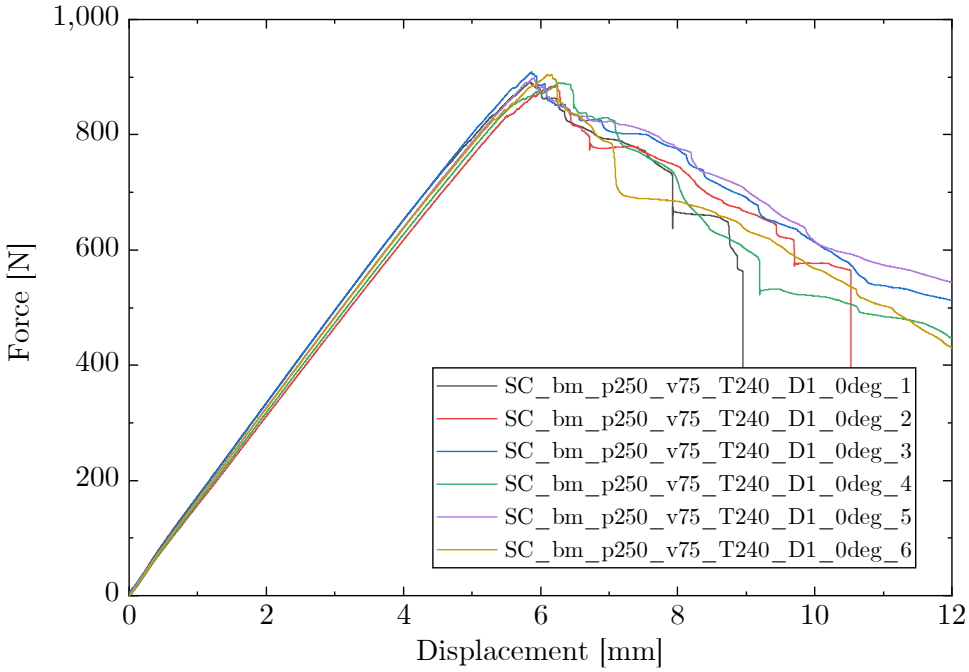

Figure A.11: Stress-strain curves of the SC-bm 4-point-bending samples in 0°-direction.

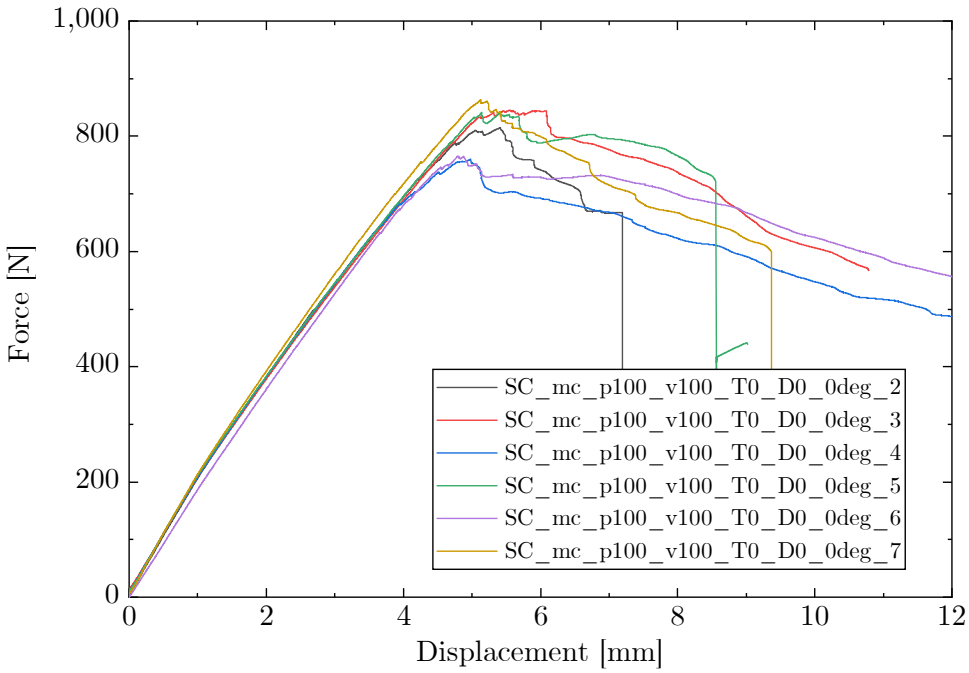

Figure A.12: Stress-strain curves of the SC-mc 4-point-bending samples in 0°-direction.

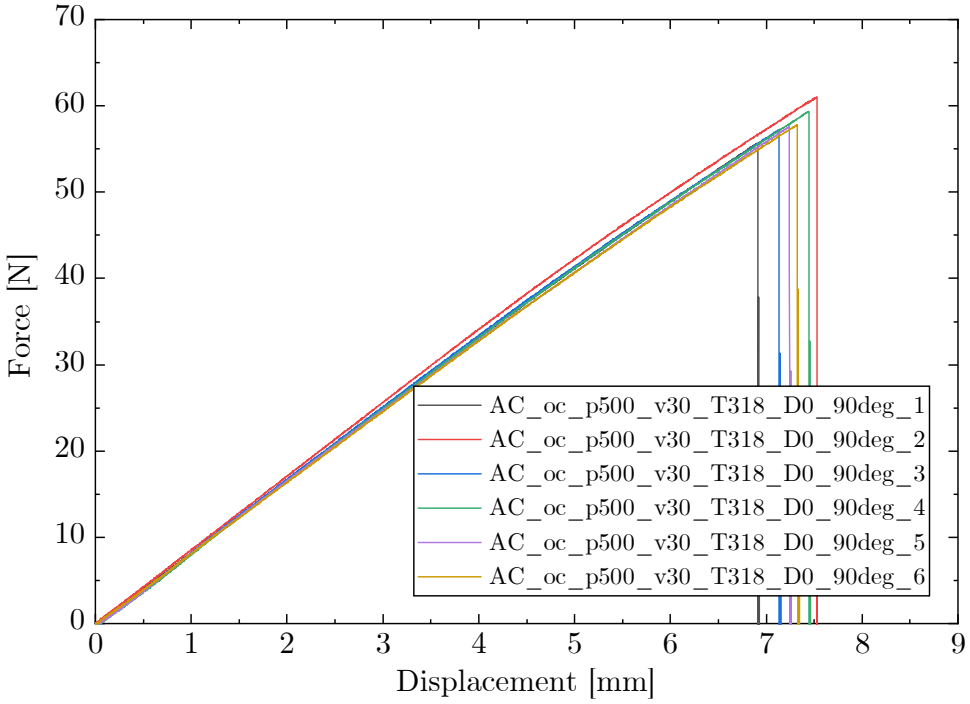

Figure A.13: Stress-strain curves of the AC-oc 4-point-bending samples in 90°-direction.

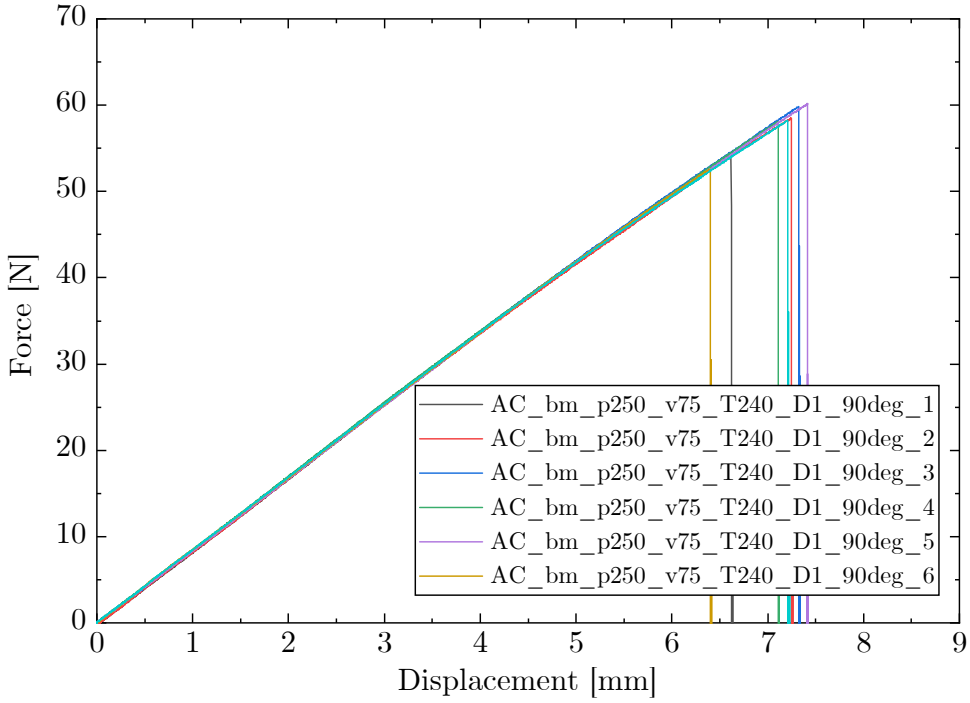

Figure A.14: Stress-strain curves of the AC-bm 4-point-bending samples in 90°-direction.

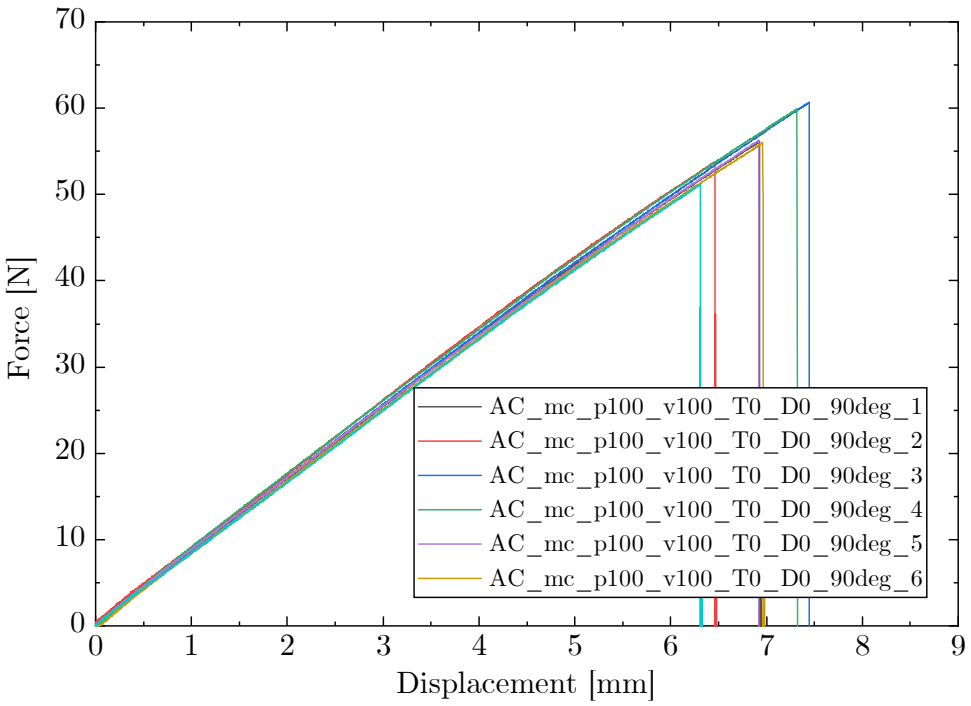

Figure A.15: Stress-strain curves of the AC-mc 4-point-bending samples in 90°-direction.

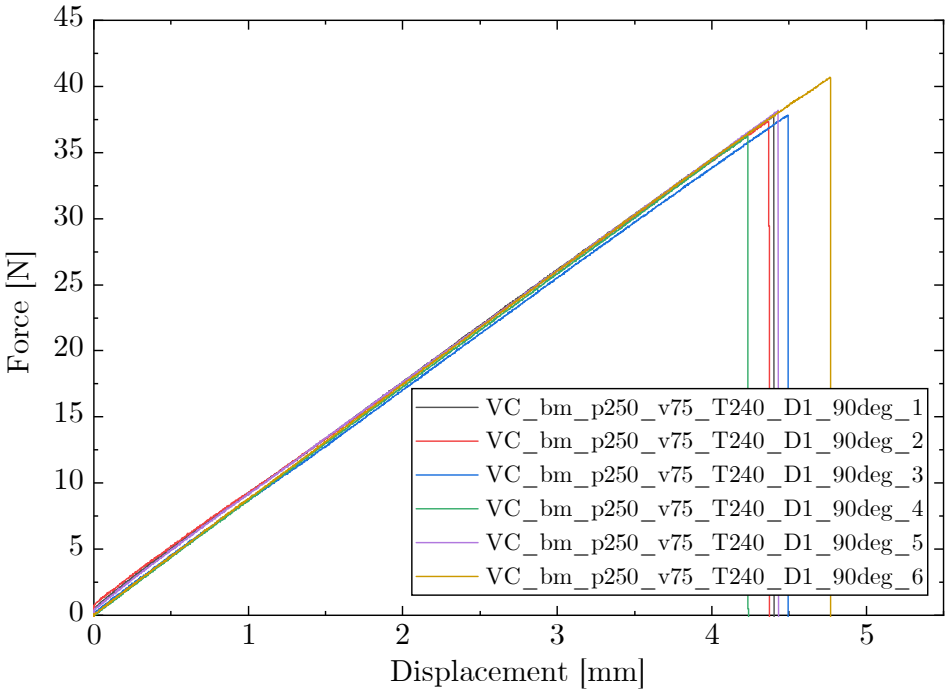

Figure A.16: Stress-strain curves of the VC-oc 4-point-bending samples in 90°-direction.

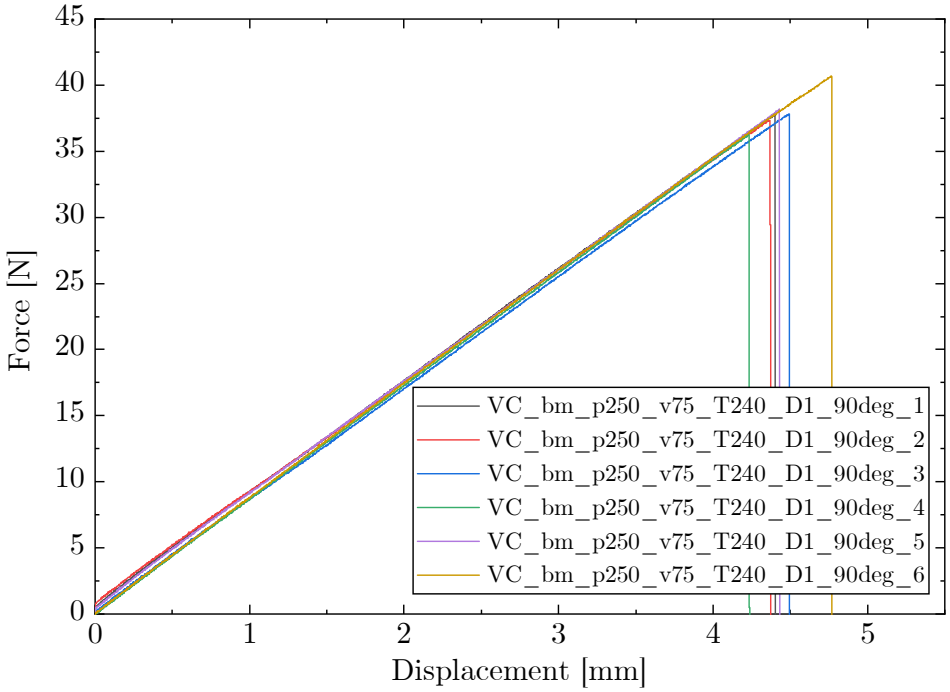

Figure A.17: Stress-strain curves of the VC-bm 4-point-bending samples in 90°-direction.

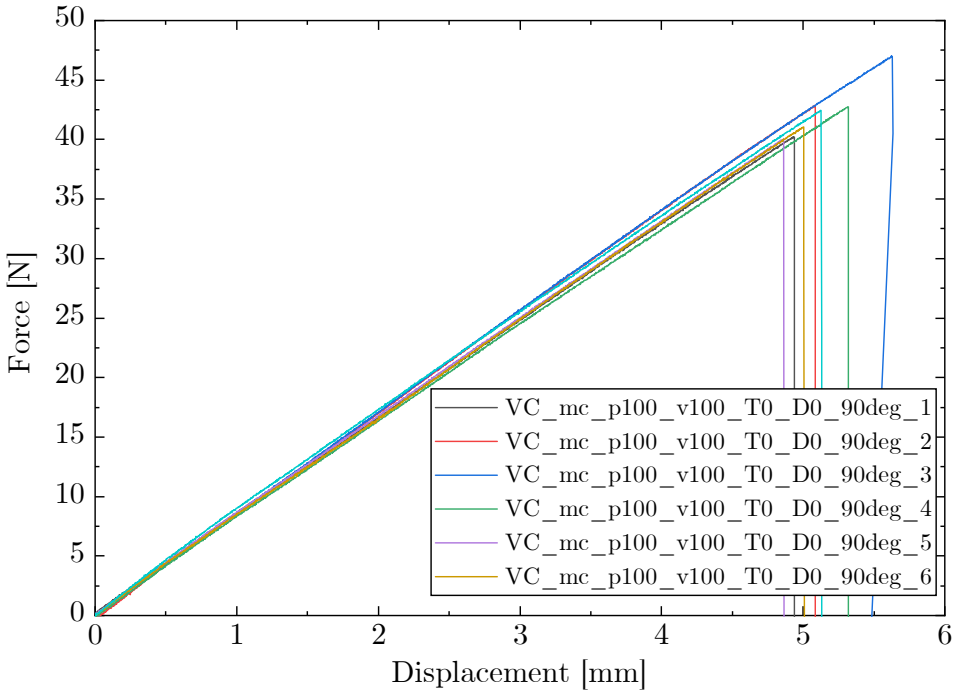

Figure A.18: Stress-strain curves of the VC-mc 4-point-bending samples in 90°-direction.

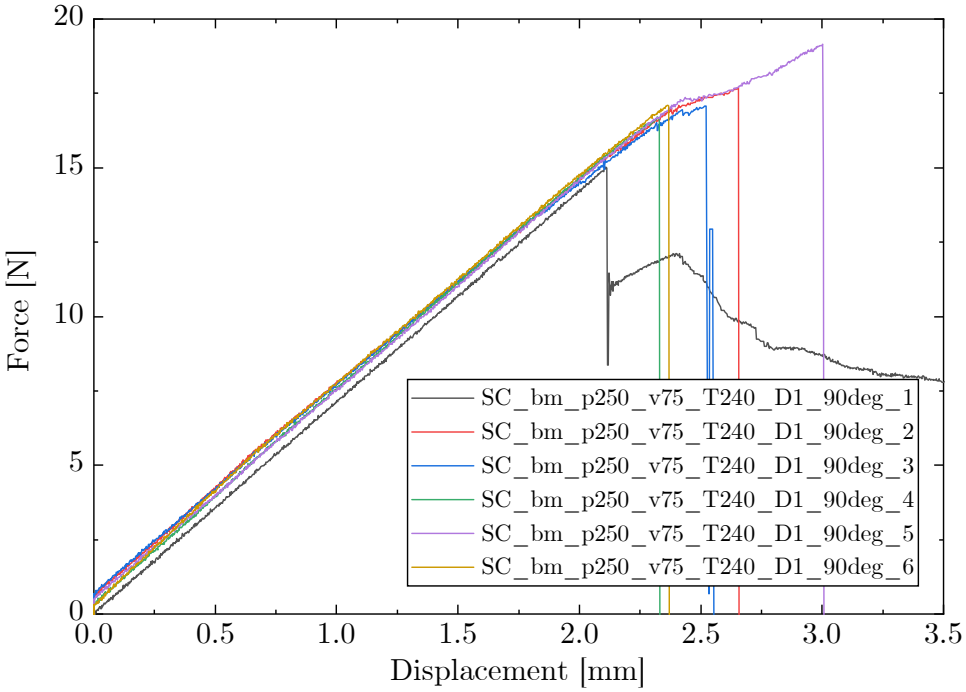

Figure A.19: Stress-strain curves of the SC-oc 4-point-bending samples in 90°-direction.

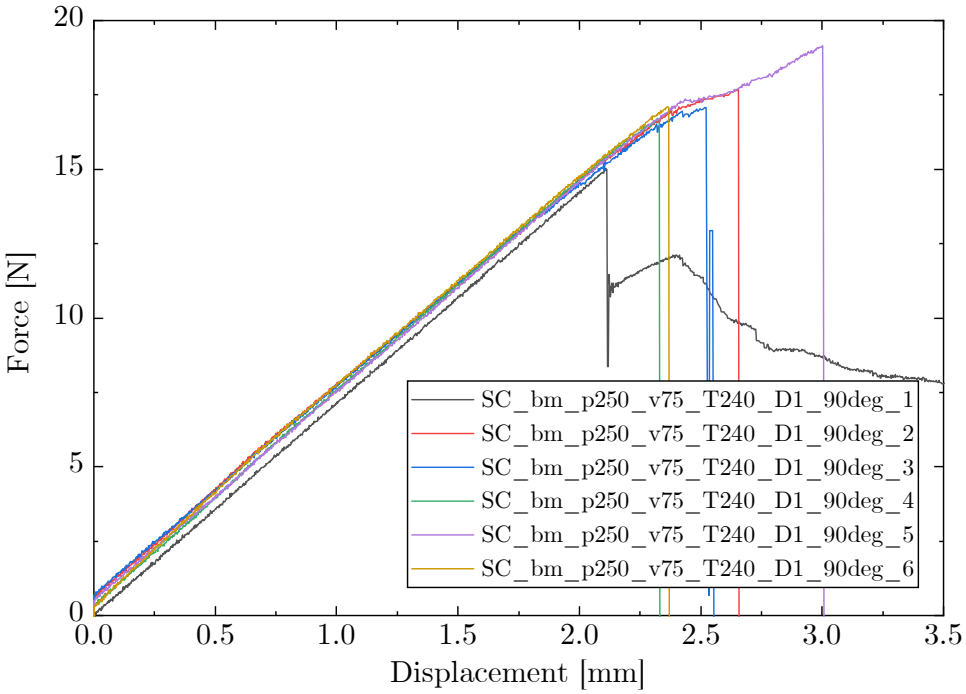

Figure A.20: Stress-strain curves of the SC-bm 4-point-bending samples in 90°-direction.

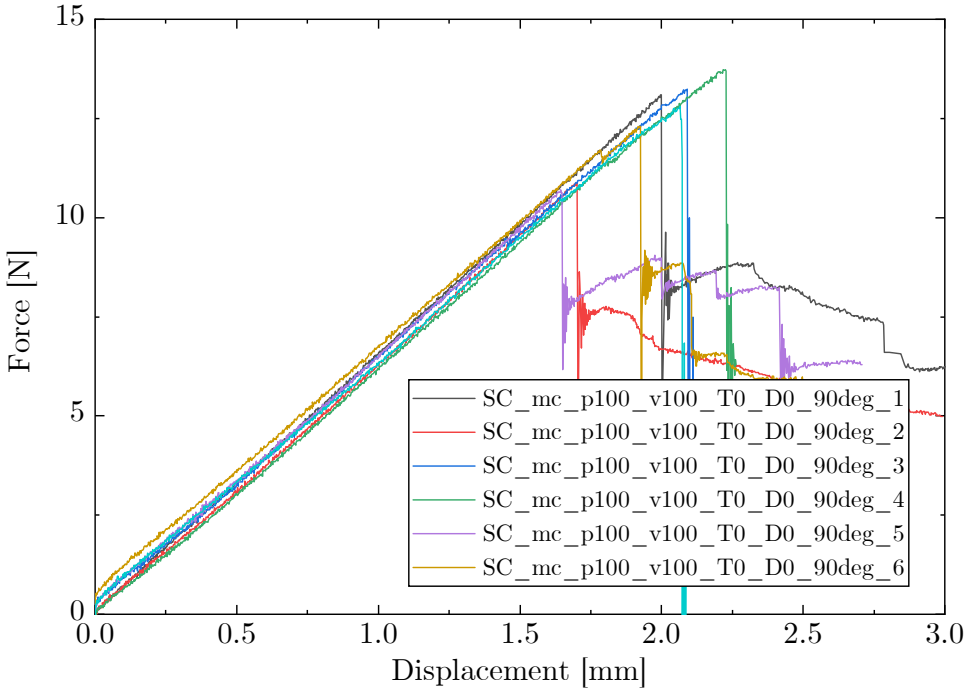

Figure A.21: Stress-strain curves of the SC-mc 4-point-bending samples in 90°-direction.

A.2.2 Interlaminar shear stress tests

Stress-strain graphs of the ILSS tests as part of the material characterization in Sec. 5.2. The graphs listed below are accompanying the result discussion in Sec. 5.2.2, emphasizing the linear elastic behavior. The graphs are referred to in Sec. 5.2.2.

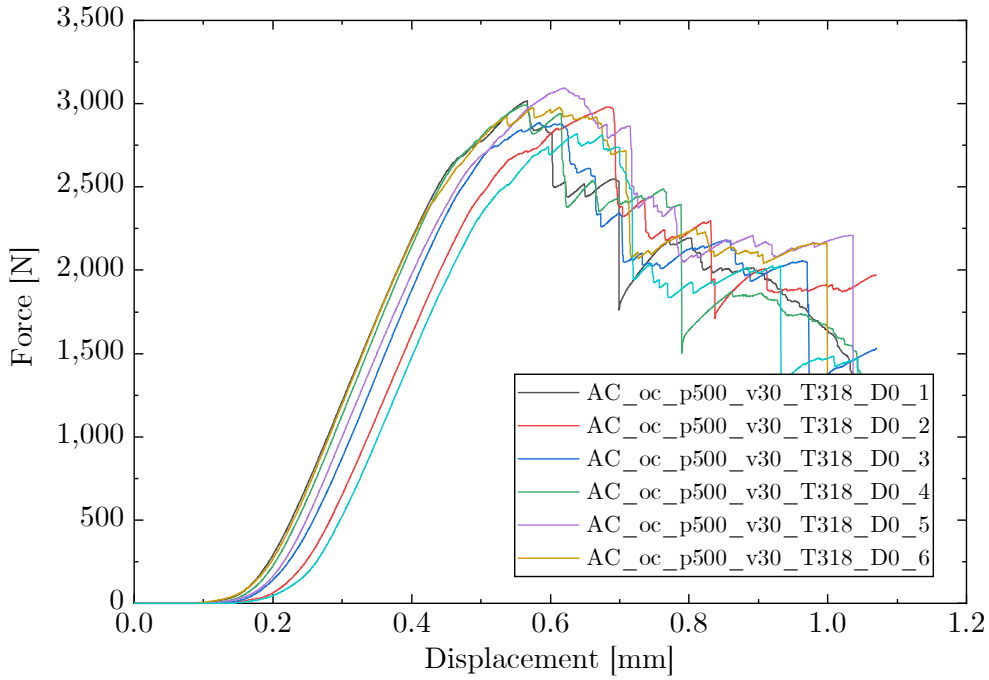

Figure A.22: Stress-strain curves of the AC-oc ILSS samples.

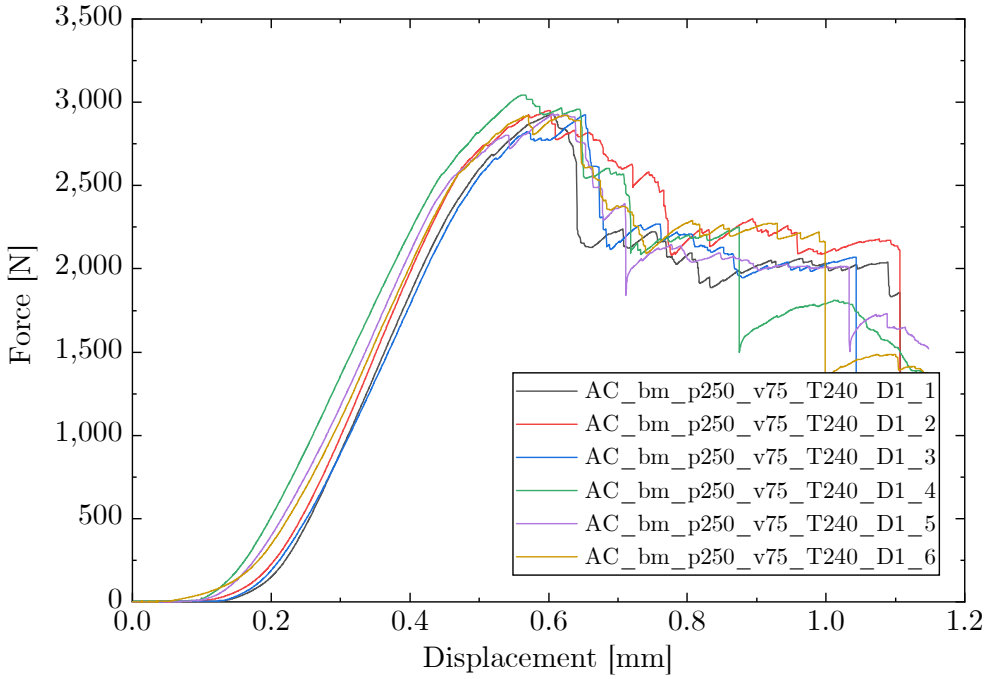

Figure A.23: Stress-strain curves of the AC-bm ILSS samples.

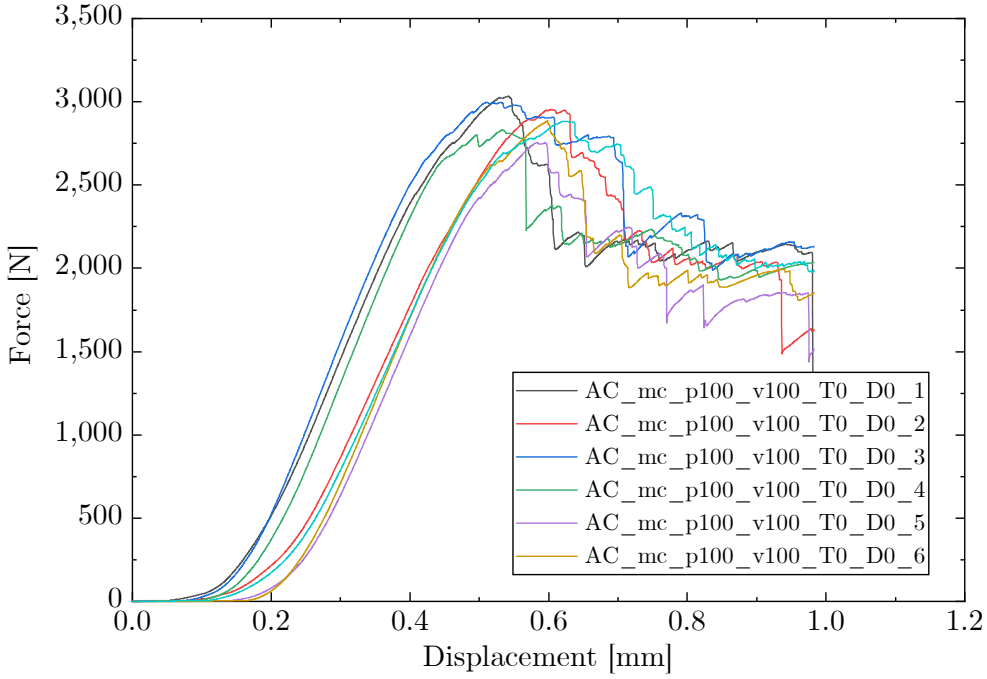

Figure A.24: Stress-strain curves of the AC-mc ILSS samples.

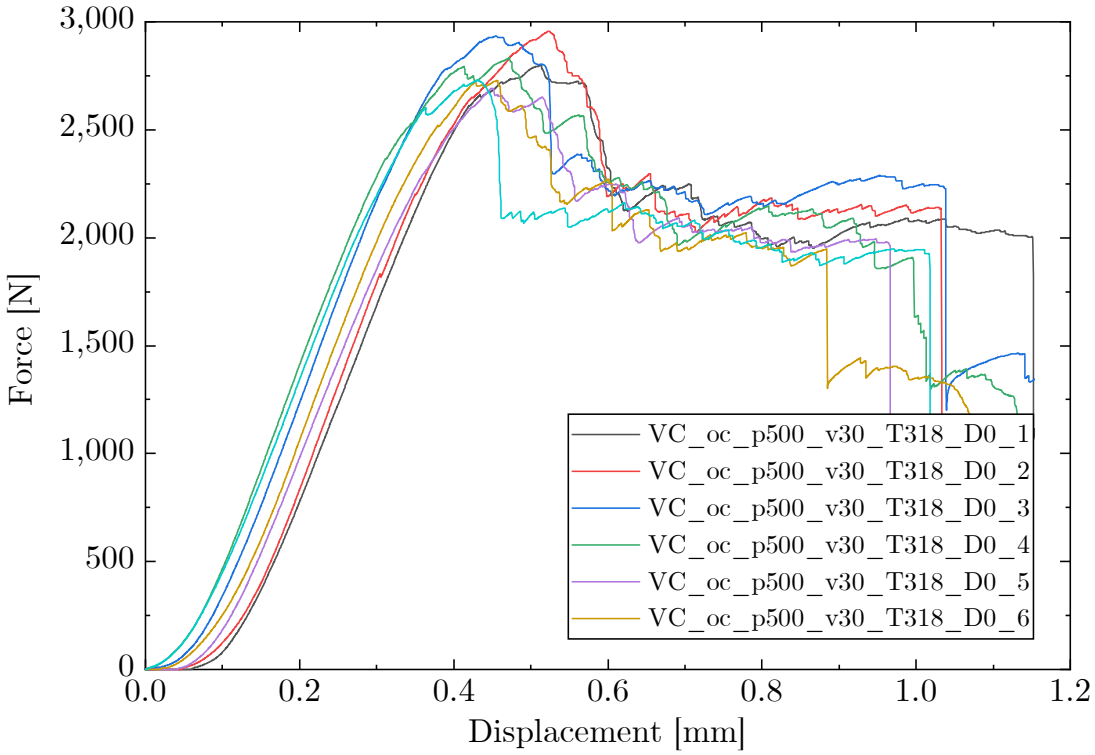

Figure A.25: Stress-strain curves of the VC-oc ILSS samples.

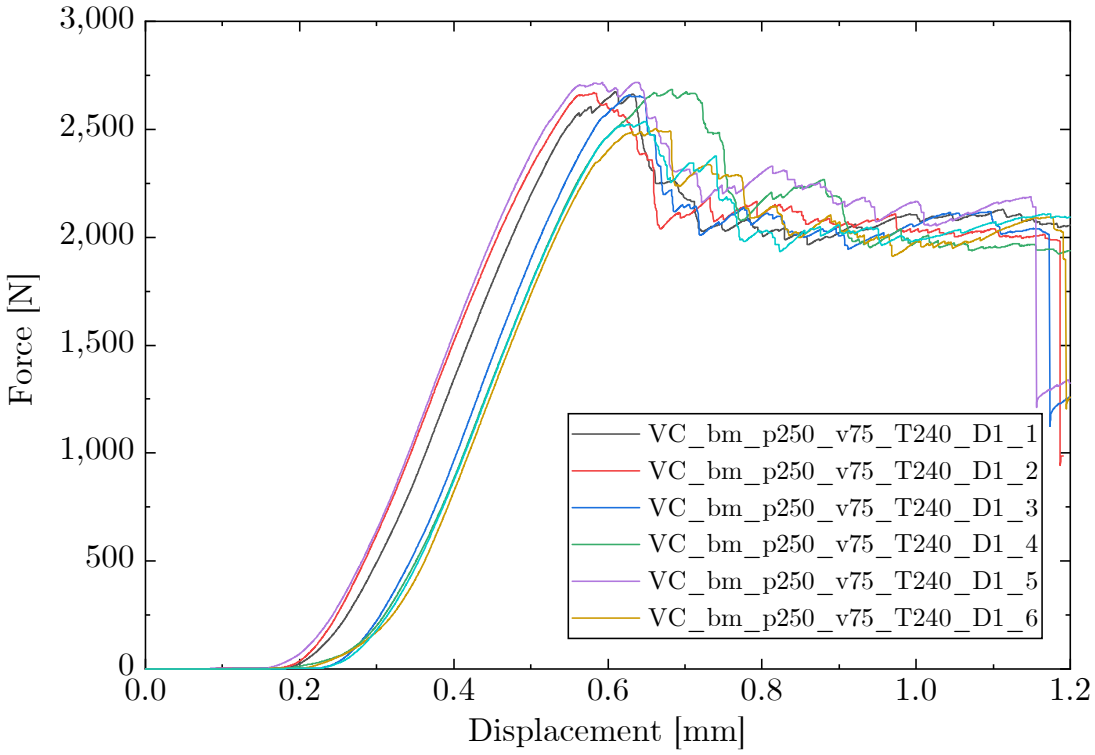

Figure A.26: Stress-strain curves of the VC-bm ILSS samples.

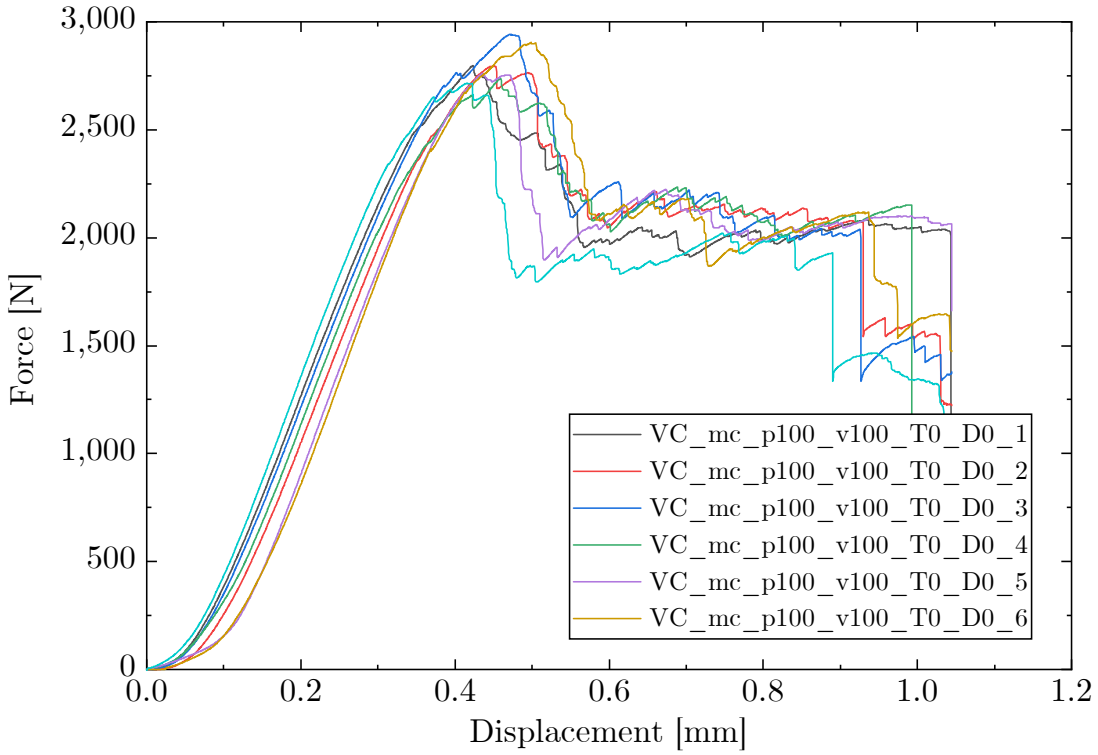

Figure A.27: Stress-strain curves of the VC-mc ILSS samples.

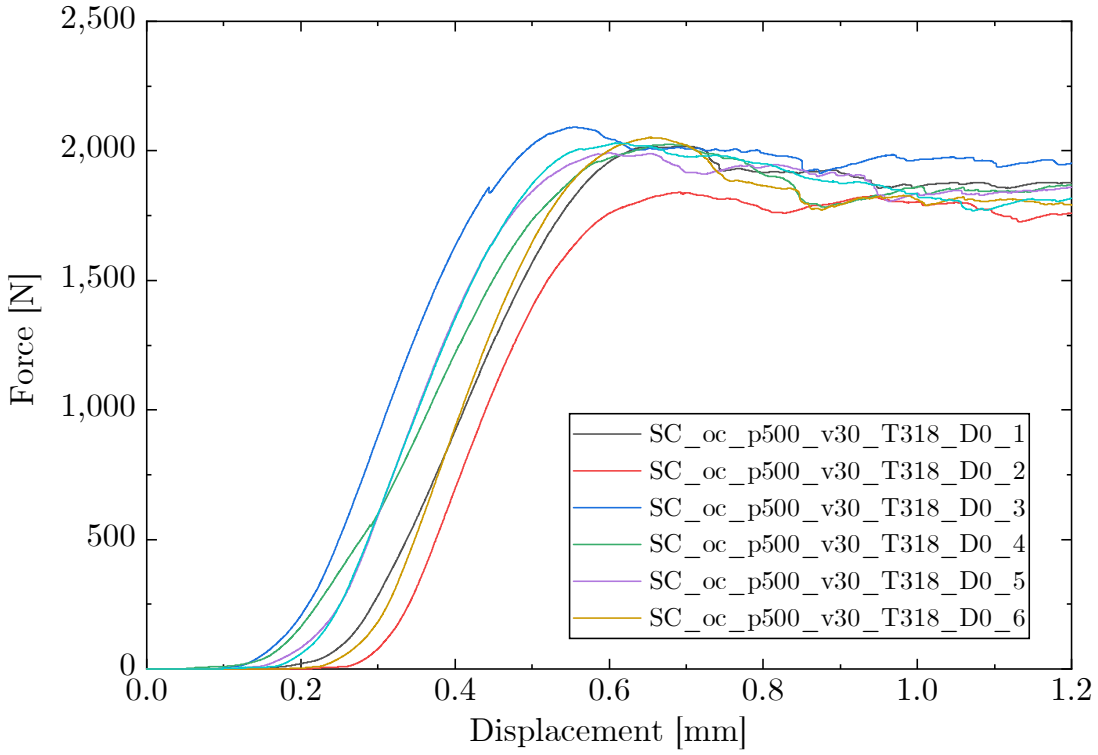

Figure A.28: Stress-strain curves of the SC-oc ILSS samples.

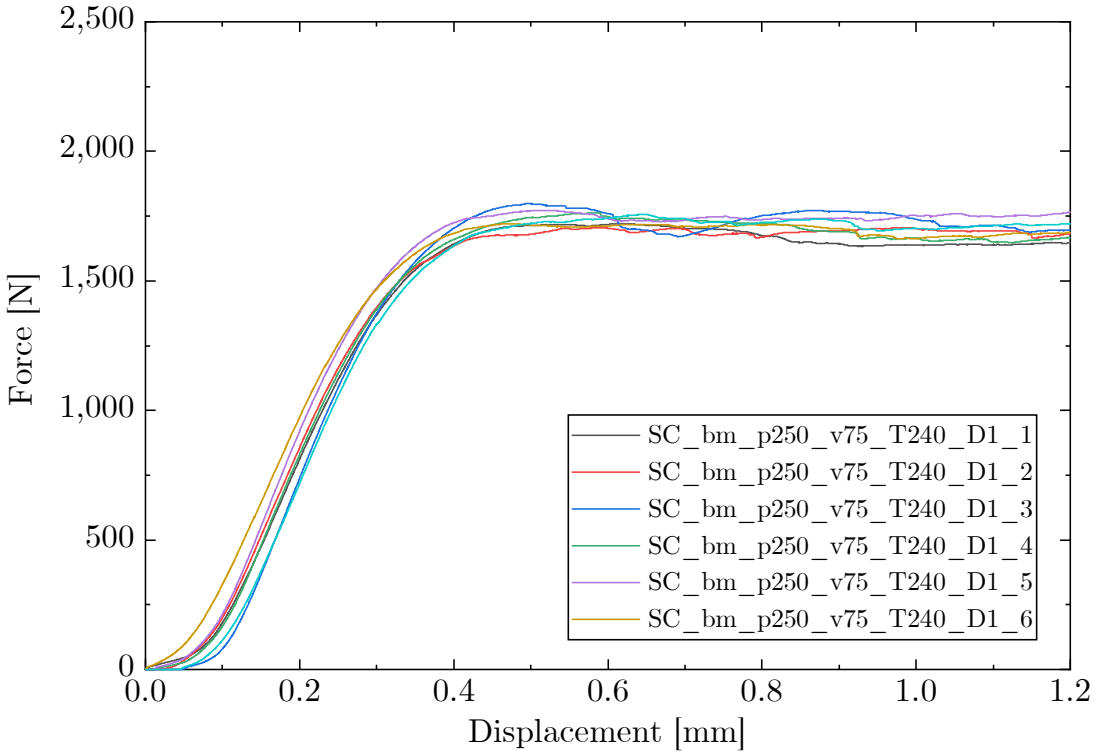

Figure A.29: Stress-strain curves of the SC-bm ILSS samples.

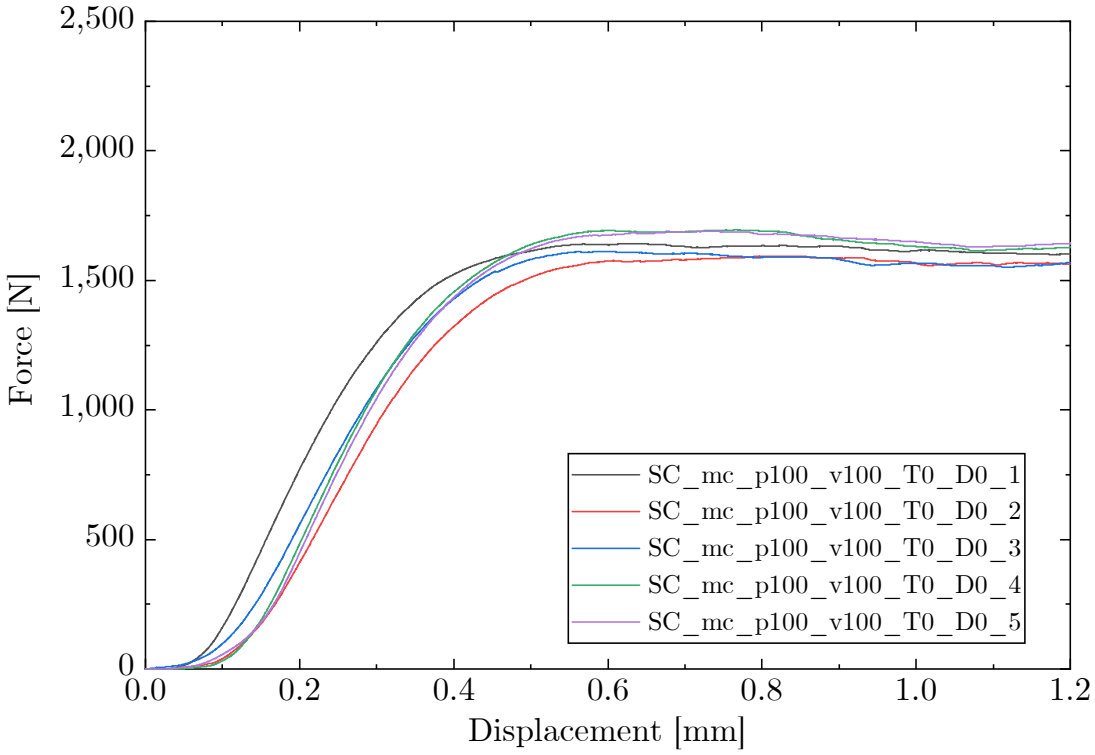

Figure A.30: Stress-strain curves of the SC-mc ILSS samples.

A.3 Normalized results of the 4-point bending test

The normalized results below accompany the result interpretation in Sec. 5.2. The graphs are referenced to in Sec. 5.2.2. In general, the FAW can be assumed constant for the flat prepreg samples for the given processing conditions. The different curing methods showed different bleeding behaviors. In the autoclave, the high pressure and temperature led to intense bleeding. With vacuum pressure only, the bleeding behavior was reduced. During soft curing, the lack of pressure led to almost no bleeding. Thus, the three different curing methods can lead to a difference in the FVC. The results were normalized to estimate the influence of this effect, but showed no significant difference to the non-normalized values and no clear trend in their difference. This indicates, that the effect of the differing FVC is negligible for the interpretation of this set of experiments. [160]

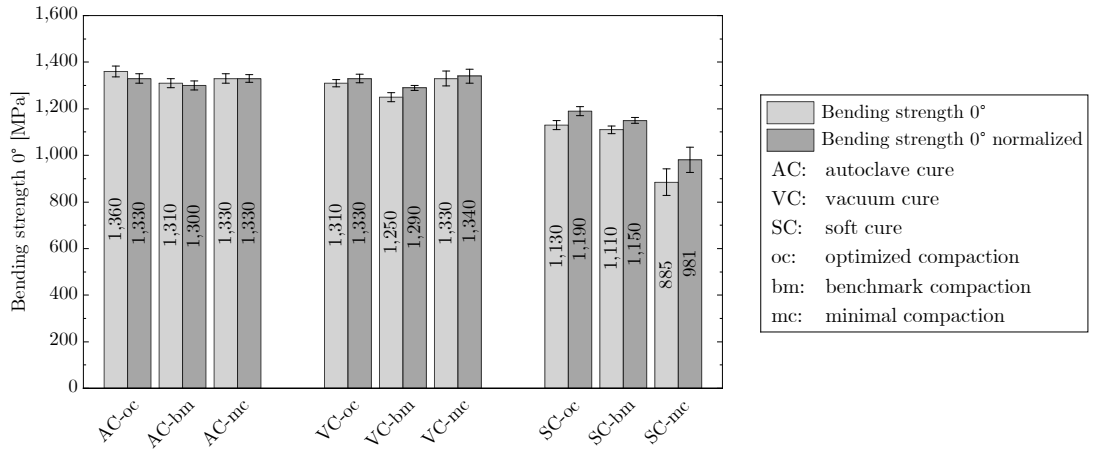

Figure A.31: Normalized bending strength in 0°-direction based on the 4-point bending test.

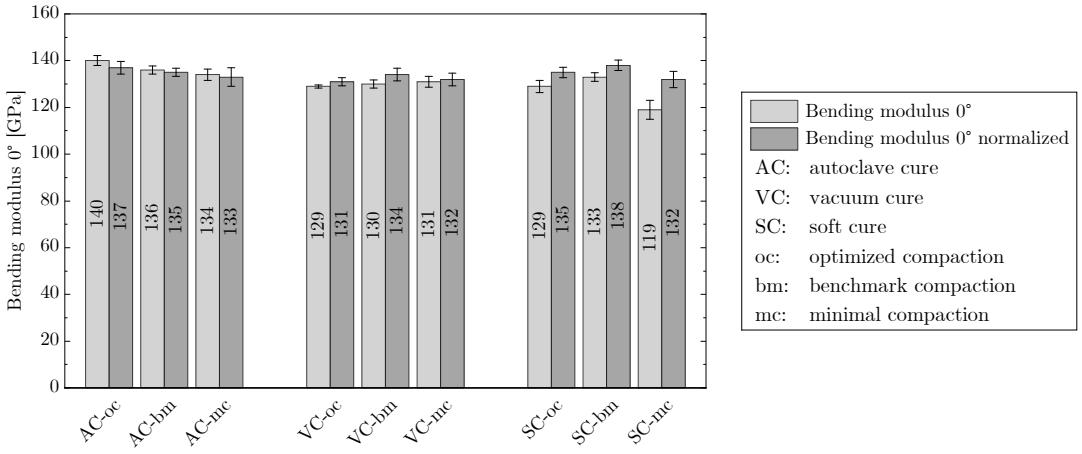

Figure A.32: Normalized bending modulus in 0°-direction based on the 4-point bending test.

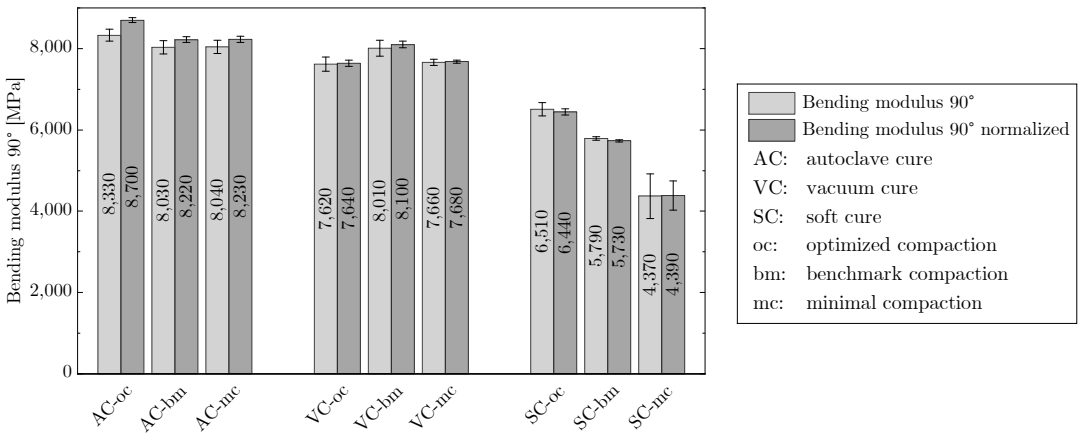

Figure A.33: Normalized bending modulus in 90°-direction based on the 4-point bending test.

A.4 Micrographs and micro CT scans

A.4.1 Micrographs of the UTM compaction experiments

a) Baseline (low pressure, low temperature, no debulking, UD)

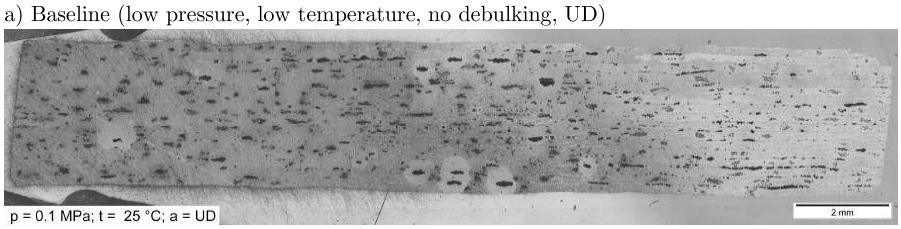

b) Temperature main effect (low pressure, high temperature, no debulking, UD)

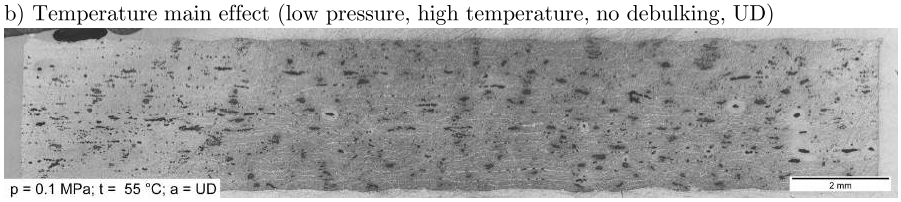

c) Debulking main effect (low pressure, low temperature, debulking, UD)

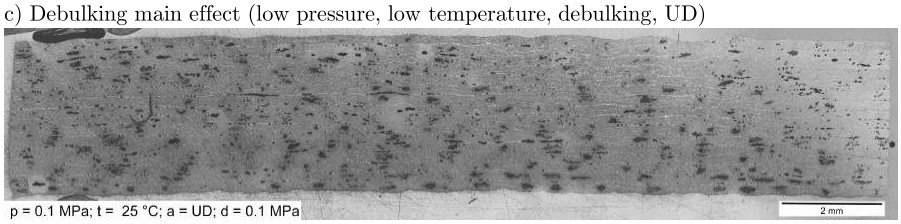

b) Pressure main effect (high pressure, low temperature, no debulking, UD)

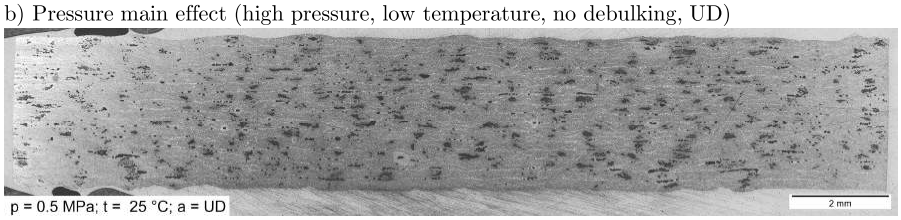

Figure A.34: Micrographs of the UTM compaction study showing different main effects of single parameter variations.

A.4.2 Micro CT scans of the mechanical characterization experiments

Micro CT scans of the samples in Sec. 5.2 were reconstructed to 3D images and cut in slices with x-, y- and z-direction. The z-slices cut the images perpendicular to the UD fibers. Fig. 5.22 in Sec. 5.2.2 shows z-slices of all samples and gives an overview on their homogeneity and porosity. X- and y-slices are listed below.

Figure A.35: Micro CT scans of the AC-oc samples – longitudinal X-slices.

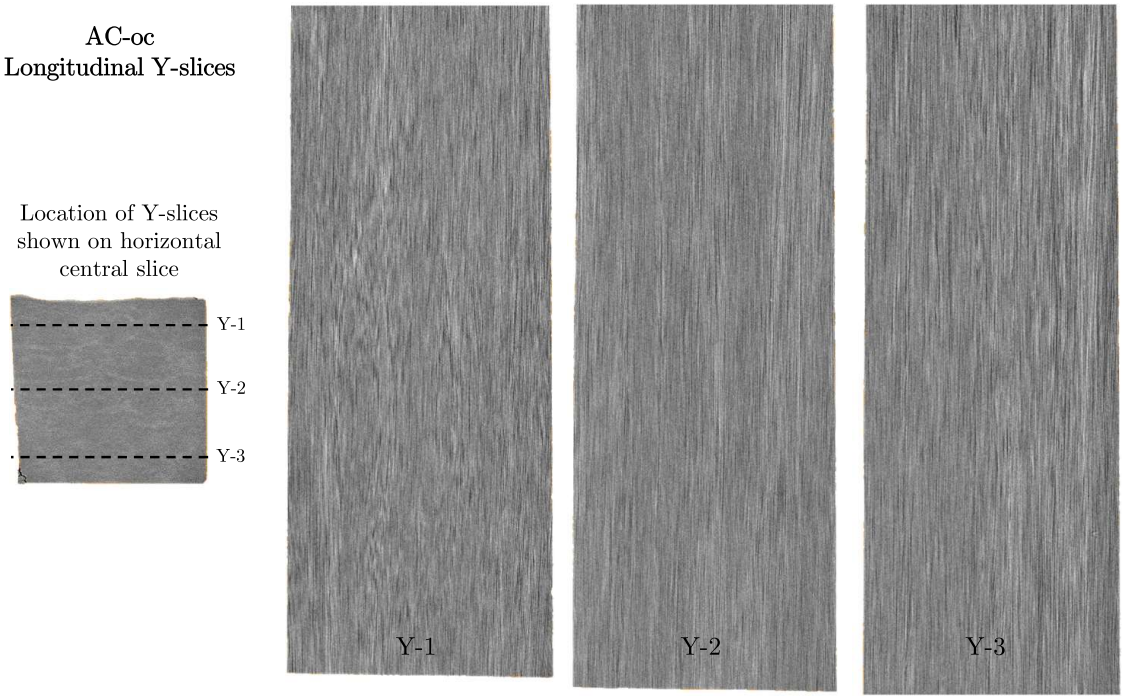

Figure A.36: Micro CT scans of the AC-oc samples – longitudinal Y-slices.

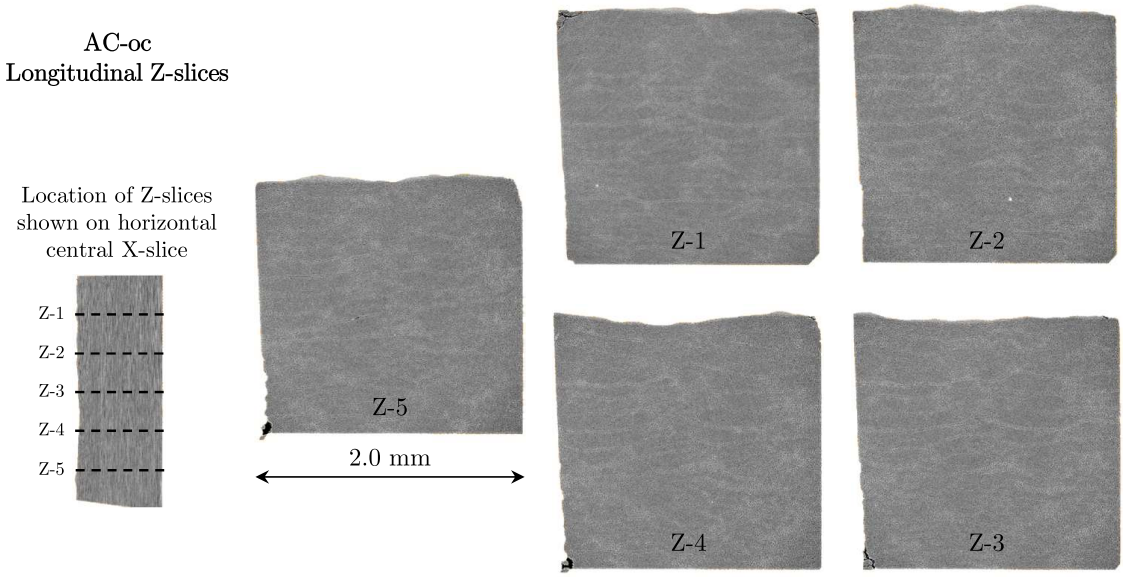

Figure A.37: Micro CT scans of the AC-oc samples – longitudinal Z-slices.

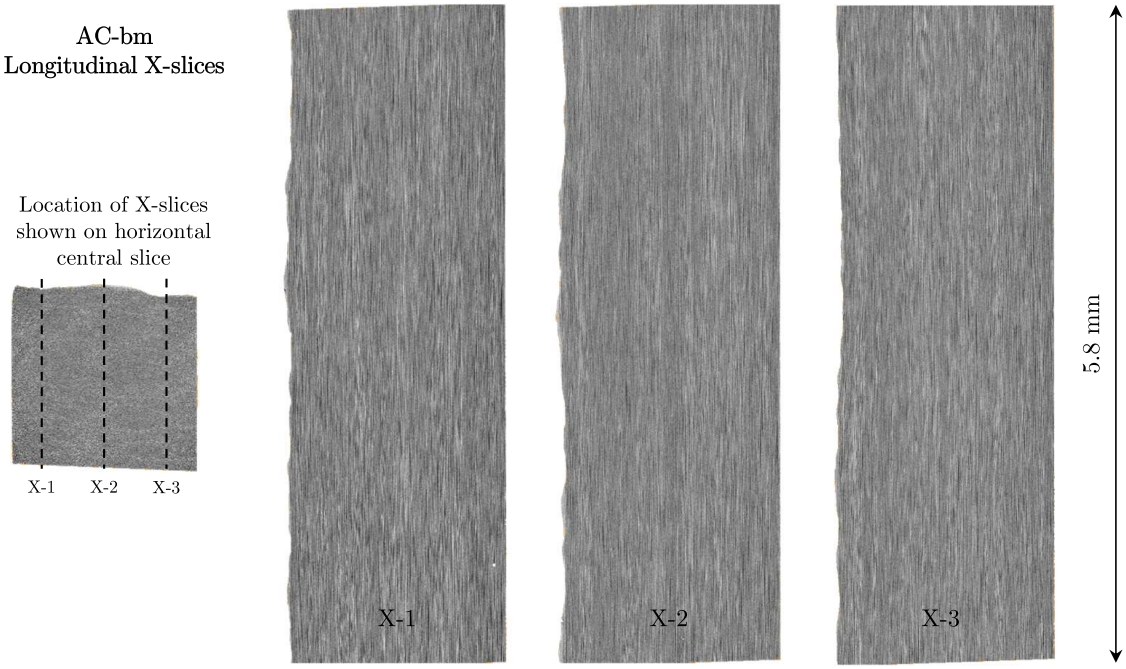

Figure A.38: Micro CT scans of the AC-bm samples – longitudinal X-slices.

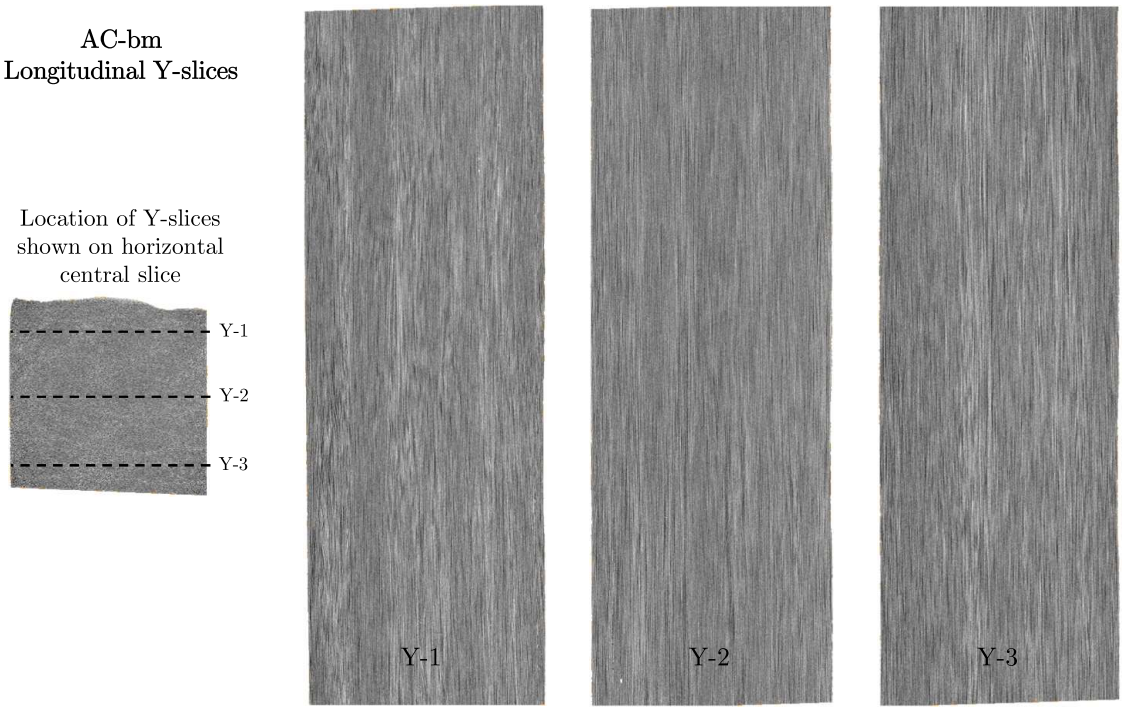

Figure A.39: Micro CT scans of the AC-bm samples – longitudinal Y-slices.

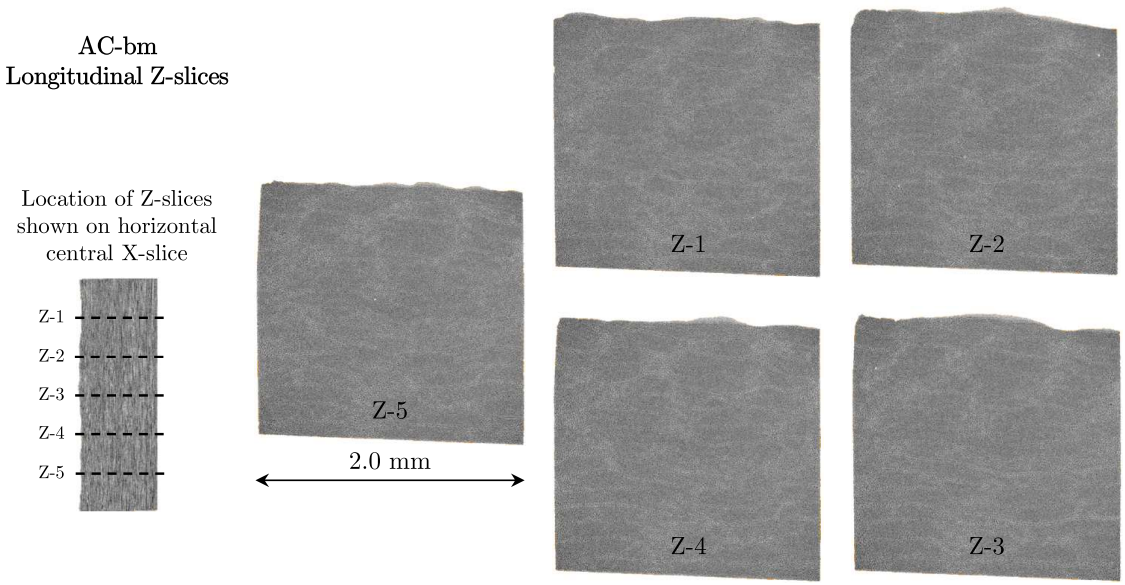

Figure A.40: Micro CT scans of the AC-bm samples – longitudinal Z-slices.

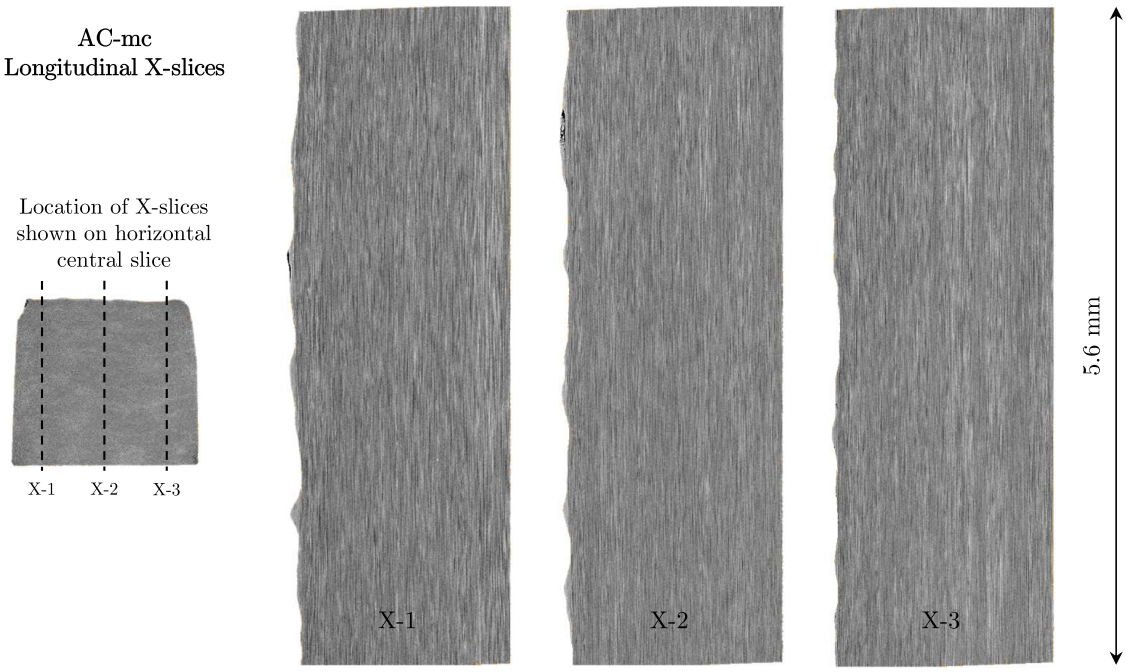

Figure A.41: Micro CT scans of the AC-mc samples – longitudinal X-slices.

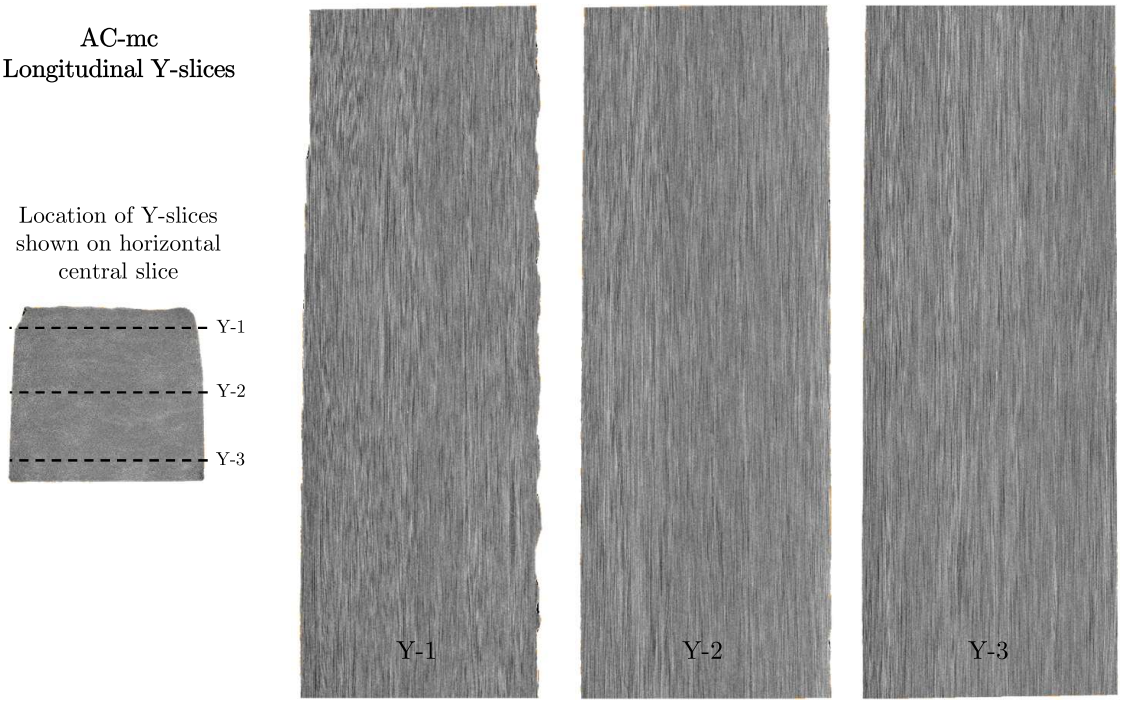

Figure A.42: Micro CT scans of the AC-mc samples – longitudinal Y-slices.

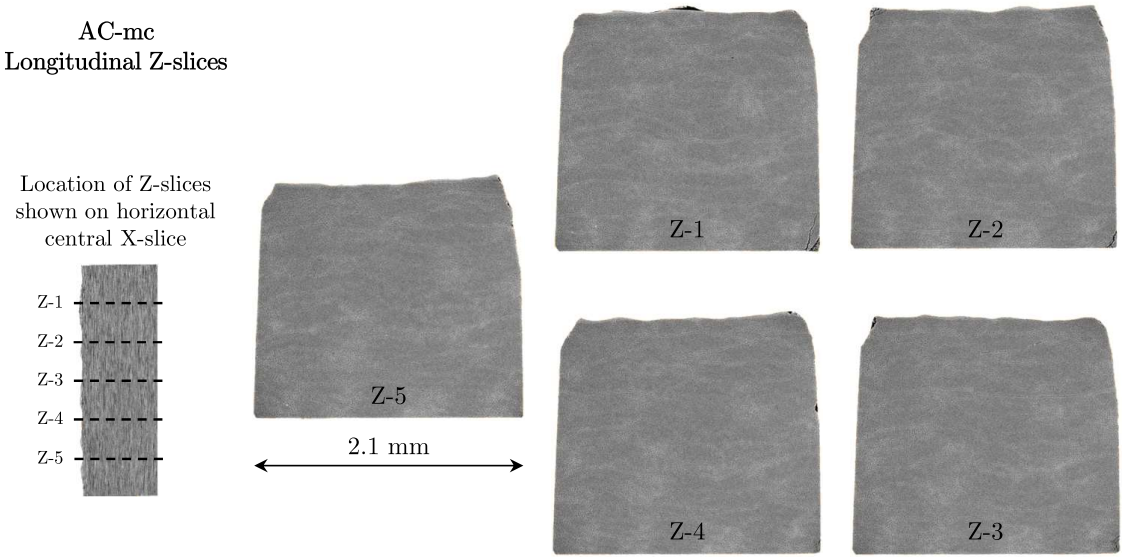

Figure A.43: Micro CT scans of the AC-mc samples – longitudinal Z-slices.

Figure A.44: Micro CT scans of the VC-oc samples – longitudinal X-slices.

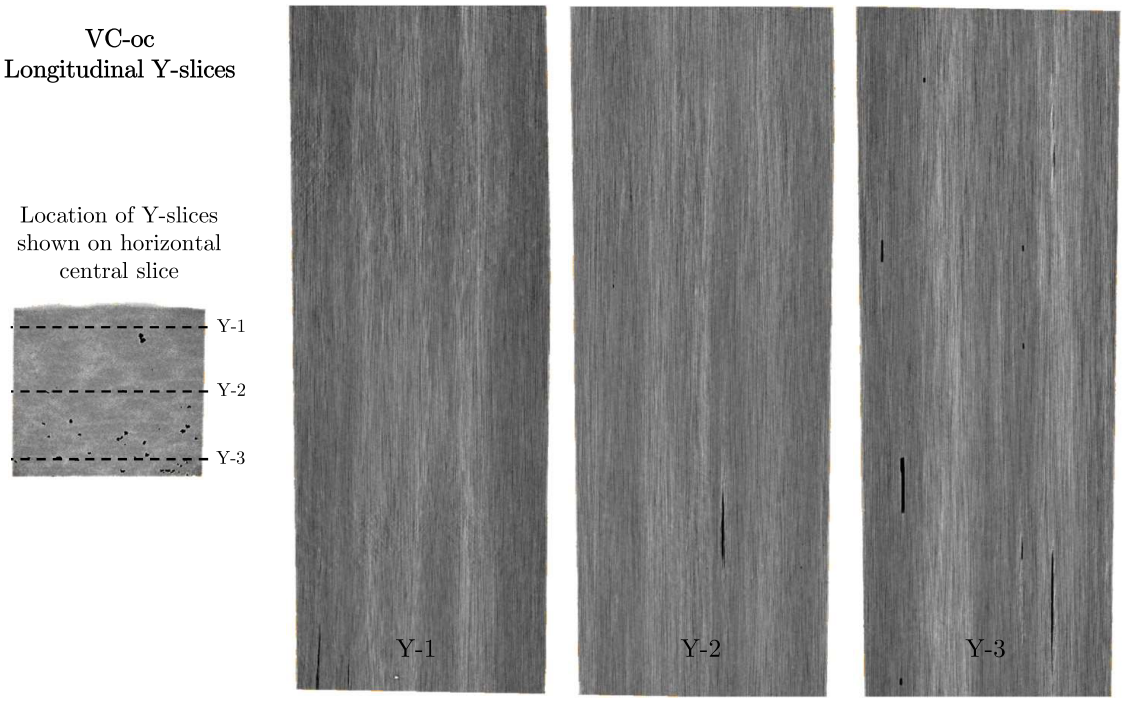

Figure A.45: Micro CT scans of the VC-oc samples – longitudinal Y-slices.

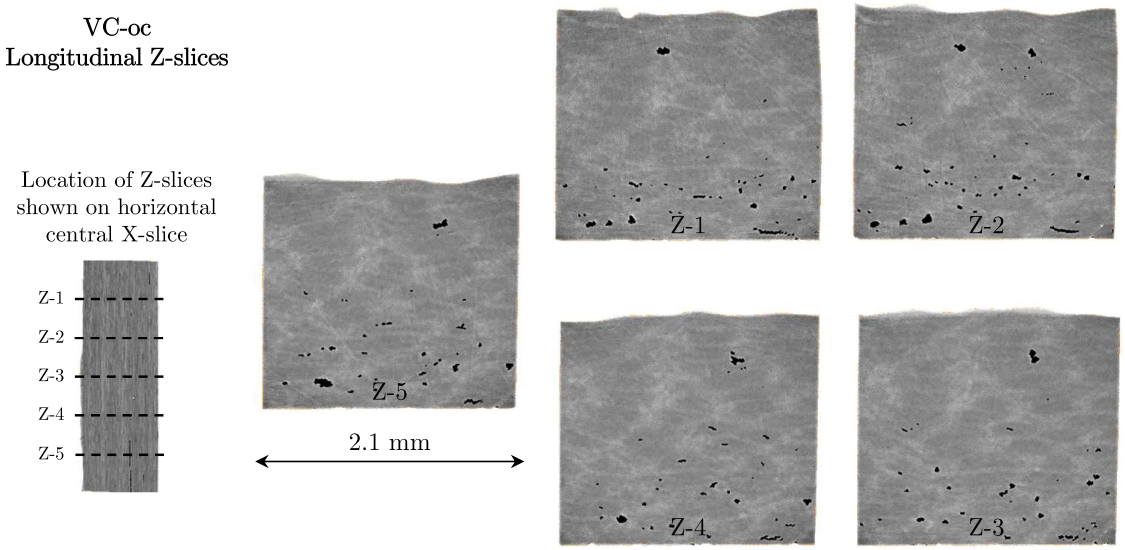

Figure A.46: Micro CT scans of the VC-oc samples – longitudinal Z-slices.

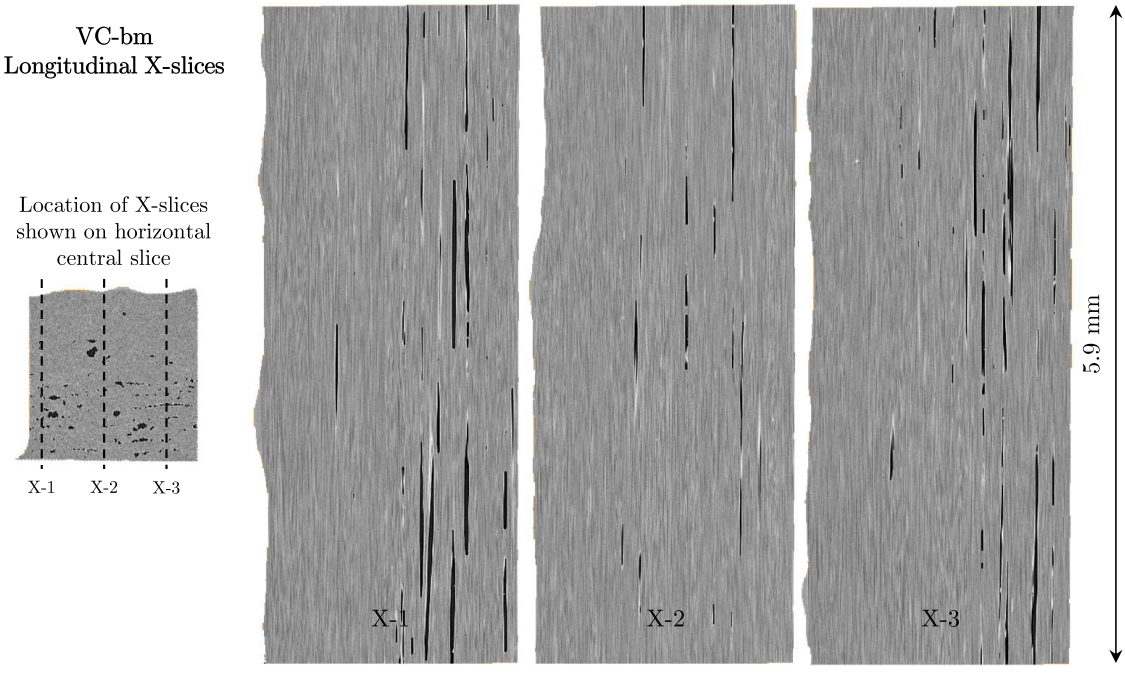

Figure A.47: Micro CT scans of the VC-bm samples – longitudinal X-slices.

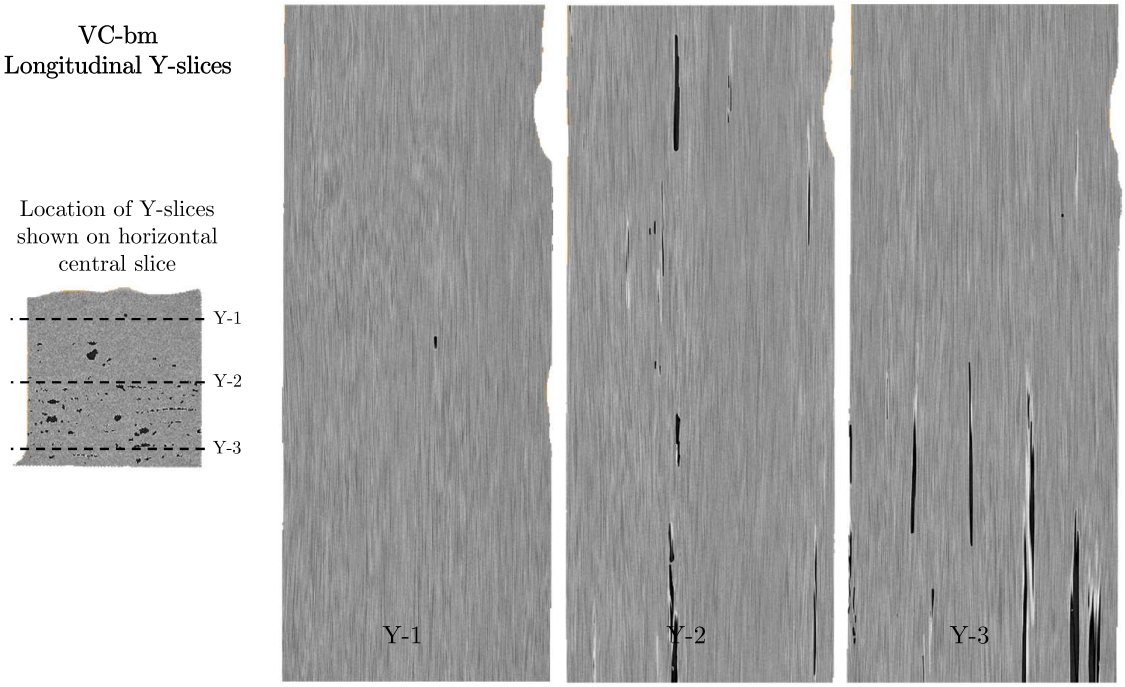

Figure A.48: Micro CT scans of the VC-bm samples – longitudinal Y-slices.

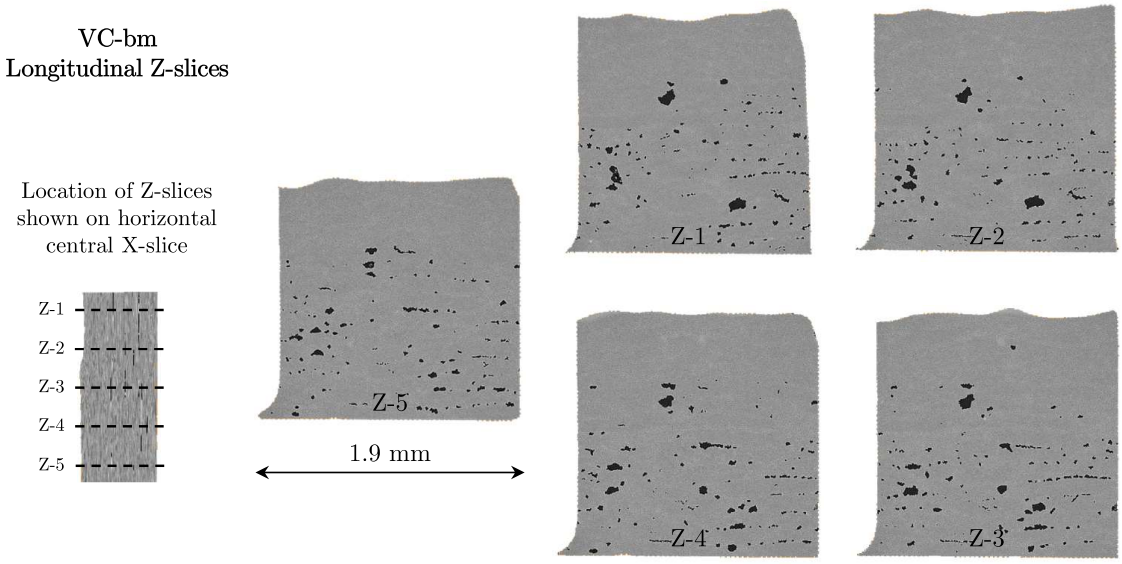

Figure A.49: Micro CT scans of the VC-bm samples – longitudinal Z-slices.

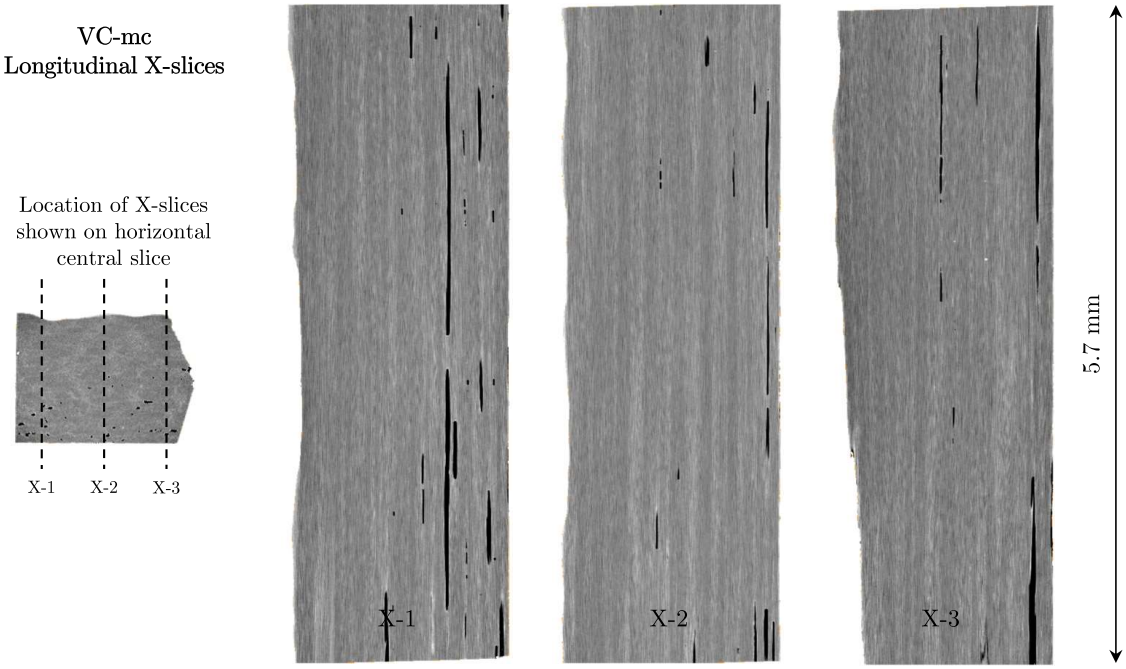

Figure A.50: Micro CT scans of the VC-mc samples – longitudinal X-slices.

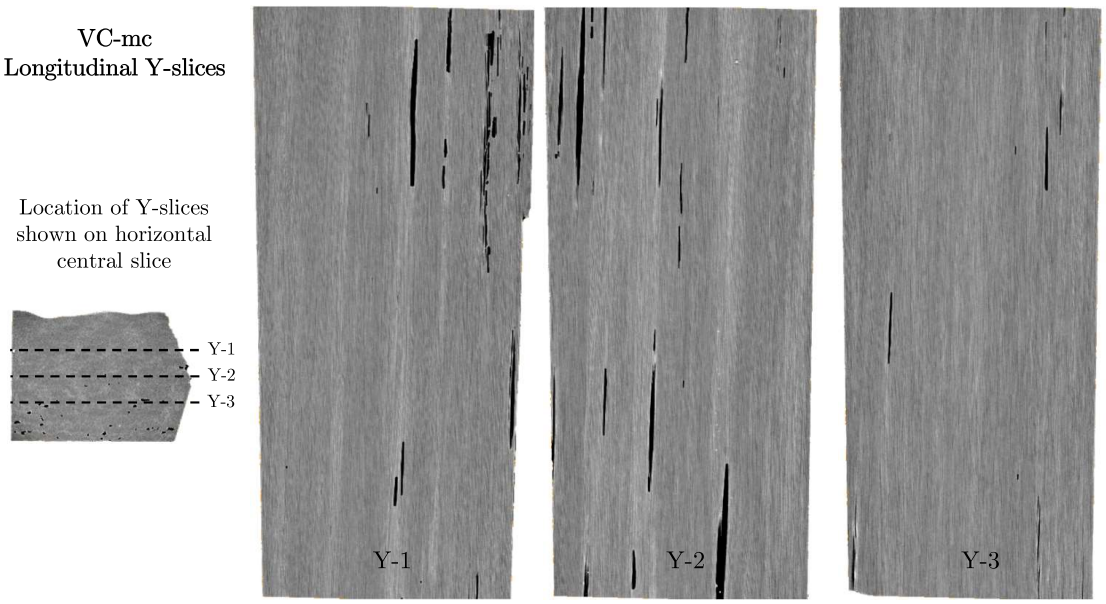

Figure A.51: Micro CT scans of the VC-mc samples – longitudinal Y-slices.

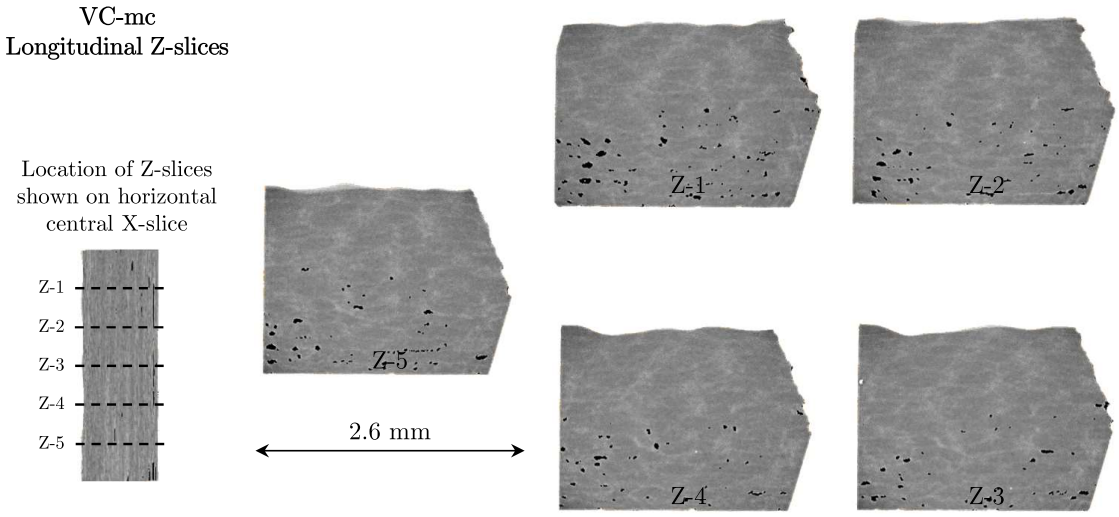

Figure A.52: Micro CT scans of the VC-mc samples – longitudinal Z-slices.

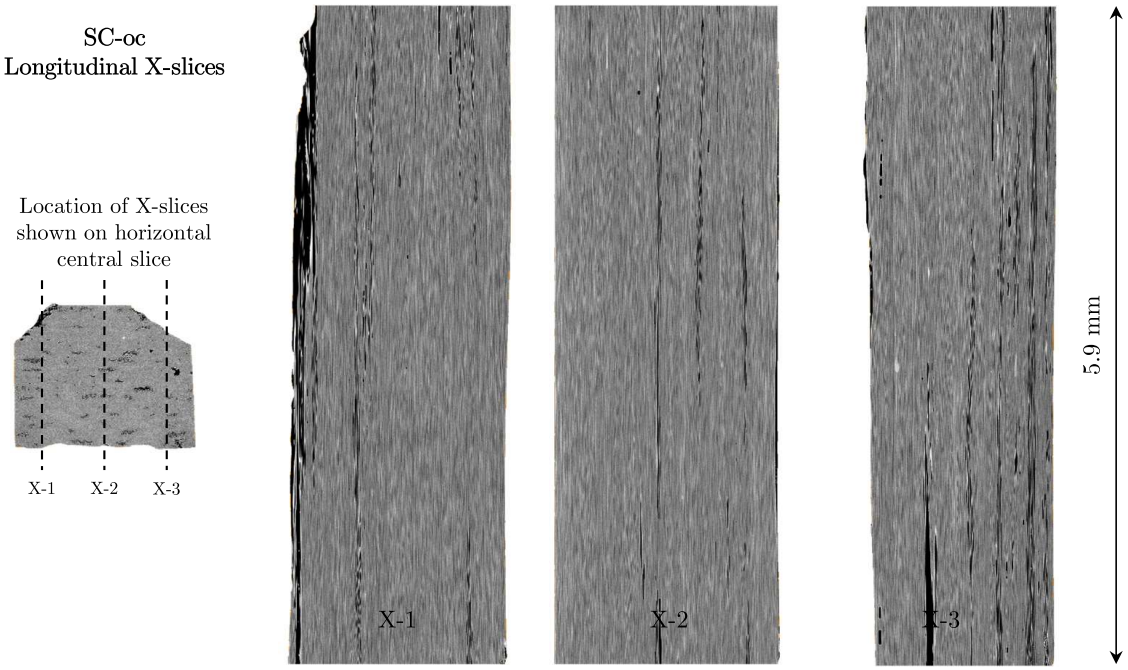

Figure A.53: Micro CT scans of the SC-oc samples – longitudinal X-slices.

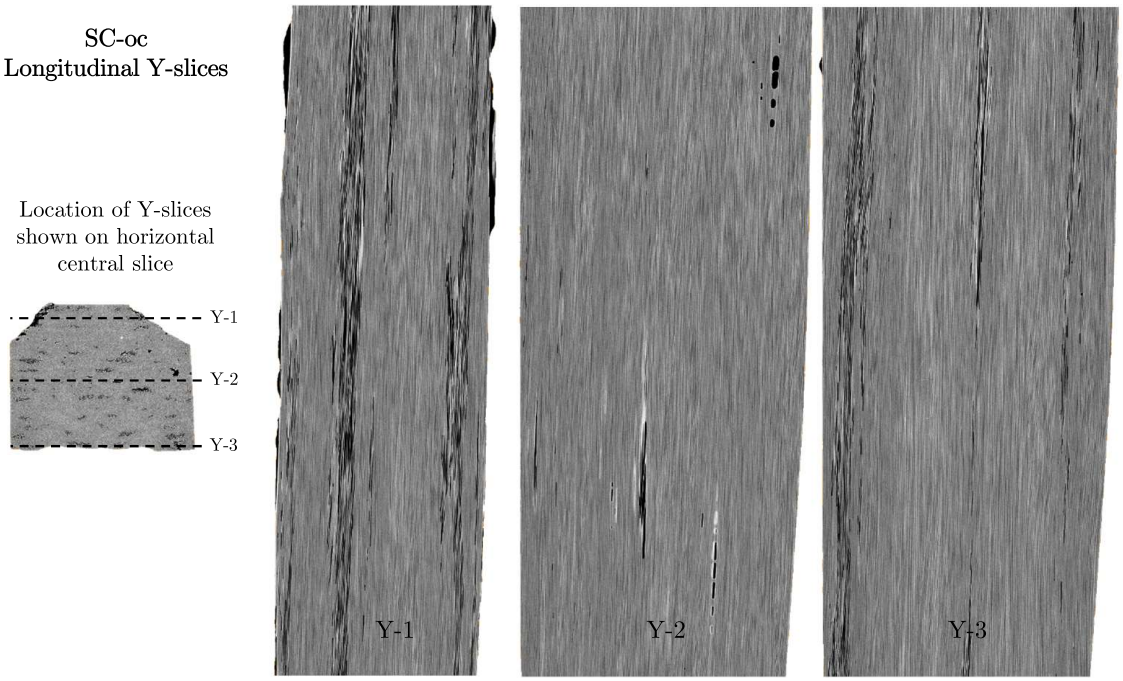

Figure A.54: Micro CT scans of the SC-oc samples – longitudinal Y-slices.

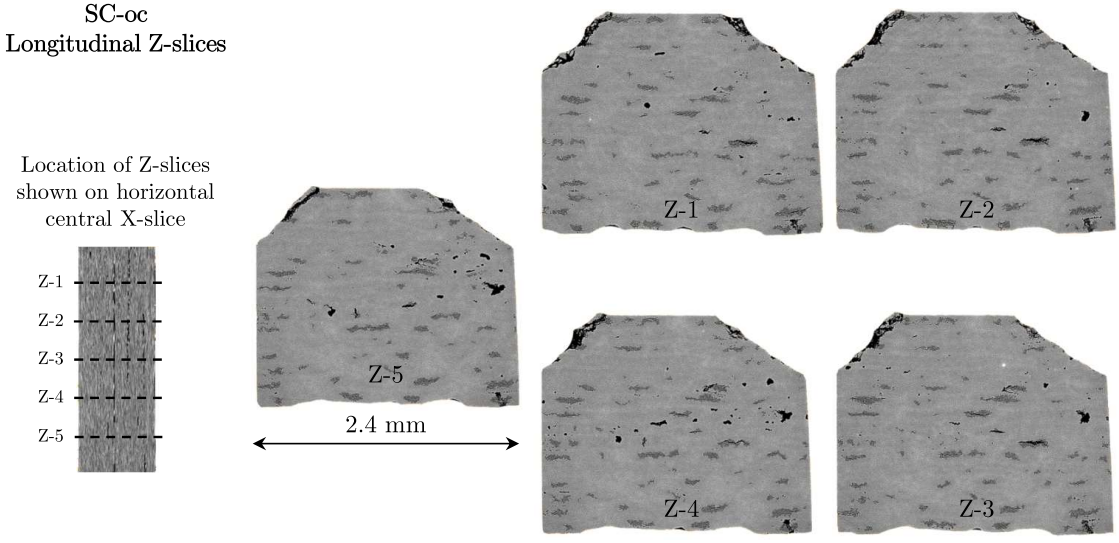

Figure A.55: Micro CT scans of the SC-oc samples – longitudinal Z-slices.

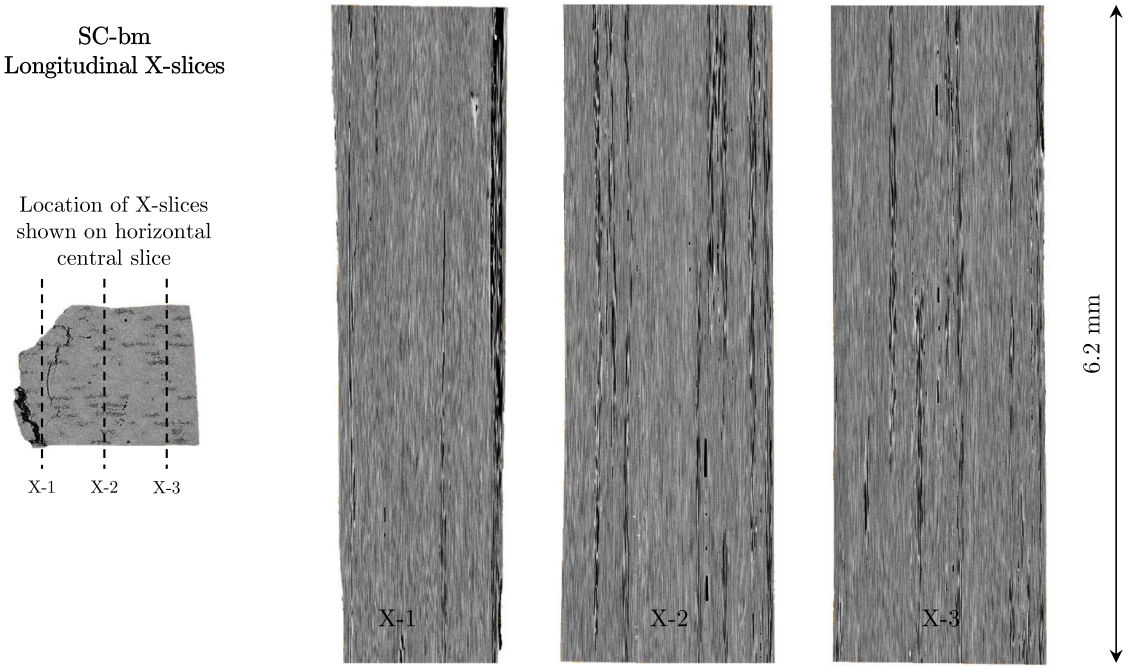

Figure A.56: Micro CT scans of the SC-bm samples – longitudinal X-slices.

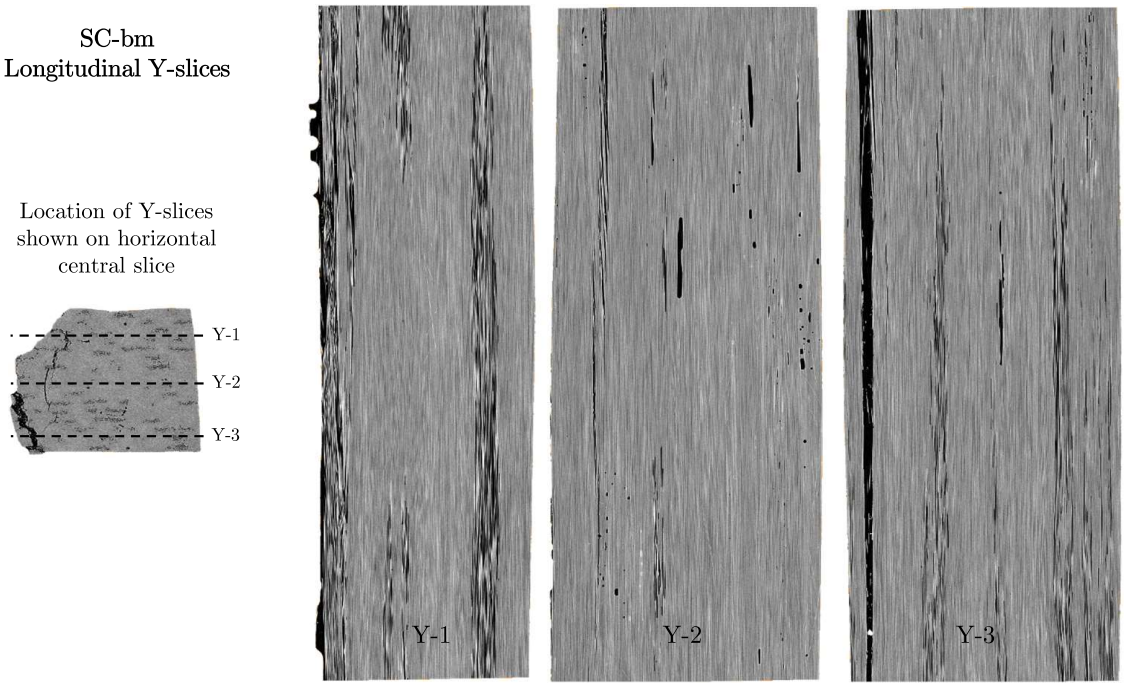

Figure A.57: Micro CT scans of the SC-bm samples – longitudinal Y-slices.

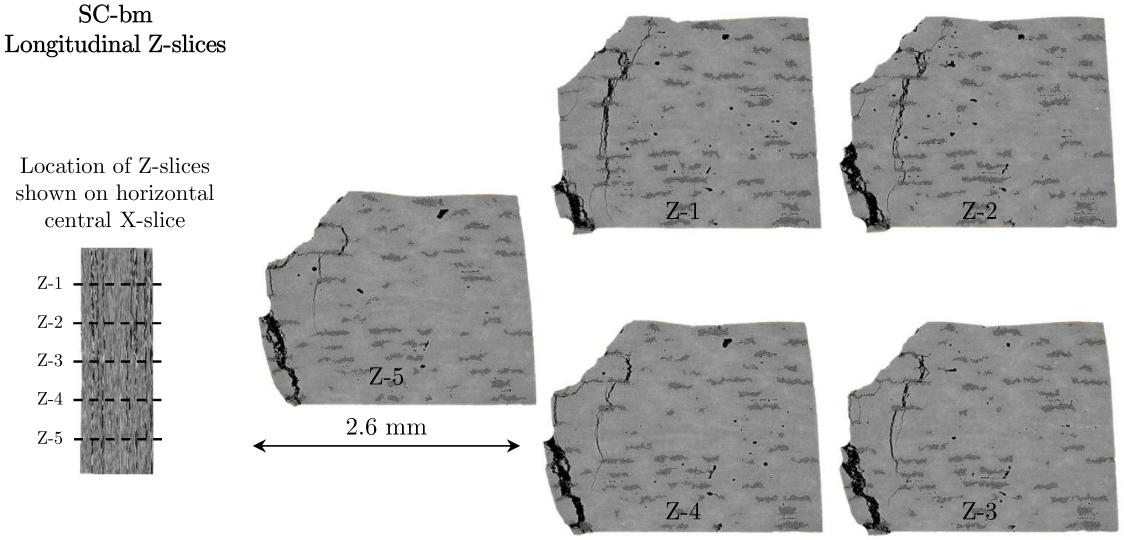

Figure A.58: Micro CT scans of the SC-bm samples – longitudinal Z-slices.

Figure A.59: Micro CT scans of the SC-mc samples – longitudinal X-slices.

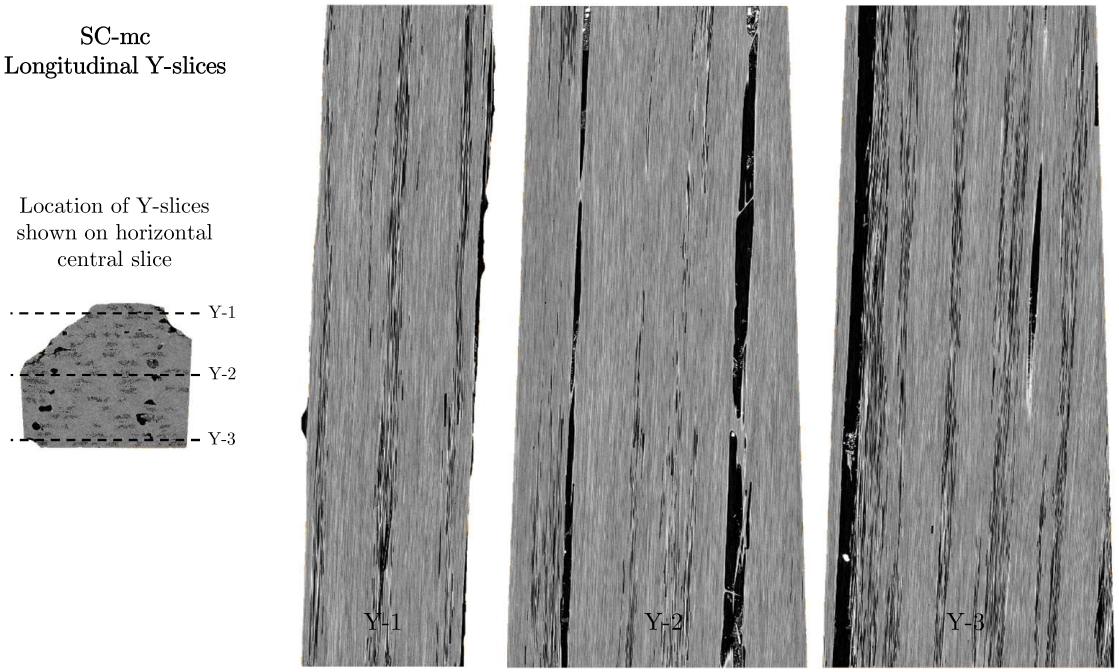

Figure A.60: Micro CT scans of the SC-mc samples – longitudinal Y-slices.

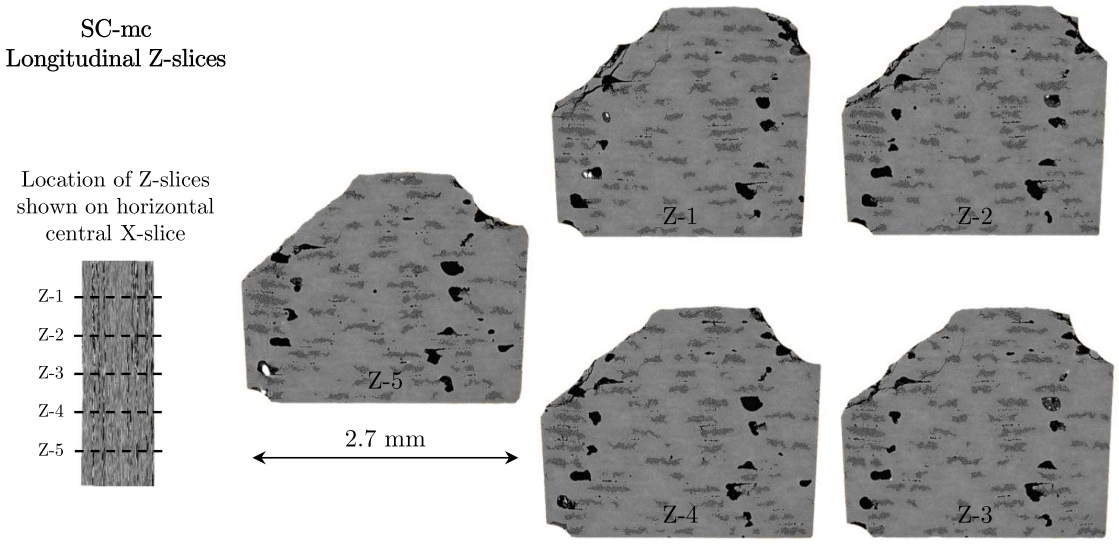

Figure A.61: Micro CT scans of the SC-mc samples – longitudinal Z-slices.

A.5 3D profilometer surface scans

Fig. 5.24 in Sec. 5.2.2 shows the surface profiles of representative areas of the different process and curing parameter samples. The graphs below show the accompanying roughness profiles of the samples.

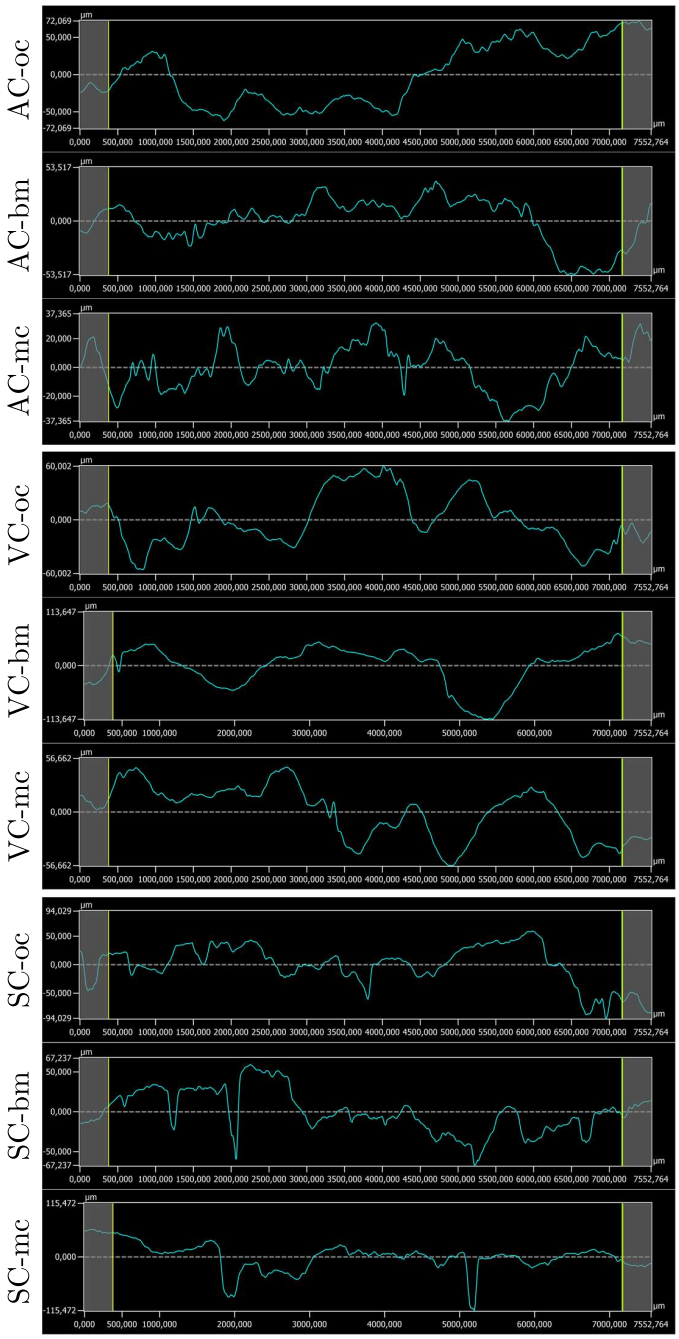

Figure A.62: 3D profilometer surface scan roughness profiles for all curing and processing parameter variations.

A.6 AFP process model details

Table A.1: Default settings of all parameters of the AFP process model.

Parameter	Unit	Default setting
Tape width	[mm]	3.175
No. of tapes per track	[-]	8
Lay-up velocity	[m/s]	0.5
Lay-up acceleration	[m/s2]	0.5
Linking velocity	[m/s]	1.0
Linking acceleration	[m/s2]	1.5
Buffer time	[s]	3
Time to/from home	[s]	3
Positioning in z-direction	[s]	3
Debulking time	[min]	25
Debulking interval	[nth ply]	15
Time for visual inspection per ply	[s]	30
Number of parts	[-]	1,000
Curing time per part	[h]	6
Parts per curing cycle	[-]	6
Finishing time per part	[min]	2
Quality inspection per part - testing	[min]	10
Quality inspection per part - evaluation	[min]	25
Cuts until cutter replacement	[-]	3,000
Time for cutter replacement	[min]	10
IR lamp lifetime	[h]	300
Time for IR lamp replacement	[min]	15
Feeding guide roller lifetime	[h]	600
Time for feeding guide roller replacement	[min]	15
Feeding guide plate lifetime	[h]	3520
Time for guide plate replacement	[min]	5
Compaction roller lifetime	[h]	300
Time for compaction roller replacement	[min]	10

A.7 Process efficiency case study detailed results

The graphs below are accompanying the use case study in chapter 6. They show the AFP process time for the five different cases at different lay-up velocities and debulking intervals. They are referred to in Sec. 6.3.3.

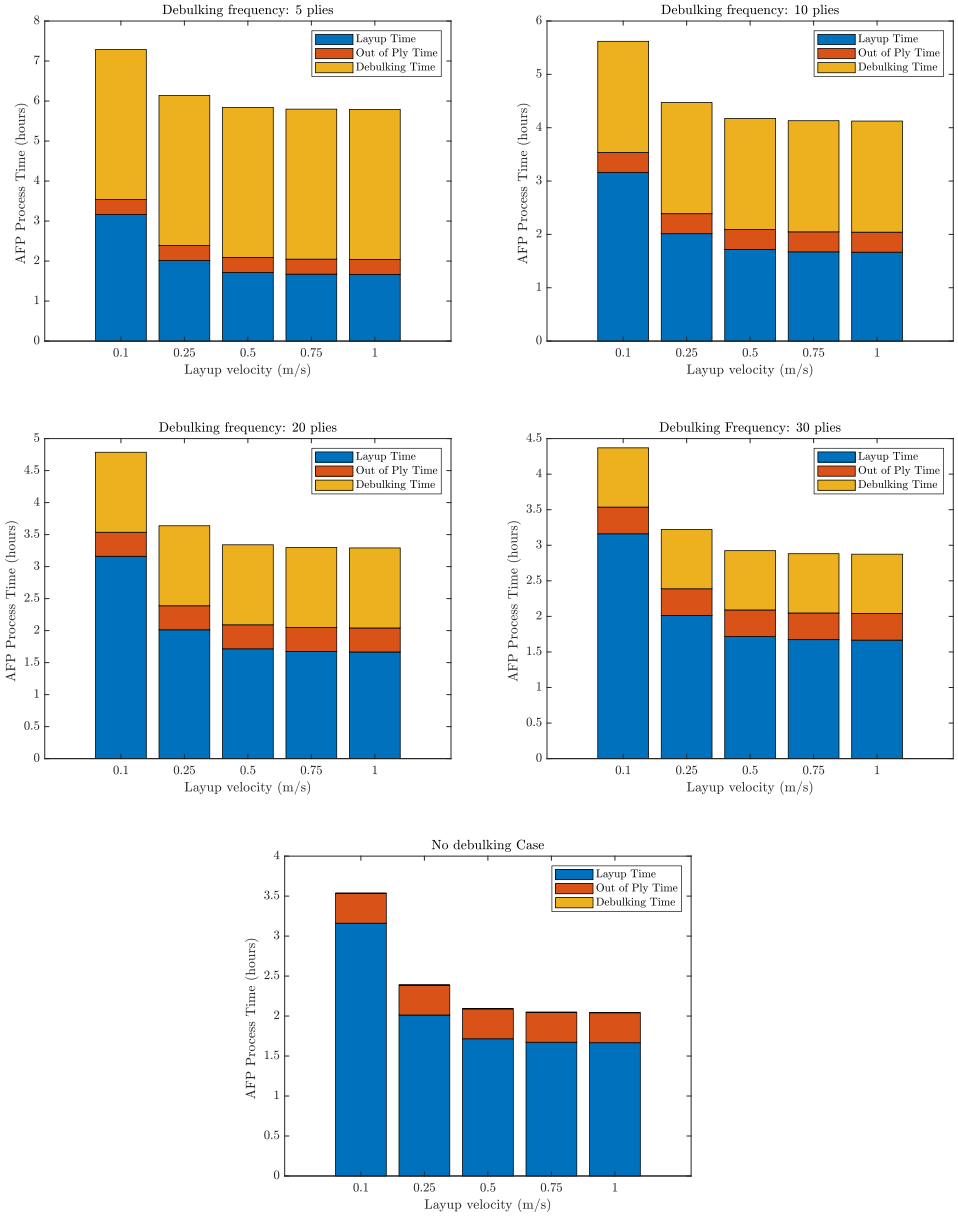

Figure A.63: Case 1 (very small panel) - influence of lay-up velocity and debulking interval on the AFP process time.

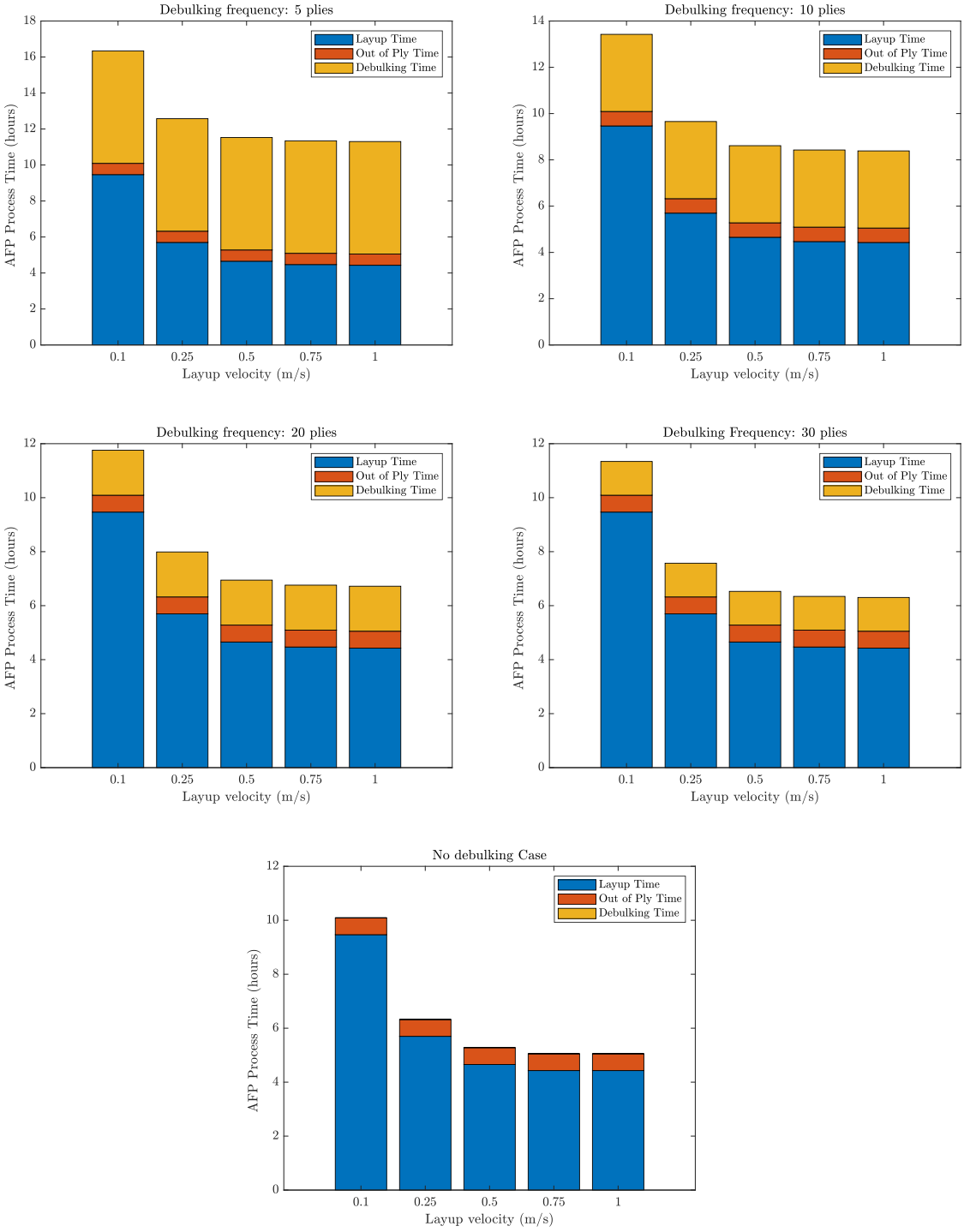

Figure A.64: Case 2 (small panel) - influence of lay-up velocity and debulking interval on the AFP process time.

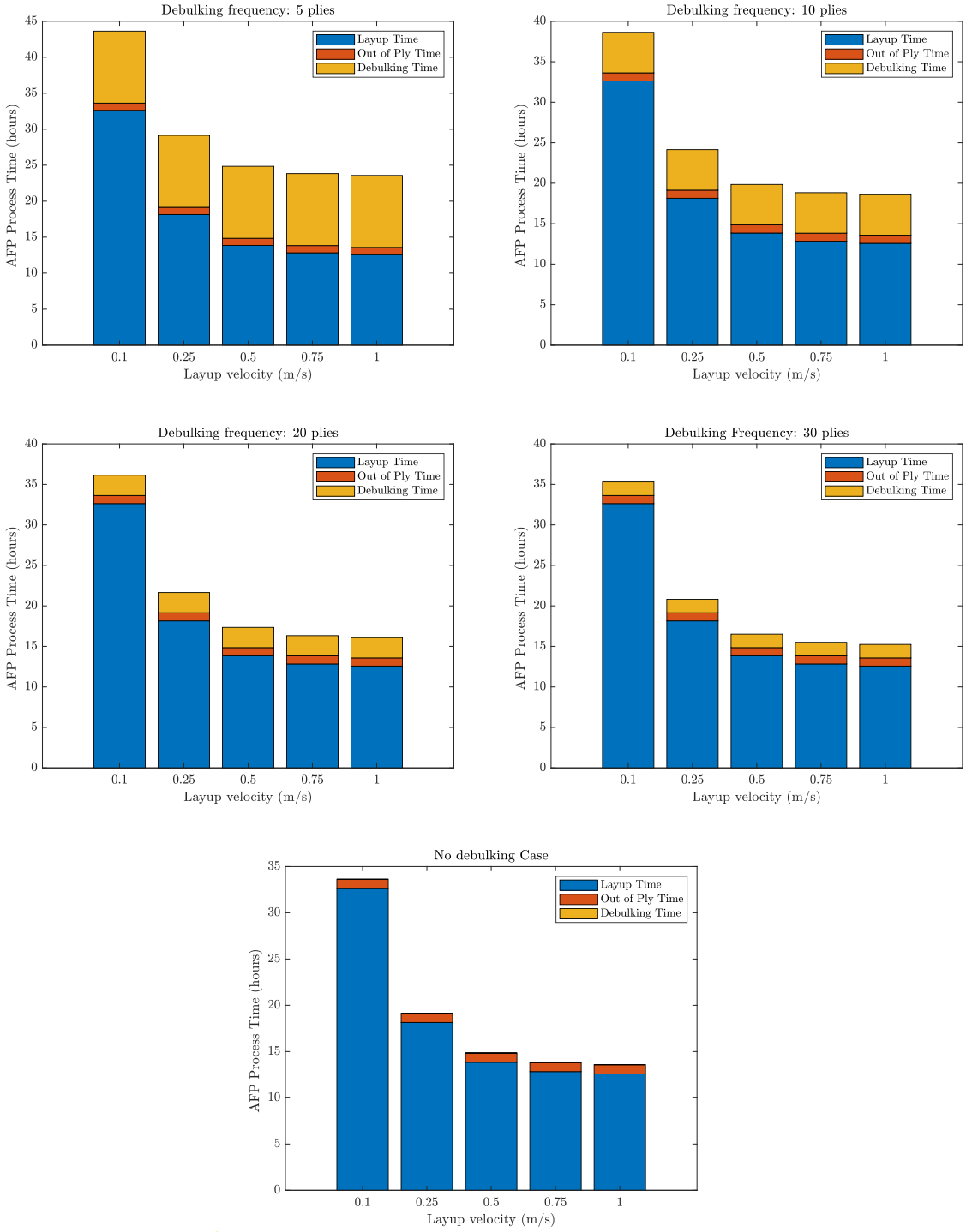

Figure A.65: Case 3 (medium panel) - influence of lay-up velocity and debulking interval on the AFP process time.

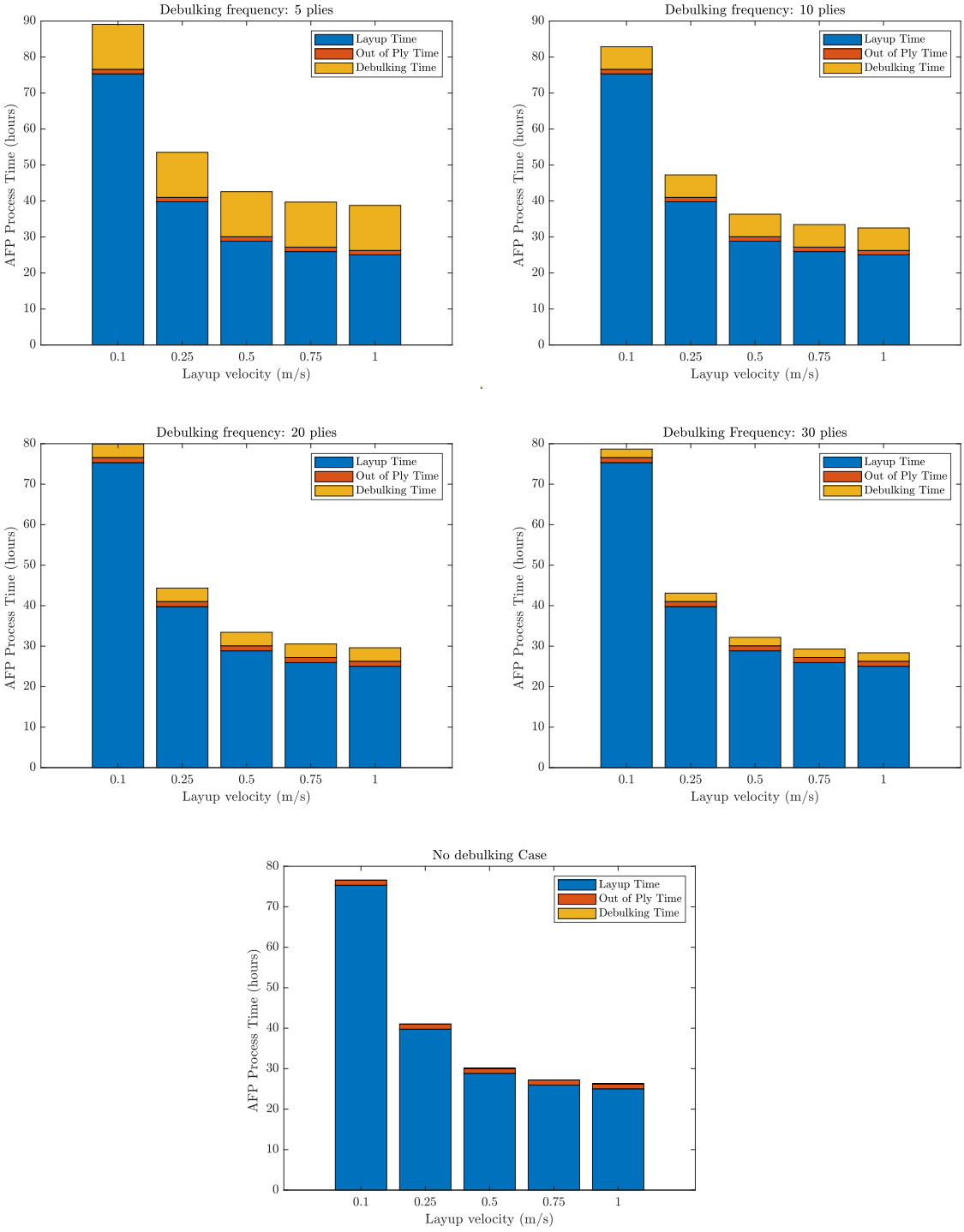

Figure A.66: Case 4 (large panel) - influence of lay-up velocity and debulking interval on the AFP process time.

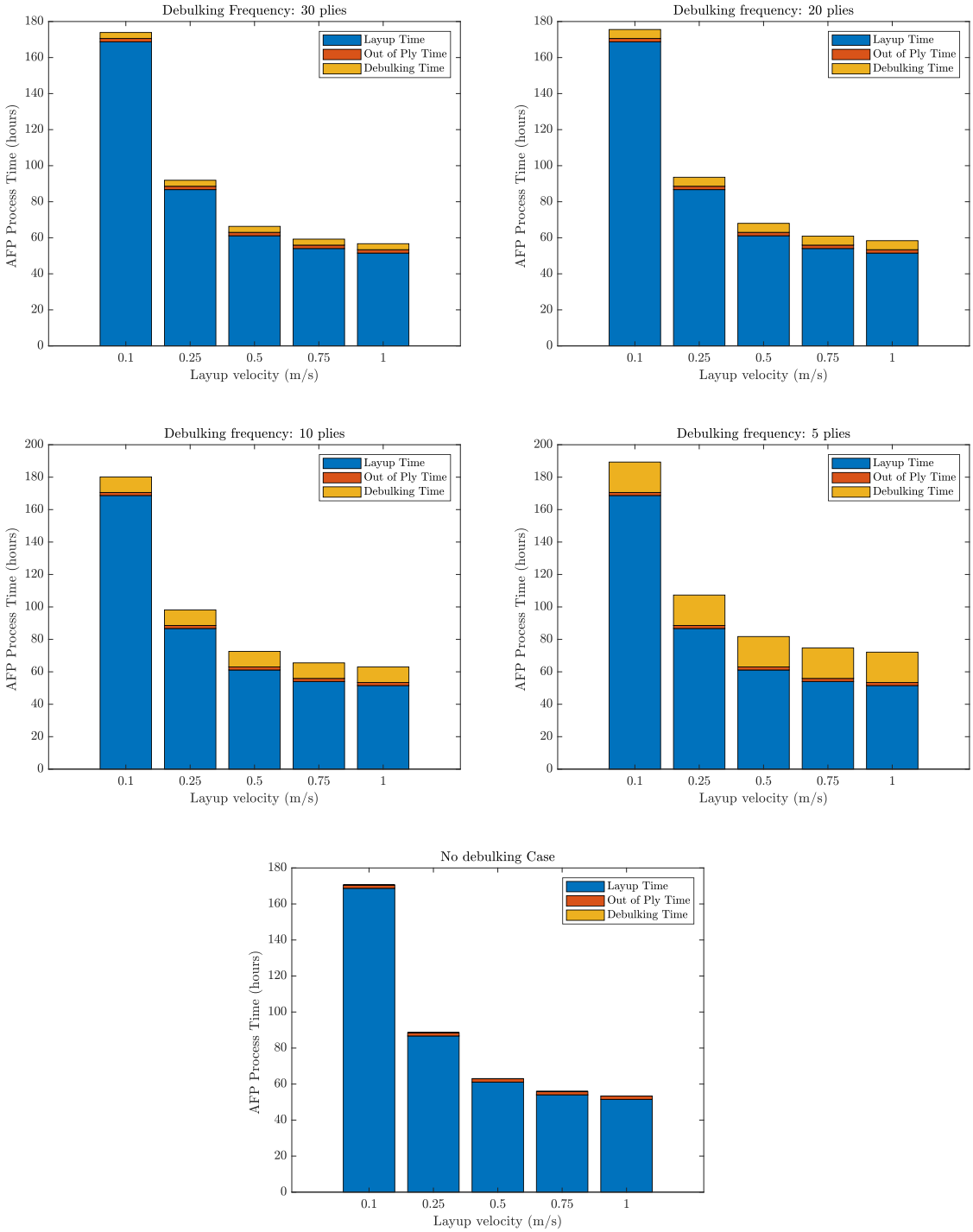

Figure A.67: Case 5 (very large panel) - influence of lay-up velocity and debulking interval on the AFP process time.

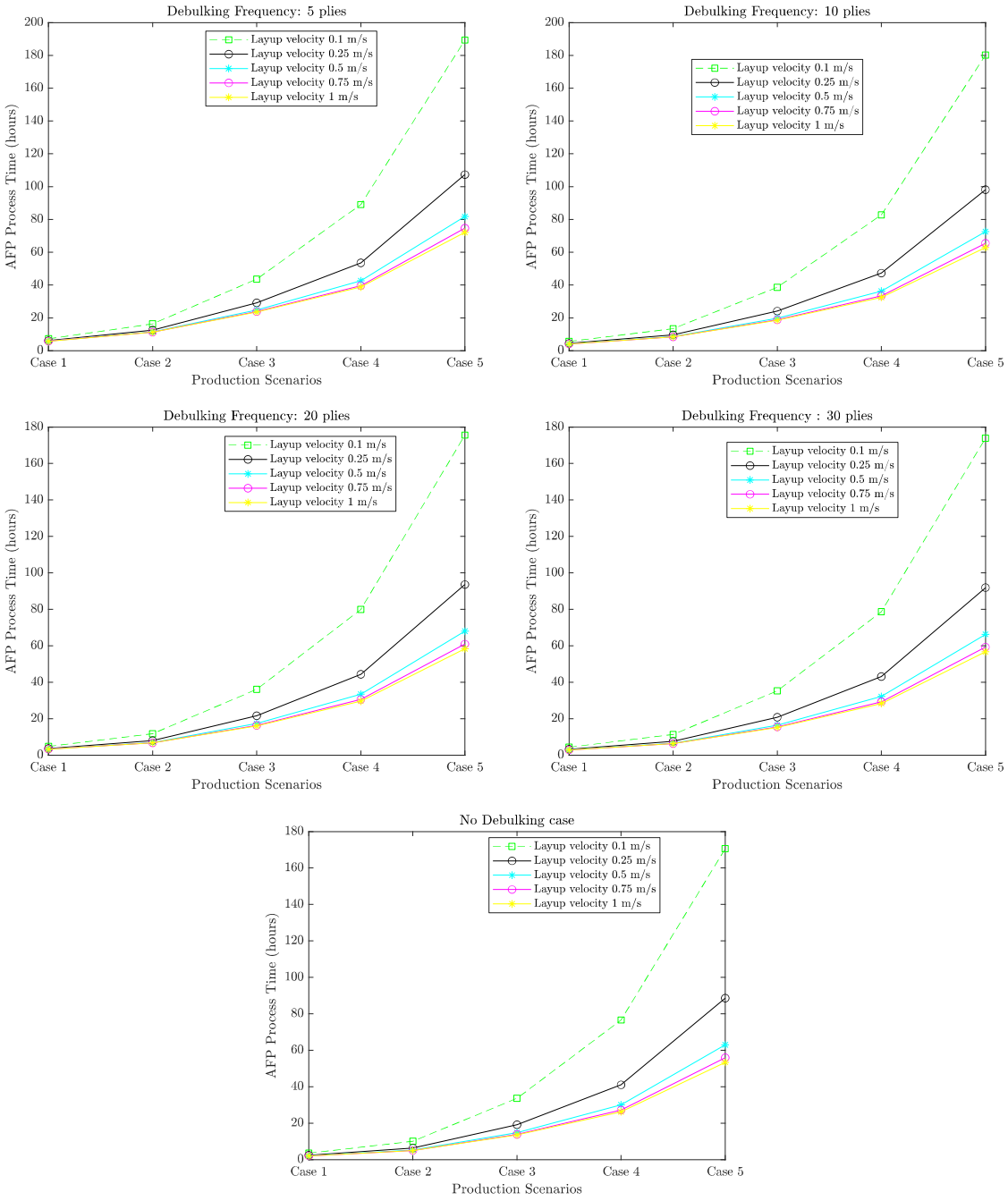

Figure A.68: Influence of lay-up velocity and debulking interval on the AFP process time.

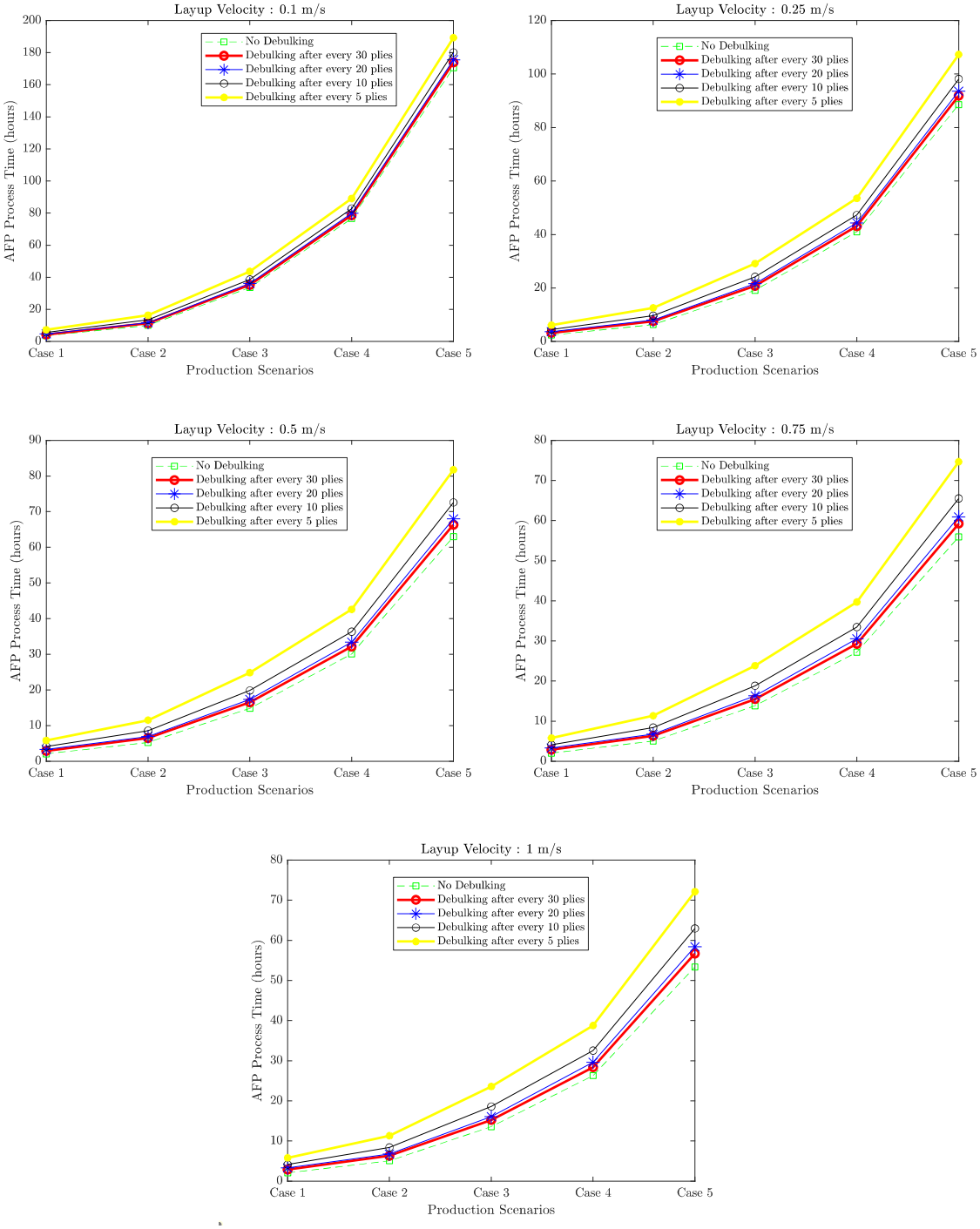

Figure A.69: Influence of debulking interval and lay-up velocity on the AFP process time.

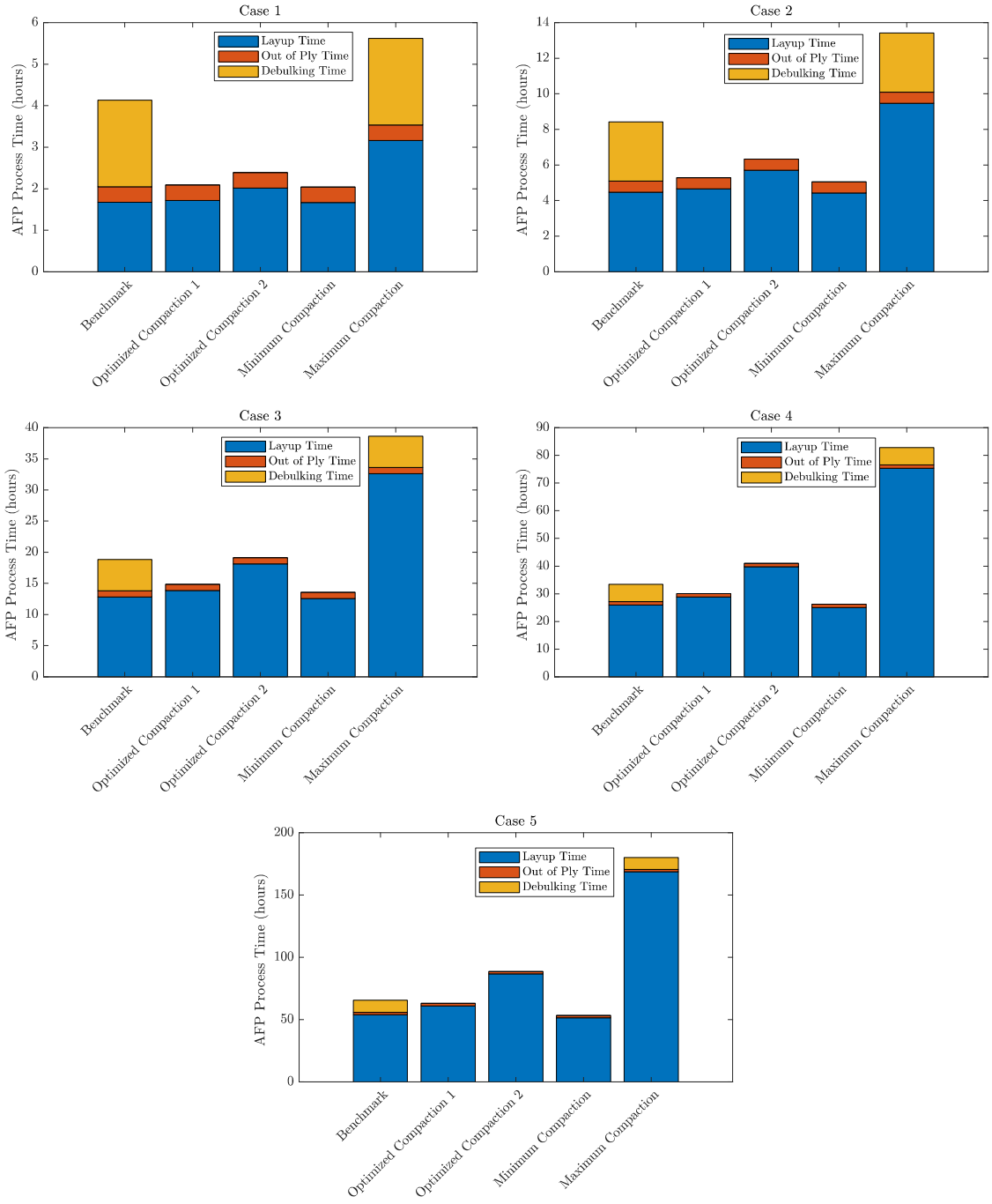

Figure A.70: Influence of the process parameter sets and different use cases on the AFP process time.

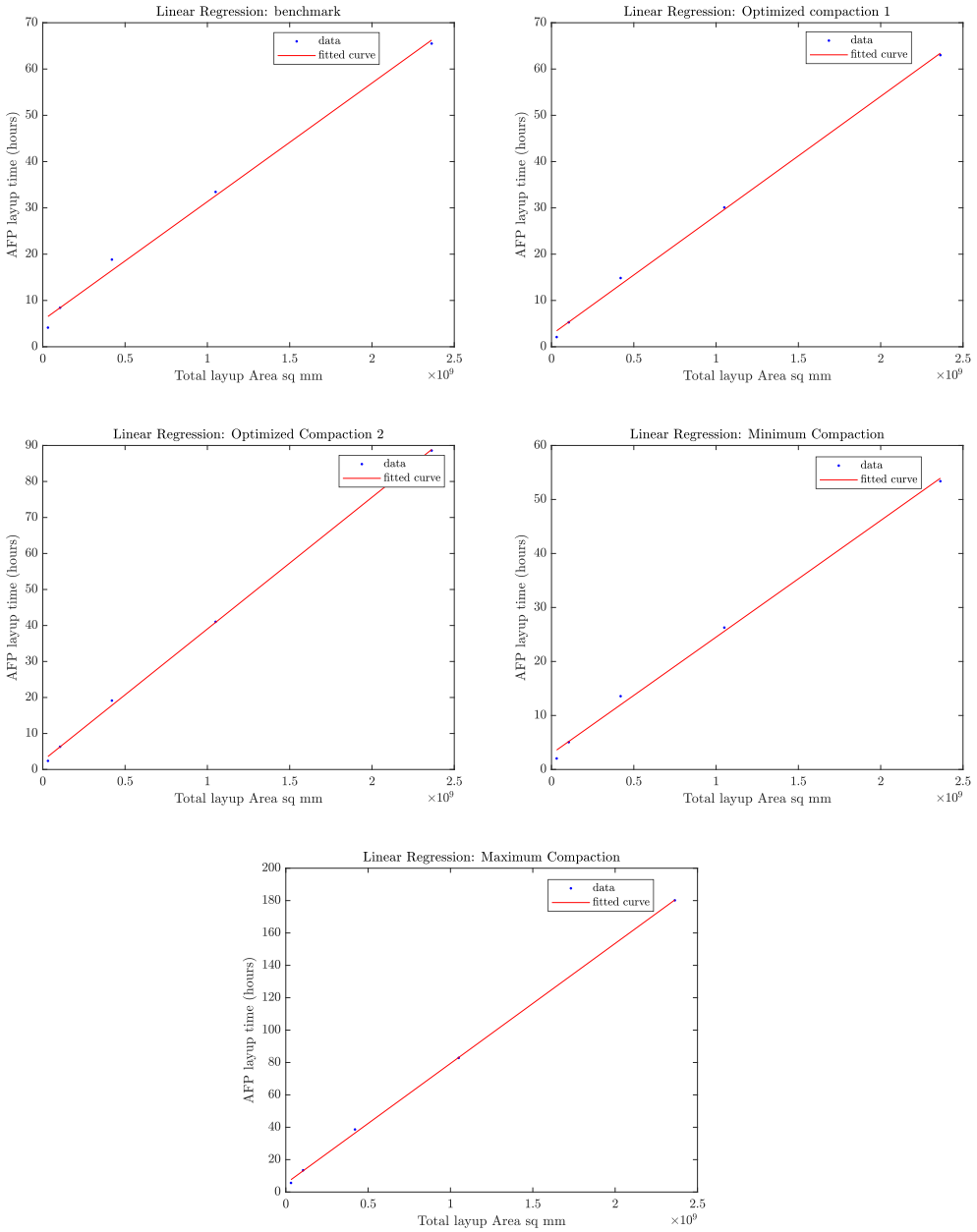

Figure A.71: Linear regression over total area.

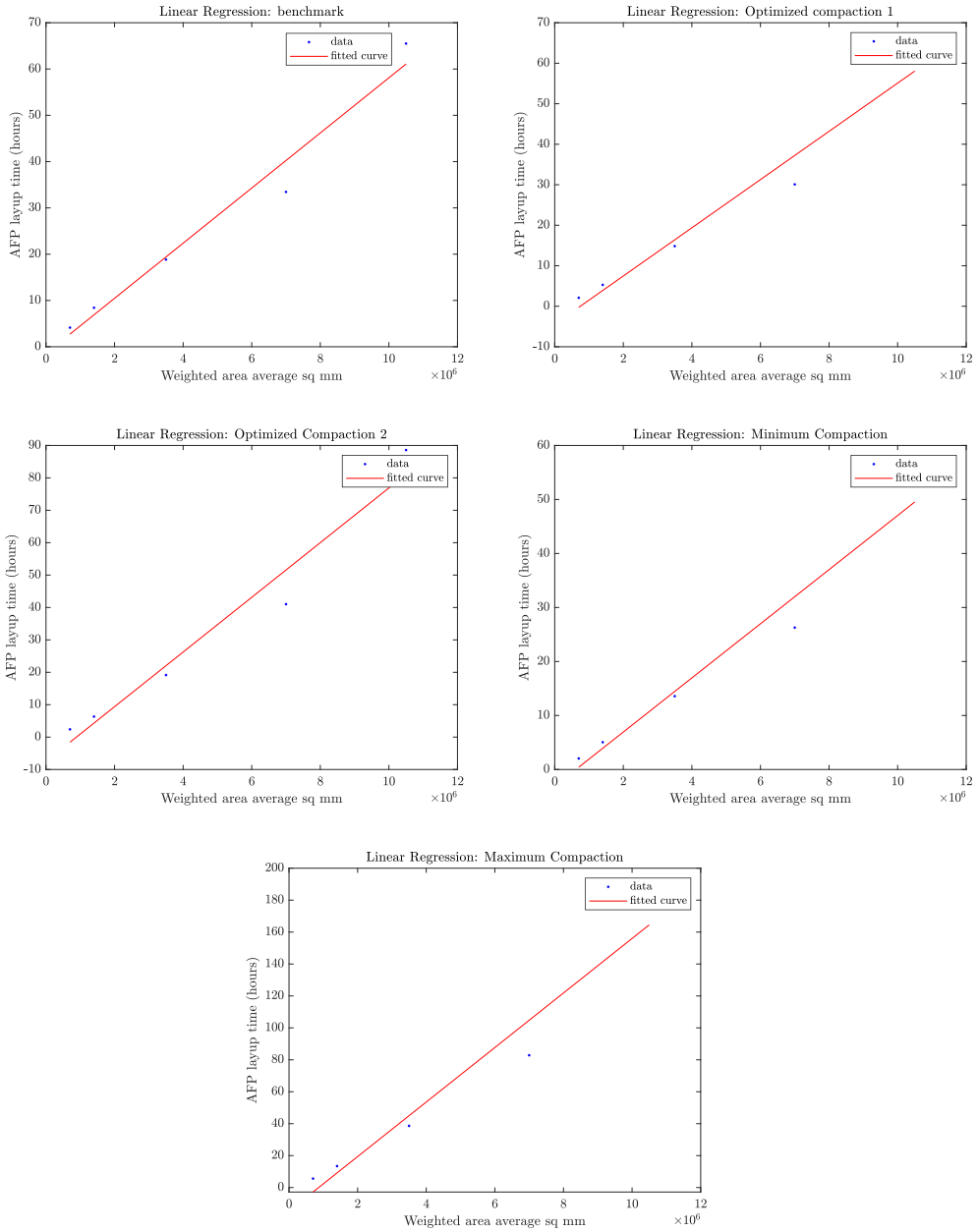

Figure A.72: Linear regression over weighted (average) area.

A.8 Product data sheet Hexcel HexPly 8552

HexPly® 8552
Epoxy matrix (180°C/356°F curing matrix)

HEXCEL®

Product Data Sheet

Description
HexPly® 8552 is a high performance tough epoxy matrix for use in primary aerospace structures. It exhibits good impact resistance and damage tolerance for a wide range of applications.

HexPly® 8552 is an amine cured, toughened epoxy resin system supplied with unidirectional or woven carbon or glass fibres.

HexPly® 8552 was developed as a controlled flow system to operate in environments up to 121ºC (250ºF).

Benefits and Features
- Toughened epoxy matrix with excellent mechanical properties
- Elevated temperature performance
- Good translation of fibre properties
- Controlled matrix flow in processing
- Available on various reinforcements
- Excellent drape and tack

Resin Matrix Properties

Rheology

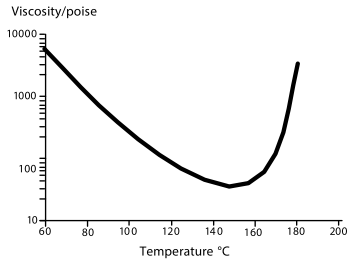

Gel Time

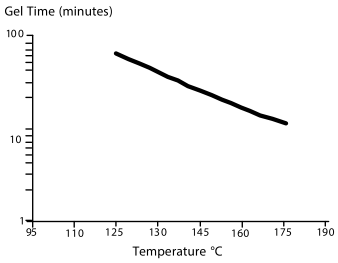

HexPly® 8552
Epoxy matrix (180°C/356°F curing matrix)

HEXCEL
Product Data Sheet

Prepreg Properties - HexPly® 8552 UD Carbon Prepregs

Physical Properties

	Units	AS4	IM7
Fibre Density	g/cm³ (lb/in³)	1.79 (0.065)	1.77 (0.064)
Filiament count/tow		12K	12K
Resin density	g/cm³ (lb/in³)	1.30 (0.047)	1.30 (0.047)
Nominal Cured Ply Thickness 8552 /35%/134	mm (inch)	0.130 (0.0051)	0.131 (0.0052)
Nominal Fibre Volume	%	57.42	57.70
Nominal Laminate Density	g/cm³ (lb/in³)	1.58 (0.057)	1.57 (0.057)

Mechanical Properties

Test	Units	Temp °C (°F)	Condition	AS4	IM7
0°Tensile Strength	MPa (ksi)	-55 (-67)	Dry	1903 (267)	2572 (373)
		25 (77)	Dry	2207 (320)	2724 (395)
		91 (195)	Dry	–	**2538 (368)***
90°Tensile Strength	MPa (ksi)	-55 (-67)	Dry	–	174 (25.3)
		25 (77)	Dry	81 (11.7)	64 (9.3)
		93 (200)	Dry	75 (10.9)	**92 (13.3)***
0°Tensile Modulus	GPa (msi)	-55 (-67)	Dry	134 (19.4)	163 (23.7)
		25 (77)	Dry	141 (20.5)	164 (23.8)
		91 (195)	Dry	–	**163 (23.7)***
90°Tensile Modulus	GPa (msi)	–	–	–	–
		25 (77)	Dry	10 (1.39)	12 (1.7)
		93 (200)	Dry	8 (1.22)	**10 (1.5)***
0°Compression Strength	MPa (ksi)	-55 (-67)	Dry	1586 (230)	–
		25 (77)	Dry	1531 (222)	1690 (245)
		91 (195)	Dry	1296 (184)	1483 (215)
0°Compression Modulus	GPa (msi)	-55 (-67)	Dry	124 (18)	–
		25 (77)	Dry	128 (18.6)	150 (21.7)
		91 (195)	Dry	122 (17.7)	162 (23.5)
0° ILSS (Shortbeam shear)	MPa (ksi)	-55 (-67)	Dry	164 (23.8)	–
		25 (77)	Dry	128 (18.5)	137(19.9)
		91 (195)	Dry	122 (14.7)	**94 (13.6)***
		25 (77)	Wet	117 (16.9)	115 (16.7)
		71 (160)	Wet	84 (12.2)	**80 (11.6)****
		91 (195)	Wet	78 (11.3)	–
In-plane Shear Strength	MPa (ksi)	25 (77)	Dry	114 (16.6)	120 (17.4)
		93 (200)	Dry	105 (15.2)	**106 (15.4)***

Bold 93°C (200°F) ***Bold* 104°C (220°F)*** ***Bold** 82°C (180°F)***

HexPly® 8552
Epoxy matrix (180°C/356°F curing matrix)

HEXCEL
Product Data Sheet

Prepreg Properties - HexPly® 8552 Woven Carbon Prepregs (AS4 Fibre)

Physical Properties

	Units	AGP193-PW	AGP 280-5H
Fibre Type	–	AS4 3K	AS4 3K
Fibre density	g/cm³ (lb/in³)	1.77 (0.065)	1.77 (0.065)
Weave	–	Plain	5HS
Mass	g/m² (oz/yd²)	193 (5.69)	286 (8.44)
Weight Ratio, Warp : Fill		50 :50	50 :50
Nominal cured ply thickness @ 37% resin content	mm (inch)	0.195 (0.0076)	0.289 (0.0114)
Nominal Fibre Volume	%	55.29	55.29
Nominal Laminate Density	g/cm³ (lb/in³)	1.57 (0.057)	1.57 (0.057)

Mechanical Properties

Test	Units	Temp°C (°F)	Condition	AGP193-PW	AGP280- 5H
0°Tensile Strength	MPa (ksi)	-55 (-67)	Dry	766 (111)	828 (120)
		25 (77)	Dry	828 (120)	876 (127)
		91 (195)	Dry	–	903 (131)
90°Tensile Strength	MPa (ksi)	-55 (-67)	Dry	710 (103)	752 (109)
		25 (77)	Dry	793 (115)	800 (116)
		93 (200)	Dry	759 (110)	772 (112)
0°Tensile Modulus	GPa (msi)	-55 (-67)	Dry	66 (9.5)	70 (10.2)
		25 (77)	Dry	68 (9.8)	67 (9.7)
		91 (195)	Dry	–	69 (10)
90°Tensile Modulus	GPa (msi)	-55 (-67)	Dry	66 (9.6)	67 (9.7)
		25 (77)	Dry	66 (9.5)	66 (9.5)
		93 (200)	Dry	68 (9.8)	65 (9.4)
0°Compression Strength	MPa (ksi)	-55 (-67)	Dry	959 (139)	–
		25 (77)	Dry	883 (128)	924 (134)
		91 (195)	Dry	759 (110)	**752 (109)**
0°Compression Modulus	GPa (msi)	-55 (-67)	Dry	60 (8.7)	–
		25 (77)	Dry	60 (8.7)	64 (9.3)
		91 (195)	Dry	61 (8.8)	**67(9.7)**
0° ILSS (Shortbeam shear)	MPa (ksi)	-55 (-67)	Dry	101 (14.6)	–
		25 (77)	Dry	84 (12.2)	79 (11.4)
		91 (195)	Dry	70 (10.2)	–
		-55 (-67)	Wet	75 (10.9)	69 (10)
		25 (77)	Wet	72 (10.4)	–
		91 (195)	Wet	59 (8.5)	–

Bold 93°C (200°F) Bold* 104°C (220°F) Bold** 82°C (180°F)

HexPly® 8552

Epoxy matrix (180°C/356°F curing matrix)

HEXCEL

Product Data Sheet

Prepreg Properties - HexPly® 8552 Woven Carbon Prepregs (IM7 Fibre)

Physical Properties

	Units	SPG 196-P	SPG 370-8H
Fibre Type	–	IM7 6K	IM7 6K
Fibre density	g/cm³ (lb/in³)	1.77 (0.064)	1.77 (0.064)
Weave	–	Plain	8HS
Mass	g/m² (oz/yd²)	196 (5.78)	374 (11.03)
Weight Ratio, Warp : Fill		50 :50	49 :51
Nominal cured ply thickness @ 37% resin content	mm (inch)	0.199 (0.0078)	0.380 (0.0150)
Nominal Fibre Volume	%	55.57	55.57
Nominal Laminate Density	g/cm³ (lb/in³)	1.56 (0.056)	1.56 (0.056)

Mechanical Properties

Test	Units	Temp°C (°F)	Condition	SPG 196-PW	SPG 370-SH
0°Tensile Strength	MPa (ksi)	-55 (-67)	Dry	979 (142)	965 (140)
		25 (77)	Dry	1090 (158)	1014 (147)
		91 (195)	Dry	–	–
90°Tensile Strength	MPa (ksi)	-55 (-67)	Dry	862 (125)	903 (131)
		25 (77)	Dry	945 (137)	959 (139)
		93 (200)	Dry	**979 (142)***	**879 (130)***
0°Tensile Modulus	GPa (msi)	-55 (-67)	Dry	85 (12.3)	86 (12.5)
		25 (77)	Dry	85 (12.3)	86 (12.4)
		91 (195)	Dry	–	–
90°Tensile Modulus	GPa (msi)	-55 (-67)	Dry	80 (11.6)	81 (11.7)
		25 (77)	Dry	80 (11.6)	81 (11.7)
		93 (200)	Dry	**79 (11.5)***	**79 (11.5)***
0° ILSS (Shortbeam shear)	MPa (ksi)	-55 (-67)	Dry	–	–
		25 (77)	Dry	88 (12.7)	90 (13)
		91 (195)	Dry	**69 (10)***	**74 (10.8)***
		25 (77)	Wet	80 (11.6)	83(12.1)
		71 (160)	Wet	**61 (8.8)****	**63 (9.1)****
		91 (195)	Wet	–	–

Bold 93°C (200°F) ***Bold* 104°C (220°F)*** ***Bold** 82°C (180°F)***

Typical Neat Resin Data

Colour	Yellow	
Density	1.301 g/cc	(0.0470 lb/in³)
Glass Transition Temperature, T_g dry	200°C	(392°F)
Glass Transistion Temperature, T_g wet	154°C	(309°F)
Tensile Strength	121 MPa	(17.5 ksi)
Tensile Modulus	4670 MPa	(0.677 msi)

Curing Conditions

Cure cycle for monolithic components

1. Apply full vacuum (1 bar).
2. Apply 7 bar gauge autoclave pressure.
3. Reduce the vacuum to a safety value of 0.2 bar when the autoclave pressure reaches approximately 1 bar gauge.
4. Heat at 1- 3°C/min (2-8°F/min) to 110°C ± 5°C (230°F ± 9°F)
5. Hold at 110°C ± 5°C (230°F ± 9°F) for 60 minutes ± 5 minutes.
6. Heat at 1-3°C/min (2-8°F/min) to 180°C ± 5°C (356°F ± 9°F)
7. Hold at 180°C ± 5°C (356°F ± 9°F) for 120 minutes ± 5 minutes.
8. Cool at 2 - 5°C (4-9°F) per minute
9. Vent autoclave pressure when the component reaches 60°C (140°F) or below.

Cure cycle for honeycomb sandwich components

1. Apply full vacuum (1 bar).
2. Apply 3.2 bar gauge autoclave pressure.
3. Reduce the vacuum to a safety value of 0.2 bar when the autoclave pressure reaches approximately 1 bar gauge.
4. Heat at 1- 3°C/min (2-8°F/min) to 110°C ± 5°C (230°F ± 9°F)
5. Hold at 110°C ± 5°C (230°F ± 9°F) for 60 minutes ± 5 minutes.
6. Heat at 1-3°C/min (2-8°F/min) to 180°C ± 5°C (356°F ± 9°F)
7. Hold at 180°C ± 5°C (356°F ± 9°F) for 120 minutes ± 5 minutes.
8. Cool at 2 - 5°C (4-9°F) per minute
9. Vent autoclave pressure when the component reaches 60°C (140°F) or below.

Note: For both cure cycles – at each stage, use the temperature shown by the leading thermocouple.

Heat-up rates are dependent on component thickness, eg, slow heat-up rates should be used for thicker components and large tools. Accurate temperature measurements of the component should be made during the cure cycles by using thermocouples.

Performance testing should accompany alternative cure cycles to ensure suitability for the particular application.

Curing Cycle for Honeycomb and Monolithic Components

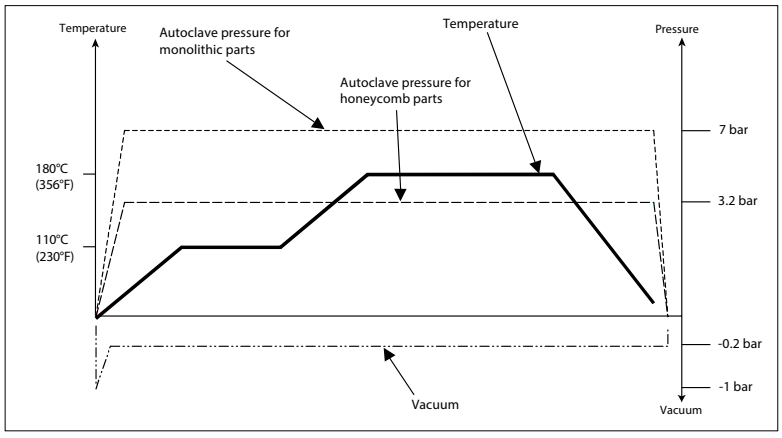

HexPly® 8552
Epoxy matrix (180°C/356°F curing matrix)

HEXCEL
Product Data Sheet

Storage Life

Tack Life:	10 days at RT (23°C/73°F)
Out Life:	30 days at RT (23°C/73°F)
Shelf Life:	12 months at -18°C(0°F) (maximum, from date of manufacture)

Definitions:

Shelf Life:	The maximum storage life for HexPly® prepreg, upon receipt by the customer, when stored continuously, in a sealed moisture-proof bag, at -18°C(0°F). To accurately establish the exact expiry date, consult the box label.
Tack Life:	The time, at room temperature, during which prepreg retains enough tack for easy component lay-up.
Out Life:	The maximum accumulated time allowed at room temperature between removal from the freezer and cure.

Precautions for Use

The usual precautions when handling uncured synthetic resins and fine fibrous materials should be observed, and a Safety Data Sheet is available for this product. The use of clean disposable inert gloves provides protection for the operator and avoids contamination of material and components.

For more information

Hexcel is a leading worldwide supplier of composite materials to aerospace and industrial markets.
Our comprehensive range includes:

- HexTow® carbon fibers
- HexForce® reinforcements
- HiMax® multiaxial reinforcements
- HexPly® prepregs
- HexMC®-i molding compounds
- HexFlow® RTM resins
- HexBond™ adhesives
- HexTool® tooling materials
- HexWeb® honeycombs
- Acousti-Cap® sound attenuating honeycomb
- Engineered core
- Engineered products
- Polyspeed® laminates & pultruded profiles
- HexAM® additive manufacturing

For U.S. quotes, orders and product information call toll-free 1-800-688-7734. For other worldwide sales office telephone numbers and a full address list, please go to:

https://www.hexcel.com/contact

FTA-072-MY20

B Publications

Publications by the author Ralf Knott né Engelhardt.

Journal papers

[J1] R. Engelhardt, R. Irmanputra, K. Brath, N. Aufenanger, K. Drechsler. Thermoset prepreg compaction during Automated Fiber Placement and vacuum debulking. *Procedia CIRP*, 85C:155-160, 2019, ISSN: 2212-8271, doi.org/10.1016/j.procir.2019.09.025.

[J2] R. Engelhardt, S. Ehard, T. Wolf, J. Oelhafen, A. Kollmannsberger, K. Drechsler. In situ joining of unidirectional tapes on long fiber reinforced thermoplastic structures by thermoplastic Automated Fiber Placement for scientific sounding rocket applications. *Procedia CIRP*, 85:192-197, 2019, ISSN: 2212-8271, doi.org/10.1016/j.procir.2019.09.015.

[J3] M. Etchegaray Bello, R. Engelhardt, D. Bublitz, K. Drechsler. Lab-scale experimental analysis of the cyclic compaction-recovery characteristics of uncured thermoset prepreg. *Advanced Manufacturing: Polymer & Composites Science*, 8(2):56–67, 2022, doi.org/10.1080/20550340.2022.2064069.

Conferences

[C1] R. Engelhardt, P. Hörmann, F. Rinker, G. Weyerer, K. Drechsler. Analysis of the cost efficiency of Automated Fiber Placement based on an extensive process breakdown. *SAMPE Europe SEICO 14 - 35th International Technical Conference & Forum*, France, 10-11 March 2014.

[C2] R. Engelhardt, K. Brath, C. Ebel, K. Drechsler. Analysis of the influence of Automated Fiber Placement and vacuum debulking on thermoset prepreg compaction. *29th Annual International SICOMP Conference on Manufacturing and Design of Composites*, Luleå, Sweden, 28-29 May 2018.

[C3] R. Engelhardt, J. Oelhafen, S. Ehard, A. Kollmannsberger, K. Drechsler. Manufacturing of a thermoplastic CFRP rocket module with integrated fiber optical temperature sensors. *29th Annual International SICOMP Conference on Manufacturing and Design of Composites*, Luleå, Sweden, 28-29 May 2018.

[C4] R. Engelhardt, K. Brath, C. Ebel, K. Drechsler. Experimental analysis of the compaction behavior during thermoset Automated Fiber Placement. *18th European Conference on Composite Materials*, Athens, Greece, 25-28 June, 2018. ISBN 978-151089693-2.

[C5] R. Engelhardt, S. Ehard, J. Oelhafen, A. Kollmannsberger, R. Amann, P. Günzel, K. Drechsler. Development of a lightweight carbon composite rocket module with integrated fiber optical temperature sensors as part of the experiment "TESOS" on REXUS 23. *24th ESA Symposium on European Rocket & Balloon Programmes and Related Research*, Essen, Germany, 16-20 June 2019. ISBN: 978-929221307-7.

[C5] R. Engelhardt, S. Ehard, J. Oelhafen, A. Kollmannsberger, R. Amann, P. Günzel, K. Drechsler. Development of a lightweight carbon composite rocket module with integrated fiber optical temperature sensors as part of the experiment "TESOS" on REXUS 23. *24th ESA Symposium on European Rocket & Balloon Programmes and Related Research*, Essen, Germany, 16-20 June 2019. ISBN: 978-929221307-7.

[C6] R. Engelhardt, S. Ehard, R. Jemmali, J. Oelhafen, A. Kollmannsberger, K. Drechsler. Post Flight Analysis of an in situ Consolidated Thermoplastic Rocket Module with Integrated Fiber Optic Temperature Sensors. *5th International Conference and Exhibition on Thermoplastic Composites (ITHEC)*, Bremen, Germany, 13 - 14 October 2020.

Poster

[P1] R. Engelhardt, S. Ehard, J. Oelhafen, A. Kollmannsberger, R. Amann, P. Günzel, K. Drechsler. Manufacturing, testing and flight of a carbon fiber reinforced polymer rocket module with integrated fiber optical temperature sensors. *2nd Symposium on Space Educational Activities*, Budapest, Hungary, 2018.

Raw data

[D1] M. Etchegaray Bello, R. Engelhardt, K. Drechsler. Dataset for cyclic compaction-recovery behavior of CF/epoxy/8552 multilayer samples. *Technical University of Munich*, 2021, doi:10.14459/2021mp1621517.

C Supervised student theses

[S1] M. Lörch. *Implementation of a MATLAB process model of Automated Fiber Placement for process time analyses.* Term project. Technical University of Munich, 2017.

[S2] K. Brath. *Analysis of compaction behavior during thermoset Automated Fiber Placement.* Master's thesis. Technical University of Munich, 2018.

[S3] M. Lörch. *Lab-scale compaction experiments for Automated Fiber Placement.* Master's thesis. Technical University of Munich, 2018.

[S4] R. Irmanputra. *Experimental analysis of vacuum debulking with prepreg laminate at elevated temperature.* Bachelor's thesis. Technical University of Munich, 2019.

[S5] C. Rädler. *Experimental analysis of the influence of autoclave curing on prepreg laminate properties.* Bachelor's thesis. Technical University of Munich, 2019.

[S6] N. Aufenanger. *Experimental analysis of the compaction behaviour during Automated Fiber Placement and autoclave curing.* Term project. Technical University of Munich, 2019.

[S7] A. Díaz de la Hoz. *Development of a compaction simulation model for the thermoset Automated Fiber Placement process.* Bachelor's thesis. Technical University of Munich & Universidad Politécnica de Madrid, 2019.

[S8] L. Bahmann. *Wet-chemical fiber volume determination of thermoset composite laminates.* Research internship. Technical University of Munich, 2019.

[S9] M. Bissinger. *Experimental analysis of vacuum debulking with thermoset prepregs*. Bachelor's thesis. Technical University of Munich, 2020.

[S10] M. Etchegaray Bello. *Lab-scale experimental analysis of the compaction behavior of uncured thermoset prepreg for Automated Fiber Placement applications*. Term project. Technical University of Munich, 2020.

[S11] S. Vogl. *Analysis of the influence of compaction during Automated Fiber Placement on the mechanical performance of composite laminates*. Term project. Technical University of Munich, 2020.

[S12] V. Barranco Martinez. *AFP compaction roller – simulation and experimental validation*. Bachelor's thesis. Technical University of Munich, 2020.

[S13] Y. Baklouti. *Fiber volume content determination of Automated Fiber Placement laminates with different compaction and curing levels*. Term project. Technical University of Munich, 2020.

[S14] M. Etchegaray Bello. *Lab-scale experimental analysis of the compaction behavior of uncured thermoset prepreg for AFP applications*. Term project. Technical University of Munich, 2020.

[S15] S. Vogl. *Optimization and Application of a Compaction Simulation Model for the Thermoset Automated Fiber Placement Process*. Master's thesis. Technical University of Munich, 2020.

[S16] C. Dsouza. *Optimization and application of a process model of the Automated Fiber Placement process for aerospace applications*. Master's thesis. Politecnico di Milano, 2020.

Parts of the following theses contributed to the underlying doctoral thesis: [S1], [S2], [S3], [S4], [S6], [S7], [S9], [S10], [S11], [S13], [S15], [S16].

Bibliography

[1] IPCC. Climate Change 2021: The Physical Science Basis. Contribution of Working Group I to the Sixth Assessment Report of the Intergovernmental Panel on Climate Change (IPCC), 2021. URL https://www.ipcc.ch/report/ar6/wg1/downloads/report/IPCC_AR6_WGI_Full_Report.pdf.

[2] European Commission. The European Green Deal: Communication from the Commission to the European Parliament, the European Council, the Council, The European Economic and Social Committee and the Committee of the Regions, 2019. URL https://eur-lex.europa.eu/legal-content/EN/ALL/?uri=COM:2019:640:FIN.

[3] S. W. Tsai. *Theory of composites design*. Think Composites, Dayton, 1992. ISBN 9780961809034.

[4] D. H.-J. A. Lukaszewicz and K. Potter. Through-thickness compression response of uncured prepreg during manufacture by automated layup. *Proceedings of the Institution of Mechanical Engineers, Part B: Journal of Engineering Manufacture*, 226(2):193–202, 2012. ISSN 0954-4054. doi: 10.1177/0954405411411817.

[5] H. Lengsfeld, F. Wolff-Fabris, J. Krämer, J. Lacalle, and V. Altstädt. *Composite technology: Prepregs and monolithic part fabrication technologies*. Hanser, Munich, 2016. ISBN 9781569905999.

[6] T. G. P. Gutowski. *Advanced composites manufacturing*. John wiley & sons, 1997. ISBN 978-0-471-15301-6.

[7] D. H.-J.A. Lukaszewicz, C. Ward, and K. D. Potter. The engineering aspects of automated prepreg layup: History, present and future. *Composites Part B: Engineering*, 43(3):997–1009, 2012. ISSN 13598368. doi: 10.1016/j.compositesb.2011.12.003.

[8] J. Sloan. ATL and AFP: Defining the megatrends in composite aerostructures. *Composites World*, 6,

30.06.2008. URL https://www.compositesworld.com/articles/atl-and-afp-defining-the-megatrends-in-composite-aerostructures.

[9] Coriolis Composites. Industry References, 25.05.2021. URL https://www.coriolis-composites.com/references/industry/.

[10] Electroimpact. Customer Solutions - Composites Manufacturing, 25.05.2021. URL https://www.electroimpact.com/products/composites-manufacturing/customer-solutions.aspx.

[11] R. F. X. Lichtinger. *Thermo-mechanical coupled simulation of the thermoset automated fibre placement process*. Dissertation, Technical University of Munich, Munich, 2016.

[12] G. Dell'Anno, I. Partridge, D. Cartié, A. Hamlyn, E. Chehura, S. James, and R. Tatam. Automated manufacture of 3D reinforced aerospace composite structures. *International Journal of Structural Integrity*, 3(1):22–40, 2012. ISSN 1757-9864. doi: 10.1108/17579861211209975.

[13] A. Hamlyn and Y. Hardy. Fibre application machine with flexible fibre supply tubes: WO2008FR00224; FR20070001453, 2009.

[14] J. Hinrichsen. A380 - Flagship aircraft for the new century. *SAMPE Journal*, 38(3):8–12, 2002.

[15] M. K. Hagnell and M. Åkermo. A composite cost model for the aeronautical industry: Methodology and case study. *Composites Part B: Engineering*, 79: 254–261, 2015. ISSN 13598368. doi: 10.1016/j.compositesb.2015.04.043.

[16] M. Szcesny, F. Heieck, S. Carosella, P. Middendorf, H. Sehrschön, and M. Schneiderbauer. The advanced ply placement process – an innovative direct 3D placement technology for plies and tapes. *Advanced Manufacturing: Polymer & Composites Science*, 3(1):2–9, 2017. ISSN 2055-0340. doi: 10.1080/20550340.2017.1291398.

[17] M. M. Torres. Multi-application head for fibre strips and method of applying said fibre strips: WO2005ES00408;ES20040001853, 2007.

[18] A. Hamlyn and Y. Hardy. Applicator head for fibres with systems of cutting and locking particular fibers: Patent: FR20070001627, 2008.

[19] R. Lichtinger, P. Hörmann, D. Stelzl, and R. Hinterhölzl. The effects of heat input on adjacent paths during Automated Fibre Placement. *Composites Part*

A: Applied Science and Manufacturing, 68:387–397, 2015. ISSN 1359835X. doi: 10.1016/j.compositesa.2014.10.004.

[20] T. Orth. A review of radiative heating in automated layup and its modelling. *Zeitschrift Kunststofftechnik*, 2:91–125, 2017. ISSN 18642217. doi: 10.3139/O999.01022017.

[21] A. Kollmannsberger. *Heating characteristics of fixed focus laser assisted Thermoplastic-Automated Fiber Placement of 2D and 3D parts*. Dissertation, Technical University of Munich, Munich, 2019. URL https://mediatum.ub.tum.de/doc/1467244/1467244.pdf.

[22] R. Engelhardt, P. Hörmann, F. Rinker, G. Weyerer, and K. Drechsler. Efficiency of Automated Fiber Placement based on an Extensive Process Breakdown. In *35th SAMPE Europe International Technical Conference & Forum (SEICO 14)*, 2014.

[23] Premium AEROTEC. CFRP door frame center Augsburg, 2021. URL https://www.premium-aerotec.com/en/media/videos/.

[24] F. C. Campbell. *Manufacturing processes for advanced composites*. Elsevier, Oxford, 2004. ISBN 9781856174152. URL http://site.ebrary.com/lib/alltitles/docDetail.action?docID=10245839.

[25] U. P. Breuer. *Commercial aircraft composite technology*. Springer International Publishing, Cham, 2016. ISBN 978-3-319-31918-6.

[26] P. E. Irving and C. Soutis, editors. *Polymer Composites in the Aerospace Industry*. Elsevier, 2020. ISBN 9780081026793.

[27] MTorres. GKN/ MTorres fiberplacement machines manufacture the rear spars of the A350 wing box, 27.07.2021. URL https://www.youtube.com/watch?v=_ouF_YmZpNc.

[28] J. Sloan. The first composite fuselage section for the first composite commercial jet. *CompositesWorld*, 1.7.2018. URL https://www.compositesworld.com/articles/the-first-composite-fuselage-section-for-the-first-composite-commercial-jet.

[29] S. Francis. Composites in the race to space. *CompositesWorld*, 31.3.2020. URL https://www.compositesworld.com/articles/composites-in-space(2).

[30] VDI. CFK Bauteile von Beginn an fehlerfrei fertigen. *VDI-Z - Integrierte Produktion*, 6, 2017. URL http://www.ingenieur.de/VDI-Z/2017/Ausgabe-06/Simulation-CAD-CAM/CFK-Bauteile-von-Beginn-an-fehlerfreifertigen?page=1.

[31] Aerospace America. Modeling structural strength, 2020. URL https://aerospaceamerica.aiaa.org/departments/modeling-structural-strength/.

[32] J. Sloan. Boeing said to be evaluating new twin-aisle program. *CompositesWorld*, 3.2.2021. URL https://www.compositesworld.com/news/boeing-said-to-be-evaluating-new-twin-aisle-program.

[33] MTorres. Automated Fiber Placement - Airbus A350 Wings, 27.07.2021. URL https://www.mtorres.es/en/communication/news/mtorres-afps-airbus-350-wings.

[34] R. Engelhardt, R. Irmanputra, K. Brath, N. Aufenanger, and K. Drechsler. Thermoset Prepreg Compaction during Automated Fiber Placement and Vacuum Debulking. *Procedia CIRP*, 85:153–158, 2019. ISSN 22128271. doi: 10.1016/j.procir.2019.09.025.

[35] D. H.-J.A. Lukaszewicz, K. D. Potter, and J. Eales. A concept for the in situ consolidation of thermoset matrix prepreg during automated lay-up. *Composites Part B: Engineering*, 45(1):538–543, 2013. ISSN 13598368. doi: 10.1016/j.compositesb.2012.09.008.

[36] S. Rao, R. Umer, and W. J. Cantwell. An Evaluation of the Compression Response of High-Performance Prepregs for Afp Applications. *Polymers and Polymer Composites*, 23(6):389–398, 2015. ISSN 0967-3911. doi: 10.1177/096739111502300604.

[37] O. J. Nixon-Pearson, JP-H Belnoue, D. S. Ivanov, K. D. Potter, and Hallett. An experimental investigation of the consolidation behaviour of uncured prepregs under processing conditions. *Journal of Composite Materials*, 51 (13):1911–1924, 2017. ISSN 0021-9983. doi: 10.1177/0021998316665681.

[38] T. Orth, M. Krahl, P. Parlevliet, and N. Modler. Optical thermal model for LED heating in thermoset-automated fiber placement. *Advanced Manufacturing: Polymer & Composites Science*, 4(3):73–82, 2018. ISSN 2055-0340. doi: 10.1080/20550340.2018.1507798.

[39] M. Di Francesco, L. Veldenz, G. Dell'Anno, and K. D. Potter. Heater power control for multi-material, variable speed Automated Fibre Placement. *Composites Part A: Applied Science and Manufacturing*, 101:408–421, 2017. ISSN 1359835X. doi: 10.1016/j.compositesa.2017.06.015.

[40] P. Monnot, D. Williams, and M. Di Francesco. Power control of a flashlamp-based heating solution for Automated Dry Fibre Placement. In *18th European Conference on Composite Materials (ECCM-18)*, Athens, Greece, 2018.

[41] K. Croft, L. Lessard, D. Pasini, M. Hojjati, J. Chen, and A. Yousefpour. Experimental study of the effect of automated fiber placement induced defects on performance of composite laminates. *Composites Part A: Applied Science and Manufacturing*, 42(5):484–491, 2011. ISSN 1359835X. doi: 10.1016/j.compositesa.2011.01.007.

[42] H. Suemasu, Y. Aoki, S. Sugimoto, and T. Nakamura. Effect of gap on strengths of automated fiber placement manufactured laminates. *Composite Structures*, 263:113677, 2021. ISSN 02638223. doi: 10.1016/j.compstruct.2021.113677.

[43] J. P.-H. Belnoue, Tassos M., O. J. Nixon-Pearson, J. Kratz, D. S. Ivanov, I. K. Partridge, K. D. Potter, and S. R. Hallett. Understanding and predicting defect formation in automated fibre placement pre-preg laminates. *Composites Part A: Applied Science and Manufacturing*, 102:196–206, 2017. ISSN 1359835X. doi: 10.1016/j.compositesa.2017.08.008.

[44] F. Heinecke and C. Willberg. Manufacturing-Induced Imperfections in Composite Parts Manufactured via Automated Fiber Placement. *Journal of Composites Science*, 3(2):56, 2019. doi: 10.3390/jcs3020056.

[45] E. Guzman-Maldonado, P. Wang, N. Hamila, and P. Boisse. Experimental and numerical analysis of wrinkling during forming of multi-layered textile composites. *Composite Structures*, 208:213–223, 2019. ISSN 02638223. doi: 10.1016/j.compstruct.2018.10.018.

[46] J. P.-H. Belnoue and S. R. Hallett. A rapid multi-scale design tool for the prediction of wrinkle defect formation in composite components. *Materials & Design*, 187:108388, 2020. ISSN 02641275. doi: 10.1016/j.matdes.2019.108388.

[47] G. G. Lozano, A. Tiwari, C. Turner, and S. Astwood. A review on design for manufacture of variable stiffness composite laminates. *Proceedings of the Institution of Mechanical Engineers, Part B: Journal of Engineering Manufacture*, 230(6):981–992, 2016. ISSN 0954-4054. doi: 10.1177/0954405415600012.

[48] M. A. Thomas, S. R. Hallett, and P. M. Weaver. Design considerations for variable stiffness, doubly curved composite plates. *Composite Structures*, 244: 112170, 2020. ISSN 02638223. doi: 10.1016/j.compstruct.2020.112170.

[49] P. Hao, D. Liu, Y. Wang, X. Liu, B. Wang, G. Li, and S. Feng. Design of manufacturable fiber path for variable-stiffness panels based on lamination parameters. *Composite Structures*, 219:158–169, 2019. ISSN 02638223. doi: 10.1016/j.compstruct.2019.03.075.

[50] M. Montemurro and A. Catapano. On the effective integration of manufacturability constraints within the multi-scale methodology for designing variable angle-tow laminates. *Composite Structures*, 161:145–159, 2017. ISSN 02638223. doi: 10.1016/j.compstruct.2016.11.018.

[51] G. A. Fiordilino, M. I. Izzi, and M. Montemurro. A general isogeometric polar approach for the optimisation of variable stiffness composites: Application to eigenvalue buckling problems. *Mechanics of Materials*, 153:103574, 2021. ISSN 01676636. doi: 10.1016/j.mechmat.2020.103574.

[52] N. Bakhshi and M. Hojjati. An experimental and simulative study on the defects appeared during tow steering in automated fiber placement. *Composites Part A: Applied Science and Manufacturing*, 113:122–131, 2018. ISSN 1359835X. doi: 10.1016/j.compositesa.2018.07.031.

[53] K. Fayazbakhsh, M. Arian Nik, D. Pasini, and L. Lessard. Defect layer method to capture effect of gaps and overlaps in variable stiffness laminates made by Automated Fiber Placement. *Composite Structures*, 97:245–251, 2013. ISSN 02638223. doi: 10.1016/j.compstruct.2012.10.031.

[54] R. P. Smith, Z. Qureshi, R. J. Scaife, and H. M. El-Dessouky. Limitations of processing carbon fibre reinforced plastic/polymer material using automated fibre placement technology. *Journal of Reinforced Plastics and Composites*, 35(21):1527–1542, 2016. ISSN 0731-6844. doi: 10.1177/0731684416659544.

[55] A. Beakou, M. Cano, J.-B. Le Cam, and V. Verney. Modelling slit tape buckling during automated prepreg manufacturing: A local approach. *Com-*

posite Structures, 93(10):2628–2635, 2011. ISSN 02638223. doi: 10.1016/j.compstruct.2011.04.030.

[56] N. Bakhshi and M. Hojjati. Time-dependent wrinkle formation during tow steering in automated fiber placement. *Composites Part B: Engineering*, 165: 586–593, 2019. ISSN 13598368. doi: 10.1016/j.compositesb.2019.02.034.

[57] W. Qu, J. Gao, Di Y., R. He, Q. Yang, L. Cheng, and Y. Ke. Automated fiber placement path generation method based on prospective analysis of path performance under multiple constraints. *Composite Structures*, 255:112940, 2021. ISSN 02638223. doi: 10.1016/j.compstruct.2020.112940.

[58] K. Heller, S. Seyfferth, K. Kind, and K. Drechsler. A Post Lay-up Tack Peel Test for Aerospace Grade Prepreg Tapes. In SAMPE Europe, editor, *SAMPE Europe Conference 2020*, 2020.

[59] B. Böckl, C. Jetten, K. Heller, C. Ebel, and K. Drechsler. Online monitoring system for the tack of prepreg slit tapes used in automated fiber placement. In *18th European Conference on Composite Materials (ECCM-18)*, Athens, Greece, 2018.

[60] A. W. Smith, A. Endruweit, G.Y.H. Choong, D.S.A. de Focatiis, and P. Hubert. Adaptation of material deposition parameters to account for out-time effects on prepreg tack. *Composites Part A: Applied Science and Manufacturing*, 133:105835, 2020. ISSN 1359835X. doi: 10.1016/j.compositesa.2020.105835.

[61] R. J. Crossley, P. J. Schubel, and D.S.A. de Focatiis. Time–temperature equivalence in the tack and dynamic stiffness of polymer prepreg and its application to automated composites manufacturing. *Composites Part A: Applied Science and Manufacturing*, 52:126–133, 2013. ISSN 1359835X. doi: 10.1016/j.compositesa.2013.05.002.

[62] A. Endruweit, G. Y.H. Choong, S. Ghose, B. A. Johnson, D. R. Younkin, N. A. Warrior, and D. S.A. de Focatiis. Characterisation of tack for unidirectional prepreg tape employing a continuous application-and-peel test method. *Composites Part A: Applied Science and Manufacturing*, 114:295–306, 2018. ISSN 1359835X. doi: 10.1016/j.compositesa.2018.08.027.

[63] Y. Wang, M. K. Chea, J. P.-H. Belnoue, J. Kratz, D. S. Ivanov, and S. R. Hallett. Experimental characterisation of the in-plane shear behaviour of

UD thermoset prepregs under processing conditions. *Composites Part A: Applied Science and Manufacturing*, 133:105865, 2020. ISSN 1359835X. doi: 10.1016/j.compositesa.2020.105865.

[64] D. Maass. Progress in automated ply inspection of AFP layups. *Reinforced Plastics*, 59(5):242–245, 2015. ISSN 00343617. doi: 10.1016/j.repl.2015.05.002.

[65] E. Oromiehie, B. G. Prusty, P. Compston, and G. Rajan. Automated fibre placement based composite structures: Review on the defects, impacts and inspections techniques. *Composite Structures*, 224:110987, 2019. ISSN 02638223. doi: 10.1016/j.compstruct.2019.110987.

[66] P. D. Juarez and E. D. Gregory. In Situ Thermal Inspection of Automated Fiber Placement for manufacturing induced defects. *Composites Part B: Engineering*, 220:109002, 2021. ISSN 13598368. doi: 10.1016/j.compositesb.2021.109002.

[67] S. Meister, M. A. M. Wermes, J. Stüve, and R. M. Groves. Review of image segmentation techniques for layup defect detection in the Automated Fiber Placement process. *Journal of Intelligent Manufacturing*, 2021. ISSN 0956-5515. doi: 10.1007/s10845-021-01774-3.

[68] C. Sacco, A. B. Radwan, T. Beatty, and R. Harik. Machine Learning Based AFP Inspection: A Tool for Characterization and Integration. In *SAMPE 2019 - Charlotte, NC*. SAMPE, 04112019. doi: 10.33599/nasampe/s.19.1594.

[69] A. Kollmannsberger, R. Lichtinger, F. Hohenester, C. Ebel, and K. Drechsler. Numerical analysis of the temperature profile during the laser-assisted automated fiber placement of CFRP tapes with thermoplastic matrix. *Journal of Thermoplastic Composite Materials*, 31(12):1563–1586, 2018. ISSN 0892-7057. doi: 10.1177/0892705717738304.

[70] C. Stokes-Griffin, A. Kollmannsberger, P. Compston, and K. Drechsler. Steel-CF/PA 6 hybrids manufactured by a laser tape placement process: Effect of first-ply placement rate on lap shear strength for garnet blasted substrates. *Procedia Manufacturing*, 29:321–328, 2019. ISSN 23519789. doi: 10.1016/j.promfg.2019.02.144.

[71] O. Çelik, D. Peeters, C. Dransfeld, and J. Teuwen. Intimate contact development during laser assisted fiber placement: Microstructure and effect of

process parameters. *Composites Part A: Applied Science and Manufacturing*, 134:105888, 2020. ISSN 1359835X. doi: 10.1016/j.compositesa.2020.105888.

[72] Y. Di Boon, S. C. Joshi, and S. K. Bhudolia. Review: Filament Winding and Automated Fiber Placement with In Situ Consolidation for Fiber Reinforced Thermoplastic Polymer Composites. *Polymers*, 13(12), 2021. doi: 10.3390/polym13121951.

[73] S. Ehard. *Untersuchung eines laserbasierten Ablegeverfahrens zur Herstellung von hybriden Metall-Thermoplast-Faserverbundstrukturen*. Dissertation, Technical University of Munich, Munich, 2019.

[74] N. Remer, L. Bortolotto, M. Jürgens, and S. Ehard. Hybrid metal-composite drive shaft unit and method of manufacturing the same: EP20150400017, 2016.

[75] C. M. Stokes-Griffin, A. Kollmannsberger, S. Ehard, P. Compston, and K. Drechsler. Manufacture of steel–CF/PA6 hybrids in a laser tape placement process: Effect of first-ply placement rate on thermal history and lap shear strength. *Composites Part A: Applied Science and Manufacturing*, 111: 42–53, 2018. ISSN 1359835X. doi: 10.1016/j.compositesa.2018.05.007.

[76] V. Zinnecker, C. M. Stokes-Griffin, A. Khudiakova, M. Wolfahrt, and P. Compston. A comparative study for shear testing of thermoplastic-based composites and metal-composite hybrids. *Composites Part A: Applied Science and Manufacturing*, 137:105953, 2020. ISSN 1359835X. doi: 10.1016/j.compositesa.2020.105953.

[77] C. M. Stokes-Griffin, A. Kollmannsberger, P. Compston, and K. Drechsler. The effect of processing temperature on wedge peel strength of CF/PA 6 laminates manufactured in a laser tape placement process. *Composites Part A: Applied Science and Manufacturing*, 121:84–91, 2019. ISSN 1359835X. doi: 10.1016/j.compositesa.2019.02.011.

[78] R. Engelhardt, S. Ehard, T. Wolf, J. Oelhafen, A. Kollmannsberger, and K. Drechsler. In Situ Joining of Unidirectional Tapes on Long Fiber Reinforced Thermoplastic Structures by Thermoplastic Automated Fiber Placement for Scientific Sounding Rocket Applications. *Procedia CIRP*, 85:189–194, 2019. ISSN 22128271. doi: 10.1016/j.procir.2019.09.015.

[79] M. Legault. Building a better tail boom. *CompositesWorld*, 1.5.2013. URL https://www.compositesworld.com/articles/building-a-better-tail-boom.

[80] F. Henne, S. Ehard, A. Kollmannsberger, B. Hoeck, Sause, M. G. R., Obermeier, G., and K. Drechsler. Thermoplastic in-situ fiber placement for future solid rocket motor casings manufacturing. In SAMPE Europe, editor, *9th SAMPE Europe Technical Conference & Table Top Exhibition (SETEC 14)*, pages 46–53, 2014. ISBN 978-1-5108-5760-5.

[81] H. Mason. Moving forward on the Multifunctional Fuselage Demonstrator (MFFD). *CompositesWorld*, 28.10.2020. URL https://www.compositesworld.com/articles/moving-forward-on-the-multifunctional-fuselage-demonstrator-mffd-.

[82] R. Engelhardt, K. Brath, C. Ebel, and K. Drechsler. Analysis of the influence of Automated Fiber Placement and vacuum debulking on thermoset prepreg compaction. In *29th Annual International SICOMP Conference on Manufacturing and Design of Composites*, 2018.

[83] R. Engelhardt, S. Ehard, R. Jemmali, J. Oelhafen, A. Kollmannsberger, and K. Drechsler. Post Flight Analysis of an in situ Consolidated Thermoplastic Rocket Module with Integrated Fiber Optic Temperature Sensors. In *5th International Conference and Exhibition on Thermoplastic Composites (ITHEC)*, pages 37–40, Bremen, Germany, 2020.

[84] L. Veldenz, M. Di Francesco, P. Giddings, B. C. Kim, and K. Potter. Material selection for automated dry fiber placement using the analytical hierarchy process. *Advanced Manufacturing: Polymer & Composites Science*, 4(4):83–96, 2018. ISSN 2055-0340. doi: 10.1080/20550340.2018.1545377.

[85] L. Veldenz. *Automated Dry Fibre Placement and Infusion Process Development for Complex Geometries*. Dissertation, University of Bristol, 2019. URL https://research-information.bris.ac.uk/en/studentTheses/automated-dry-fibre-placement-and-infusion-process-development-fo.

[86] M. Y. Matveev, F. G. Ball, I. A. Jones, A. C. Long, P. J. Schubel, and M. V. Tretyakov. Uncertainty in geometry of fibre preforms manufactured with Automated Dry Fibre Placement and its effects on permeability. *Journal of Composite Materials*, 52(16):2255–2269, 2018. ISSN 0021-9983. doi: 10.1177/0021998317741951.

[87] A. R. Aziz, M. A. Ali, X. Zeng, R. Umer, P. Schubel, and W. J. Cantwell. Transverse permeability of dry fiber preforms manufactured by automated

fiber placement. *Composites Science and Technology*, 152:57–67, 2017. ISSN 02663538. doi: 10.1016/j.compscitech.2017.09.011.

[88] L. Veldenz, M. Di Francesco, S. Astwood, P. Giddings, B. C. Kim, and K. D. Potter. Assessment of Steering Capability of Automated Dry Fibre Placement through a Quantitative Methodology. In *3rd Symposium on Automated Composites Manufacturing (ACM3)*, 2017. ISBN 978-1-60595-431-8.

[89] O. Meyer. *Kurzfaser-Preform-Technologie zur kraftflussgerechten Herstellung von Faserverbundbauteilen*. Dissertation, University of Stuttgart, 2008.

[90] G. Gardiner. Cevotec's MAI ACoSaLUS project aims for full automation of composite sandwich structure production. *Composites World*, 15.09.2021. URL www.compositesworld.com/news/cevotecs-mai-acosalus-project-aims-for-full-automation-of-composite-sandwich-structure-p

[91] U. G. K. Wegst, H. Bai, E. Saiz, A. P. Tomsia, and R. O. Ritchie. Bioinspired structural materials. *Nature materials*, 14(1):23–36, 2015. ISSN 1476-1122. doi: 10.1038/NMAT4089.

[92] A. Lovatt and H. Shercliff. Material selection and processing: Material Selection Charts, 2002. URL http://www-materials.eng.cam.ac.uk/mpsite/interactive_charts/spec-spec/NS6Chart.html.

[93] D.H.-J.A. Lukaszewicz and K. D. Potter. The internal structure and conformation of prepreg with respect to reliable automated processing. *Composites Part A: Applied Science and Manufacturing*, 42(3):283–292, 2011. ISSN 1359835X. doi: 10.1016/j.compositesa.2010.11.014.

[94] D. van Ee and A. Poursartip. HexPly 8552 Material Properties Database for use with COMPRO CCA and Raven, 2009. URL https://www.wichita.edu/research/NIAR/Research/hexcel-8552/Additional-Documents-2.pdf.

[95] Hexcel. HexPly® 8552 Product Data Sheet: UD Carbon Prepregs, 2020. URL https://www.hexcel.com/user_area/content_media/raw/HexPly_8552_eu_DataSheet.pdf.

[96] R. Hill. A self-consistent mechanics of composite materials. *Journal of the Mechanics and Physics of Solids*, 13(4):213–222, 1965. ISSN 00225096. doi: 10.1016/0022-5096(65)90010-4.

[97] T. G. Gutowski, Z. Cai, S. Bauer, D. Boucher, J. Kingery, and S. Wineman. Consolidation Experiments for Laminate Composites. *Journal of Composite Materials*, 21(7):650–669, 1987. ISSN 0021-9983. doi: 10.1177/002199838702100705.

[98] T. G. Gutowski. Resin flow/fiber deformation model for composites. *SAMPE Q.; (United States)*, 16:4, 1985. URL https://www.osti.gov/biblio/5490235.

[99] T. G. Gutowski, J. Kingery, and D. Boucher. Experiments in composites consolidation: fiber deformation. *ANTEC 86*, pages 1316–1320, 1986.

[100] F. Robitaille and R. Gauvin. Compaction of textile reinforcements for composites manufacturing. I: Review of experimental results. *Polymer composites*, 19(2):198–216, 1998.

[101] F. Robitaille and R. Gauvin. Compaction of textile reinforcements for composites manufacturing. II: Compaction and relaxation of dry and H2O-saturated woven reinforcements. *Polymer composites*, 19(5):543–557, 1998.

[102] F. Robitaille and R. Gauvin. Compaction of textile reinforcements for composites manufacturing. III: Reorganization of the fiber network. *Polymer composites*, 20(1):48–61, 1999.

[103] G. D. Smith and A. Poursartip. A Comparison of Two Resin Flow Models for Laminate Processing. *Journal of Composite Materials*, 27(17):1695–1711, 1993. ISSN 0021-9983. doi: 10.1177/002199839302701704.

[104] P. Hubert and A. Poursartip. A Review of Flow and Compaction Modelling Relevant to Thermoset Matrix Laminate Processing. *Journal of Reinforced Plastics and Composites*, 17(4):286–318, 1998. ISSN 0731-6844. doi: 10.1177/073168449801700402.

[105] P. Hubert and A. Poursartip. Aspects of the Compaction of Composite Angle Laminates: An Experimental Investigation. *Journal of Composite Materials*, 35(1):2–26, 2001. ISSN 0021-9983. doi: 10.1177/002199801772661849.

[106] C. M. ÓBrádaigh, G. B. McGuinness, and R. B. Pipes. Numerical analysis of stresses and deformations in composite materials sheet forming: central indentation of a circular sheet. *Composites Manufacturing*, 4(2):67–83, 1993. ISSN 09567143. doi: 10.1016/0956-7143(93)90074-I.

[107] P. Hubert and A. Poursartip. A method for the direct measurement of the fibre bed compaction curve of composite prepregs. *Composites Part A: Applied Science and Manufacturing*, 32(2):179–187, 2001. ISSN 1359835X. doi: 10.1016/S1359-835X(00)00143-3.

[108] H. Darcy. *Les fontaines publiques de la ville de Dijon.* Les fontaines publiques de la ville de Dijon. Exposition et application des principes à suivre et des formules à employer dans les questions de distribution d'eau: ouvrage terminé par un appendice relatif aux fournitures d'eau de plusieurs villes au filtrage des eaux et à la fabrication des tuyaux de fonte, de plomb, de tole et de bitume. Dalmont, 1856. URL https://books.google.de/books?id=42EUAAAAQAAJ.

[109] B. T. Astrom. *Manufacturing of polymer composites.* CRC Press, London, 1997. ISBN 9780203748169.

[110] M. Li, Y. Gu, Z. Zhang, and Z. Sun. A simple method for the measurement of compaction and corresponding transverse permeability of composite prepregs. *Polymer composites*, 28(1):61–70, 2007.

[111] A. A. Somashekar, Simon Bickerton, and Debes Bhattacharyya. An experimental investigation of non-elastic deformation of fibrous reinforcements in composites manufacturing. *Composites Part A: Applied Science and Manufacturing*, 37(6):858–867, 2006. ISSN 1359835X.

[112] S. Comas-Cardona, P. Le Grognec, C. Binetruy, and P. Krawczak. Unidirectional compression of fibre reinforcements. Part 1: A non-linear elastic-plastic behaviour. *Composites Science and Technology*, 67(3-4):507–514, 2007. ISSN 02663538.

[113] V. Michaud, S. Sequeira Tavares, A. Sigg, S. Lavanchy, and J. A.E. Månson. Low pressure processing of high fiber content composites. In *8th international conference on flow processes in composite materials (FPCM8), Douai, France*, 2006.

[114] Z. Cai and T. Gutowski. The 3-D deformation behavior of a lubricated fiber bundle. *Journal of Composite Materials*, 26(8):1207–1237, 1992. ISSN 0021-9983.

[115] H. Sarrazin and G. S. Springer. Thermochemical and mechanical aspects of composite tape laying. *Journal of Composite Materials*, 29(14):1908–1943, 1995. ISSN 0021-9983.

[116] S. W. Park and R. A. Schapery. Methods of interconversion between linear viscoelastic material functions. Part IóA numerical method based on Prony series. *International Journal of Solids and Structures*, 36(11):1653–1675, 1999.

[117] P. Ludwik. On the influence of the speed of deformation in case of enduring deformations with special regard to the after-effects. *Phys. Zeit*, 10:411–417, 1909.

[118] J. P.-H. Belnoue, O. J. Nixon-Pearson, D. Ivanov, and S. R. Hallett. A novel hyper-viscoelastic model for consolidation of toughened prepregs under processing conditions. *Mechanics of Materials*, 97:118–134, 2016. ISSN 01676636. doi: 10.1016/j.mechmat.2016.02.019.

[119] J. P.-H. Belnoue, O. J. Nixon-Pearson, A. J. Thompson, D. S. Ivanov, K. D. Potter, and Hallett. Consolidation-driven defect generation in thick composite parts. *Journal of Manufacturing Science and Engineering*, 140(7):071006, 2018.

[120] J. P.-H. Belnoue, Dmitry S. Ivanov, and Stephen R. Hallett. Kinematically enhanced constitutive modelling: A viable option for the simulation of the manufacturing of full-scale composite parts. In *ECCM18 - 18th European Conference on Composite Materials, Athens, Greece, 24-28th June 2018*, 2018.

[121] Coriolis Composites. Coriolis C1: The difference in Automated Fiber Placement, 2021. URL https://www.coriolis-composites.com/fiber-placement-machines/coriolis-c1/.

[122] H. Hertz. Ueber die Berührung fester elastischer Körper. *Journal für die reine und angewandte Mathematik (Crelles Journal)*, 1882(92):156–171, 1882. ISSN 0075-4102. doi: 10.1515/crll.1882.92.156.

[123] K. L. Johnson. *Contact mechanics*. Cambridge Univ. Press, Cambridge, 9. print edition, 2003. ISBN 0521347963.

[124] R. Lichtinger, J. Lacalle, R. Hinterhölzl, U. Beier, and K. Drechsler. Simulation and experimental validation of gaps and bridging in the automated fiber placement process. *Science and Engineering of Composite Materials*, 22(2):131–148, 2015. ISSN 0792-1233. doi: 10.1515/secm-2013-0158.

[125] R. Irmanputra. *Experimental analysis of vacuum debulking with prepreg laminate at elevated temperature.* Bachelor's thesis, Technical University of Munich, Munich, 2019.

[126] M. Bissinger. *Experimental analysis of vacuum debulking with thermoset prepregs.* Bachelor's thesis, Technical University of Munich, Munich, 2020.

[127] GOM Gmbh. ATOS III: Optical Precision Measuring Machine (User Manual), 2021. URL https://www.gom.com/en/products/high-precision-3d-metrology.

[128] Vacuubrand. MV 10 NT diaphragm pump: Manual, 2021. URL https://www.vacuubrand.com/context/manuals/en/20901280.pdf.

[129] D.S.-C. Liu and P. Hubert. Bulk factor characterization of heated debulked autoclave and out-of-autoclave carbon fibre prepregs. *Composites Part B: Engineering*, 219:108940, 2021. ISSN 13598368. doi: 10.1016/j.compositesb.2021.108940.

[130] C. Hall, C. Ward, D. S. Ivanov, and K. D. Potter. The compaction of uncured toughened prepreg laminates in relation to automated forming. In *15th European Conference on Composite Materials (ECCM-15)*, Venice, Italy, 2012.

[131] D. Budelmann, H. Detampel, C. Schmidt, and D. Meiners. Interaction of process parameters and material properties with regard to prepreg tack in automated lay-up and draping processes. *Composites Part A: Applied Science and Manufacturing*, 117:308–316, 2019. ISSN 1359835X. doi: 10.1016/j.compositesa.2018.12.001.

[132] M. Etchegaray Bello. *Lab-scale experimental analysis of the compaction behavior of uncured thermoset prepreg for Automated Fiber Placement applications.* Term project, Technical University of Munich, Munich, 2020.

[133] M. Lörch. *Lab-scale compaction experiments for Automated Fiber Placement.* Master's thesis, Technical University of Munich, Munich, 2018.

[134] Díaz de la Hoz, A. *Development of a compaction simulation model for the thermoset Automated Fiber Placement process.* Bachelor's thesis, Technical University of Munich, Munich, 2019.

[135] S. Vogl. *Optimization and Application of a Compaction Simulation Model for the Thermoset Automated Fiber Placement Process*. Master's thesis, Technical University of Munich, Munich, 2020.

[136] M. Etchegaray Bello, R. Engelhardt, D. Bublitz, and K. Drechsler. Lab-scale experimental analysis of the cyclic compaction-recovery characteristics of uncured thermoset prepreg. *Advanced Manufacturing: Polymer & Composites Science*, 8(2):56–67, 2022. doi: 10.1080/20550340.2022.2064069.

[137] M. Etchegaray Bello, R. Engelhardt, and K. Drechsler. Dataset for cyclic compaction-recovery behavior of CF/epoxy/8552 multilayer samples, 2021. URL https://mediatum.ub.tum.de/1621517.

[138] P. Hubert, A. Johnston, A. Poursartip, and K. Nelson. Cure Kinetics and Viscosity Models for Hexcel 8552 Epoxy Resin. In L. Repecka and F. F. Saremi, editors, *2001: A materials and processes odyssey*, Science of advanced materials and process engineering series, pages 2341–2354. Society for the Advancement of Material and Process Engineering, Covina, Calif., 2001.

[139] D. S. Ivanov, Y. Li, C. Ward, and K. D. Potter. Transitional behaviour of prepregs in automated fibre deposition processes. In S. V. Hoa and P. Hubert, editors, *International Conference on Composite Materials 2013 (ICCM-19)*, pages 1381–1391. Curran Associates, Inc, Red Hook, NY, 2013. ISBN 978-1-62993-199-9.

[140] ASTM D3171-15, Standard Test Methods for Constituent Content of Composite Materials, ASTM International, 2015. URL www.astm.org.

[141] R. Engelhardt, S. Ehard, J. Oelhafen, A. Kollmannsberger, R. Amann, P. Günzel, and K. Drechsler. Development of a Lightweight Carbon Composite Rocket Module with Integrated Fiber Optical Temperature Sensors as Part of the Experiment "TESOS" on REXUS 23. In *ESA Symposium on European Rocket and Balloon Programmes and Related Research*, Essen, Germany, 2019. ISBN 9789292213077.

[142] K. Brath. *Analysis of compaction behavior during thermoset Automated Fiber Placement*. Master's thesis, Technical University of Munich, Munich, 2018.

[143] N. Aufenanger. *Experimental analysis of the compaction behaviour during Automated Fiber Placement and autoclave curing*. Term project, Technical University of Munich, Munich, 2019.

[144] S. Vogl. *Analysis of the influence of compaction during Automated Fiber Placement on the mechanical performance of composite laminates.* Term project, Technical University of Munich, Munich, 2020.

[145] GOM Gmbh. ATOS Capsule: Optical Precision Measuring Machine (User Manual), 2021. URL https://www.gom.com/en/products/high-precision-3d-metrology/atos-capsule.

[146] J. Geng. Structured-light 3D surface imaging: a tutorial. *Advances in Optics and Photonics*, 3(2):128, 2011. doi: 10.1364/AOP.3.000128.

[147] J. L. Devore, N.. Farnum, and J. Doi. *Applied statistics for engineers and scientists.* Cengage Learning, Stamford, CT, 3rd edition, 2014. ISBN 9781285972428.

[148] J. Lawson. *Design and analysis of experiments with R.* Texts in statistical science series. CRC Press, Boca Raton, FL, 2015. ISBN 978-1439868133.

[149] Keyence. 3D Profilometer Modellreihe VR: Oberflächenmessung, Kontur-, Ebenheits-, und Rauheitsmessung, 2018. URL https://www.keyence.de/ss/products/measure-sys/vr/.

[150] S. Sommacal, A. Miles, P. Compston, and M. Saadatfar. Advanced micro-CT imaging and microstructure characterization of carbon fiber reinforced 3D printed materials. In *ICTMS 2019 - International Conference on Tomography of Materials & Structures*, Cairns, Australia, 2019. URL https://currinda.s3.amazonaws.com/ann/Abstrakt-FullPaper/192/5c7cfc1f4c228-ICTMS2019_SSommacal_etal.pdf.

[151] DIN EN 2563:1997-03, Aerospace series - Carbon fibre reinforced plastics - Unidirectional laminates; determination of apparent interlaminar shear strength; German version EN 2563:1997, 1997.

[152] DIN EN ISO 14125:2011-05, Fibre-reinforced plastic composites - Determination of flexural properties (ISO 14125:1998 + Cor.1:2001 + Amd.1:2011); German version EN ISO 14125:1998 + AC:2002 + A1:2011, 2011.

[153] DIN EN 2561:1995-11, Aerospace series - Carbon fibre reinforced plastics - Unidirectional laminates - Tensile test parallel to the fibre direction; German version EN 2561:1995, 1995.

[154] DIN EN 2597:1998-08, Aerospace series - Carbon fibre reinforced plastics; unidirectional laminates - Tensile test perpendicular to the fibre direction; German version EN 2597:1998, 1998.

[155] DIN EN ISO 527-1:2019-12, Plastics - Determination of tensile properties - Part 1: General principles (ISO 527-1:2019); German version EN ISO 527-1:2019, 2019.

[156] DIN EN ISO 527-5:2010-01, Plastics - Determination of tensile properties - Part 5: Test conditions for unidirectional fibre-reinforced plastic composites (ISO 527-5:2009); German version EN ISO 527-5:2009, 2010.

[157] W. Grellmann and S. Seidler. *Polymer testing*. Hanser, Cincinnati, Ohio, 2007. ISBN 978-1-56990-410-7.

[158] D. B. Miracle. *A.S.M. handbook*. American Society of Metals, Materials Park, 2001. ISBN 0871707039.

[159] R. P. Theriault and Gottfried W. Ehrenstein. *Polymeric Materials*. Carl Hanser Verlag, 2019. ISBN 9783446214613.

[160] SAE-International. *Composite materials handbook CMH-17*. SAE International on behalf of CMH-17, [Warrendale, Pa.], 2017. ISBN 0768084504.

[161] M. Mehdikhani, L. Gorbatikh, I. Verpoest, and S. V. Lomov. Voids in fiber-reinforced polymer composites: A review on their formation, characteristics, and effects on mechanical performance. *Journal of Composite Materials*, 53 (12):1579–1669, 2019. ISSN 0021-9983. doi: 10.1177/0021998318772152.

[162] R. Ganesan. Experimental characterization of interlaminar shear strength. In *Delamination Behaviour of Composites*, pages 117–137. Elsevier, 2008. ISBN 9781845692445. doi: 10.1533/9781845694821.1.117.

[163] M. N. Bureau and J. Denault. Fatigue resistance of continuous glass fiber-/polypropylene composites: consolidation dependence. *Composites Science and Technology*, 64(12):1785–1794, 2004. ISSN 02663538. doi: 10.1016/j.compscitech.2004.01.016.

[164] W. D. Bascom and J. B. Romans. Microvoids in Glass-Resin Composites. Their Origin and Effect on Composite Strength. *Industrial & Engineering Chemistry Product Research and Development*, 7(3):172–178, 1968. ISSN 0196-4321. doi: 10.1021/i360027a003.

[165] Y. Li, Q. Li, and H. Ma. The voids formation mechanisms and their effects on the mechanical properties of flax fiber reinforced epoxy composites. *Composites Part A: Applied Science and Manufacturing*, 72:40–48, 2015. ISSN 1359835X. doi: 10.1016/j.compositesa.2015.01.029.

[166] L. Liu, B.-M. Zhang, D.-F. Wang, and Z.-J. Wu. Effects of cure cycles on void content and mechanical properties of composite laminates. *Composite Structures*, 73(3):303–309, 2006. ISSN 02638223. doi: 10.1016/j.compstruct.2005.02.001.

[167] D. E. W. Stone and B. Clarke. Ultrasonic attenuation as a measure of void content in carbon-fibre reinforced plastics. *Non-Destructive Testing*, 8(3): 137–145, 1975. ISSN 00291021. doi: 10.1016/0029-1021(75)90023-7.

[168] J.-M. Tang, W. I. Lee, and G. S. Springer. Effects of Cure Pressure on Resin Flow, Voids, and Mechanical Properties. *Journal of Composite Materials*, 21 (5):421–440, 1987. ISSN 0021-9983. doi: 10.1177/002199838702100502.

[169] K. M. Uhl, B. Lucht, H. Jeong, and D. K. Hsu. Mechanical Strength Degradation of Graphite Fiber Reinforced Thermoset Composites Due to Porosity. In D. O. Thompson and D. E. Chimenti, editors, *Review of Progress in Quantitative Nondestructive Evaluation*, pages 1075–1082. Springer US, Boston, MA, 1988. ISBN 978-1-4612-8275-4. doi: 10.1007/978-1-4613-0979-6-24.

[170] DIN EN ISO 25178-1:2016-12, Geometrical product specifications (GPS) - Surface texture: Areal - Part 1: Indication of surface texture (ISO 25178-1:2016); German version EN ISO 25178-1:2016, 2016.

[171] M. Lörch. *Implementation of a MATLAB process model of Automated Fiber Placement for process time analyses.* Term project, Technical University of Munich, Munich, 2017.

[172] C. Dsouza. *Optimization and application of a process model of the Automated Fiber Placement process for aerospace applications.* Master's thesis, Politecnico di Milano, Milan, 2020.

[173] H. Wildemann. *Produktionscontrolling: Systemorientiertes Controlling schlanker Produktionsstrukturen*, volume 9 of *TCW*. TCW, Transfer-Centrum-Verl., München, 3rd edition, 1997. ISBN 9783931511104.